EIT2024

THE 24TH INTERNATIONAL CONFERENCE ON BIOMEDICAL APPLICATIONS OF ELECTRICAL IMPEDANCE TOMOGRAPHY

第24届国际电阻抗成像生物医学应用会议

PROCEEDINGS

Edited By

Lixin Xie | Feng Fu | Yun Long | Huiqing Ge | Qing Pan | Zhanqi Zhao

27th-30th June, 2024 Hangzhou, China
2024年6月27-30日 中国 杭州

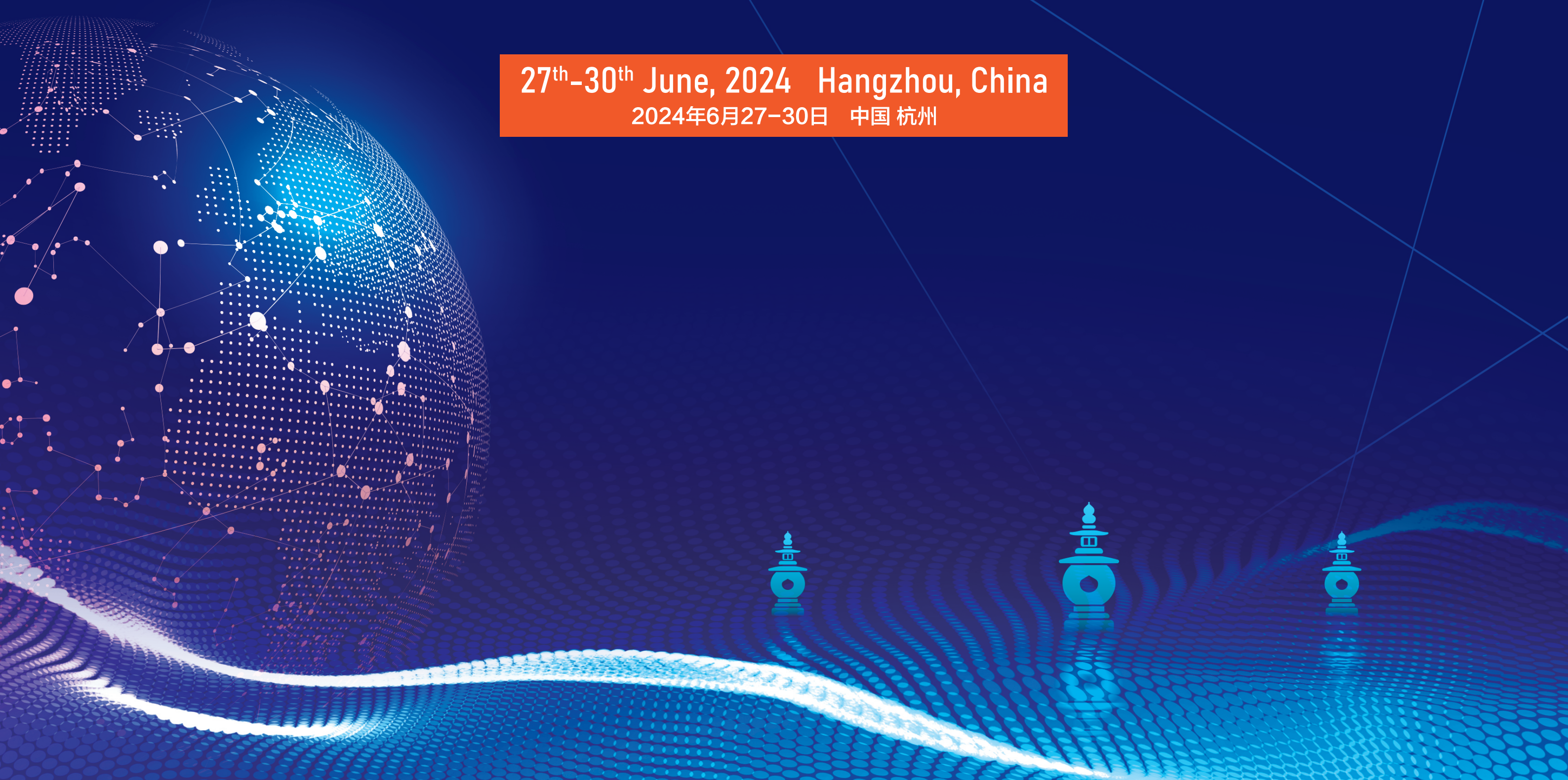

Table of Contents

Effects of Recruitment Maneuver on Regional Respiratory Mechanics in Patients with Acute Hypoxemic Respiratory Failure

Rui Zhang[1], Jiayi Guan[1], Ruoming Tan[1], Lei Li[1], Jie Huang[1], Jing Xu[2], Jialin Liu[2], Hongping Qu[1], Zhanqi Zhao[3,4,5]

[1]Department of Critical Care Medicine, Ruijin Hospital, Shanghai Jiao Tong University School of Medicine, Shanghai, China
[2]Department of Geriatrics, Ruijin Hospital, Shanghai Jiao Tong University School of Medicine, Shanghai, China
[3]School of Biomedical Engineering, Guangzhou Medical University, Guangzhou, China
[4]Department of Critical Care Medicine, Peking Union Medical College Hospital, Chinese Academy of Medical Sciences, Beijing, China
[5]Institute of Technical Medicine, Furtwangen University, Villingen-Schwenningen, Germany

Abstract: The recruitment-to-inflation (R/I) ratio is a simple bedside method to evaluate the potential for lung recruitment. We developed a method that to calculate the regional R/I ratios of the whole lung by EIT. We found that regional R/I ratios provided regional information to predict the potential effect of RM on lung regional respiratory mechanics. We included 30 patients with acute hypoxemic respiratory failure, and we found that Regional R/I ratios provided regional information to predict the potential effect of RM on lung regional respiratory mechanics.

1 Introduction

The recruitment-to-inflation (R/I) ratio is a simple bedside method to evaluate the potential for lung recruitment (PLR) and identify patients who could benefit from high positive end-expiratory pressure (PEEP). Using electrical impedance tomography (EIT), we developed a method to calculate the regional R/I ratios of the whole lung, non-dependent (ventral) and dependent (dorsal) lung. The aim of this study was to assess the ability of regional R/I ratios on predicting PEEP-induced changes in collapssion and overdistention, estimated by regional compliances.

2 Methods

This was an observational study. EIT recordings were taken during a recruitment maneuver (RM), with PEEP levels ranging from 5 to 15 (cmH2O). We calculated the R/I ratio for the whole lung (R/I GLOBAL), as well as for the dorsal (R/I D) and ventral (R/I V) regions. A high potential for lung recruitability (PLR) was defined as an R/I ratio above the median value for the study population. Additionally, we measured the regional change in compliance (ΔCrs) resulting from the RM. A higher R/I ratio signifies greater lung compliance, indicating a larger volume of lung recruited relative to the volume of overdistension. Conversely, a lower R/I ratio suggests a higher risk of overdistention without effective recruitment upon PEEP increase.A high potential lung recruitability (PLR) was defined as an R/I ratio exceeding the median for the population.

3 Results

The study included 30 patients with acute hypoxemic respiratory failure, with a mean PaO2/FiO2 ratio of 182 ± 75 and a mean respiratory system compliance of 21±4 mL/cmH2O. The median R/I GLOBAL was 1.51 [1.11-1.75]. The R/I for the dorsal region (R/I D) was significantly higher than that for the ventral region (R/I V) (median R/I ratio of 0.98 [0.78–1.25] vs. 0.62 [0.42–0.83], p<0.001). The value of median R/I D to median R/I GLOBAL was 0.64, and the value of median R/I V to median R/I GLOBAL was 0.41. A higher R/I D correlated with a greater decrease in dorsal lung compliance (Crs) (r=-0.712, p=0.015) due to alveolar collapse at low PEEP levels. Patients with a high regional (dorsal lung) PLR exhibited a lower ΔCrs in the dorsal lung compared to those with a low regional (dorsal lung) PLR (p<0.001).

4 Conclusion

Regional R/I ratios provided regional information to predict the potential effect of RM on lung regional respiratory mechanics.

5 Acknowledgements

The authors would like to express their gratitude to EIT 2024.

References

[1] Chen L, Del Sorbo L, Grieco DL, Junhasavasdikul D, Rittayamai N, Soliman I, Sklar MC, Rauseo M, Ferguson ND, Fan E, Richard JM, Brochard L. Potential for Lung Recruitment Estimated by the Recruitment-to-Inflation Ratio in Acute Respiratory Distress Syndrome. A Clinical Trial. Am J Respir Crit Care Med. 2020 Jan 15; 201(2): 178-187. doi: 10.1164/rccm.201902-0334OC

[2] Pavlovsky B, Desprez C, Richard JC, Fage N, Lesimple A, Chean D, Courtais A, Mauri T, Mercat A, Beloncle F. Bedside personalized methods based on electrical impedance tomography or respiratory mechanics to set PEEP in ARDS and recruitment-to-inflation ratio: a physiologic study. Ann Intensive Care. 2024 Jan 5; 14(1): 1. doi: 10.1186/s13613-023-01228-4. PMID: 38180544.

[3] Pettenuzzo T, Sella N, Lorenzoni G, Calore A, Zarantonello F, Andreatta G, De Cassai A, Gregori D, Boscolo A, Navalesi P. The recruitment-to-inflation ratio is correlated with EIT-derived collapse and overdistention in COVID- 19 ARDS. Am J Respir Crit Care Med. 2022; 206(10): 1284-6.

Improved Data-Driven EIT Imaging for Temporal Sequences using Recurrent Neural Networks

Jacob Thönes[1] and Sascha Spors[1]

[1]Institute of Communications Engineering, University of Rostock, Rostock, Germany, jacob.thoenes@uni-rostock.de

Abstract: Data-driven reconstruction techniques using deep neural network (DNN) architectures are applied more frequently in the field of electrical impedance tomography (EIT). The solution of the underlying ill-posed inverse problem may benefit from the possibilities of machine learning (ML). This contribution demonstrates, how knowledge on recurring sequences of EIT measurements (e.g. breathing cycles) may be used to improve the reconstruction. A combination of a Long Short-Term Memory (LSTM) and an Variational Autoencoder (VAE) is used.

1 Introduction

EIT is an established clinical procedure for monitoring the pulmonary system of intensive care patients. Especially in clinical applications, the reliability of imaging is important. One potential approach for enhancement involves the training of a recurrent network to learn the breathing cycle. Our approach could contribute to a more precise recognition of deviations from the established cycle.

2 Methods

To reconstruct the conductivity distribution γ from the voltage data $\mathbf{V}$, the inverse EIT problem is solved by a combination of a VAE and a mapper, which can be described as the mapping $\Gamma : \mathbf{V} \mapsto \gamma$ [1].

2.1 Data Acquisition

For our in-silico study data was simulated using the pyEIT [2] Python package. Therefore, a thorax finite element mesh (FEM) with 16 electrodes was created. The simulation model does not include the electrode-skin contact impedance. The empty area has a conductivity value of 1. For representing the lungs two circles were placed inside this area with a conductivity of 10. By increasing and decreasing the size of the circles, inhalation, and exhalation are approximated, see figure 1.

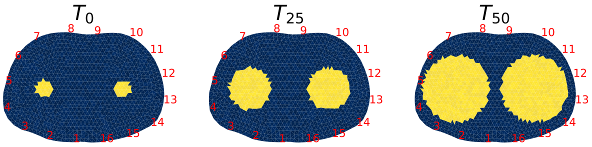

Figure 1: Excerpts from the simulated data set.

A breathing period T_t consists of $N = 100$ $(0 \leq t \leq N-1)$ frames. For each sample, normal distributed noise was added to all mesh elements $\gamma \in \mathbb{R}^{1912}$ for better generalization during the training. The generated voltage time series data set consists of 100 periods, i.e. 10 000 samples. For the model training, $L = 8\,000$, and for testing $2\,000$ of the samples were used.

2.2 Reconstruction Model

The VAE is a generative probabilistic model that consists of an encoder Φ and a decoder Ψ. Between these components, a compact representation of the conductivity distribution γ, called latent space $\mathbf{z} \in \mathbb{R}^8$, is learned. The mapper Ξ links the voltage data to the lower dimensional latent representation during supervised learning. The final reconstruction model architecture is described in equation (1).

$$\Gamma := \Xi \circ \Psi : \mathbf{V} \mapsto \mathbf{z} \mapsto \gamma \tag{1}$$

A mapper a) is trained with a single voltage vector $\mathbf{V} = \{\mathbf{v}_t\}$ and maps it to the latent space $\mathbf{z}_t$ at time $(0 \leq t \leq L-1)$. The mapper b) and mapper c) are trained with the current and a sequence of $l = 3$ past voltage data samples $\mathbf{V} = \{\mathbf{v}_{t-3}, \mathbf{v}_{t-2}, \mathbf{v}_{t-1}, \mathbf{v}_t\}$ at time $(l \leq t \leq L-1)$. Mapper c) has the same architecture as mapper b), but with an LSTM layer before the output. An LSTM network is designed to capture and learn patterns in sequential data. So the LSTM module is responsible for estimating the correlation in the temporal series of features inferred from the VAE [3].

3 Result

Figure 2 evaluates the three mapper architectures based on the deviation between the ground truth and the reconstructed conductivity distribution from equation (1). The deviation is computed by counting the difference of FEM elements representing the lungth and the empty ground. It can be seen that with prior knowledge of past measurements, more precise reconstruction is possible.

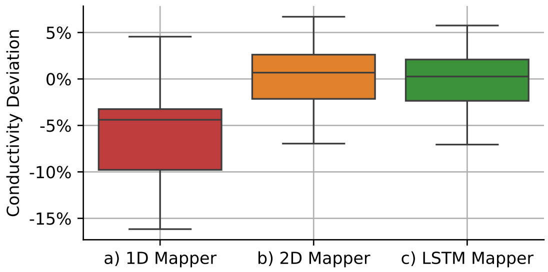

Figure 2: Performance comparison of the three mappers for unseen samples.

4 Conclusions

The presented results agree with the assumption, that the incorporation of memory into a DNN for absolute EIT imaging improves the reliability. The full code is available on GitHub [4].

5 Acknowledgements

Funded by the Deutsche Forschungsgemeinschaft (DFG, German Research Foundation) – SFB 1270/2 - 299150580.

References

[1] Seo, Jin Keun, et. al. A learning-based method for solving ill-posed nonlinear inverse problems: a simulation study of lung EIT, *SIAM journal on Imaging Sciences*, 1275–1295, 2019

[2] B. Liu, et. al. pyeit: A python based framework for electrical impedance tomography, *SoftwareX*, vol. 7, pp. 304-308, 2018

[3] Lin, Shuyu, et. al. Anomaly detection for time series using vae-lstm hybrid model, *IEEE*, 4322–4326, 2020

[4] Thönes, Jacob, Improved Data-Driven EIT Imaging for Temporal Sequences using Recurrent Neural Networks, *https://github.com/spatialaudio/Data-Driven-EIT-Imaging-using-Recurrent-Neural-Networks*, 2023

Image Reconstruction Based on an Improved Dense Fully Connected Network for Brain Electrical Impedance Tomography

Luanjun Wang[1,2], Yanyan Shi[1,2], Yating Li[1] and Feng Fu[2]
[1]Henan Normal University, Xinxiang, China, yyshi113@hotmail.com
[2]Forth Military Medical University, Xi'an, China

Abstract: To solve the ill-posed inverse problem in the electrical impedance tomography (EIT), a new image reconstruction method based on an improved dense full convolutional neural network (Y-DCNN) is proposed. Simulation results show that cerebral haemorrhage can be accurately reconstructed by the proposed method.

1 Introduction

As a functional imaging technique, electrical impedance tomography (EIT) is able to reconstruct conductivity distribution change in human tissues when there is pathological variation. Comparing with other tomography techniques such as computed tomography (CT) and magnetic resonance imaging (MRI), EIT has the advantages of non-invasiveness, low-cost and radiation-free. Therefore, EIT shows its great potential in different medical fields. However, the main drawback of EIT is its low spatial resolution. To solve the problem, deep learning methods have been preferred in the image reconstruction of EIT. A method based on a hybrid network which combines convolutional neural network and transformer is proposed to obtain high-quality reconstructed images in [1]. In [2], an imaging method which combines convolutional neural network with D-bar method is proposed. In this paper, a Y-DCNN based image reconstruction method is proposed to map the nonlinear relationship between measured voltage and conductivity distribution.

2 Methods

The overall structure of the proposed method based on Y-DCNN is shown in Figure 1. The network mainly includes one convolution block, three different dense convolution blocks, connection layer, global average pooling and full connection layer. For an EIT system equipped with 16 electrodes, the input of the network is 16 × 12 boundary measurement voltage data. Improved dense convolutional blocks of different types are used to obtain information from the data of different scales. As a result, the network is more sensitive to the input data. Meanwhile, the activation function is placed before the convolutional layer and the pre-activation strategy is adopted. This simplifies the training process of the network and improves the generalization performance. Besides, the problem of gradient disappearing can be more efficiently solved than the traditional approach of applying activation functions. The risk of network overfitting is reduced by utilizing dense blocks and transition blocks. Mixed pooling preserves more input features and effectively prevents information loss. The connection layer combines the parallel input features of the previous layer. Finally, a predicted conductivity change vector containing 2777 pixels can be obtained from the output. In the study, a three-layer head model is built in the simulation. By changing the position and size of the inclusion which simulate cerebral hemorrhage, a large number of training dataset is generated. There are 10235 samples in the training dataset and the testing dataset includes 1383 samples. Each sample contains 192 boundary voltage data. Images reconstructed for three models are shown in Figure 2. The performance of the proposed method is compared with three deep leaning methods (FCNN, CNN and Densenet) in the previous studies. It is observed that the size and the location of the cerebral hemorrhage are more accurately recovered in the images reconstructed by the proposed method than the other three methods. In addition, the background is clearer and free of artifacts.

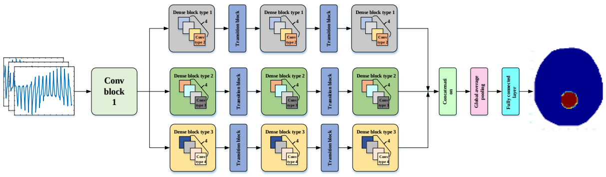

Figure 1: The overall structure of the proposed method.

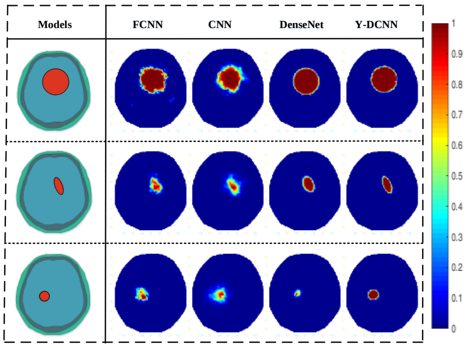

Figure 2: Comparison of image reconstruction with the four different deep leaning methods.

3 Conclusions

In this study, a deep learning-based Y-DCNN method is proposed for image reconstruction of haemorrhage in the brain EIT. In the future, the proposed method will be estimated by phantom experiments.

4 Acknowledgements

This work is supported by National Natural Science Foundation of China under Grant 52277234.

References

[1] Y. Y. Shi, et al. *IEEE Trans. Instrum. Meas*, 72: 4504612, 2023.
[2] S. J. Hamilton, A. Hänninen, A. Hauptmann, and V. Kolehmainen *Physiol. Meas*, 40: 074002, 2019.

Time-constant-domain Electrical Impedance Tomography (*tcd*EIT) for Dermis Layer Visualization

Kiagus Aufa Ibrahim[1], Prima Asmara Sejati[1], Marlin Ramadhan Baidillah[2], Shinsuke Akita[1], and Masahiro Takei[1]

[1]Chiba University, Chiba, Japan kiagus2@chiba-u.jp
[2]National Research and Innovation Agency, Jakarta, Indonesia

Abstract: Time-constant-domain Electrical impedance tomography (*tcd*EIT) and a spatial shifted measurement pattern for dermis layer visualization has been proposed. The objective is to image the conductivity distribution in the dermis layer in different sodium-ion concentrations. The *tcd*EIT has three steps which are (1) spatial-shifted pattern, (2) distribution of relaxation times (DRT), and (3) dermis concentration visualization. The simulation results show that at $\psi = 1$, the reconstructed image show high accuracy inside the dermis area.

1 Introduction

Excess sodium-ion concentration in the dermis layer of the skin is linked to serious diseases, such as psoriasis and hypertension. The visualization of the dermis layer is able to provide information about the sodium-ion concentration level related to the skin diseases to aid in their diagnosis [1]. This paper presents a novel approach using electrical impedance tomography (EIT) to image the conductivity distribution in the dermis layer in different sodium-ion concentrations.

2 Methods

The *tcd*EIT has three steps which are (1) spatial shifted measurement pattern, as shown in Figure 1, based on quasi-adjacent measurement pattern, there are three variations $\psi = \{0,1,2\}[-]$, (2) distribution of relaxation times (DRT), and (3) dermis concentration imaging. The predicted impedance of DRT, $\mathbf{Z}_{\mathrm{drt}}$ is represented by the following equation [2]:

$$\mathbf{Z}_{\mathrm{drt}}(f) = \mathbf{Z}'_{\infty} + \int_0^{\infty} \frac{\gamma(\ln\tau)}{1+j2\pi f\tau} \mathrm{d}(\ln\tau) \qquad (1)$$

where $\mathbf{Z}'_{\infty}$ is the resistance at the high frequency, $\gamma(\ln\tau)$ is the distribution function of relaxation time, f is the frequency, and τ is the relaxation time. The correlation between measured impedance, $\mathbf{Z}_{\mathrm{meas}}$ and $\mathbf{Z}_{\mathrm{drt}}$ provides insight into the conductivity distribution in dermis layer, $\boldsymbol{\sigma}^{\mathrm{d}}$. In order to reconstruct $\boldsymbol{\sigma}^{\mathrm{d}}$, Gauss-Newton image reconstruction is used [3]. In order to evaluate the proposed method, sodium-ion concentrations $c^{Na} = \{5, 10, 15, 20, 25, 30, 35, 40, 45, 50\}[\mathrm{mM}]$ are used in simulation.

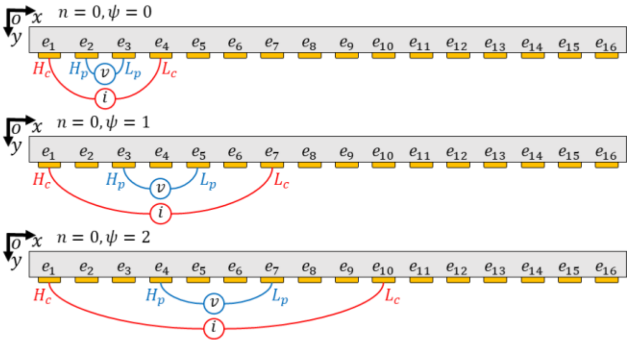

Figure 1: Spatial-shifted measurement pattern.

3 Results

Figure 2 shows the simulation results of *tcd*EIT with various sodium-ion concentrations c^{Na} and the region of interest (ROI) of the dermis layer (black square). The sodium concentration c^{Na} is shown by the red portion of the reconstructed images. At $\psi = 1$, the image of sodium-ion concentration distribution is emphasized on the ROI, which increases the measurement accuracy.

4 Conclusions

Time-constant-domain Electrical impedance tomography (*tcd*EIT) and a spatial shifted measurement pattern was evaluated to visualize the sodium-ion concentration in the dermis layer. Based on the simulations result, the proposed method has successfully visualized the sodium-ion concentration distribution at $\psi = 1$.

5 Acknowledgements

The authors would like to express their gratitude to Isnan Nur Rifai and Ridwan Wicaksono for helping the simulation and image analysis.

References

[1] IN Rifai, et al *Meas.Sci.Tech.*, 34: 074006, 2023.
[2] TH Wan et al. *Electrochimica Acta*, 184: 483-99, 2015.
[3] PN Darma et al *IEEE Sens. J*, 20: 9469-79, 2020.

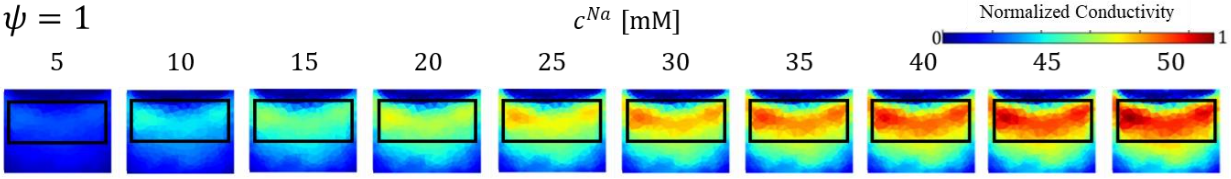

Figure 2: *tcd*EIT result based on simulation at $\psi = 1$.

Structural Visualization in Porcine Lymphedema Subcutaneous Adipose Tissue Phantoms by Four-Dimensional Open Electrical Impedance Spectro-tomography (4D-*o*EIST)

Yiqun Tang[1], Ryoma Ogawa[2*], Songshi Li[2], Shinsuke Akita[3], Masahiro Takei[2]
[1]Department of Mechanical Engineering, Division of Fundamental Engineering, Graduate School of Science and Engineering, Chiba University, Chiba 263-8522, Japan
[2]Graduate School of Engineering, Chiba University, Chiba 263-8522, Japan
[3]Department of Plastic, Reconstructive, and Esthetic Surgery, Chiba University Hospital, Chiba 263-8522, Japan

Abstract: The structure changes of hypertrophy and fibrosis in ex-vivo lymphedema subcutaneous adipose tissue (LE-SAT) at different lymphedema stages have been characterized by porcine phantoms and visualized by the four-dimensional open electrical impedance spectro-tomography implemented with variational autoencoder (4D-oEIST). The 4D-oEIST has 3 steps, Step 1: Characteristic frequency analysis by the distribution of relaxation time (DRT) analysis, Step 2: 4D-oEIST image reconstruction at characteristic frequencies, Step 3: Image post-processing by variational autoencoder. In order to validate the structural visualization capabilities of 4D-oEIST, porcine LE-SAT fibrosis and hypertrophy phantoms are prepared. In the measurements of the porcine LE-SAT hypertrophy phantoms and fibrosis phantoms within a frequency range of 100Hz-5MHz, the characteristic frequency f_c^{hy} and f_c^{fib} are found. Then by reconstructing the conductivity difference $\Delta\sigma_f$ by 4D-oEIST, the corresponding images for the structural changes are obtained.

1 Introduction

An innovative 4-dimensional open electrical impedance spectro-tomography (4D-*o*EIST) for visualizing the structural change of lymphedema subcutaneous adipose tissue (LE-SAT) is proposed in this paper. Comparing to computed tomography (CT) and magnetic resonance imaging (MRI), it is able to capture the different structure in LE-SAT tissue without radiation damage or agent injection [1, 2]. In previous study, a single row 16-electrode EIT sensor is developed to measure tissue conductivity change to visualize the sodium concentration in the dermis layer [3]. However, it has the restriction of identifying different targets and lack of spatial resolution. In order to improve this method, this research developed 1) 4×4 planar senor to improve the spatial resolution, 2) 4D-oEIST to identify fibrosis and hypertrophy in LE-SAT validated by finding the characteristic frequency f_c^{fib} and f_c^{hy} for fibrosis and hypertrophy, respectively, and reconstruct the 4D-*o*EIST image at f_c^{fib} and f_c^{hy}.

2 Methods

2.1 Figures and tables

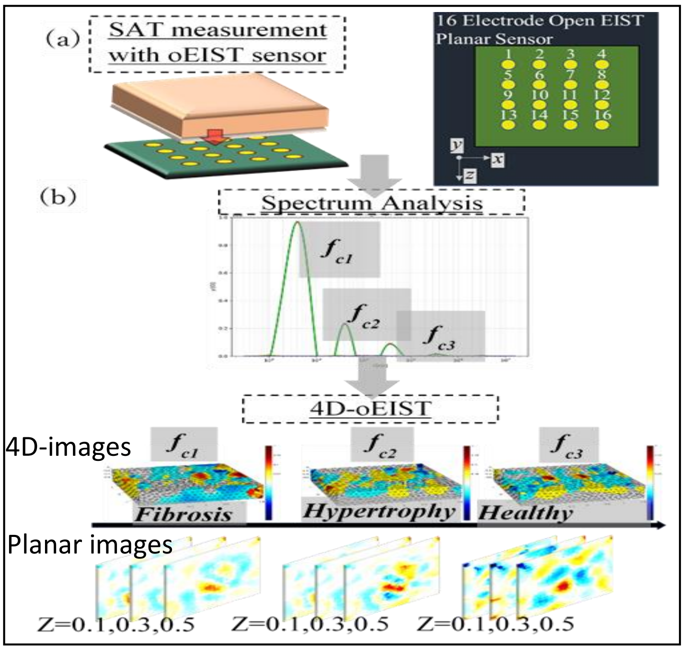

Fig. 1 (a) schematic of 4D-*o*EIST planar sensor and SAT measurement, (b) schematic flow of 4D-*o*EIST method

2.2 Equations

Equations should be placed on separate lines and numbered

$$Z(\omega) = R_\infty + \frac{R_0 - R_\infty}{1+(j\omega\tau)^\alpha} \tag{1}$$

$$J_{ij}(x,y,z) = -\int_{voxel} \nabla u(I^i) \cdot \nabla \mathrm{u}(I^j)\mathrm{dH} \tag{2}$$

$$\Delta Z = Z_{f_{c_1}} - Z_{f_{c_2}} = J_{ij}\Delta\sigma \tag{3}$$

3 Conclusions

This paper developed the 4D-*o*EIST method and validate its ability to identify fibrosis and hypertrophy, as 2 structure changes in LE-SAT.

4 Acknowledgements

This work was supported by JSPS KAKENHI [grant numbers JP19J00240, JP21K14072], JST SPRING [grant number J22HJ00001] and Chiba University [grant number J09KF00610].

References

[1] Hadjis, N., Carr, D., Banks, L., & Pflug, J. (1985). *American Journal of Roentgenology*, 144(2), 361-364.
[2] Salehi, B.P., Sibley, R.C., Friedman, R., Kim, G., Singhal, D., Loening, A.M. and Tsai, L.L. (2023), *J Magn Reson Imaging*, 57: 977-991.
[3] Isnan Nur Rifai et al 2023 Biomed. Phys. Eng. Express 9 045013.

EIT Gesture Recognition with Temporal Convolutional Networks

Guanghong Huang[1], Wentao Wang[1] and Hancong Wu[1]

[1]South China University of Technology, Guangzhou, China, hancongwu@scut.edu.cn

Abstract: This work demonstrates the limb position effect on EIT-based gesture recognition. We investigate the application of temporal convolutional networks (TCN) for the mitigation of limb position effect.

1 Introduction

Gesture recognition is an important tool for human-computer interaction. As a non-invasive sensing technique, EIT has been applied in gesture recognition in recent years [1]. Compared with camera-based and myoelectric-based techniques, EIT is more robust to the line-of-sight occlusion and measuring noise, respectively. However, due to the deformation of the muscle when changing limb position, EIT signals related to hand motion intention are easily overwhelmed by those due to limb movement [2]. In this study, we demonstrate the application of TCN for EIT based gesture recognition. The accuracy under untrained limb positions is compared.

2 Methods

Experimental protocol

We ran an experiment with two able-body subjects to test the limb position effect on EIT gesture classification. As can be seen in Figure 1, 8 electrodes were evenly distributed on the wrist and the forearm of the subject respectively. Subjects repeated six gestures 10 times in five different limb positions (middle, up, down, left and right), with a duration of 3 seconds and an interval of 5 seconds. EIT signals were collected at 50 kHz stimulation frequency.

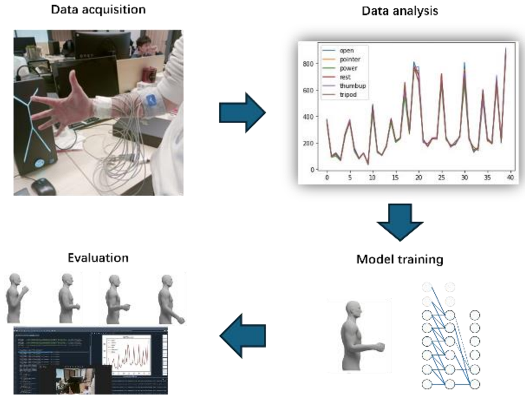

Figure 1: Experimental protocol.

Data analysis

The classifier was trained in middle limb position and tested in other limb positions with conventional machine learning based methods to demonstrate the limb position effects [3, 4]. Both raw data and calibrated data were evaluated. To better extract the temporal information in the EIT signals, we used the TCN model for feature extraction. 6 distinct structures by combining 3 different numbers of convolutional layers and 2 kernel sizes were compared.

3 Results

As can be seen in Table 1, although conventional classifiers classified the gesture correctly in the trained position, significant accuracy drop is observed when limb position changes, especially with the absolute voltage data. To extract the temporal information using TCN, we adopted a 400ms window with 100ms overlap, and tested by 6 different structures (Table 2). With 2 dilation layer and 5 kernels in each layer, TCN could maintain over 97% accuracy in untrained limb positions. The model has only 0.08M parameters, which is easy to train and suitable for the implementation in wearable devices.

Table 1: Comparison between different preprocessing methods and classifiers

Data type	Accuracy Limb position	Classifier				
		CNN	LDA	KNN	MLP	SVM
Voltage difference	Middle	0.9910	0.9660	0.9813	0.9877	0.9857
	Untrained positions	0.8778	0.8682	0.8973	0.8634	0.9171
Absolute voltage	Middle	0.9727	0.9992	0.9996	0.9536	0.8783
	Untrained positions	0.5928	0.2054	0.6345	0.5852	0.6262

Table 2: Classification accuracy and model size of TCN with different structure settings

Kernel size	5			10		
Dilation factor	[1,2]	[1,2,4]	[1,1,2,4]	[1,2]	[1,2,4]	[1,1,2,4]
Middle position	0.9913	0.9930	0.9933	0.9937	0.9953	0.9950
Untrained positions	0.9724	0.9675	0.9619	0.9669	0.9621	0.9511
Model size	0.08M	0.12M	0.16M	0.15M	0.23M	0.31M

4 Discussions

Change of limb positions significantly affect the forearm EIT signals for making a gesture. Although the time-different calibration eliminates the common errors in EIT measurement, factors such as the gravity effect change the conductivity distributions of the forearm. Therefore, it is difficult to classify the gestures with just spatial information. In this study, we investigate the potential of TCN for robust EIT gesture recognition against limb position effect. Significant improvement can be observed with a relatively small model.

5 Acknowledgements

This work is supported by the National Key R&D Program of China under Grant 2022YFB4500600, Guangdong Provincial Key Laboratory of Human Digital Twin under Grant 2022B1212010004, Pazhou Lab PZL2023ZZ0006.

References

[1] Yao, J. *et al. IEEE J Biomed Health Inform*, 2019.
[2] Hahne, J. M. *et al. IEEE Sens. J.*, 2021.
[3] Wu, Y. *et al. IEEE Trans. Biomed. Circuits Syst.*, 2018.
[4] Vaquero-Gallardo, *et al.* . *Low Power Electron. Appl.*, 2022.

Frequency-difference Cell Imaging with Flexible Micro-EIT Sensor

Hao Fang[1], Ronald B. Liu[1], Zhe Liu[1], Pierre Bagnaninchi[2], Yunjie Yang[1]
[1]SMART Group, Institute for Imaging, Data and Communications, School of Engineering, The University of Edinburgh, UK
[2]Centre for Regenerative Medicine, Institute for Regeneration and Repair, The University of Edinburgh, UK

Abstract: We develop a flexible miniature Electrical Impedance Tomography (EIT) sensor tailored for imaging naturally cultured cell clusters based on calibration-free frequency-difference (FD) imaging. We detail its design, fabrication, and integration with the FD image reconstruction algorithm. The effectiveness of the presented sensor for FD imaging is verified by real-world experiments.

1 Introduction

EIT is gaining prominence for its application in tissue and cellular imaging [1]. In such applications, the prevailing operation involves centrifuging the cultured cell suspension to obtain large cell clusters ($\sim$ 3 mm in diameter), in order to be imaged by conventional-sized EIT sensors (e.g., $\sim$ 15 mm in diameter). However, it faces a significant limitation when it comes to imaging naturally cultured tissue samples, such as cell clusters that usually range between 300 to 800 µm in diameter. These dimensions fall below the effective imaging capacity of conventional-sized EIT sensors.

To address these limitations, we develop a flexible, miniature EIT sensor with 16 electrodes, specifically tailored for naturally cultured cell cluster imaging. We employ FD imaging to avoid impractical calibration and Structure-Aware Sparse Bayesian Learning (SA-SBL) [2] is adopted to for low-noise EIT image reconstruction.

2 Method

Sensor design: we designed and fabricated a miniature 16-electrode EIT sensor using a flexible printed circuit board (FPC). Fig. 1 shows the schematic and real sensor. This sensor has an external dimension of 15 mm by 15 mm with a thickness of 0.2 mm. It interfaces with external devices through a 7.2 mm by 100 mm flexible PCB belt. The effective imaging region is at the center, forming a circular area with a diameter of 3 mm. Boundary electrodes are fabricated with half-hole technology. It is affixed to a transparent glass slide to contain a culture medium.

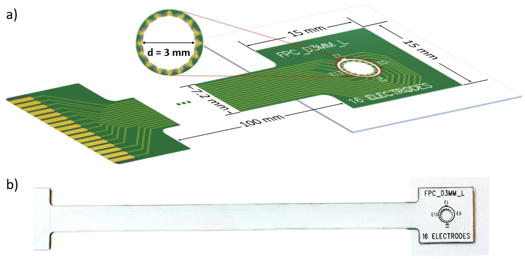

Figure 1: a) Schematic of the miniature EIT sensor. b) Fabricated flexible miniature EIT sensor.

Image reconstruction: we employ FD-EIT imaging, a technique that applies excitation currents at two distinct frequencies and measures the voltage difference between the two frequencies. The linearized model of FD-EIT is:

$$\mathbf{J}\Delta\boldsymbol{\sigma} = \Delta\mathbf{V} = \mathbf{V}_{f_o} - \mathbf{V}_{f_r}, \tag{1}$$

where $\mathbf{J}$ is the sensitivity matrix; $\Delta\boldsymbol{\sigma}$ represents the conductivity change distribution; $\mathbf{V}_{f_o}$ and $\mathbf{V}_{f_r}$ represent the voltage measurements at the observation frequency f_o and the reference frequency f_r, respectively.

SA-SBL is employed for FD-EIT image reconstruction due to its superior noise-resistance capability:

$$\overline{\Delta\boldsymbol{\sigma}} = \min_{\Delta\boldsymbol{\sigma}\in\mathbb{R}^{N\times 1}} \log p(\Delta\mathbf{V}|\Delta\boldsymbol{\sigma}) + \lambda \log p(\Delta\boldsymbol{\sigma};\boldsymbol{\Theta}), \tag{2}$$

where $\log p(\cdot)$ is a parametric log prior, $\boldsymbol{\Theta}$ is the hyperparameter and λ is the regularization parameter.

3 Results

We utilized the flexible miniature EIT sensor to sequentially measure the voltage data induced by the injected current at frequencies of 10 kHz, 40 kHz, 50 kHz, and 60 kHz. The 10 kHz was set as the reference frequency, while 40 kHz, 50 kHz, and 60 kHz were utilized as observation frequencies to assess variations. Fig. 2 shows that the conductivity of the cell cluster increases with the frequency of the current (40 kHz $\sim$ 60 kHz), demonstrating the effectiveness of the miniature sensor in cell imaging. Note that alongside conductivity changes, size variations in imaging result from the target's electrical properties differing across frequencies. Nonetheless, it is important to acknowledge that the reconstructed images still contain artifacts, primarily stemming from imperfections in hardware design.

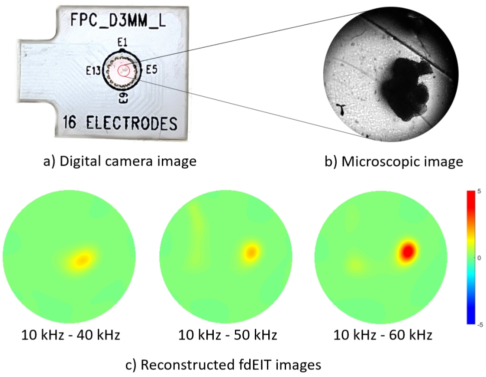

a) Digital camera image
b) Microscopic image
10 kHz - 40 kHz
10 kHz - 50 kHz
10 kHz - 60 kHz
c) Reconstructed fdEIT images

Figure 2: Images of cell cluster: a) digital camera, b) microscopic image, and c) reconstructed FD-EIT images.

4 Conclusions

We demonstrate a flexible miniature EIT sensor that can effectively image naturally cultured cell clusters in real-world setups. Future work will optimize sensor signal and image quality, with the aim of applying it for real-time cell/tissue imaging.

References

[1] Y. Yang, et al., "Scaffold-Based 3-D Cell Culture Imaging Using a Miniature Electrical Impedance Tomography Sensor," IEEE Sens. J., 2019.

[2] S. Liu, et al., "Image Reconstruction in Electrical Impedance Tomography Based on Structure-Aware Sparse Bayesian Learning," IEEE Trans. Med. Imaging., 2018.

Contactless EIT for Lung Respiratory Monitoring

Yuxi Guo[1], Yandan Jiang[2], Manuchehr Soleimani[3] and Maomao Zhang[1*]
[1]Shenzhen Institute for Advanced Study, University of Electronic Science and Technology of China, Shenzhen, China,
[*]m.zhang@uestc.edu.cn
[2]Zhejiang University, Hangzhou, China
[3]University of Bath, Bath, UK

Abstract: This work proposes the application of contactless electrical impedance tomography (CEIT) for monitoring lung respiration. A multi-physics model combining biomechanical and electric fields was established. The feasibility of applying CEIT for respiratory monitoring is confirmed and the impact of different excitation frequencies on both impedance measurements and image reconstruction in CEIT was investigated through simulations.

1 Introduction

The contact-based method of measuring impedance in EIT leads to high electrode-skin contact impedance which represents significant obstacle to the medical application of EIT. Additionally, long-term use of the EIT belt also poses a risk of pressive injury to the human body. CEIT is a novel technique that measures impedance using voltage excitation method with no need for conductive pathways between the electrodes and the human body, eliminating the requirement for full contact. It effectively addresses the contact impedance issues of traditional EIT and has the potential to be used as a wearable device, offering convenience, comfort and hygiene to the patients/users. CEIT holds great research significance in the field of biomedical science. Yandan Jiang *et. al*. proposed the application of CEIT in brain imaging [1]. This study conducted a simulation work on the application of contactless EIT in monitoring.

2 Methods

The lung motion model [2] and CEIT model is illustrated in Fig. 1. Biomechanical field is applied to dynamically simulate lung motion. The respiratory motion is modeled as a contact problem, and CT images of the lungs at end-exhalation and end-inhalation are segmented to establish the initial geometry model and constrained geometry model serving as the contact condition, respectively. The CT data is sourced from the Cancer Imaging Archive (TCIA). The CEIT sensor consists of 16 electrodes and is positioned between the fourth and sixth intercostal space, away from thorax with air gaps. And electric field is applied to generate the contactless impedance measurement. The conductivity and relative permittivity of the air gap are set to 0 S/m and 1, respectively. 21 respiratory phases are uniformly selected from end-exhalation to end-inhalation, and their impedance values are measured through voltage excitation method to simulate dynamic monitoring of the respiratory process. The sensitivity matrix of CEIT is constructed from the plane of the thorax where the electrodes located. The time-difference imaging method is employed to reconstruct images for each respiratory phase. This work investigates the CEIT imaging and measurement of excitation frequency in the range of 500 kHz to 20 MHz.

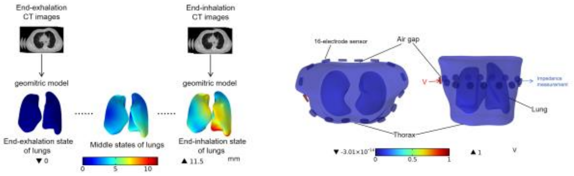

(a) (b)

Figure 1: (a) Lung motion model. (b) CEIT model.

3 Results and Conclusion

This work represents an initial exploration of the application of CEIT in lung respiratory monitoring through simulation. The feasibility of applying CEIT in respiratory monitoring is confirmed. The amplitude of impedance measurement is highly dependent on frequency. The higher the frequency is, the more pronounced the changes are in the impedance amplitude during the respiratory process. The change in impedance phase during the respiratory process is much more significant than the impedance amplitude. As the frequency increases, the change in impedance phase becomes greater.

Based on the measurement accuracy of the E4990A Impedance Analyzer, random noise of $e(\%)$ is added to magnitude and $e/100$ (%) is added to phase, respectively. The reconstructed images at different frequencies and different noise level (e=1%, 0.1%, 0.01%) based on the impedance amplitude and phase are shown in Fig. 2. At higher frequencies, the quality of the reconstructed images is better. The reconstruction based on impedance phase is less affected by noise, resulting in better image reconstruction quality compared to the reconstruction based on impedance amplitude.

This work confirmed the feasibility of using CEIT for monitoring lung respiration. CEIT can work on voltage excitation allowing wider range of frequencies. For the measurement and image reconstruction of impedance amplitude and phase, higher excitation frequencies lead to better results.

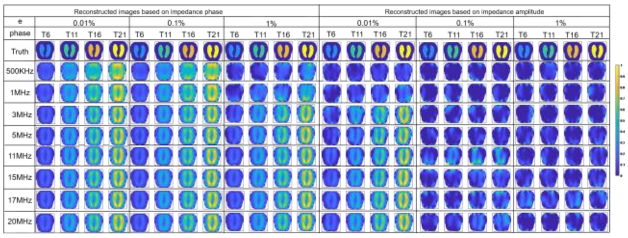

Figure 2: Reconstructed images.

References

[1] Jiang, Y. D., & Soleimani, M. *IEEE transactions on medical imaging*, 38(9), 2104-2113.

[2] Zhu, Liying, et al. *IEEE Transactions on Instrumentation and Measurement*, 2023.

A Dynamic Imaging Method of Capacitively Coupled Electrical Impedance Tomography (CCEIT)

Yimin Wu[1], Yandan Jiang[1], HaiFeng Ji[1], Baoliang Wang[1] and Manuchehr Soleimani[2]

[1]State Key Laboratory of Industrial Control Technology, College of Control Science and Engineering, Zhejiang University, Hangzhou, China, ydjiang@zju.edu.cn

[2]Engineering Tomography Laboratory (ETL), Department of Electronic and Electrical Engineering, University of Bath, Bath, UK

Abstract: This work presents a novel dynamic imaging method of capacitively coupled electrical impedance tomography (CCEIT), which is applicable in both industrial processes and biomedical applications. In the method, the dynamic imaging model is developed by introducing the spatiotemporal correlation of the dynamic change of the target distribution.

1 Introduction

As a contactless alternative to electrical impedance tomography (EIT), capacitively coupled electrical impedance tomography (CCEIT) provides a new, effective, and contactless approach to impedance imaging [1]. However, as a newly proposed technique, research for CCEIT is still insufficient, especially for the imaging in dynamic processes [2]. In the past decades, researchers have made efforts to develop dynamic EIT, providing a useful reference for the study of CCEIT. However, most previous works are based on the Kalman filter (KF) methods with the “random work model” for state evaluation [3-5]. Generally, the distribution of dynamic process/medium exhibits significant regularity over time, such as the changes in the shape of the thorax during respiration. The “random work model” is unable to identify this important feature, hence missing the spatiotemporal correlation of the dynamic change. This work focuses on a new dynamic imaging method for CCEIT. Considering the spatiotemporal change regularity of the target distribution in the dynamic process, a dynamic imaging model with improved state evolution will be developed.

2 Measurement Principle

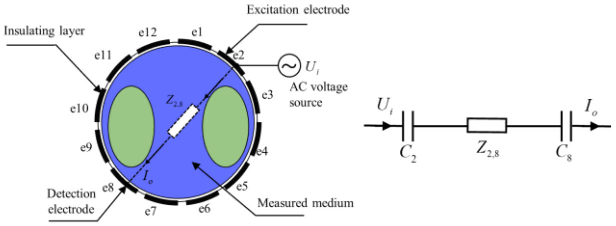

Fig. 1: Measurement principle of CCEIT.

Figure 1 shows the measurement principle of a 12-electrode CCEIT sensor, where an insulating layer is introduced to keep the electrodes and the measured biomedical medium not in direct contact. Labeling the 12 electrodes as e1, e2, ..., e12, and taking the electrode pair e2–e8 as an example, the equivalent circuit of the measurement electrode pair can be represented by two coupling capacitances C_2, C_8 in series with an impedance $Z_{2,8}$. C_2 / C_8 is formed by the electrodes e2 / e9 with the insulating layer and the target medium. When the excitation AC voltage is applied, the current reflects the conductivity distribution of the measured medium can be measured for subsequent impedance calculation. In this work, the real part of the measured impedance is utilized.

3 Dynamic imaging model for CCEIT

Unlike the random walk model where the identity matrix is used as the transfer matrix and the spatiotemporal evolution of the distribution is ignored, an efficient adaptive learning model for state evolution is designed. It recursively learns the transfer matrix from the states of previous multiple moments. Based on the above analysis, the dynamic imaging model using KF-based methods for CCEIT can be formulated as:

$$\begin{cases} G_t = H_t G_{t-1} + \omega_{t-1} \\ P_t = S G_t + \varepsilon_t \end{cases} \tag{1}$$

where $P_t \in \mathbb{R}^{N\times 1}$ is the projection vector. $S \in \mathbb{R}^{N\times M}$ is the sensitivity matrix and $G_t \in \mathbb{R}^{N\times 1}$ is the gray value vector of the reconstructed image at t. ω_{t-1} and ε_t are the state noise and measurement noise. $H_t \in \mathbb{R}^{M\times M}$ is the state transfer matrix learned with the learning coefficient λ as:

$$H_t = \underset{H_t}{argmin} \frac{1}{2} \sum_{\tau=1}^{t-1} \left(\lambda^{t-\tau} \left\| G_{\tau|\tau} - H_t G_{\tau-1|\tau-1} \right\|_2^2 \right) \tag{2}$$

4 Image Reconstruction Results

A phantom study using saline and plastic rods of varying sizes to simulate the respiration process was carried out to verify the effectiveness of the proposed method. Fig.2 presents the image reconstruction results. It is found that the reconstructed images obtained by the proposed method accurately reflect the practical medium distribution, along with the size variations over time.

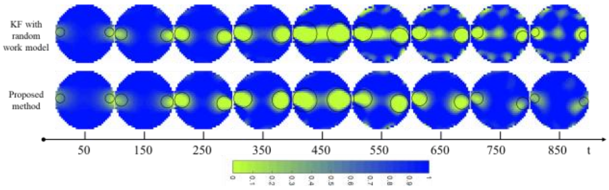

Fig. 2: Image reconstruction results

5 Conclusions

In this work, a dynamic imaging method of CCEIT is proposed. The results of the phantom case study for respiration imaging show the potential of the method in practical applications.

References

[1] YD Jiang, et al. *IEEE Access*, 6: 27069-27079, 2018.
[2] YD Jiang, et al. *IEEE Trans Med Imag*, 38(9): 2104-2113, 2019.
[3] GH Liang, et al. *IEEE Trans Instrum Meas*, 70: 4501012, 2021.
[4] M Vauhkonen, et al. *IEEE Trans Biomed Eng*, 45(4): 486-493, 1998.
[5] F C Trigo, et al. *IEEE Trans Biomed Eng*, 51(1): 72-81, 2004.

On a Focusing Sensing Method for Contactless Brain Imaging

Weiming Li[1], Yandan Jiang[1], Manuchehr Soleimani[2], HaiFeng Ji[1] and Baoliang Wang[1]

[1]State Key Laboratory of Industrial Control Technology, College of Control Science and Engineering, Zhejiang University, Hangzhou, China, ydjiang@zju.edu.cn

[2]Engineering Tomography Laboratory (ETL), Department of Electronic and Electrical Engineering, University of Bath, Bath, UK

Abstract: In this work, a focusing sensing method of capacitively coupled electrical impedance tomography (CCEIT) is proposed for contactless brain imaging, where a focusing excitation approach is adopted to reduce the influence of scalp and skull on impedance imaging.

1 Introduction

Electrical impedance tomography (EIT) has been widely studied and applied in medical field [1]. However, traditional EIT still has some limitations. One is the relatively large and variable electrode-skin contact impedance, which leads to measurement errors [2]. Although efforts have been made to model or calculate the contact impedance, the adverse influence of the contact impedance still exists. Capacitively coupled electrical impedance tomography (CCEIT) was proposed as a contactless alternative of EIT, which provides a new approach for biomedical applications [3]. Our previous work has showed the potential of CCEIT in brain imaging [4], but the research is still insufficient. In the brain imaging case, another problem of impedance imaging is the high impedance posed by skull, obstructing the detection depth of the effective signal in the region of interest (ROI) and limiting the imaging sensitivity [5]. This work aims to seek an effective sensing method to overcome the above limitations. By introducing the focusing excitation approach to improve the CCEIT technique, a brain imaging method with contactless feature and higher sensitivity deep into the ROI is presented. Simulation will be undertaken to validate the method.

2 The focusing sensing method of CCEIT

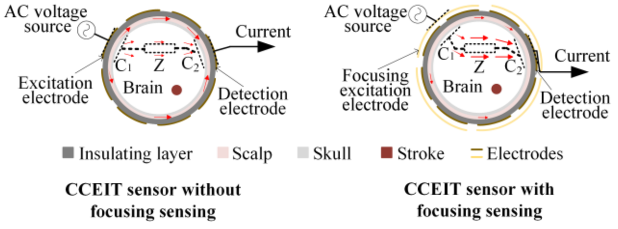

CCEIT sensor without focusing sensing **CCEIT sensor with focusing sensing**

Figure 1: Measurement principle of CCEIT for brain imaging.

Figure 1 shows the measurement principle of CCEIT sensor without (left) and with (right) focusing sensing. The equivalent circuit of the measurement electrode pair in both the two sensors can be represented by the interested impedance Z in series with two capacitances C1 and C2. But in traditional CCEIT, due to the highly conductive scalp and the highly resistive skull, most signal goes through the scalp layer. While with the focusing sensing method, because of the equipotential property of the large focusing excitation electrode, more signal will go into the ROI, increasing the detection sensitivity. A 3D CCEIT sensor with focusing sensing is designed, which consists of 4 excitation electrodes, 24 detection electrodes, and two insulation layers. Fig. 2 illustrates the structure of the sensor with focusing sensing.

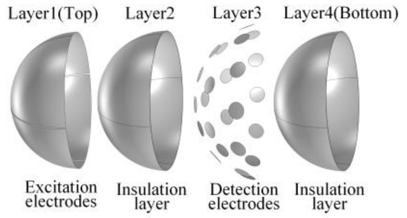

Figure 2: Structure of the sensor with focusing sensing.

3 Simulation validation

Simulation was conducted to verify the proposed method, which compares three aspects including the projection intensity, the sensitivity distribution and the image reconstruction performance of the CCEIT sensor without and with focusing sensing. Projection intensity is defined as the average of all the independent projections. An excitation signal of 3.3 V in amplitude and 10 MHz in frequency was applied. Simulation results show that the focusing sensing method can effectively improve the projection intensity. Meanwhile, the average sensitivity of the sensor with focusing sensing is more than 5 times higher than that of the traditional sensor. And focusing sensing can improve the sensitivity in the centre region of ROI and increase the sensitivity distribution uniformity. Fig. 3 presents the image reconstruction results reconstructed by the linear back projection (LBP) algorithm. Compared with the non-focusing case, focusing sensing makes sense in obtaining better imaging results.

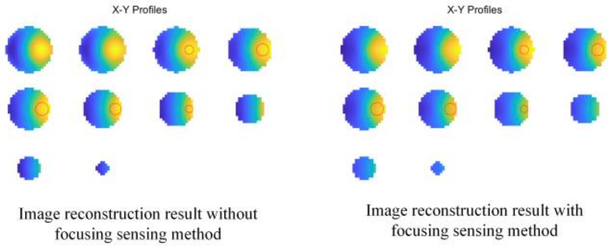

Image reconstruction result without focusing sensing method Image reconstruction result with focusing sensing method

Figure 3: Image reconstruction results

4 Conclusions

This work shows the good application potential of CCEIT with a novel focusing sensing method in brain imaging.

References

[1] T Dowrick, et al. *Physiol Meas*, 36(6): 1273-1282, 2015.
[2] V Kolehmainen, et al. *IEEE Trans Med Imag*, 27(10): 1404-1414, 2008.
[3] BL Wang, et al. *IEEE Trans Instrum Meas*, 62(5): 1017-1024, 2013.
[4] YD Jiang, et al. *IEEE Trans Med Imag*, 38(9): 2104-2113, 2019.
[5] AT Tidswell1, et al. *Physiol Meas*, 22(1): 177-185, 2001.

EIDORS Version 3.12

Andy Adler[1] and Bartłomiej Grychtol[1]

[1]Systems and Computer Engineering, Carleton University, Ottawa, Canada, adler@asce.carleton.ca

Abstract: This paper announces the release of version 3.12 of the EIDORS software suite. We review its new features, and discusses its growth and use.

1 Introduction

We proudly announce the release of EIDORS version 3.12, for the 24th Int. Conf. on Biomedical Applications of EIT, in July 2024. The software is available at eidors.org and licensed under the GNU GPLv2 or GPLv3. Archived versions are now available on Zenodo [1–5], and all versions available on sourceforge.net [11–15]

EIDORS provides free software algorithms for forward modelling and inverse solutions of Electrical Impedance and (to some extent) Diffusion-based Optical Tomography, in medical, industrial and geophysical settings. EIDORS also aims to share data and promote collaboration.

2 New Features

Release 3.12 of EIDORS builds upon a strong foundation in reconstruction algorithms, adding and improving a number of aspects.

- D-bar solver with Dirichlet-Neumann estimation
- New data formats (Sciospec and HDF5)[7]
- Improved solver preconditioning
- Improved Octave support
- New faster hash (xxHash) for object caching
- Improved Control of netgen refinement
- 3D perfusion and $\dot{V}$/Q analysis tools[6]
- Improved FFT-based filtering functions
- Expanded data contributions (e.g. fig.2)
- Improved Instrument models
- Expanded shape library with new species shapes
- (As always) speed-ups and bug fixes

3 Growth

EIDORS-related citations continue to grow. Current citation results are shown in table 1. The EIDORS code-base is growing (fig. 1) with significant effort being applied to improving test coverage, refining performance and implementing new features. In 2012, a `dev` (development) staging area was created for contributions in progress.

Table 1: EIDORS Citations (May 2024, scholar.google.com).

Paper	Date	Citations
[8] A MATLAB package for the EIDORS project …	2001	336
[9] Image reconstruction algorithms for …	2002	194
[10] A Matlab toolkit for three-dimensional …	2002	564
[11] EIDORS: Towards a community-based …	2005	38
[12] Uses and abuses of EIDORS: An extensible …	2006	956
[13] Simple FEMs aren't as good as we thought …	2008	26
[15] EIDORS version 3.9	2017	34
[15] EIDORS version 3.10	2019	5

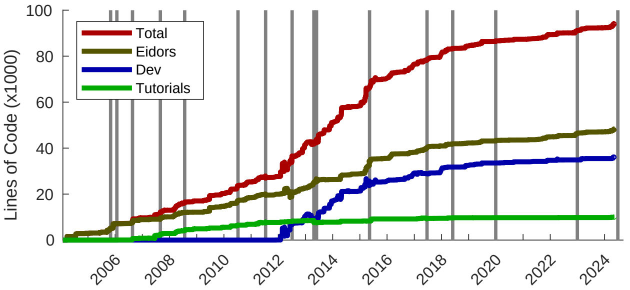

Figure 1: Lines of Code (LoC) in Matlab files in the EIDORS code-base vs. time; Total (red), EIDORS (i.e. release branch, brown), Tutorials (green), development code (blue). Releases are indicated by gray bars (The 3.12 release is at the right).

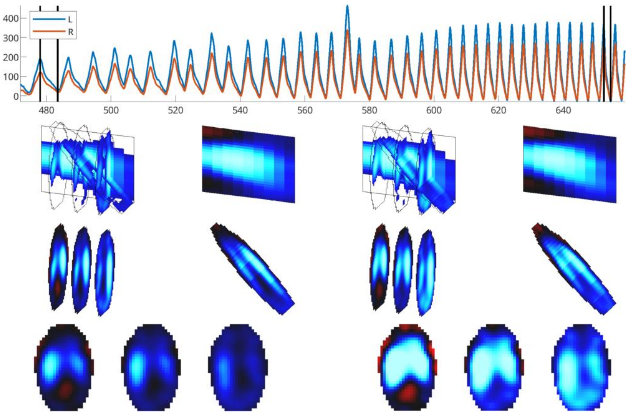

Figure 2: Reconstruction of 3D EIT data from a horse during baseline (left) and rebreathing (right). Data are reconstructed into a parasagittal slice, modified frontal slice, and three transverse slices. Middle: normalized to the maximum in each image. Bottom: normalized to the same limit. Source: eidors.org/data_contrib/db-horse3d-2024

4 Discussion

The structure of EIDORS has been relatively stable due, in part, to some early design choices: a modular framework and data structure, cross-platform support, integration of meshing, tutorials, and the contributed data repository. These aspects, along with an open source code-base, have enabled EIDORS to maintain research relevance. Version 3.12 (hopefully) continues the tradition.

References

[1] Adler A, "EIDORS v3.11", DOI:10.5281/zenodo.7495740, 2022.
[2] Adler A, "EIDORS v3.10", DOI:10.5281/zenodo.3247168, 2019.
[3] Adler A *et al*, "EIDORS v3.9.1", DOI:10.5281/zenodo.1257670, 2018.
[4] Adler A *et al*, "EIDORS v3.9", DOI:10.5281/zenodo.583266, 2017.
[5] Adler A *et al*, "EIDORS v3.8", DOI:10.5281/zenodo.17559, 2015.
[6] Araos J, *et al*, "$\dot{V}$/Q analysis with 3D EIT", p25, Conf EIT 2023.
[7] Possner L, *et al*, "HDF5-based data format …", p39, Conf EIT 2023.
[8] Vauhkonen & M, *et al*, *Physiol Meas*, 22:107–111, 2001.
[9] Polydorides N, *Ph.D. thesis*, U Manchester, UK, 2002.
[10] Polydorides N, Lionheart WRB, *Meas Sci Tech*, 13:1871–1883, 2002.
[11] Adler A, Lionheart WRB, *Proc EIT2005*, London, UK, 2005.
[12] Adler A, Lionheart WRB, *Physiol Meas* 27:S25–S42, 2006.
[13] Adler A, Borsic A *et al*, *Proc EIT2008*, Hannover, NH, USA, 2008.
[14] Adler A *et al*, *Proc EIT2015*, p.19, Neuchâtel, Switzerland, 2015.
[15] Adler A *et al*, *Proc EIT2017*, p.63, Dartmouth, NH, USA, 2017.

Dynamic EIT Reconstruction with Low-Rank and Sparse Prior

Baojie Zhang[1] and Xiaoyan Chen[1]

[1]College of Electric Information and Automation, Tianjin University of Science and Technology, Tianjin, China, cxywxr@tust.edu.cn

Abstract: Electrical Impedance Tomography (EIT) has the advantage of temporal resolution. However, the EIT inverse problem suffers from low spatio-temporal resolution reconstruction due to ill-posedness. This paper proposes a framework with low-rank and sparse priors for dynamic EIT imaging for lung respiration from boundary *V-t* data. The results show satisfactory performance.

1 Introduction

EIT is a novel imaging modality in biomedical applications, particularly for lung-respiratory monitoring [1]. Due to the nonlinear and ill-posed nature of EIT, the results are poor with blurry shape and error conductivities. This paper proposes a dynamic EIT-solving framework with low-rank and sparse constraints, fully considering the spatial and temporal correlations of the spatio-temporal matrix, while a novel variable splitting algorithm combined with total variation regularizations is proposed to address dynamic EIT matrix reconstruction.

2 Methods

In dynamic EIT imaging, the change of pixel$x_i$can be represented as spatio-tempiral matrix with respect to timet_i as follows $\mathbf{\Gamma} = \begin{bmatrix} \gamma(x_0,t_0) & \cdots & \gamma(x_0,t_r) \\ \vdots & \ddots & \vdots \\ \gamma(x_{n-1},t_0) & \cdots & \gamma(x_{n-1},t_r) \end{bmatrix}$. The rows of $\mathbf{\Gamma}$ represent the distribution of spatial pixels, The columns of $\mathbf{\Gamma}$ represent the time pixel distribution.

To exploit both the sparse and low-rank properties of the matrix, the problem can be formulated as follows:

$$\mathbf{\Gamma}^* = \underset{\Gamma}{\operatorname{argmin}} \left\| \mathcal{A}(\mathbf{\Gamma}) - \boldsymbol{b} \right\|^2 + \lambda_1 \cdot \varphi(\mathbf{\Gamma}) + \lambda_2 \cdot \psi(\mathbf{\Gamma}) \tag{1}$$

where, $\lambda_1 \; and \; \lambda_2$ are regularization weights, $\psi(\mathbf{\Gamma}) = \left\| \Phi^H \mathbf{\Gamma} \mathbf{\Psi} \right\|_{\ell_1}$ is a surrogate for the $\ell_0$term and $\varphi(\mathbf{\Gamma}) = \|\mathbf{\Gamma}\|_p^p$. When, $p \geq 1$, the cost function is convex and hence will have a unique minimum. To adapt to the sparse nature of image gradients, the total variation (TV) penalty is employed to constrain the data consistency term.

Due to the presence of spectral and sparse penalties in the improved model, it is not straightforward to utilize nuclear norm minimization. We present the regularization dynamic imaging framework as an unconstrained problem with augmented Lagrange multiplier method

$$\begin{aligned} \mathcal{L}_{\beta_1,\beta_2}(\mathbf{\Gamma}; \mathbf{R}, \mathbf{S}_i) = {} & \left\| \mathcal{A}(\mathbf{\Gamma}) - \boldsymbol{b} \right\|^2 \\ & + \lambda_1 \varphi(\mathbf{R}) + \lambda_2 \left\| \sqrt{\sum_{i=0}^{q-1} \|\mathbf{S}_i\|^2} \right\|_{\ell_1} \\ & + \frac{\beta_1}{2} \|\mathbf{\Gamma} - \mathbf{R}\|^2 + \frac{\beta_2}{2} \sum_{i=0}^{q-1} \left\| \boldsymbol{\Phi}_i^H \mathbf{\Gamma} \boldsymbol{\Psi}_i - \mathbf{S}_i \right\|^2 \end{aligned} \tag{2}$$

Here, the $\mathbf{R}$ and $\mathbf{S}_i$ are auxiliary variables. The Eq. (2) is solved by a three-stage alternating direction minimization scheme below (3)

$$\begin{cases} \mathbf{\Gamma}_{n+1} = \underset{\mathbf{\Gamma}}{\operatorname{argmin}} \left\| \mathcal{A}(\mathbf{\Gamma}) - \boldsymbol{b} \right\|^2 + \frac{\beta_1}{2} \|\mathbf{\Gamma} - \mathbf{R}_n\|^2 \\ \; + \frac{\beta_2}{2} \sum_{i=0}^{q-1} \left\| \boldsymbol{\Phi}_i^{\mathrm{H}} \mathbf{\Gamma} \boldsymbol{\Psi}_i - \mathbf{S}_{i,n} \right\|^2; \\ \mathbf{R}_{n+1} = \underset{\mathbf{R}}{\operatorname{argmin}} \left\| \mathbf{\Gamma}_{n+1} - \mathbf{R} \right\|^2 + \frac{2\lambda_1}{\beta_1} \varphi(\mathbf{R}); \\ \mathbf{S}_{i,n+1} = \underset{\{\mathbf{S}_i\}}{\operatorname{argmin}} \sum_{i=0}^{q-1} \left\| \boldsymbol{\Phi}_i^{\mathrm{H}} \mathbf{\Gamma} \boldsymbol{\Psi}_i - \mathbf{S}_i \right\|^2 + \\ \; \frac{2\lambda_2}{\beta_2}{}_2 \left\| \sqrt{\sum_{i=0}^{q-1} \|\mathbf{S}_i\|^2} \right\|_{\ell_1} \; (i = 0, 1, \cdots, q-1) \end{cases} \tag{3}$$

The solution of first subproblem in (3) can be solved using CG method

$$\begin{aligned} \mathbf{\Gamma}_{n+1} = {} & \left(\mathcal{A}^{\mathrm{T}} \mathcal{A} + \frac{\beta_1}{2} \mathcal{I} + \frac{\beta_2}{2} \sum_{i=0}^{q-1} \mathcal{Q}_i^{\mathrm{T}} \mathcal{Q} \right)^{-1} \\ & \times \left(\mathcal{A}^{\mathrm{T}} \boldsymbol{b} + \frac{\beta_1}{2} \mathbf{R} + \frac{\beta_2}{2} \sum_{i=0}^{q-1} \mathbf{S}_i \right) \end{aligned} \tag{4}$$

The second subproblem in (3) is solved using SVD-algorithm expressing as

$$\mathbf{R}_{n+1} = \left(\mathcal{S}_{\frac{\lambda_1}{\beta_1}} \circ \mathcal{T} \right) (\mathbf{R}_n, \mathbf{S}_{i,n}) \tag{5}$$

where $\mathcal{S}_{\frac{\lambda_1}{\beta_1}}(\mathbf{\Gamma}_{n+1}) = \sum_{i=0}^{\min\{n,T\}} \left(\sigma_i - \frac{\lambda_1 \sigma_i^{p-1}}{\beta_1} \right)_+ \mathbf{u}_i \mathbf{v}_i^*$, and the third subproblm can be solved by

$$\mathbf{S}_{i,n+1} = \frac{\mathcal{Q}_i(\mathbf{\Gamma}_{n+1})}{\sum_{i=0}^{q-1} \left\| \mathcal{Q}_i(\boldsymbol{\Gamma}_{n+1}) \right\|^2} \times \left(\sum_{i=0}^{q-1} \left\| \mathcal{Q}_i(\mathbf{\Gamma}_{n+1}) \right\|^2 - \frac{\lambda_2}{\beta_2} \right)_+ \tag{6}$$

3 Results and Conclusions

We conducted a respiratory model with lungs, heart, spine, and aorta. We selected 11 frames to illustrate the reconstructions using (3)-(6). Figure 1 illustrates the changes of lung conductivity during the one respiratory cycle. This research provides an effective idea to show a clear view of lung-respiratory processes, which might realize a real-time monitoring promoting the clinical application for EIT.

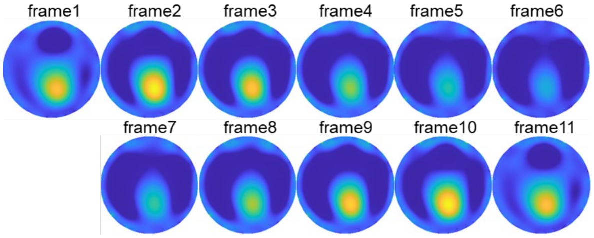

Figure 1: The dynamic reconstructions of EIT.

References

[1] Spadaro, Savino and Mauri, Tommaso *Critical Care*, 22:1–9, 2018

Sensitivity of pair-drive EIT in circular domains

Andy Adler
Systems and Computer Engineering, Carleton University, Ottawa, Canada, adler@sce.carleton.ca

Abstract: EIT systems typically stimulate and measure the body across pairs of electrodes. The optimum electrode configuration to maximize sensitivity and resolution has been considered in several papers. We derive analytic expressions for the sensitivity and its spatial derivatives in order to help give insight into system design.

1 Introduction

Most EIT devices are pair-drive: pairs of electrodes are used to stimulate and measure from the body. There has been some discussion in the EIT literature about the best choice of angle between the driving electrodes (also called the "skip" pattern, referring to the number of electrodes "skipped" between the active pairs). This literature [1, 2, 3] has concluded that EIT sensitivity improves dramatically with pair-drive angle. However, this improved sensitivity appears to be at the expense of resolution, and larger skip patterns have less ability to resolve the two lungs. One proposed explanation of this effect is that the resolution depends both on the sensitivity and its spatial derivative [4].

In order to further explore this issue, this paper develops analytic expressions for the sensitivity of pair-drive EIT, from which an intuition of the compromises can be determined.

2 Sensitivity Calculations

The pair-drive configuration is illustrated below (Fig 1).

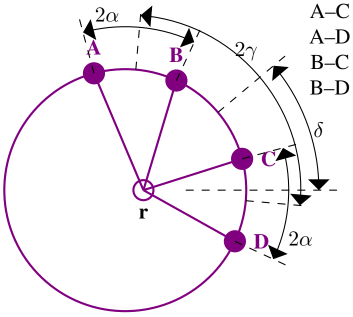

$$\begin{array}{llll} \text{A–C} = & 2\gamma & \text{A+C} = & 2(\delta+\alpha) \\ \text{A–D} = & 2(\gamma+\alpha) & \text{A+D} = & 2\delta \\ \text{B–C} = & 2(\gamma-\alpha) & \text{B+C} = & 2\delta \\ \text{B–D} = & 2\gamma & \text{B+D} = & 2(\delta-\alpha) \end{array}$$

$$\begin{aligned} \text{A} &= \delta+\gamma+\alpha \\ \text{B} &= \delta+\gamma-\alpha \\ \text{C} &= \delta-\gamma+\alpha \\ \text{D} &= \delta-\gamma-\alpha \end{aligned}$$

$$\begin{aligned} \alpha &= \tfrac{1}{2}(\text{A–B}) = \tfrac{1}{2}(\text{C–D}) \\ \gamma &= \tfrac{1}{4}(\text{A}+\text{B}-\text{C}-\text{D}) \\ \delta &= \tfrac{1}{4}(\text{A}+\text{B}+\text{C}+\text{D}) \end{aligned}$$

Figure 1: Unit radius circular or cylindrical domain with electrodes. Sensitivity at point, r (location (x, y)) is calculated, using drive pair (A→B) and measurement pair (C→D).

Initially, consider monopolar stimulation and measurement (stimulation with one electrode, S, and measurement with one electrode, M) and denote the sensitivity J, using an adjoint-field formulation

$$J_{\mathrm{r;S\to M}} \propto \nabla V_S(\mathrm{r}) \cdot \nabla V_M(\mathrm{r}) = \frac{\vec{\mathrm{r}}_\mathrm{S}}{\|\mathrm{r}_\mathrm{S}\|^d} \cdot \frac{\vec{\mathrm{r}}_\mathrm{M}}{\|\mathrm{r}_\mathrm{M}\|^d} \qquad (1)$$

where $\vec{\mathrm{r}}_\mathrm{S} = \vec{\mathrm{r}} - \vec{\mathrm{S}}$, $\vec{\mathrm{r}}_\mathrm{M} = \vec{\mathrm{r}} - \vec{\mathrm{M}}$, and d is the dimension of the model (2 or 3 D). The equation simplifies at the centre $\mathrm{r} = 0$, $J_\mathrm{r} \propto \cos(\mathrm{S} - \mathrm{M})$; notation is (ab)used to consider points to be angles or vectors.

Pair-drive and measurement may be derived from the monopolar case, using $J_\mathrm{r} = J_{\mathrm{r;A\to C}} - J_{\mathrm{r;A\to D}} - J_{\mathrm{r;B\to C}} + J_{\mathrm{r;B\to D}}$. Sensitivity for r at the centre is:

$$\begin{aligned} S_{\mathrm{r}=0} &= \cos(\text{A–C}) - \cos(\text{A–D}) - \cos(\text{B–C}) + \cos(\text{B–D}) \\ &= \cos(2\gamma)\sin^2(\alpha) \qquad (2) \end{aligned}$$

in terms of the angles defined in Fig 1.

3 Spatial derivatives of sensitivity

Equations for the spatial derivatives, ∇J, are more complicated. We show $\frac{\partial}{\partial x} J_\mathrm{r}$; $\frac{\partial}{\partial y} J_\mathrm{r}$ is obtained by rotation of δ.

$$\begin{aligned} \frac{\partial}{\partial x} J_{\mathrm{r;S\to M}} \propto & \frac{\mathrm{r}_{\mathrm{S},x} + \mathrm{r}_{\mathrm{M},x}}{(\|\mathrm{r}_\mathrm{S}\|\|\mathrm{r}_\mathrm{M}\|)^d} \\ & - d(\vec{\mathrm{r}}_\mathrm{S} \cdot \vec{\mathrm{r}}_\mathrm{M}) \frac{\mathrm{r}_{\mathrm{S},x}\|\mathrm{r}_\mathrm{M}\|^2 + \mathrm{r}_{\mathrm{M},x}\|\mathrm{r}_\mathrm{S}\|^2}{(\|\mathrm{r}_\mathrm{S}\|\|\mathrm{r}_\mathrm{M}\|)^{d+2}} \qquad (3) \end{aligned}$$

At the centre, $\vec{\mathrm{r}} = 0$:

$$\nabla J_{\mathrm{r}=0} \propto \left(\cos(\text{S–M}) - \tfrac{1}{d}\right) \begin{bmatrix} \cos(\mathrm{S}) + \cos(\mathrm{M}) \\ \sin(\mathrm{S}) + \sin(\mathrm{M}) \end{bmatrix} \qquad (4)$$

For pair drive, we can calculate

$$\nabla J_{\mathrm{r}=0} \propto \begin{bmatrix} \cos(\delta) \\ \sin(\delta) \end{bmatrix} \cos(3\gamma)\sin^2(\alpha)\cos(\alpha) \qquad (5)$$

Finally, the ratio of spatial derivative to sensitivity is

$$\frac{\|\nabla J_\mathrm{r}\|}{J_\mathrm{r}} \propto \frac{\cos(3\gamma)}{\cos(2\gamma)} \cos(\alpha) \qquad (6)$$

4 Discussion

It is hoped that analytic expressions for pair-drive sensitivity provide insight into the compromises involved in EIT systems design.

The formulae for pair-drive sensitivity take a surprisingly simple form and are a function of simple trigonometric expressions for the central point in a cylindrical domain. In a full pair-drive system, γ and δ are rotated around and so will integrate to unity. The remaining factor is the sensitivity to the "skip" distance, α. Because of the additional $\cos(\alpha)$ factor, the resolving component of ∇J decreases as skip increases. Antother interesting effect is the $\cos(3\gamma)$ vs $\cos(2\gamma)$, although it's unclear how this affects a full EIT measurement.

References

[1] A Adler, PO Gaggero, Y Maimaitijiang, "Adjacent Stimulation and Measurement Patterns Considered Harmful", *Physiol Meas*, 32:731–744, 2011.

[2] D Isaacson, "Distinguishability of conductivities by electric current computed tomography", *IEEE T Med Imaging* 5:91–95, 1986.

[3] WRB Lionheart *et al*"Generalized optimal current patterns and electrical safety in EIT", *Physiol Meas* 22:85–90, 2001.

[4] A Adler, Z Zhao, "Resolution as a function of Stimulation and Measurement Patterns", p. 68, *Conf EIT 2023* Aachen, Germany

$\mathbb{C}$EIT: A Novel EIT Imaging Method based on Complex-value U-Net

Zichen Wang[1], Tao Zhang[1], Tianchen Zhao[1], Qi Wang[1]
[1]School of Electrical and Information Engineering, Tiangong University, Tianjin, China, wangzc@tiangong.edu.cn

Abstract: Currently, real-valued deep convolutional neural networks (CNNs) can usually reconstruct only images describing the resistivity or permittivity distributions, which ignore the complex natures of electrical properties in the EIT task. In this paper, we use a UNet designed by complex convolutional operations to improve the reconstruction quality of complex conductivity images for EIT, referred to $\mathbb{C}$EIT. The results show that the method can effectively represent the distribution images of resistivity and permittivity simultaneously.

1 Introduction

Electrical impedance tomography (EIT) is a visual technique that shows the conductivity and permittivity distributions of the body domain in clinical applications. Nowadays, the learning-based methods, especially the CNNs-based models for solving inverse problems[1], only utilize the real-value information seldom taking into account the complex electrical parameters. In this paper, we proposed a novel U-Net framework with complex convolution operations to reconstruct lung conductivity and permittivity images that are of clinical usefulness in distinguishing certain conditions (e.g., pneumothorax and hyperinflation)[2].

2 Methods

The EIT image describes the complex electrical distribution of organs, which can be expressed by the following Laplace equation

$$\nabla \cdot (\gamma(\boldsymbol{r}) \nabla u(\boldsymbol{r})) = 0, \boldsymbol{r} \in \Omega \tag{1}$$

where the $\gamma(\boldsymbol{r}) = \sigma(\boldsymbol{r}) + \mathrm{j}\omega\varepsilon(\boldsymbol{r})$ denotes the admittivity, $\sigma(\boldsymbol{r})$ is the conductivity and $\varepsilon(\boldsymbol{r})$ is the permittivity, $u(\boldsymbol{r})$ is the electric potential.

The admittivity distributions could be denoted as a complex-value matrix $\boldsymbol{x} \in \mathbb{C}$, thus, we propose a U-Net similar to a real-value CNN to reconstruct complex-EIT images[3], referred to the $\mathbb{C}$EIT. The $\mathbb{C}$EIT and details are shown in Fig. 1, where the input is a complex-value feature map with the size of $256 \times 256 \times 1$ initially computed by the L_2 regularization. This complex feature is split into real and imaginary feature maps.

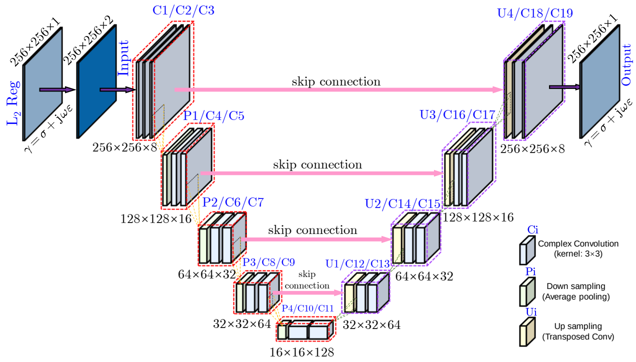

Figure 1: The architecture of $\mathbb{C}$EIT.

The $\mathbb{C}$EIT is composed of three blocks, complex convolution, radial BN, and $\mathbb{C}$ReLU function. The complex feature denotes as $A = A_x + \mathrm{j}A_y$, the kernel denotes as $K = K_x + \mathrm{j}K_y$, three operations are calculated as follows:

$$A \circledast K = (A_x \circledast K_x - A_y \circledast K_y) + \mathrm{j}(A_y \circledast K_x + A_x \circledast K_y) \tag{2}$$

$$R_{BN} = \left(\frac{R - \mu_R}{\sqrt{\sigma_R^2 + \epsilon}} \right) \gamma + \beta + \tau \tag{3}$$

$$\mathbb{C}\mathrm{ReLU} = \mathrm{ReLU}(\mathrm{Re}(A)) + \mathrm{j}\mathrm{ReLU}(\mathrm{Im}(A)) \tag{4}$$

Moreover, the real-value average pooling or transposed convolution is introduced to aggregate features or reconstruct features in two adjacent modules.

3 Results and Conclusions

We give the reconstructions using L_2 regularization and $\mathbb{C}$EIT, as shown in Fig. 2. It can be concluded that the complex-based CNN can accurately reconstruct the conductivity and permittivity distributions. Therefore, the $\mathbb{C}$EIT can further realize the information of the real and imaginary parts and also realize the analysis of the magnitude and phase information of the EIT image. This method provides a new parameter visualization scheme for clinical applications, which have clinical usefulness in distinguishing between injured conditions such as a pneumothorax and hyperinflation [2].

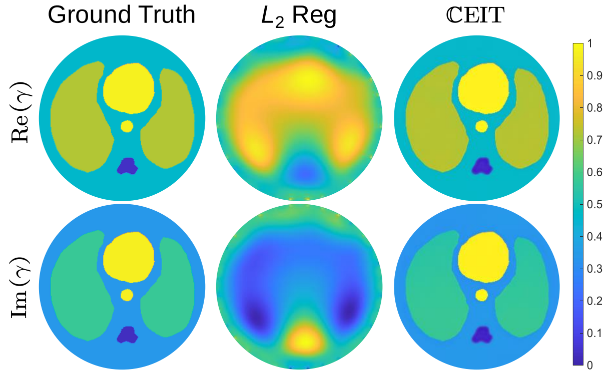

Figure 2: The reconstructions with different methods.

References

[1] Wang, Ge and Ye, Jong Chul and De Man, Bruno *Nature Machine Intelligence*, 12(2):737–748, 2020

[2] Hamilton, Sarah J and Mueller, Jennifer L *IEEE Transactions on Medical Imaging*, 32(4):757–769, 2013

[3] Ronneberger, Olaf *et al MICCAI 2015*, p.234–241, Munich, Germany, October 5-9, 2015

Electrical Impedance Tomography (EIT) Sensor Design for Early Diabetic Foot Ulcers (DFUs) Detection

Yunqian Wang[1], Bo Sun[1], Tong Zhao[1], Songpei Hu[2] and Jiafeng Yao[2]

[1]Xi'an University of Technology, Xi'an, China, bosun0814@gmail.com

[2]Nanjing University of Aeronautics and Astronautics, Nanjing, China

Abstract: Optimization of sensor design for the detection of diabetic foot ulcers (DFUs) is achieved by coupling of electromagnetic simulation and electrical impedance tomography (EIT) method. Firstly, the concentration regions of plantar pressure throughout the gait cycle are tested to determine the high-risk regions for ulcers susceptibility. Secondly, the electrodes' location is set to two regions (forefoot and heel) according to the plantar pressure concentration area during a gait cycle. Each area is equipped with 16 electrodes in total, $e = 4 \times 4$. Thirdly, a simplified plantar tissue model is imaged in three dimensions by using electromagnetic simulation coupled with the EIT method to derive the optimal electrode size for the sensor design, $D = 8$ mm. In addition, electrode number 6 (central electrode) is used as the constant electrode to obtain the optimal measurement pattern, which has the highest Image Correlation Coefficient $ICC = 0.7364$.

1 Introduction

- The region of plantar pressure concentration is highly susceptible to ulcers [1].
- The EIT method is sensitive to changes in the electrical properties of biological tissues caused by diabetic foot ulcers [2, 3].
- Electromagnetic simulation is used to set boundary conditions for each layer of plantar tissue to visualize the effect of electrode size and excitation pattern on imaging accuracy.

2 Method

2.1 Design of EIT sensors based on high-risk regions for ulcers

Figure 1 shows the acquisition of regions at high-risk for ulcers based on plantar pressure distribution thereby determining the EIT sensor electrode arrangement. The position of the plantar sensor is in the main loading areas of the forefoot and heel.

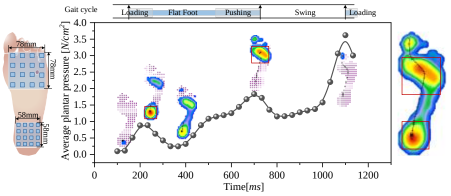

Figure 1: Design of EIT sensor electrode arrangement based on plantar pressure distribution.

2.2 Imaging DFUs by EIT method

Figure 2 shows the EIT three-dimensional image reconstructed from the boundary voltages of each excitation by placing the plantar sensor under a simplified electromagnetic simulation model of three-layer plantar tissue. The reconstruction of EIT image is based on the conductivity difference $\boldsymbol{\sigma}^C$ between DFUs and normal tissues, which is calculated as follows:

$$\boldsymbol{\sigma}^C = \mathbf{J}^T \Delta \mathbf{Z} - (\mathbf{J}^T \mathbf{J} + \mu \mathbf{I}_{AC})^{-1} \mathbf{J}^T \Delta \mathbf{Z} \qquad (1)$$

where, $\Delta \mathbf{Z}$ is the impedance difference, $\mathbf{J}$ is the Jacobian matrix, $\mathbf{I}_{\mathrm{AC}}$ is the excitation current.

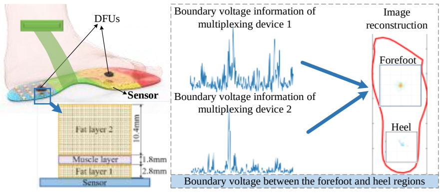

Figure 2: Diagram of early detection of DFUs using EIT method.

3 Results

Figure 3 shows the electromagnetic simulation results for EIT sensor design optimization. The image correlation coefficient $ICC = 0.6050, 0.7109, 0.3354$ when the electrode size is $D = 4, 8, 12$ mm, respectively; $ICC = 0.6927, 0.7364, 0.6651$ when the number of constant electrode e_g is 3, 6, 16. The ICC is expressed by following equation:

$$ICC = \frac{\sum_{g=1}^{M}\left(\langle \Delta\sigma_g^C \rangle - \overline{\langle \Delta\sigma^C \rangle}\right)\left(\Delta\sigma_g^C - \overline{\Delta\sigma^C}\right)}{\sqrt{\sum_{g=1}^{M}\left(\langle \Delta\sigma_g^C \rangle - \overline{\langle \Delta\sigma^C \rangle}\right)^2 \sum_{g=1}^{M}\left(\Delta\sigma_g^C - \overline{\Delta\sigma^C}\right)^2}} \qquad (2)$$

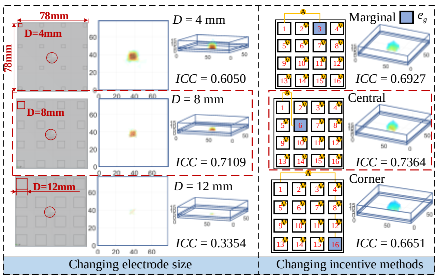

Figure 3: The electromagnetic simulation results for EIT sensor design optimization.

4 Conclusions

The key findings of this study are as follows:

1. The position of the plantar sensor is arranged in the main loading area of the forefoot and heel.
2. The optimal electrode size for the EIT sensor design is D = 8 mm; electrode number 6 (center electrode) is used as the constant electrode for the best measurement pattern with the highest image correlation coefficient $ICC = 0.7364$.

References

[1] H Abri, M Aalaa, M Sanjari, MR Amini, MR Mohajeri-Tehrani, B Larijani *Diabetes Metab Disord*, 18(1): 33-39, 2019.

[2] Mathur A, Nayak HC, Rajput S, Roy S, Nagabooshanam S, Wadhwa S, Kumar R *Chemosensors*, 9(12): 339, 2021.

[3] BY Liu, B Yang, CH Xu, JY Xia *SoftwareX*, 7: 204-208, 2018.

Double-layer electrical impedance tomography for identification of upper airway closure: a preliminary study with PSG and CT

Tingting Zhang[1,2], Tong In Oh[1,2], You Jeong Jeong[1,2], Sang-Wook Kim[3]

[1]Department of Biomedical Engineering, Kyung Hee University, Seoul, Republic of Korea , zttysu@khu.ac.kr

[2]Medical Science Research Institute, Kyung Hee University Hospital, Seoul, Republic of Korea
[3]Department of Otorhinolaryngology, Gyeongsang National University College of Medicine and Gyeongsang National University Hospital, Jinju, Republic of Korea.

Abstract: This study aims to investigate the feasibility of utilizing two-layer electrical impedance tomography to identify obstruction sites (retropalatal vs. retroglossal levels) in the upper airway during sleep, thereby aiding in the design of surgical interventions in clinical practice.

1 Introduction

The first-line treatment for obstructive sleep apnea (OSA) is continuous positive airway pressure (CPAP). However, long-term compliance with CPAP is not consistently high despite various attempts to improve it [1]. Therefore, it is necessary to develop an alternative non-CPAP therapy which requires effective patient selection methods. EIT can noninvasively identify upper airway narrowing or closure during sleep by attaching a single array of electrodes to the face, and the feasibility has been confirmed by polysomnography (PSG) [2]. In this work, we investigate whether the double-layer EIT system can differentiate between retropalatal and retroglossal collapse during sleep.

2 Methods

One healthy subject and 26 patients diagnosed with OSA were recruited for the study. The severity of OSA was confirmed through full-night PSG. On another night, two layers of electrodes for Electrical Impedance Tomography (EIT) were attached along the face and neck of the participants, as shown in Figure 1, including the regions of the retropalatal and retroglossal airways, respectively.

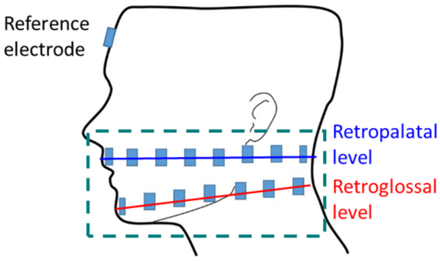

Figure 1: Two layers of electrodes were attached along the face and neck of the subjects.

The participants slept on the table of a computerized tomography (CT) machine while wearing a portable PSG device to confirm respiratory events. This setup allowed for comprehensive monitoring and multidimensional assessment of the upper airway dynamics during sleep, providing valuable insights into the mechanisms underlying OSA. Continuous data from EIT were collected, and for each subject, one baseline (awake) and eleven CT scans associated with respiratory events were obtained for each subject (286 scans in total). The upper airway dynamics were reconstructed and extracted from the measured EIT data using the source consistency EIT algorithm [3]. The correlation was analyzed between the size of upper airway in CT images and that in EIT images to validate the study.

3 Results

In Figure 2, synchronized EIT data and signals from the portable sleep monitoring device are described. The bottom images depict sets of CT images and their corresponding reconstructed EIT images at the retropalatal and retroglossal levels. The vertical dotted red line stands for the timing when the CT scan and their corresponding electrical conductivity data were obtained during hypopnea.

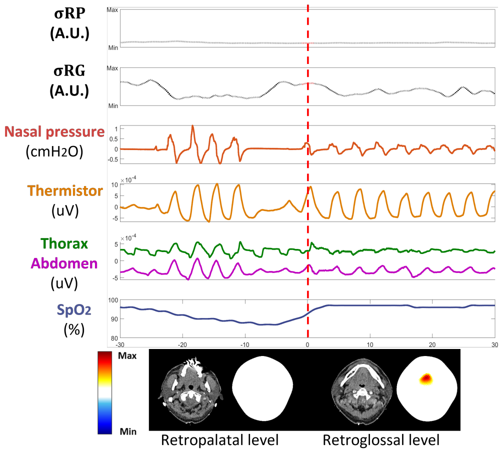

Figure 2: An example of synchronized EIT data, CT images, and signals from PSG during a hypopnea event.

4 Conclusions

Multi-layer EIT can be a useful noninvasive monitoring technique to identify the obstruction sites during sleep in OSA patients.

5 Acknowledgements

This work was supported by the National Research Foundation of Korea(NRF) grant funded by the Korea government(MSIT) (RS-2023-00246576) and NRF-2020R1A2C1008975.

References

[1] BW Rotenberg, C Vicini, EB Pang, KP Pang, *J Otolaryngol Head Neck Surg*,45: 23, 2016.

[2] G Ayoub, TH Dang, TI Oh, SW Kim, EJ Woo *Scientific reports*, 10:1637, 2020

[3] T Zhang, GY Jang, TI Oh, KW Jeung, H Wi, EJ Woo *SIAM Journal on Applied Mathematics*, 80(1):499-520, 2020.

Development of a Portable EIT System Based on Android Platform with Wi-Fi Data Transmission

Fusheng You[1], Qibo Xuan[1], Guodong Zhang[1], Honghao Tang[1] and Xuyang Huo[2]

[1]UTRON Technology Co. Ltd, Hangzhou, China, yfusheng@263.net

[2]School of Biomedical Engineering (BME), Jilin Medical University, Jilin, China

Abstract: A low-power and portable EIT system based on Android platform was developed. The system may be used in bedside or integrated with ventilator for monitoring lung ventilation. Based on Pad/Mobile Phone for Android system, battery powered, more than 20fps, Wi-Fi data transmission and small size (15x8x2.5cm) make it ideal for most portable applications.

1 Introduction

In the clinical applications of electrical impedance tomography (EIT), a data acquisition system (DAS) with smaller size, lower weight, and high speed fits better for the needs of bedside monitoring or patient transportation. Such features of DAS module, such as small form factors (low mass/volume), low power, and compatible with other medical devices, make it easier integrated with ventilators or monitors [1].

2 Methods

The system mainly includes EIT DAS module, user APP based on Android platform, and electrode belts. Fig. 1 shows the structure diagram of the system. The 16-electrodes belt was connected to the EIT DAS, the measured impedance data were transmitted to PAD or Mobile phone via Wi-Fi; the received data were analyzed and reconstructed by EIT APP based on Android platform.

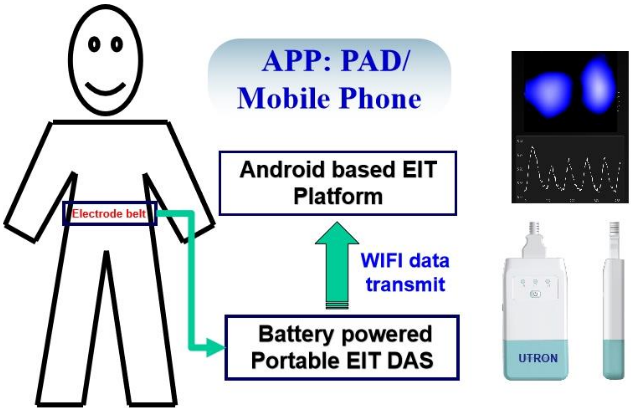

Figure 1: Structure diagram of the system

2.1 DAS design

DAS powered by battery is essential for reducing size and weight. A multi-frequency FPGA-based DAS [2] with single current source and single voltage measurement channel provides many features, such as low cost, low power, and high-speed. Sine signal generated by DDS on the FPGA was converted to analog domain via a high speed digital-to-analog converter (DAC), and a high speed analog-to-digital converter (ADC) was used to sample measured voltages for the digital demodulation. Low power MCU was applied to transfer the demodulated impedance data and to receive the system configurations via Wi-Fi module.

2.2 APP design

The EIT APP was developed based on Android studio and HUAWEI MatePad (DBR-W00, Qualcomm Snapdragon 865 CPU, 8G memory, 128G SD, 2560X1600 pixel resolutions). The APP includes the commonly used functions, such as start-up registering, system setup, data processing, dynamic image reconstruction, contact impedance analyzing and data storage, etc. The APP also runs well based on the HUAWEI Mobile phone (ALP-TL100, HiSilicon Kirin 970 CPU, 4G memory, 64G SD, 2560X1440 pixel resolution).

2.3 DAS specification

The specifications of the DAS include: size 15x8x2.5cm, weight less than 150g; accuracy 60dB; imaging speed >20fps; frequency 50kHz (20-200KHz adjustable); 16 PET disposable electrodes; CCS <5mA RMS; battery power time >10h; power consumption <3W; battery charge port USB mini/Type-C; supportable data transmission mode: BLE/Wi-Fi/Serial Port or CAN/SPI/USB/GPIO; data storage SD card support.

3 Conclusions

Preliminary results in healthy and patients show that the system could acquire dynamic EIT images at a speed of 20fps for lung ventilation monitoring.

The DAS will be integrated with ventilator system to gain a real-time feed-back from EIT for guiding ventilation parameter configurations.

4 Acknowledgements

The authors would like to express their gratitude to the Key Project Grant of the MOST (2022YFC2404803), China.

References

[1] K Farnham and R Halter. *Conf 23rd*, EIT 2023, Aachen, Germany, P79.

[2] XT Shi, et.al. DOI 10.1109/JSEN.2018.2836336, IEEE Sensors.

Feasibility of Noninvasive Electrical Impedance Tomography Monitoring to Predict Neurological Dysfunction after Total Aortic Arch Replacement

Chen Yang[1], Wenjing Zhu[2, 3], Yitong Guo[2], Xuetao Shi[2], Zhenxiao Jin[1]

[1]Xijing Hospital, Xi’ an, China. yangch_23@163.com
[2]Fourth Military Medical University, Xi’ an, China.
[3]Northwestern Polytechnical University, Xi’ an, China.

Abstract: The noninvasive electrical impedance tomography system was adopted to 375 patients underwent total aortic arch replacement to monitor their cerebral impedance intraoperatively. Average resistivity value (ΔARV) and maximum asymmetry index (MAI) during hypothermic circulatory arrest was significant differences in patients with Neurological dysfunction (ND)(+) and patients without ND(-) (P = 0.041; P = 0.034). EIT is a promising technique to provide an option for multimodal cerebral monitoring in total aortic arch replacement surgery.

1 Introduction

Neurological dysfunction (ND) is one of the most common complications after total aortic arch replacement (TAAR). The aim of this study was to investigate the correlation between EIT extracted parameters and ND, so as to assess the feasibility of EIT for intraoperative monitoring of the total aortic arch replacement.

2 Methods

375 patients were monitored intraoperatively using the EIT equipment (EH-300, UTRON Technology Co., Ltd., Hangzhou, China) (Figure1). Details of surgery and EIT data acquisition have been described previously.[1] The primary end point was the neurological dysfunction (defined as stroke, transient neurological deficit or coma).[2] The secondary end point was in-hospital mortality.

In order to reflects overall changes in cerebral resistivity, we extract five parameters during hypothermic circulatory arrest (HCA) period: average resistivity value (ΔARV_{HCA}), maximum resistivity asymmetry index ($MRAI_{HCA}$), time integral of resistivity asymmetric index ($TRAI_{HCA}$), k_{HCA} and maximum asymmetry index (MAI_{HCA}).

2.1 Figures and tables

EIT extracted parameters of patients with and without neurological dysfunction are displayed in Table 1. ΔARV_{HCA} and MAI_{HCA} was significant differences in patients with ND(+) and patients without ND(-). However, there was no significant difference in other parameters.

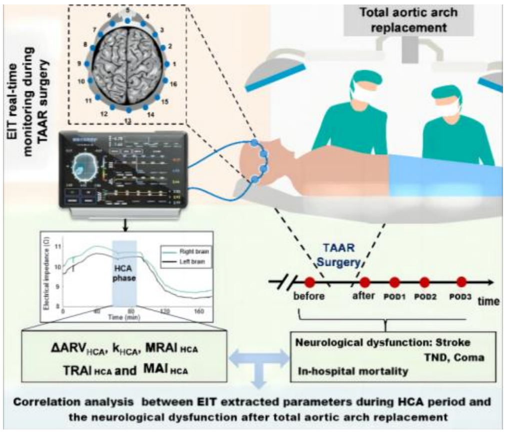

Figure 1: Graphical abstract

2.2 Equations

$$\mathrm{ARV} = \frac{1}{\mathrm{M}}\sum \mathrm{A_k\, x_k}, \mathrm{k} = 1, \ldots, \mathrm{M} \tag{1}$$

ARV reflects the change of electrical impedance of the whole brain during surgery.

$$\Delta \mathrm{ARV_{HCA}} = \mathrm{ARV_{after\ HCA}} - \mathrm{ARV_{before\ HCA}} \tag{2}$$

$$\mathrm{k_{HCA}} = \frac{\Delta \mathrm{ARV_{HCA}}}{\mathrm{t_{HCA}}} \tag{3}$$

$$RAI = ARV_L - ARV_R \tag{4}$$

$$TRAI = \int_{start\ of\ HCA}^{end\ of\ HCA} RAI \cdot dt \tag{5}$$

$$\mathrm{AI} = \frac{ARV_L - ARV_R}{\mathrm{ARV}} \tag{6}$$

3 Conclusions

EIT can provide an option for multimodal cerebral monitoring in total aortic arch replacement surgery.

References

[1] Li, Yandong, Zhang, Ding, Liu, Benyuan, et al. JOURNAL OF CARDIOTHORACIC AND VASCULAR ANESTHESIA, 32 (6): 2469-2476, 2018.

[2] Sultan, Ibrahim, Bianco, Valentino, Patel, Himanshu J, et al. JOURNAL OF THORACIC AND CARDIOVASCULAR SURGERY, 161 (5): 1713-1720.e1, 2019

Table 1: EIT extracted parameters of patients with and without neurological dysfunction.

Variable	All (N=375)	ND(-) (N=169)	ND(+) (N=209)	*P*-value
ΔARV_{HCA}(AU)	-0.003±0.035	0.007±0.035	-0.007±0.035	0.041
K_{HCA}(10^{-3}AU/min)	-0.033±0.864	0.045±0.936	-0.096±0.798	0.118
$MRAI_{HCA}$(AU)	0.011±0.014	0.012±0.018	0.010±0.010	0.171
$TRAI_{HCA}$(AU)	6.481±18.776	6.295±21.119	6.632±16.708	0.866
MAI_{HCA}	0.048±0.055	0.055±0.069	0.042±0.038	0.034

AixTOM - The mfEIT research platform from Aachen

Urban Jacobs[1], Tobias Menden[1], Steffen Leonhardt[1]
[1]Medical Information Technology, RWTH Aachen University, Aachen, Germany, jacobs@hia.rwth-aachen.de

Abstract: This contribution describes a self-developed, FPGA-based EIT research platform. The resulting device allows any measurement pattern, up to five simultaneous excitation frequencies and any reconstruction algorithm.

1 Introduction

As commercial EIT systems usually only grant limited access to their configuration, the Chair of Medical Information Technology (MedIT) is currently developing its own EIT research platform named *AixTOM*. It is characterised by open interfaces, multifrequency current injection, arbitrary measurement patterns and reconstruction algorithms, and easy expandability on both the hardware and software side. AixTOM, depicted in Fig. 1, will be made available to third parties when conducting publicly funded research.

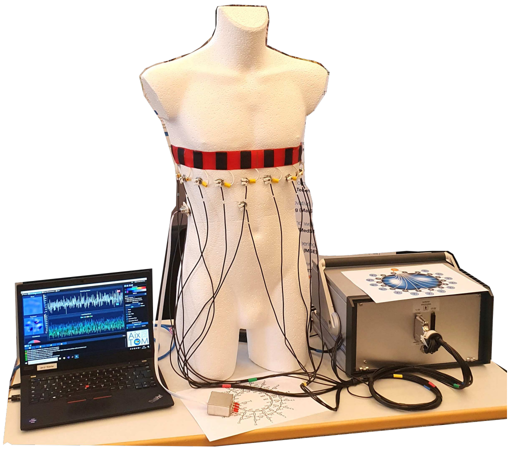

Figure 1: AixTOM in action (on an electrical phantom).

2 Methods

2.1 Hardware

The hardware design is depicted in Fig. 2. The central unit is a Xilinx Zynq-7000 FPGA. To reduce production costs, the ready-made evaluation kit ZC706 was chosen. D/A and A/D conversion are done by the expansion card FMC 144. Power conditioning, current generation, multiplexing and signal amplification are handled by circuit boards developed in-house. These boards are in the form of plug-in units to keep the hardware expandable. To maximise patient safety, the Ethernet connection to the controlling PC runs through a fiber optic cable. The supply voltage of 24 V is provided by a medical power supply. Overcurrent is prevented by a hard-wired emergency shutdown.

This system allows up to five simultaneous excitation frequencies in the range of 40 kHz to 1 MHz. For now only sinusoidal signals are supported, but this could be changed in the FPGA firmware. The frame rate depends on the selected FFT resolution, it goes from 10 - 50 fps. 32 arbitrarily selectable channels for exterior electrodes are provided. Additionally, there are four channels for interior electrodes (e.g. for use in the esophagus). However, these have not yet been connected and tested.

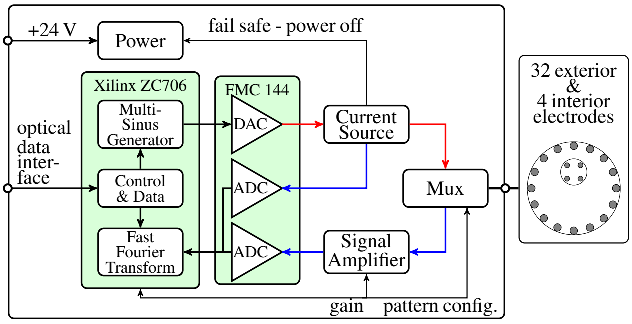

Figure 2: AixTOM hardware schematic (modified from [1]).

2.2 Software

Initially, an AixTOM software based on MATLAB and EIDORS was written. In 2023, the development of a new software was started, see Fig. 3. This software runs independently from MATLAB, which requires a license, and is more user-friendly and optically pleasing. It is designed in such a way that it can easily be extended by new reconstruction algorithms, or even new tabs to switch to different research contexts like lung perfusion imaging.

Patient Name
Male Sex
0 Patient-ID
21.0 years Age
1.80 m Height
72.50 kg Weight
Comment
Auto-weight (?)
Animal (?)

[11:39:07] [App] AixTOM-Gui 1.0.0 has started execution.

Figure 3: New AixTOM user interface.

3 Conclusion and Outlook

The result is a multi-frequency EIT device that can be connected to an ordinary PC via Ethernet. The data can be retrieved via a TCP socket, which gives the user unlimited freedom in software and reconstruction methods. The same applies to the measurement pattern, as the multiplexers determining it can be set from the PC. Non-EIT-related bioimpedance measurements (in the range of 0.1 - 50 Ω) are also possible.

The system is currently being ported to a more up-to-date FPGA board. Human approval is also being sought (as of February 2024).

4 Acknowledgements

Thanks go to Astrid Warkentin, Cedric Trödel, Soufian Noor and Oskar Beaujean for the ongoing development of the new software.

References

[1] T Menden *Frequenz-differentielle elektrische Impedanztomographie zur thorakalen Gewebedifferenzierung* RWTH Publications, DOI: 10.18154/RWTH-2023-01248 , 2023

Beyond Simplism: Unveiling Bias in EIT Perfusion Models

Diogo F. Silva[1] and Steffen Leonhardt[1]

[1]Chair for Medical Information Technology, RWTH Aachen University, Aachen, Germany, silva@hia.rwth-aachen.de

Abstract: This study addresses inherent biases in perfusion derived from contrast EIT imaging due to oversimplified double-compartment model assumptions, by setting it against a more general four-compartment model. The former shown to likely be inadequate for over 75% of pixels in porcine imaging data, which calls for either more advanced modelling or better study design practices to improve the reliability of the technique.

1 Introduction

Thoracic EIT is pivotal for non-invasive lung perfusion metrics using indicator-bolus imaging. Traditionally, this is analyzed via a double-compartment model, where heart region signals indicate blood mixing from both heart chambers (two peaks), and lung signals suggest a single compartment (one peak) which are fitted with a gamma-variate function or directly analysed for perfusion metrics [1]. However, discrepancies arise, notably in the mediastinum region, where signals defy expected gamma-variate shapes, as in Fig. 1, and EIT's partial volume effect questions the use of hard binary compartment classification. This study critiques existing model biases, advocating for refined methodologies to bolster EIT's accuracy and reliability.

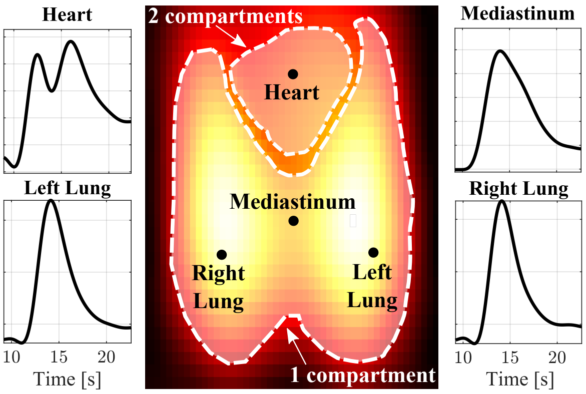

Figure 1: Typical compartment assumptions and key pixels.

2 Methods & Materials

To compare with current methodologies, we replicated the double-compartment model from [1] and extended our analysis to a more nuanced four-compartment model, accommodating simultaneous compartment presence in pixels to address existing model limitations. A 60-second EIT recording from an intubated healthy porcine subject injected with 10 mL of 0.9% NaCl was reconstructed using the GREIT algorithm [2] and pre-processed to remove high-frequency noise and cardiac information, trends, and baseline drift. Region-of-interest (ROI) delineation employed the k-means hard clustering method from [1] which uses normalized mean transit-time and peak amplitude values extracted from pre-processed pixel signals to sort the pixels into so-called *pre-lung*, *lung*, and *post-lung* classes. Ultimately, *lung* pixels are analysed as single compartments, claiming the *pre-lung* and *post-lung* information is mixed into a 2-compartment region corresponding to the heart. The segmented ROIs are compared with the four-compartment model ROIs in Fig. 2. We applied the four-compartment model through non-negative matrix factorization (extended from [3]) of the data matrix $Y \in \mathbb{R}^{T\times 1}$ into a temporal dynamics $X \in \mathbb{R}^{T\times 4}$ and a spatial matrix $A \in \mathbb{R}^{4\times P}$ where T and P are the number of samples and pixels, respectively. Normalizing matrix A with the pixel-wise sum of all component amplitudes approximates the relative regional significance of each component.

3 Results & Discussion

By thresholding at 5%, a map indicating the number of relevant components in each pixel N was obtained, with these findings presented above in Fig. 2. Analysis reveals the double-compartment model's validity holds mainly in central heart and peripheral lung pixels. Conversely, it fails in 75.10% of the image pixels with regions where up to three additional relevant components may be missing. Moreover, belt placement and anatomical variations, such as in the relative positioning of lungs to the heart in human and porcine subjects, as illustrated below in Fig. 2, contribute to this skewing of perfusion estimates later on.

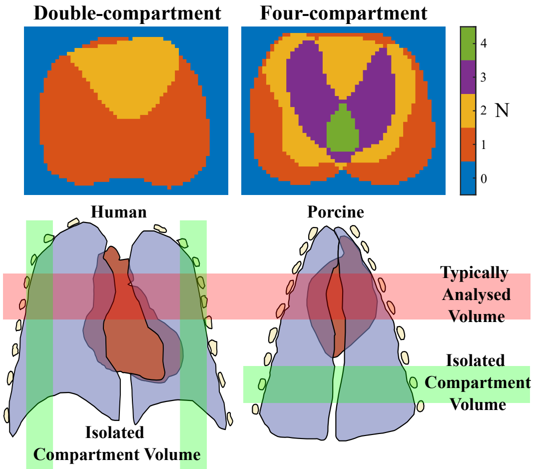

Figure 2: Number of pixel compartments (N) identified by both models (above). Subject anatomy and target volumes (below).

4 Conclusions & Outlook

Our findings reveal a spatially-varying bias in EIT perfusion studies, rooted in oversimplified model assumptions. Future research must pivot towards sophisticated algorithms capable of managing up to four (at least) compartments per pixel, and/or better identifying true single-compartment pixels, while also considering the subject's anatomy and belt positioning to mitigate compartment mixing.

References

[1] M Kircher, *et al. IEEE Trans Med Imaging*, 40(1):251-261, 2021
[2] A Adler, *et al. Physiol Meas.*, 30(6):S35-55, 2009
[3] B Hentze, *et al. Physiol Meas.*, 39(6):065004, 2018

Multi-modal EIT Imaging with Hologram-Guided Group Sparsity

Ronald B. Liu[1,3], Hao Fang[1], Xavier Casadevall i Solvas[3], Pierre O. Bagnaninchi[2], Zhe Liu[1*], Yunjie Yang[1]

[1]SMART Group, Institute for Imaging, Data and Communications, School of Engineering, The University of Edinburgh, UK,zz.liu@ed.ac.uk
[2]Centre for Regenerative Medicine, Institute for Regeneration and Repair, The University of Edinburgh, UK
[3]Biomimetics Group, Department of Biosystems, Catholic University of Leuven, Belgium

Abstract: We introduced a dual-modal imaging technique combining Electrical Impedance Tomography (EIT) and Lens-Free Imaging (LFI). Our approach, using the Hologram-Guided Group Sparsity (HGGS) algorithm with a hologram, can reconstruct high-quality conductivity distribution with more accurate structural information.

1 Introduction

Multi-modal EIT imaging is proposed to enhance image reconstruction quality by incorporating additional information. LFI is an emerging imaging technique that utilizes diffraction and projection patterns, i.e. holograms, without traditional lenses. The compact setup and large Field-Of-View (FOV) of LFI make it promising for various biomedical imaging tasks. Integrating high-resolution 2D hologram data from LFI with EIT can enhance conductivity reconstruction quality with improved structural information [1].

2 Method

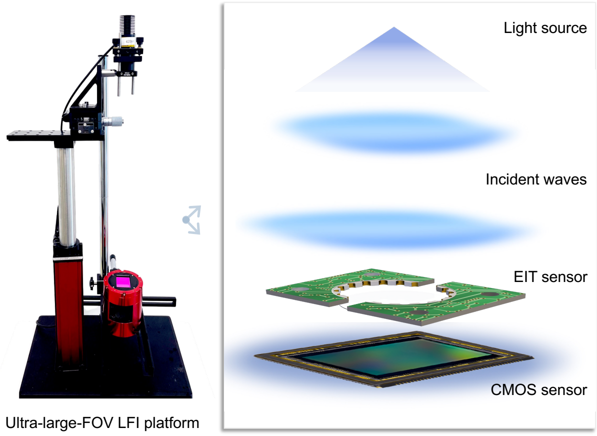

Figure 1: Left: the LFI setup. Right: Schematic of our dual-modal imaging setup. The hologram of the sample in the EIT sensor is captured by a CMOS sensor at the bottom.

The platform combines a 16-electrode EIT sensor with an ultra-large FOV telescope cold camera, shown in Figure 1. The light source is LED with a wavelength of $420\,nm$.

The binary mask images are automatically generated by the Segment Anything Model (SAM) [2] from holograms. After calibration, we labelled individual pixels as N groups to express conductivity changes ($\boldsymbol{\Delta\sigma}$) in individual regions.

The reconstruction is conducted by optimization based on weighted group-level constraint and Total Variation (TV) constraint:

$$\begin{cases} \min_{\Delta\boldsymbol{\sigma}} & \sum_{i=1}^{N} \omega_i \left\| \Delta\boldsymbol{\sigma}_{g_i} \right\|_2 + \left\| \Delta\boldsymbol{\sigma} \right\|_{TV} \\ \text{s.t.} & \boldsymbol{J}\Delta\boldsymbol{\sigma} = \Delta\boldsymbol{V} \end{cases} \tag{1}$$

where $\sum_{i=1}^{N} \omega_i \left\| \Delta\boldsymbol{\sigma}_{g_i} \right\|_2$ is the weighted $l_{2,1}$ norm and ω_i is the weight for i^{th} group, $\|\Delta\boldsymbol{\sigma}\|_{TV}$ denotes the isotropic TV norm to smooth the estimated EIT image. To solve Eq. (1) we adopted accelerated ADMM with an over-relaxation step [1].

3 Results

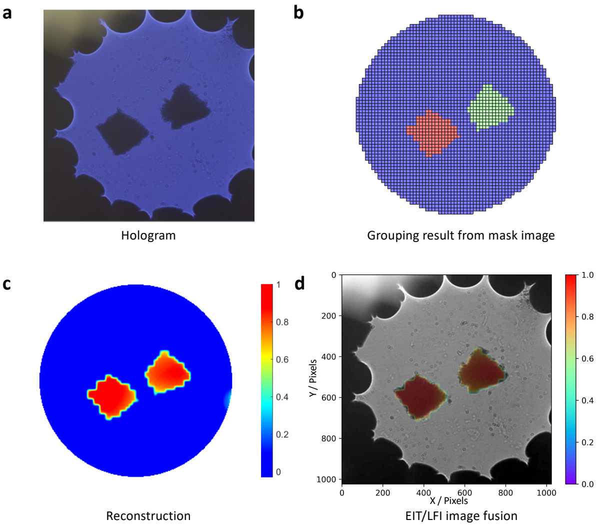

Figure 2: **a** hologram; the mask is generated from **a** by semantic segmentation. **b**, pixel grouping from the mask. **c**, the reconstruction result by optimization (64 × 64 pixels). **d**, EIT/LFI image fusion of **a** and **c** with the semantic mask.

Figure 2 shows the reconstruction results of real-world experiments. The hologram captured by the camera under LFI shows the clear boundary of the object in the EIT sensor. After applying SAM [2], we generate a binary mask image (1024 × 1024 pixels) for pixel grouping. The fused result showcases both high-resolution object morphological features and conductivity distribution.

4 Conclusions

We introduced HGGS, a dual-modal imaging approach merging EIT and LFI, showcasing improved conductivity contrasts in EIT reconstruction. Future work includes extending the method to 3D imaging and exploring dynamic imaging of tissues/cells.

References

[1] Z. Liu, et al., "Image Reconstruction of Electrical Impedance Tomography Based on Optical Image-Guided Group Sparsity", IEEE Sens. J., 2021.
[2] A. Kirillov, et al., "Segment Anything", ICCV 2023.

Detection of Severe Cerebral Haemorrhage by a Multi-Frequency Magnetic Induction Tomography Device: a Clinical Trial

Xing Jin[1], Cheng Chen[1], Jiaxun Xie[1], Lei Mao[1], and Ruigang Liu[1]

[1]Hangzhou Utron Technology Co., Ltd., Hangzhou, China, ruigang@hotmail.com

Abstract: A Class II medical device registration clinical trial has been conducted for Utron MH-200, a multi frequency magnetic induction tomography (MIT) device used to assist in the detection of severe haemorrhagic stroke larger than 30mL. 132 stroke patients from three hospitals were enrolled. The sensitivity, specificity, and accuracy of auxiliary recognition for cerebral haemorrhage greater than or equal to 30mL were 90.16%, 92.96%, and 91.67%, respectively.

1 Introduction

Stroke is a common disease with high incidence rate, high disability rate and high mortality, which brings heavy burden to society and families. Although imaging examinations such as CT and MRI can accurately diagnose stroke, the number of hospitals with these devices and experienced doctors is limited and unevenly distributed. Screening for severe stroke patients before transportation to the hospital is a feasible option.

Stroke symptoms such as intracranial haemorrhage and ischaemia will lead to changes in the distribution of electrical impedance. Therefore, both EIT (Electrical Impedance Tomography) and MIT have the potential to be competent for this task. MIT is more competitive due to its non-contact nature.

2 Methods

Utron MH-200 is a multi-frequency MIT device produced by Hangzhou Utron Technology Co., Ltd., originating from the Fourth Military Medical University, as in Fig. 1 and [1–4]. MH-200 is designed for rapid detection of stroke. The frequency range is from 15MHz to 35MHz, with a step size of 1MHz.

Figure 1: Utron MH-200.

2.1 Overview of clinical trial

Starting from July 2022, Sir Run Run Shaw Hospital, affiliated with the School of Medicine of Zhejiang University, conducted a multicentre clinical trial as the team leader to verify the accuracy and safety of MH-200, Class II medical device, in assisting in screening for severe haemorrhagic stroke, refers to a haemorrhagic stroke of 30mL or more.

The clinical trial follows a double-blind principle. Inclusion criteria: 1) 18 years old and above, regardless of gender; 2) After CT and/or MRI examination, clinical diagnosis of acute stroke; 3) It is expected that the test equipment can be safely worn for at least 5 minutes. As of October 2023, a total of 132 stroke patients were enrolled, including 61 cases of severe cerebral haemorrhage greater than or equal to 30mL (positive), 71 cases of cerebral haemorrhage less than 30mL and ischaemic stroke (negative).

Head CT/MRI scanning and interpretation serve as the gold standard to calculate accuracy indicators such as sensitivity and specificity. Another control is the NIHSS (National Institute of Health stroke scale).

MH-200 provides a set of dual frequency differential reconstructed images and a one-dimensional index, MBA (Mean Bio-impedance Asymmetry), for determining positive and negative results.

2.2 Results of clinical trial

The sensitivity, specificity, and accuracy of MH-200 assisted recognition for severe cerebral haemorrhage $\geqslant$ 30mL were 90.16%, 92.96%, and 91.67%, respectively. The AUC (Area Under the Curve) of ROC (Receiver Operating Characteristic) for MBA assisted recognition of $\geqslant$30mL intracerebral haemorrhage is 0.8996, significantly higher than that of NIHSS with AUC of 0.7686, as in Fig. 2.

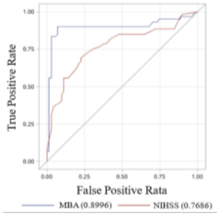

Figure 2: ROC curve of MBA and NIHSS.

3 Conclusions

The clinical trials have shown that Utron MH-200 can assist in the diagnosis of severe haemorrhagic stroke with over 90% accuracy, providing an optional medical device for pre-hospital triage.

References

[1] Q Chen, R Liu, C Wang, R Liu *Meas Sci Technol*, 32: 035402, 2021.

[2] T Zhang, X Liu, W Zhang, M Dai, C Chen, X Dong, R Liu, C Xu *Physiol Meas*, 42: 065004, 2021.

[3] T Zhang, W Zhang, X Liu, M Dai, Q Xuan, X Dong, R Liu, C Xu *IEEE T Instrum Meas*, 71: 4005713, 2022.

[4] Y Jiao, T Zhang, C Fan, H Cao, M Chao, L Han, W Zhang, L Mao, R Liu, C Xu, L Wang *Physiol Meas*, 44: 035012, 2023.

High-speed Impedance Imaging-based Cardiopulmonary Function Monitoring in OSA Patients During CPAP Titration Study

You Jeong Jeong[1,2], Tingting Zhang[1,2] and Tong In Oh[1,2]

[1]Department of Biomedical Engineering, Kyung Hee University, Seoul, Republic of Korea, tioh@khu.ac.kr
[2]Medical Science Research Institute, Kyung Hee University Hospital, Seoul, Republic of Korea

Abstract: To optimize CPAP treatment for OSA patients, this study employs PSG and high-speed impedance imaging to observe and quantify changes in ventilation, blood perfusion, and the V/Q ratio under varying pressures during the CPAP titration study. It provides insights for finding a patient-specific optimal pressure.

1 Introduction

Continuous positive airway pressure (CPAP) is the primary therapeutic approach for obstructive sleep apnea (OSA) patients. In hospitals, patients sleep all night long wearing CPAP masks and polysomnography (PSG) sensors, and a CPAP titration study is performed to find the optimal pressure for each patient by adjusting the pressure of the CPAP device [1]. Despite these efforts, CPAP titration studies report that 28-50% fail to find the optimal pressure [2]. In addition to factor analysis to prevent failure in CPAP titration studies, research was performed to set sub-optimal CPAP using different standards for each doctor or to estimate effective CPAP using AI technology [3].

In this study, we intend to evaluate the patient's ventilation and blood perfusion under the optimal pressure found in the conventional manual CPAP titration study using the PSG sensors and high-speed impedance imaging. In addition, we would like to observe changes in the subject's cardiopulmonary status under pressure around the optimal pressure. Through this, we aim to provide insight that can complement the conventional CPAP titration study based on the number of event occurrences.

2 Methods

Thirty patients diagnosed with OSA and prescribed CPAP (AirSense S10, ResMed, USA) were recruited from the Department of Otorhinolaryngology at Kyung Hee University Hospital. Consent was obtained from all patients participating in the study (IRB No. KHMC-2022-07-038). An overnight sleep was conducted in the sleep laboratory while performing the conventional manual CPAP titration study. Next to PSG (Embla S7000, Medcare, Iceland) measurements, Epad^{TM} (Bilab, Korea) electrodes for impedance imaging were additionally attached to the chest, acquiring 100 impedance images per second using AirTom (Bilab, Korea). Fig. 1 shows the sensors and electrodes measured by PSG and AirTom during the CPAP titration study. After removing the motion artifact from the measured data [4], respiratory-related and cardiac-related signals were separated using the source consistency algorithm. We calculated the averages of tidal volume (TV), minute ventilation (MV), stroke volume (SV), cardiac output (CO), and ventilation-perfusion (V/Q) ratio for each pressure level on the CPAP device using EIT images. Additionally, we computed the standard deviation of the regional ventilation delay (sdRVD), which presents the difference in the time it takes for air to fill the lungs from the images. As shown in Fig. 2, at the optimal pressure from conventional CPAP titration study, we observed an increase in MV and a decrease in CO, resulting in an elevated V/Q ratio, and noted the greatest reduction in sdRVD.

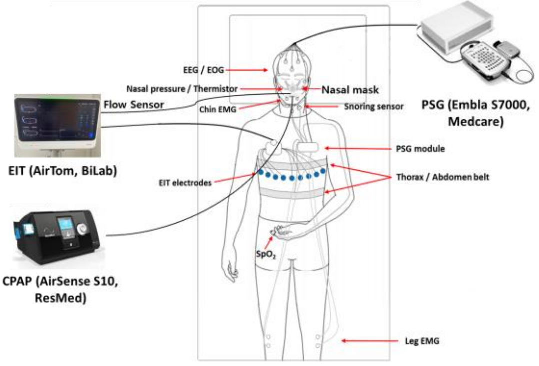

Figure 1: Experimental setup: A full-night CPAP titration study with simultaneous measurements of PSG and impedance images.

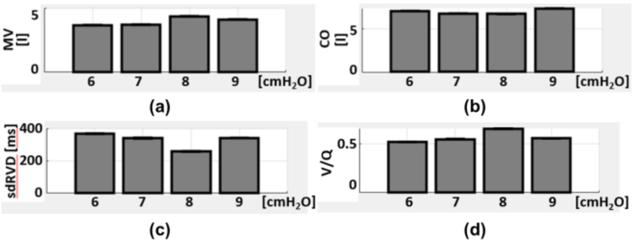

Figure 2: An example of changes in (a) MV, (b) CO, (c) sdRVD, and (d) V/Q ratio when increasing the pressure of the CPAP device from 6 to 9 cmH_2O.

3 Conclusions

Analyzing these physiological responses aims to provide valuable insights into adjusting CPAP settings to enhance treatment efficacy and patient comfort.

4 Acknowledgements

This research was supported by a National Research Foundation (NRF) grant (NRF2020R1A2C1008975) and MOTIE (20006024) in Korea.

References

[1] C A Kushida, A Chediak, R B Berry *J Clin Sleep Med*, 4(2): 157-171, 2008.
[2] A Gupta, G Shukla *Sleep Breath*, 22: 401-409, 2018.
[3] A E Solh, M Akinnusi, A Patel *Sleep Breath*, 13: 325-330, 2009.
[4] T H Dang, G Y Jang, K Lee Sensors, 23: 1-15, 2023.

Cross-frequency Fusion in CFSF-Net for Enhanced Time-difference Electrical Impedance Tomography

Xiang Tian[1], Jian’an Ye[1], Xuetao Shi[1], Feng Fu[1] and Canhua Xu[1]

[1]Department of Biomedical Engineering, the Fourth Military Medical University, Xi’an, China, xiangtian@fmmu.edu.cn

Abstract: A cross-frequency spatial information fusion network (CFSF-Net) imaging method based on multi-path structure is proposed to improve the spatial resolution of the time difference EIT (tdEIT), and the effectiveness and stability of the algorithm are verified by simulation experiments under different noise levels.

1 Introduction

Electrical impedance tomography (EIT) images the inside of the measured body based on the impedance characteristics of biological tissues, which shows an excellent application prospect in many fields such as lung function monitoring, breast cancer screening and stroke detection [1]. However, as a nonlinear and ill-posed imaging technology, the spatial resolution of EIT still needs to be further improved [2]. We propose a cross-frequency spatial information fusion network (CFSF-Net) method, the cross-frequency spatial information between time difference conductivity images at multiple frequencies is extracted through multi-path structure in this method to achieve higher quality tdEIT imaging.

2 Methods

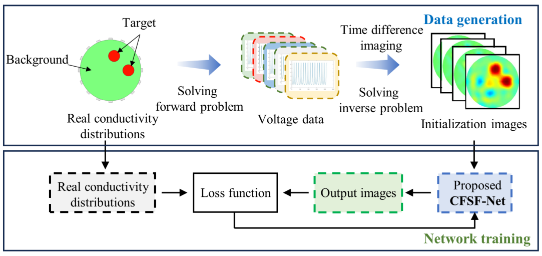

Figure 1: Framework of the CFSF-Net imaging method.
The framework of the CFSF-Net method includes two main parts: data generation and network training.

First, the voltage data at multiple frequencies were generated using a simulation model with 16 Ag/AgCl electrodes was built in COMSOL. Using the conventional tdEIT imaging algorithm [3], we then acquired initial images of conductivity distribution as this dataset for deep learning network training.

The structure of the CFSF-Net is detailed in Fig. 2. In the initialization module, voltage data are transformed into corresponding conductivity distribution images using the imaging algorithm. The cross-frequency information extracting module receives these conductivity distribution images, which represents spatial information at various frequencies, and uses them to extract the spatial-related information between the advanced features of the images. Finally, the extracted features are merged and up-sampled in the information fusion module to generate the predictive tdEIT image.

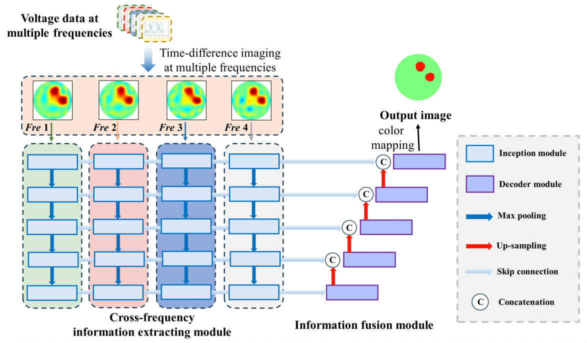

Figure 2: Detailed structure of CFSF-Net, which is mainly composed of a traditional time difference imaging module, a cross-frequency information extraction module and an information fusion module.

2.1 Results

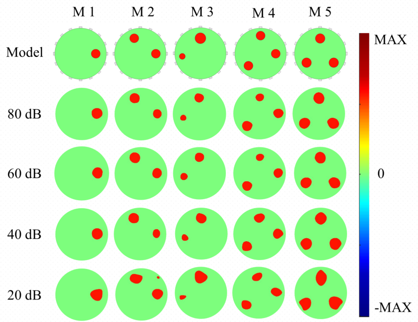

Figure 3: Reconstruction results under test data of different noise levels (80–20 dB).

Fig. 3 reveals that the CFSF-Net imaging algorithm performs exceptionally well on test data across conventional noise levels, ranging from 80 to 40 dB, and accurately reconstructs target sizes and shapes, although the targets shape is deformed under 20 dB strong noise.

3 Conclusions

In this study, the imaging quality of tdEIT was improved by combining the spatial information between conductivity images at different frequencies, and the effectiveness of the algorithm was verified by simulation experiments. In the future, the method can be extended to imaging fields such as magnetic induction tomography.

References

[1] A. Adler and A. Boyle, “Electrical impedance tomography: Tissue properties to image measures,” IEEE Trans. Biomed. Eng., vol. 64, no. 11, pp. 2494–2504, Nov. 2017.

[2] X. Liu et al., “Fast iterative shrinkage-thresholding algorithm with continuation for brain injury monitoring imaging based on electrical impedance tomography,” Sensors, vol. 22, no. 24, 2022, Art. no. 9934.

[3] L. Hu, H. Wang, B. Zhao, and W. Yang, “A hybrid reconstruction algorithm for electrical impedance tomography,” Meas. Sci. Technol., vol. 18, no. 3, 2007, Art. no. 813.

A Channel Consistency Metric Method for EIT Systems

Yulin Min[1], Andy Adler[2], Qifan Wang[1], Tao Dai[1]
[1] Sealand Technology Ltd., Chengdu, China
[2] Systems and Computer Engineering, Carleton University, Ottawa, Canada

Abstract: Reciprocity accuracy indicates the consistency of corresponding reciprocal pairs. Evaluating this accuracy typically requires the measurement pattern and stimulation pattern to be interchangeable. In this work, we propose a novel pattern-insensitive method offering system-level channel consistency assessment without this constraint.

1 Introduction

Reciprocity accuracy[1] compares the measurements of corresponding reciprocal pairs. To measure the voltage of a corresponding reciprocal pair, the EIT system must be designed with the ability to swap the pattern of stimulation and measurement. For example, evaluating a system with "opposite-stimulation-adjacent-measurement" pattern requires the additional implementation of "adjacent-stimulation-opposite-measurement" capability. While some methods[2] assess channel consistency through visual analysis of images, this work proposes a novel pattern-insensitive metric method for quantitative evaluation. This method eliminates the dependence on specific patterns, enabling system-level channel consistency assessment for any EIT system configuration.

2 Methods

A circular circuit layout on PCB is essential for this method. Figure 1(Left) illustrates a PCB design for a 16-electrode system. In this design, the resistances between adjacent electrode pairs are identical.

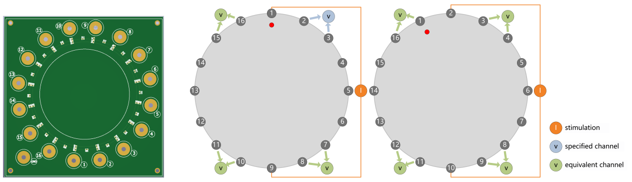

Figure 1: Left: PCB for 16-electrode EIT system. Middle: Equivalent channels of the 1st measurement channel during the proceeding of 1-9 stimulation.Right:4 additional equivalent channels

Consider a 16-electrode system with opposite-stimulation-adjacent-measurement pattern, specifying a stimulation pair and a measurement pair designates a channel. When the stimulation pair remains unchanged, three additional channels with matching voltage amplitude can be identified for this channel, as illustrated in Figure 1 (Middle). These channels are typically situated at symmetric positions. Due to the continuous symmetry of circular circuits, changing the stimulation pair should result in 4 additional channels at corresponding relative positions showing the same amplitude, as illustrated in Figure 1 (Right). Thus, iterating over 16 stimulation pairs reveals 16 * 4 equivalent channels sharing identical voltage amplitude, which are combined into an equivalent group for the specified channel. The reference voltage of a channel is obtained by averaging the voltages of all channels in its corresponding equivalent group. This process requires stimulating all available electrode pairs and measuring the voltages at the same relative positions. Consequently, this reference voltage demonstrates a statistical characteristic of the channels at system-level. By comparing the channel voltage with its corresponding reference voltage, we can assess the system-level channel consistency, as shown in equation (1).

$$c_i = 1 - \frac{\left|\, |v_i| - mean(|\hat{\boldsymbol{v}}_{equivalent\_group(i)}|) \,\right|}{mean(|\hat{\boldsymbol{v}}_{equivalent\_group(i)}|)} \qquad (1)$$

c_i denotes the consistency of channel i, where $i \in all\_channels$, v_i denotes the measurement voltage of channel i, $\hat{\boldsymbol{v}}_{equivalent\_group(i)}$ denotes the measurement voltages of all channels in the equivalent group of channel i.

3 Results

We constructed two EIT systems with different circuits and calculated their channel consistency described in the previous section. The results are shown in Figure 2. The x-axis represents the channel number, and the y-axis represents the channel consistency calculated using equation (1). Higher channel consistency indicates that the corresponding channel have stronger statistical resemblance with other equivalent channels. Based on the results, we can select the system that exhibits more uniform current distribution across its circuits .

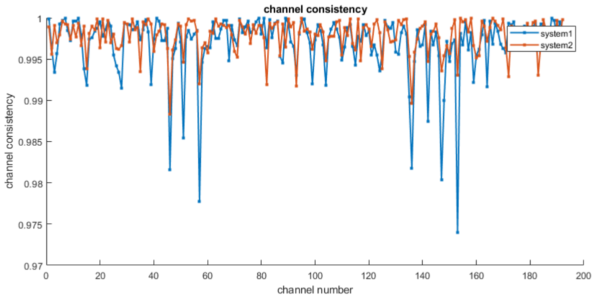

Figure 2: Channel consistency analysis reveals better circuit balance in system 2 compared to system 1.

4 Conclusions

In this paper, we propose a novel channel consistency metric method and detail its application to a 16-electrode EIT system with opposite-stimulation-adjacent-measurement pattern. Furthermore, by utilizing the inherent symmetry of circular circuits, we can extend the applicability of this method to systems with diverse electrode numbers and stimulation-measurement patterns.

References

[1] Yasin, M., Böhm, S., Gaggero, P.O. and Adler, A., *Physiological measurement*, 32(7), p.851, 2011

[2] Xu, Y., Yan, Z., Han, B. and Dong, F., *IEEE Transactions on Instrumentation and Measurement*, 70, pp.1-10, 2020

Digital Multi-frequency Phase Detection Method of MIT

Cheng Chen[1], Jiaxun Xie[1], Lei Mao[1], and Ruigang Liu[1]

[1]Hangzhou Utron Technology Co., Ltd., Hangzhou, China, chenchenghenry@hotmail.com

Abstract: The accuracy and stability of data detection in MIT (Magnetic Impedance Tomography) systems are key indicators of system performance. This study achieves a system detection signal-to-noise ratio of over 70dB and a relative drift of 0.08% per hour by adopting digital direct sampling of orthogonal sequences for phase detection.

1 Introduction

Magnetic Induction Tomography (MIT) reconstructs images of the intracranial impedance distribution by detecting the eddy current phase values of targets obtained through coils without contact with the human body. The eddy current signal is very weak and superimposes with the excitation signal. Therefore, the MIT phase identification system requires a high signal-to-noise ratio and low phase drift to reconstruct the correct impedance distribution.

2 Methods

Because the phase signal of MIT is directly proportional to the frequency difference of the excitation, a higher frequency excitation signal is chosen to obtain better detection signals. At the same time, to achieve a better dynamic range, a higher bit depth for the AD conversion is required. Combining these two factors places high demands on the AD chip. The usual method [1] involves down-converting the frequency before AD sampling, such as using a superheterodyne down-conversion scheme.

The key component in this process is the mixer used for down-conversion. The nonlinearity and temperature drift characteristics of analog mixers limit the overall improvement in measurement accuracy. Considering that the system's demodulation signal is a single-frequency signal, we adopt a digital direct sampling down-conversion scheme, as shown in Fig. 1. According to the Nyquist sampling theorem, this method can also obtain the complete information of the original signal. Digital down-conversion effectively reduces the nonlinearities, temperature drift, and noise introduced by analog mixing/down-conversion, thereby achieving the goal of low noise and low temperature drift.

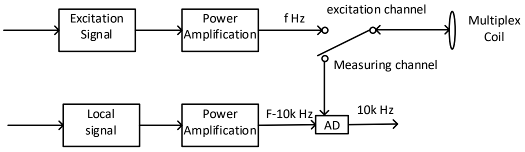

Fig. 1. Digital direct sampling quadrature sequence phase detector circuit

The signal source employs Direct Digital Synthesis (DDS) technology to generate an excitation sinusoidal waveform, with the capability to vary the frequency within the range of 15 MHz to 30 MHz The DDS chip used is the AD9958, which features a built-in dual-channel 10-bit DAC, capable of generating two 500 MSPS signals, with a 32-bit frequency control word. In application, one output is used as the excitation signal source, and the other output serves as the clock signal for AD sampling, as shown in Fig. 2.

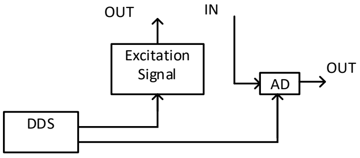

Fig. 2. Excitation signal and AD timing control schematic diagram

Based on this, we developed a system, Utron MH-200, which operates within a frequency range of 15 MHz to 35 MHz, with a step size of 1 MHz. The system's overall signal-to-noise ratio reaches 70dB, and the long-term phase drift is less than 0.08%, as shown in Fig. 3. This performance surpasses that reported in the literature, such as 13.56 MHz: 60dB, 0.16% [1], 20 MHz: 64.96dB, 0.33%, and 27 MHz: 60.12dB, 0.54% [2].

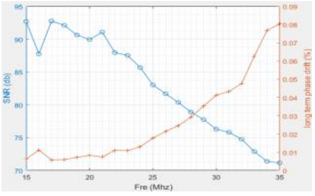

Fig. 3. Digital direct sampling system for measuring signal-to-noise ratio and drift

3 Conclusions

The method above demonstrates that within the MIT system, digital direct sampling of orthogonal sequences for phase detection achieves a higher detection signal-to-noise ratio and lower relative drift compared to superheterodyne phase detection.

References

[1] Q Chen, R Liu, C Wang, R Liu *Meas Sci Technol*, 32: 035402, 2021.
[2] T Zhang, W Zhang, X Liu, M Dai, Q Xuan, X Dong, R Liu, C Xu *IEEE T Instrum Meas*, 71: 4005713, 2022.

A 3D Brain EIT Imaging System Based on A Microcontroller with 20 Electrodes Configuration

Siyuan Bai[1], Lei Wang[1], and Xuetao Shi[2]

[1]The Institute of Medicine, Northwestern Polytechnical University, Xi’an, China
[2]The School of Biomedical Engineering, Fourth Military Medical University, Xi’an, China

Abstract: A simple 3D brain EIT data acquisition system with 20 channels is developed based on the STM32 microcontroller. This new hardware has very simple materials and control logic, and it takes very little time to set up (two hours is enough). The results of the tank experiment show that the system can accurately identify and locate the target.

1 Introduction

The human brain is a volumetric conductor with a three-dimensional structure, and the injected current flows in all directions simultaneously. However, 2D brain EIT lose the conduction information outside the measurement plane. To address the limitation of two-dimensional imaging in locating the depth of targets and expand the application scope of brain EIT, it is necessary to establish a 3D brain EIT imaging platform.

2 Methods

The core of the data acquisition system is the STM32F103C8T6 microcontroller powered by 3.3V. The IO ports are connected to a multiplexers to select the excitation and measurement channels. The AD module converts analog signals to digital voltage. The serial module receives data and sends it to the host computer. The system workflow is shown in Figure 1.

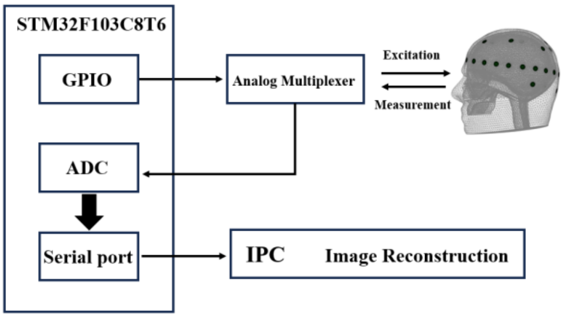

Figure 1: System working principle.

In COMSOL, a head-shaped tank model is designed with electrode layout referencing the EEG 10-5 system, placing a total of 20 copper electrodes with a diameter of 1cm, some of which are located at the occipital and central vertex regions to improve vertical resolution. Mainly driven by electrodes with large spacing at different heights to reduce scalp shunting effects, allowing more effective current to penetrate the skull and enter brain tissue [1]. Voltage is collected in a spiral manner from adjacent channels.

3D images are reconstructed using the GREIT algorithm [2]. The inverse model contains 23K elements.

3 Results

The operation of the entire system is shown in Figure 2. Saturated calcium sulfate solution (0.25 S/m, similar to brain tissue) serves as the background. Imaging of perturbation targets at 6 different positions (agar, 0.7 S/m, Simulated blood inclusion) is conducted, and the images are displayed as a 3D model containing the targets, as shown in Figure 3. The results indicate that the system can effectively identify and locate the targets.

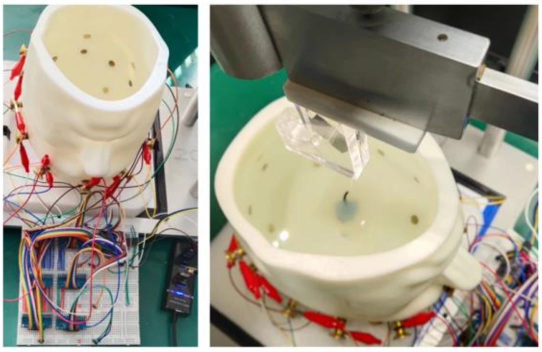

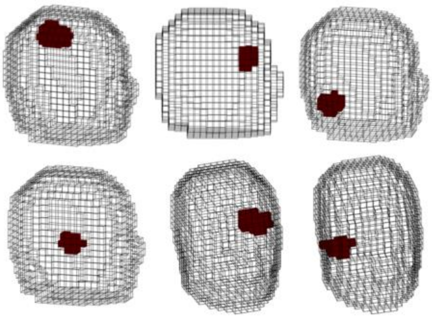

Figure 3: Imaging results (The targets are distributed at the top, front, back, center, left, and right).

4 Conclusions

The brain EIT signal acquisition system with 20 electrode configurations developed based on microcontroller successfully obtained useful data in Simulated head-shaped tank experiments, achieving 3D imaging of targets. The ongoing work involves constructing a deep learning model to further enhance imaging speed and resolution.

References

[1] T. Ouypornkochagorn, N. Terzija, P. Wright, J. L. Davidson, N. Polydorides, and H. McCann, "Scalp-Mounted Electrical Impedance Tomography of Cerebral Hemodynamics," IEEE Sens J, vol. 22, no. 5, pp. 4569-4580, Mar 1. 2022.

[2] Grychtol, Bartłomiej et al. “3D EIT image reconstruction with GREIT.” Physiological measurement vol.37, 6 (2016): 785-800. doi:10.1088/0967-3334/37/6/785.

A Preliminary Study on the Application of Electrical Impedance Tomography Based on Cerebral Perfusion Monitoring to Intracranial Pressure Changes

Yu Wang[1], Weichen Li[2], Weice Wang[3], Mingxu Zhu[3], Xiaoheng Yan[1*] and Xuetao Shi[3*]

[1]Liaoning Technical University, Huludao, China
[2]Northwest University, Xi'an, China
[3]Air Force Medical University, Xi'an, China, shixuetao@fmmu.edu.cn

Abstract: In intracranial pathologic conditions of intracranial pressure (ICP) disturbance or hemodynamic instability, maintaining appropriate ICP may reduce the risk of ischemic brain injury. As a non-invasive functional imaging technique, the sensitivity of electrical impedance tomography (EIT) to cerebral hemodynamic changes has been preliminarily confirmed. However, no team has conducted a feasibility study on the dynamic detection of ICP by EIT technology from the perspective of non-invasive whole-brain blood perfusion monitoring. In this study, human brain EIT image sequence was obtained by in vivo measurement, from which a variety of indicators that can reflect the tidal changes of the whole brain impedance were extracted, in order to establish a new method for non-invasive monitoring of ICP changes from the level of cerebral blood perfusion monitoring.

1 Introduction

Intracranial pressure (ICP) monitoring is an indispensable part of clinical care for many life-threatening brain injuries such as intracerebral hemorrhage, subarachnoid hemorrhage and malignant stroke [1]. Based on the previous research [2] on brain electrical impedance tomography (EIT) measurement technology and imaging algorithm of our team, in this study, we focused on the monitoring of cerebral blood perfusion status during Valsalva maneuver (VM) intervention [3]. In order to explore the rule of ICP status and acute changes of intracranial perfusion through perfusion monitoring index extracted by impedance blood flow signal and reconstructed image non-invasively.

2 Methods

2.1 Data collection

The jointly developed EIT system (EC-100 PRO) uses a disposable EIT electrode tape (EH-PET-16-CS, UTRON Technology Co., Ltd., Hangzhou, China) with 16 electrodes attached to the subject's head. At the same time, the medical elastic bandage was tightly wrapped around the electrode to temporarily block the influence of scalp blood flow while assisting in fixing the electrode. Data were collected from the resting period of the subjects (9 males and 3 females, age 27.50 ± 3.34), and photoplethysmography (PPG) signals of the subjects' fingers were recorded synchronously during the collection, which was used as a reference for heart activity during the experiment. The overall experimental process is shown in **Figure 1**.

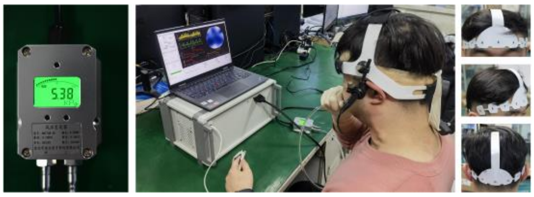

Figure 2: Experimental environment.

2.2 Data analysis

Pulse Delay Time (*PDT*) was calculated by equation (1)

$$PDT = M_{PPG} - M_{EIT} \tag{1}$$

M_{PPG} (M_{EIT}) is the moment when the changing rate of the ascending branch of PPG (EIT) signal is the largest in each perfusion cycle. The unit of *PDT* is ms. The mean value of *PDT* was calculated with ten perfusion cycles.

3 Conclusions

In the stable phase of baseline period (BP), intervention period (IP), and recover period (RP), it can be seen that the value of IP was greater than that of other period (**Figure 2**).

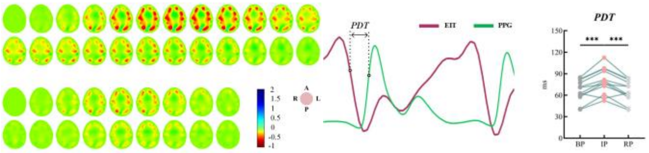

Figure 2: Result of statistical analysis of EIT cerebral blood perfusion monitoring index

This study used EIT to reflect the changes of cerebral blood perfusion under VM intervention, which provided a new idea for ICP monitoring. The result showed that EIT reconstructed images visually demonstrated the changes of intracranial blood perfusion status during the rise of ICP, and the perfusion monitoring indexes extracted from the reconstructed images could sensitively describe the differences of cerebral blood perfusion status under different ICP environments.

4 Acknowledgements

The authors thank all the subjects for their participation in this study.

References

[1] GWJ Hawryluk, *et al*. Intracranial pressure: current perspectives on physiology and monitoring. *Intensive Care Med*. 2022.
[2] B Yang, *et al*. Comparison of electrical impedance tomography and intracranial pressure during dehydration treatment of cerebral edema. *Neuroimage Clin*. 2019.
[3] Sami Nimer, Ghazal. Valsalva maneuver in echocardiography. *J Echocardiogr*, 2016.

Correlation between Electrical Impedance Tomography and Intracranial Pressure

Mingxu Zhu[1], Weichen Li[2], Yu Wang[3], Junyao Li[1], Weice Wang[1], Guobin Gao[3], Xuetao Shi[1]
[1] Department of Biomedical Engineering, Air Force Medical University, Xi’an, China, shixuetao@fmmu.edu.cn
[2]School of Life Sciences, Northwest University, Xi'an 710127, China
[3] Faculty of Electrical and Control Engineering, Liaoning Technical University, Huludao, China

Abstract: Intracranial pressure(ICP) monitoring is of great significance in guiding the diagnosis, treatment and efficacy evaluation of nervous system diseases. In this study, the feasibility of electrical impedance tomography (EIT)as a noninvasive ICP monitoring technique was evaluated by comparing the dynamic blood perfusion parameters extracted from EIT images with ICP.

1 Introduction

Increased ICP is an important cause of secondary brain injury, and ICP monitoring has become an important part of brain monitoring after traumatic brain injury[1]. At present, the invasive ICP monitoring commonly used in clinical practice has high accuracy, but it is prone to complications such as infection, hemorrhage, and neurological deficit[2]. Electrical impedance tomography (EIT) is a method that can present cross-sectional images of the electrical properties of the brain. Increased ICP affects blood volume changes in cerebral vessels[3], and changes in blood volume cause changes in impedance[4]. Therefore, EIT is expected to be used in ICP monitoring to improve the early identification of secondary brain injury and observe the effect of therapeutic intervention. In this study, we focused on the correlation between EIT and ICP to lay the foundation for the use of EIT in ICP monitoring.

2 Methods

In a study involving six domestic pigs under general anesthesia, we periodically injected arterial blood into their brains to to induce intracranial pressure changes.The procedure was as follows: 2 ml of blood was infused every 10 min for a total of five sessions Fig.1.EIT using EC-100 PRO (UTRON Technology Co., Ltd., Hangzhou, China) was monitored synchronously with ICP throughout the procedure. Invasive intracranial pressure monitoring was used to verify whether intracranial pressure had changed. The perfusion parameters were extracted from the global region of EIT images, and the correlation between the perfusion parameters after blood injection and ICP values was analysed. The perfusion parameters are shown in Fig2.

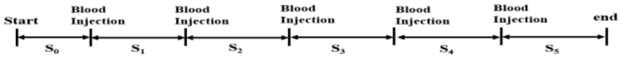

Figure 1: Timeline of experimental progress. S0: baseline period; Si(i=1,2,3,4,5): the i-th blood transfusion.

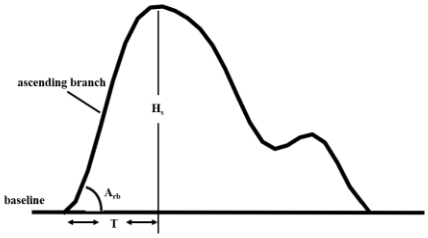

Figure 2: A perfusion cycle waveform map was obtained from the EIT image sequence. Hs: the amplitude of the ascending branch; Arb: angle between the ascending branch and the baseline; IV: the volume of blood circulating in an artery per unit of time ($^{H_s}/_{T}$); S: the area of the region enclosed by the perfusion waveform and baseline.

3 Results & Discussion

The perfusion parameters extracted from EIT images were significantly negatively correlated with intracranial pressure (Table 1, P<0.001).It can be seen from the results that the correlation varies greatly in each period. The main reason is that EIT reflects the ICP level by monitoring the changes of hemodynamics and blood flow physiological parameters of intracranial vessels. The correlation between perfusion parameters and ICP is low due to the cerebral autoregulation(CA) when the amount of bleeding is small. When the bleeding reaches a certain degree, the CA cannot regulate the stability of cerebral blood flow, and the correlation becomes stronger.

4 Conclusion

In this study, we constructed an animal model of intracranial hypertension to demonstrate the significant correlation between EIT and ICP. The results suggest that EIT may be a promising method for non-invasive ICP monitoring.

References

[1] Hawryluk, Gregory W J et al. Intensive care medicine vol. 48,10 (2022)
[2] Canac, Nicolas et al. Fluids and barriers of the CNS vol. 17,1 40. 23 Jun. 2020,
[3] Steiner LA et al. British Journal of Anaesthesia. 2006;97(1):26-38.
[4] Bodo M et al Physiological Measurement. 2015;36(10):N115-N126.

Table 1: Mean correlation between EIT parameters and ICP in different periods.

Parameter	**Period**				
	S_1	**S_2**	**S_3**	**S_4**	**S_5**
S	-0.12±0.34	-0.58±0.35	-0.80±0.10	-0.88±0.06	-0.92±0.01
H_s	-0.19±0.34	-0.65±0.24	-0.69±0.12	-0.88±0.04	-0.91±0.01
IV	-0.14±0.16	-0.58±0.17	-0.53±0.29	-0.81±0.13	-0.86±0.05
A_{rb}	0.16±0.40	-0.21±0.53	-0.56±0.43	-0.91±0.03	-0.85±0.01

Study of EIT Saline Contrasted Lung Perfusion Imaging and Ventilation/Perfusion Matching in Different Body Positions

Tixin Han[1], Yifan Liu[1] Meng Dai[1] and Feng Fu[1]

[1]Air Force Medical University, Xi’an, China fengfu@fmmu.edu.cn

Abstract: The study aimed to compare regional lung ventilation, lung perfusion and ventilation/perfusion (V/Q) matching in different body positions using electrical impedance tomography (EIT). The results found regional alternatives in the distributions of lung ventilation and lung perfusion, which reveals the sensitivity and instantaneity of EIT in lung functional imaging.

1 Introduction

Body position changes can alter pulmonary ventilation by affecting lung volume and diaphragm position, as well as the dilation and elasticity of pulmonary vessels, thereby altering the distribution of pulmonary artery and venous blood flow [1]. Different postures may cause a mismatch in the ventilation/perfusion (V/Q) ratio, affecting gas exchange and blood oxygen saturation. As a result, it is important to investigate the role of body position in understanding the physiological and pathological processes of pulmonary gas exchange.

EIT can effectively depict the physiological process of gas volume changes of breathing and blood passing through the pulmonary circulation. Saline contrasted EIT method evaluates pulmonary perfusion by measuring the degree of impedance decrease caused by saline indicator transferring through the pulmonary circulation, which reflects real-time changes in pulmonary blood perfusion [2]. Currently, most studies on changes in posture of EIT bedside monitoring focus on pulmonary ventilation, with few reports on changes in pulmonary perfusion and V/Q match. In view of this, our study observed healthy piglets under mechanical ventilation as experimental subjects and mainly focused on investigating the distribution and V/Q match changes of pulmonary perfusion using saline contrasted EIT in four different body positions: supine, prone, lateral right, and lateral left.

2 Methods

Ten pigs (35-45 kg) were anaesthetised and mechanically ventilated. Body position changes were made in a sequential order, 30 minutes each: Supine; Lateral Right (right lung positioned up); Prone; Lateral Left (left lung positioned up). At the end of each step (15 minutes), EIT measurement was acquired. Relative lung perfusion was assessed with EIT and central venous injection of 5% saline (10 ml) during breath holds. The EIT reconstruction was done in EIDORS using GREIT algorithm [3].

2.1 Data processing and image reconstruction

Ventilation images were created from a 1-minute recording of continuous mechanical ventilation. The time domain difference in impedance between the end of expiration and the end of inspiration was calculated and averaged.

The perfusion image was created by capturing the movement of a bolus through the lungs during a breath hold. Relative perfusion was calculated using the max slope of regional impedance-time curves.

The VQ match parameters was calculated by identifying three regions: regions that were only ventilated (R_V), regions that were only perfused (R_P) and regions both ventilated and perfused (R_{V+P}).

$$\begin{aligned} VQMatch\% &= R_{V+Q} / (R_V + R_Q + R_{V+Q}) \times 100\% \\ DeadSpace\% &= R_V / (R_V + R_Q + R_{V+Q}) \times 100\% \\ Shunt\% &= R_Q / (R_V + R_Q + R_{V+Q}) \times 100\% \end{aligned} \tag{1}$$

2.2 Imaging result of different body positions

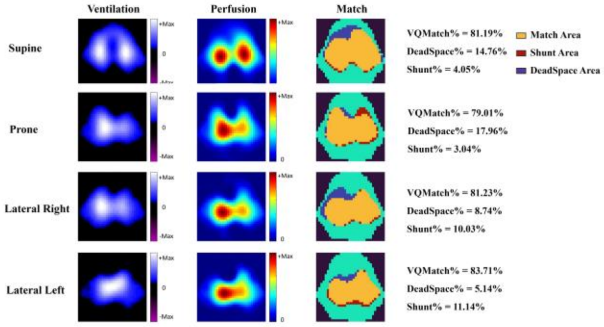

Figure 1: Imaging result of different body positions.

3 Conclusions

In this research, we evaluated the regional distribution of ventilation and blood flow of healthy piglets in four different body positions through EIT. The results showed that changes in measurement position can lead to changes in the lung's gravity-dependent zone, which in turn affects the distribution of regional lung ventilation and lung perfusion. EIT can sensitively image alterations in lung ventilation and lung perfusion caused by changes in body position.

4 Acknowledgements

The authors would like to express their gratitude to National Key Research and Development Program of China (grant number: 2022YFC2404800).

References

[1] Wieslander B, Ramos J G, Ax M *Journal of Cardiovascular Magnetic Resonance*, 21: 69, 2019.
[2] He H, Chi Y, Long Y *American Journal of Respiratory and Critical Care Medicine*, 202: 1464-1468, 2020.
[3] Adler A, Arnold J H, Bayford R *Physiol Meas*, 30: 35-55, 2009.
[4] Borges J B, Suarez-Sipmann F, Bohm S H *Journal of Applied Physiology*, 112: 225-236, 2012.

Multi-frame Multi-scale Data Fusion Strategy to Suppress EIT Image Artifacts

Jian'an Ye[1,2], Xiang Tian[1,2], Pu Wang[1,2], Tixin Han[1,2], Canhua Xu[1,2] and Feng Fu[1,2]

[1]Department of Biomedical Engineering, Fourth Military Medical University, Xi'an, China, jiananye00@163.com

Abstract: In order to reduce the effect of noise on EIT reconstructed images to improve the image quality, we propose a multiscale residual convolutional neural network (MS-1DResCNN) for post-processing of EIT data by exploiting the correlation between multi-frame conductivity data, and experimentally validate the algorithmic performance of this model under the condition of 30 dB noise interference.

1 Introduction

The effectiveness of electrical impedance tomography (EIT) for monitoring pathological changes in human brain tissue, lung function imaging, and other medical fields has been well documented [1]. Dynamic measurements of EIT voltage signals are susceptible to noise, vibration, and other disturbances. Due to the pathological and unsuitable nature of the reconstruction of the EIT inverse problem, these interferences can lead to a large number of artifacts in the reconstructed image, which reduces the quality of the reconstruction [2]. Researchers usually use some regularization methods to improve the stability and accuracy of the solution, these methods can reduce the impact of noise on the inverse problem solving to a certain extent, but due to its non-analogue and non-linear characteristics, how to effectively inhibit the impact of noise on the reconstruction of the EIT image to improve the stability of the algorithm is still a key issue in the current research, with the development of deep learning methods, which provides a new way of thinking and solutions for the further development of EIT.

2 Methods

In this study, we combine the EIT inverse problem with convolutional neural network [3] to propose a multi-scale convolutional neural network-based post-processing method that performs feature fusion and noise artifact suppression on multi-frame sequentially initialized conductivity data obtained by the traditional EIT reconstruction algorithm, so as to obtain a higher quality reconstructed image of the distribution of conductivity change of a disturbed target and improve the robustness of the traditional DLS algorithm.

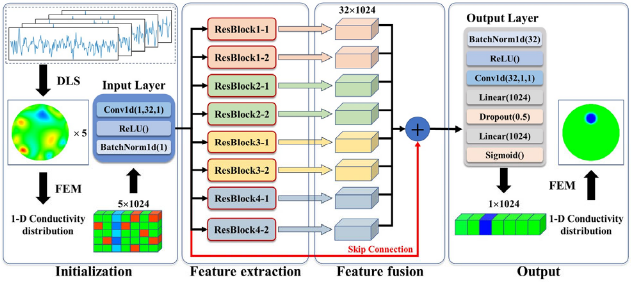

Figure 1: MS-1DResCNN network architecture

The DLS [4] algorithm is used to pre-establish five consecutive frames of conductivity distribution data, and then extract the feature information of multi-frame EIT conductivity distribution and the target position information related to the finite element veto partitions through the network, to distinguish the target and artifacts from the reconstructed image, and then remove the artifacts in the reconstructed image after the network processing, to restore the accurate target information.

2.1 Result

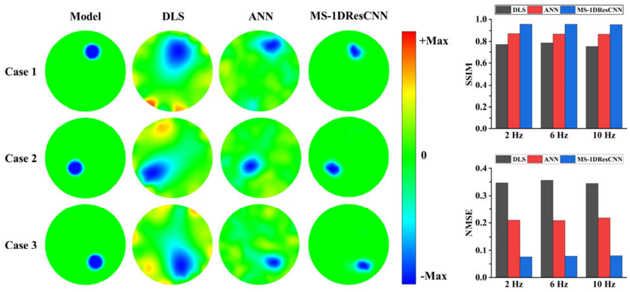

Figure 2: Reconstruction results and metrics calculations at 30 dB noise

We conducted experiments with different target locations under 30 dB noise, and the results, as shown in Fig. 2, show that there are no artifacts in the reconstructed images and the target locations are clear and unambiguous in the MS-1DResCNN method of this study. According to the structural similarity index (SSIM) is improved by 23.89% and 9.77%, respectively, and the normalized mean square error (NMSE) index value is reduced by 77.69% and 63.27%, respectively.

3 Conclusions

The deep learning model proposed in this paper is able to exploit the real-time nature of dynamic EIT to fuse the target feature information in multi-frame conductivity distribution data, reduce the interference artifacts in the images, and provide higher quality reconstructed images for EIT in subsequent real-time monitoring studies.

References

[1] Feng Fu, Bing Li, Meng Dai. et al., PLoS ONE, vol. 9, no. 12, p. e113202, 2014.

[2] Weirui Zhang, Tao Zhang, Xuechao Liu. et al., IEEE Access, vol. 9, pp. 141999–142011, 2021.

[3] Le Wu, Aiping Liu, Xu Zhang, et al, IEEE Trans. Instrum. Meas., vol. 71, pp. 1–10, 2022.

[4] Xuechao Liu, Tao Zhang, Jian'an Ye. *et al.*, *Sens.*, vol. 22, no. 24, p. 9934, Dec. 2022.

Research on the Relationship between Blood Dielectric Parameters and Blood Gas Indicators

Wang Weice[1], Li Weichen[2], Wang Yu[3], Zhu Mingxu[1], Jin Zhenxiao[5] and Shi Xuetao[1,2]
[1]Department of Biomedical Engineering, Air Force Medical University, Xi’an, China
[2]School of Life Sciences, Northwest University, Xi'an 710127, China
[3]Faculty of Electrical and Control Engineering, Liaoning Technical University, Huludao, China
[4]Xijing Hospital, Xi’an, China

Abstract: The blood dielectric parameters are significantly influenced by their composition. This paper systematically studied the correlation between the blood dielectric parameters and various blood gas indicators of patients undergoing extracorporeal circulation surgery, and used stepwise regression method to screen key indicators for predicting the dielectric parameters.

1 Introduction

Blood is a key tissue that spreads throughout the body, and its dielectric parameters are significantly influenced by various factors such as frequency and composition. The significant changes in blood dielectric parameters can have an impact on the monitoring of blood flow perfusion in important organs by EIT, leading to the inability to accurately monitor and warn of the occurrence of reperfusion and hypoperfusion, which affects the application of EIT in areas such as cerebral blood flow perfusion monitoring [1] and pulmonary perfusion abnormalities in respiratory diseases [2]. At the same time, when using chest impedance method to monitor the stroke output and cardiac output of patients with circulatory disorders, accurate values of blood resistivity are required [3]. Furthermore, studying the relationship between blood dielectric parameters and composition can provide a deeper understanding of the changes in physical properties caused by physiological and chemical changes in biological tissues, build a bridge between biochemical and physical properties, and provide researchers with more parameter indicators. Therefore, it is necessary to study the variation of blood dielectric parameters with their composition at various frequencies.

2 Methods

This study was approved by the Medical Ethics Committee of Xijing Hospital. Intraoperative blood was collected from patients undergoing extracorporeal circulation surgery, and 10Hz-100MHz dielectric parameter measurements and blood gas analysis were performed at 37 ℃. The real and imaginary parts of electrical resistivity were calculated [4]. Shapiro-Wilk normality tests were performed on the real and imaginary parts and various blood gas indicators at each frequency point. Based on this, Spearman correlation analysis was performed on the dielectric parameters and blood gas indicators. Screening for blood gas indicators that have a significant impact on blood dielectric parameters. At the same time, in order to use blood gas indicators to predict dielectric parameters, a stepwise regression method was used to establish an empirical formula between dielectric parameters and blood gas indicators, and a residual PP plot was drawn to prove that the regression residuals follow a normal distribution. A residual scatter plot was drawn to demonstrate the absence of heteroscedasticity. Finally, a prediction model was established.

3 Results

We analyzed the correlation between the real and imaginary parts of electrical resistivity and blood gas indicators. As shown in Figure 1, the thermal maps of the real part at 10, 100, 1k, 50k, 100k, 1M, 10M, and 100MHz can be obtained, and some blood gas indicators significantly correlated with dielectric parameters can be obtained.

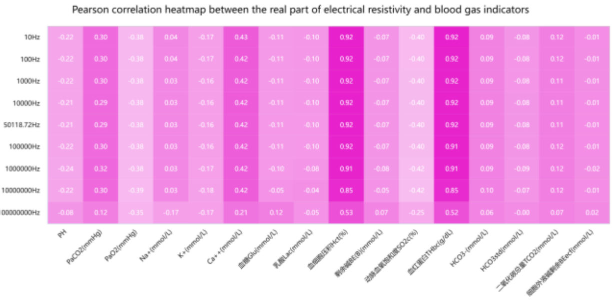

	PH	PaCO2(mmHg)	PaO2(mmHg)	Na+(mmol/L)	K+(mmol/L)	Ca++(mmol/L)	血糖Glu(mmol/L)	乳酸Lac(mmol/L)	血细胞压积Hct(%)	剩余碱BE(B)(mmol/L)	动脉血氧饱和度SO2c(%)	血红蛋白THbc(g/dL)	HCO3-(mmol/L)	HCO3std(mmol/L)	二氧化碳总量TCO2(mmol/L)	细胞外液碱剩余BEecf(mmol/L)
10Hz	-0.22	0.30	-0.38	0.04	-0.17	0.43	-0.11	-0.10	0.92	-0.07	-0.40	0.92	0.09	-0.08	0.12	-0.01
100Hz	-0.22	0.30	-0.38	0.04	-0.17	0.42	-0.11	-0.10	0.92	-0.07	-0.40	0.92	0.09	-0.08	0.12	-0.01
1000Hz	-0.22	0.30	-0.38	0.03	-0.16	0.42	-0.11	-0.10	0.92	-0.07	-0.40	0.92	0.09	-0.08	0.11	-0.01
10000Hz	-0.21	0.29	-0.38	0.03	-0.16	0.42	-0.11	-0.10	0.92	-0.07	-0.40	0.92	0.09	-0.08	0.11	-0.01
50118.72Hz	-0.21	0.29	-0.38	0.03	-0.16	0.42	-0.11	-0.10	0.92	-0.07	-0.40	0.92	0.09	-0.08	0.11	-0.01
100000Hz	-0.22	0.30	-0.38	0.03	-0.16	0.42	-0.11	-0.10	0.92	-0.07	-0.40	0.91	0.09	-0.08	0.12	-0.01
1000000Hz	-0.24	0.32	-0.38	0.03	-0.17	0.42	-0.10	-0.08	0.91	-0.08	-0.42	0.91	0.09	-0.09	0.12	-0.02
10000000Hz	-0.22	0.30	-0.39	0.03	-0.18	0.42	-0.05	-0.04	0.85	-0.05	-0.42	0.85	0.10	-0.07	0.12	-0.01
100000000Hz	-0.08	0.12	-0.35	-0.17	-0.17	0.21	0.12	-0.05	0.53	0.07	-0.25	0.52	0.06	-0.00	0.07	0.02

Figure 1: Pearson correlation heatmap between the real part of electrical resistivity and blood gas indicators.

At the same time, we conducted stepwise regression analysis on the real and imaginary parts of resistivity at various frequencies and established prediction models, such as the stepwise regression analysis model for the real part of resistivity at 50kHz: $\mathbf{Real_{(50kHz)}=126.281 + 0.573*X_{PaCO2}-0.905*Y_{Na}+ 3.016*Z_{Hct}}$, with a determination coefficient of 0.879.

4 Conclusions

The established model can accurately predict blood dielectric parameters by utilizing changes in blood gas indicators, and this study determined the degree of influence of each component on dielectric parameters.

References

[1] Li, Y, Zhang, D, Liu, B, et al. Noninvasive Cerebral Imaging and Monitoring Using Electrical Impedance Tomography During Total Aortic Arch Replacement. J CARDIOTHOR VASC AN. 2018; 32 (6): 2469-2476. doi: 10.1053/j.jvca.2018.05.002

[2] Frerichs, I, Dargaville, PA, Rimensberger, PC. Regional pulmonary effects of bronchoalveolar lavage procedure determined by electrical impedance tomography. Intensive Care Med Exp. 2019; 7 (1): 11. doi: 10.1186/s40635-019-0225-6

[3] Kubicek, W. G., Karnegis, J. N., Patterson, R. P., Witsoe, D. A., Mattson, R. H.: Development and evaluation of an impedance cardiac output system. Aerospace Med. 37, 1208 (1966).

[4] Wang W, Li W, Liu B, et al. Temperature dependence of dielectric properties of blood at 10 Hz‐100 MHz [J]. Frontiers in Physiology, 2022: 2300.

Feasibility Study of Cerebral Perfusion Monitoring during Total Aortic Arch Surgery using Cerebral Contrast-enhanced Electrical Impedance Tomography

Wenjing Zhu[1,2], Chen Yang[3], Yitong Guo[2], Jing Ma[2], Xiuming Chen[4], Zhenxiao Jin[3], and Xuetao Shi[2]

[1]Northwestern Polytechnical University, Xi'an, China, zhuwenjing@mail.nwpu.edu.cn
[2]Fourth Military Medical University, Xi'an, China
[3]Xijing Hospital, Xi'an, China
[4]Utron Tech Co., Ltd, Hangzhou, China

Abstract: It is crucial to monitor cerebral perfusion in order to reduce the incidence of postoperative brain damage after total aortic arch replacement (TAAR). In response to the characteristics of different periods in TAAR, we selected different contrast agents and extracted relevant parameters reflecting blood perfusion. The monitoring results of 29 patients showed that our established cerebral contrast-enhanced electrical impedance tomography perfusion method can monitor cerebral blood flow perfusion during TAAR with good signal intensity and image quality.

1 Introduction

About 30-50% patients [1] experience brain damage after total aortic arch replacement (TAAR). The high risk of cerebral malperfusion [2] during the surgery is a major factor contributing to postoperative brain damage. Monitoring the cerebral perfusion during surgery can reduce or minimize the probability of brain damage occurrence. The aim of this study was to develop a cerebral contrast-enhanced impedance tomography perfusion method for monitoring cerebral perfusion during TAAR.

2 Methods

29 patients who underwent TAAR at Xijing Hospital during 2023 were monitored intraoperatively using EC-100 PRO (UTRON Technology Co., Ltd., Hangzhou, China). In three stages, contrast agent was injected via the arterial port of the cardiopulmonary bypass in a bullet-like manner. For both cooling and rewarming platform period, a 20ml solution of 10%NaCl was used as the contrast agent; while for the hypothermic circulatory arrest (HCA) period, a 20ml solution of 3%NaCl was used. Before and after injecting the contrast agent, blood gas parameters were measured to control sodium ion levels within the normal range of 135-145mmol/L. To reflect the cerebral perfusion, we extracted three parameters related to contrast-enhanced imaging: time to peak (TP), peak amplitude (PAM), and peak area (PAR) (Figure 2).

2.1 Figures and tables

Figure 1 showed the monitoring process and the parameter extraction method. Figure 2 displayed impedance change and cerebral perfusion imaging after an injection of contrast agent in a patient during the cooling platform period.
Table 1 showed the impedance parameter performance after contrast injection in different periods.

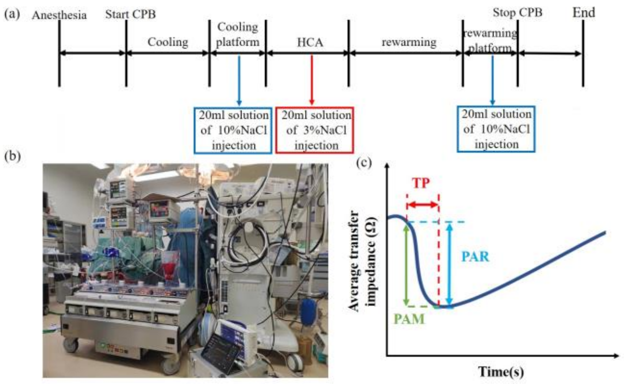

Figure 1: Perioperative monitoring and parameter extraction. (a) Procedure of surgery and timing of contrast agent injection. (b) Scene of intraoperative monitoring. (c) Extraction of parameters reflecting blood flow perfusion.

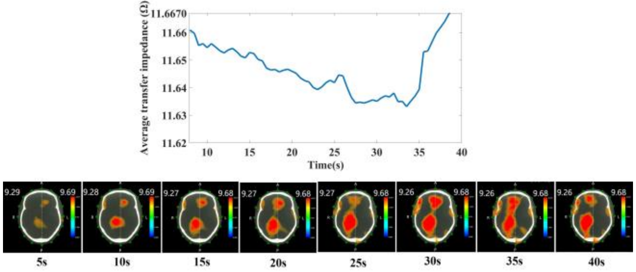

Figure 2: A contrast-enhanced imaging result of a patient in cooling platform period.

Table 1: Parameters related to contrast-enhanced imaging during three different stages of TAAR.

	cooling	HCA	rewarming
TP (s)	31±9	21±8	21±5
PAM (AU)	360±200	812±420	660±235
PAR (%)	0.23±0.02	0.5±0.3	0.27±0.01

3 Conclusions

In this clinical pilot study, we developed a cerebral contrast-enhanced impedance tomography perfusion method applicable to TAAR.

References

[1] Haldenwang P L, Wahlers T, Himmels A European journal of cardio-thoracic surgery, 42(5): e115-20, 2012.
[2] Shimamoto T, Komiya T General Thoracic & Cardiovascular Surgery, 62(7): 398-406, 2014.

Impedance Changes during Seizures Based on Dynamic Cerebral Blood Perfusion EIT: a Preliminary Study

Xiaoxiao Bai[1], Jiaming Xu[1], Jingrong Yang[1] and Lei Wang[1*]

[1]Institute of Medical Research, Northwestern Polytechnical University, Xi’an, China, bmewanglei@nwpu.edu.cn

Abstract: An attempt can be made to evaluate the state of seizures by impedance changes related to cerebral blood perfusion. In this study, seizures were induced by kainic acid in rats, and impedance data and PPG signal were collected simultaneously using dynamic cerebral blood perfusion EIT system and finger pulse oximeter. The impedance parameters were calculated to measure the impedance changes.

1 Introduction

During epileptic seizures, the abnormal discharge of neurons in the brain will lead to an increase in energy consumption and changes in regional cerebral blood flow (rCBF) [1-2]. This CBF response may be regarded as a symbol of seizures. Due to the high conductivity of blood [3], increased cerebral blood perfusion during seizures will cause impedance changes of brain issue, which shows that electrical impedance tomography (EIT) has the feasibility of detecting seizures. The purpose of this study was to determine whether EIT can detect and image the dynamic impedance changes caused by cerebral blood perfusion during seizures in real time.

2 Methods

The 16-electrode ring array was first fixed on the exposed skull surface of rats using 16 skull nails, and then the EIT system with the acquisition speed of 40 frames/s was connected and continuously monitored rats for 6-8h. At about 1h of monitoring, rats were administered by intraperitoneal injection with 4.2 mg/kg kainic acid (KA) at a constant speed. About 2h after administration, the rats had behaviors such as hunch-up in back, stiffness in body and tail, indicating the rats were in seizures. The finger pulse oximeter was simultaneously clipped on the hind limbs of rats to collect photoplethysmography (PPG) signals.

After data acquisition, the raw EIT data was filtered by a bandpass filter (3-7Hz) to remove the baseline drift and respiratory interference to obtain the independent impedance changes related to cerebral blood perfusion. Then, the EIT images were reconstructed and the average resistivity value (ARV) of the entire brain was calculated. To measure the impedance changes resulting from cerebral blood perfusion, the amplitude of impedance change (ΔZ), waveform area (S) and inflow velocity (IV) of ARV in each cardiac cycle were calculated. The data were presented as the mean ± SD.

3 Results and Conclusions

The experiment successfully monitored the dynamic impedance changes similar to the cardiac cycle in rats (Figure 1). The blood flow to the brain increases and cerebral impedance decreases during cardiac contraction and cardiac diastole is the opposite process [4]. This is consistent with our results.

According to the statistics of impedance parameters (Table 1), we found that compared with the normal state, the impedance changes were larger and faster when the rats were in seizure, which may be related to the increased energy consumption and cerebral blood flow regulation. In addition, there were also differences in impedance change between the early and later stage of seizures, which suggested that the progress and degree of cerebral neural activity may affect the cerebral blood perfusion.

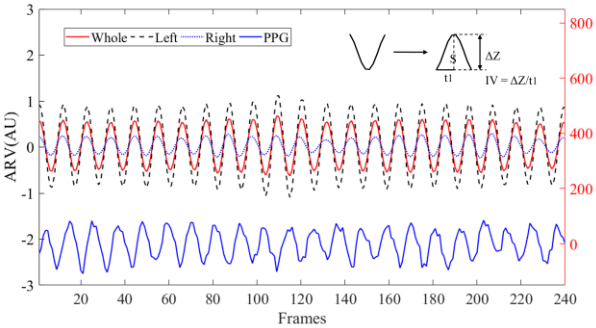

Figure 1: The impedance changes related to cerebral blood perfusion in different brain regions and PPG during seizures lasting 6s, and the schema of impedance parameters.

The results suggested that impedance changes caused by changes in CBF during seizures can be detected and imaged by dynamic cerebral blood perfusion EIT and this technique will can be a powerful tool for monitoring the seizures in the future.

4 Acknowledgements

The work was supported by the No. 51907162 and 2024SF-YBXM-451.

References

[1] J. Falco-Walter, *Seminars in Neurology*, 40(6): 617-623, 2020.
[2] K. Oommen and J. Kopel, *Proceedings (Baylor University. Medical Center)*, 35(4): 492-497, 2022.
[3] P. M. Bonovas *et al. Physiological measurement*, 22(1): 65-76, 2001.
[4] G. Anand, *et al. Physiological measurement*, 42(3), 2021.

Table 1: Statistics of impedance parameters of ARV in 3 rats in normal state, 30min and 2h after the onset of seizures.

	Normal			Seizure 30min			Seizure 2h		
	ΔZ	S	IV	ΔZ	S	IV	ΔZ	S	IV
No. 1	0.06±0.006	1.01±0.11	0.58±0.06	0.23±0.03	4.05±0.59	2.34±0.33	0.29±0.02	5.35±0.37	2.79±0.20
No. 2	0.23±0.01	4.24±0.25	2.34±0.14	0.47±0.03	8.51±0.59	4.57±0.33	0.86±0.17	15.99±3.20	7.60±1.46
No. 3	0.24±0.008	3.72±0.17	4.11±0.13	0.27±0.03	4.20±0.61	4.76±0.40	0.25±0.02	3.45±0.33	4.70±0.34

Flexible Electrical Impedance Tomography by Robots

Zhuoqi Cheng[1]

[1]Mærsk Mc Kinney Møller Instituttet, University of Southern Denmark, Odense, Denmark, zch@mmmi.sdu.dk

Abstract: This paper presents the use of robotics in assisting the data acquisition procedure for EIT. Instead of attaching electrodes on the object conventionally, the integrated robots can re-locate the electrodes to different locations during the measurement, which greatly improve the sensing flexibility. Preliminary simulations illustrate the system's feasibility in localizing different non-homogeneous regions and precisely reconstruct a focused region.

1 Introduction

Among the past decades, Electrical Impedance Tomography (EIT) technology has been widely implemented in many different areas including medical imaging, industrial process control, and geophysical subsurface exploration [1]. Conventionally, the EIT measurement setup either employs probes consisting of a set of electrodes in a fixed configuration [4], or it involves attaching a series of electrodes directly onto the object's surface [3]. A notable limitation of these approaches includes the long duration required for attaching electrodes to the object under test (OUT) or the complexities involved in probe manufacturing. In addition, the fixed electrodes configuration also constrains the imaging resolution, particularly when EIT is used for inspecting a relatively big area.

2 Methods

The Robot-Assisted Electrical Impedance Sensing (RAEIS) system has been developed by the Medical Robotics lab of the University of Southern Denmark recently [2]. The concept of RAEIS is to mobilize the electrodes which can be controlled by the robot to different locations on the OUT during the EIT measurement process. By this means, the proposed system is able to achieve higher sensing flexibility and adaptive resolution.

As shown in Fig. 1(A), the RAEIS system, designed for medical applications showcase, utilizes surgical forceps, which are commonly employed in electrosurgery, as electrodes. A tripolar sensing configuration is used: one forceps is used for current source injection and another is used for voltage measurement. Each forceps' movement is controlled by an individual robot. Through monitoring the change of impedance, the tissue contact can be detected and assured. Additionally, a ground electrode is required to be attached on the object both to complete the circuit and serve as a reference potential.

During the measurement procedure, a grid of positions are firstly defined in the region of interest (ROI), for instance, a 4×4 array. Then the data collection requires to move the current source electrode to each position of the grid for injecting excitation current, and to control the voltage measurement electrode to the other positions for electric potential measurement.

3 Results

Thanks to the involvement of robots, the data acquisition procedure can be conducted in different locations and in different scales. Fig. 1(B) illustrates two examples based on simulation. The setup is based on a 4×4 grid, and involves two non-homogeneous regions, one with lower conductivity (blue) and one with higher conductivity (red).

The reconstruction results are shown on the right of the corresponding simulation setup. When the sensing spans a larger area, the reconstruction image can identify both non-homogeneous regions, while their shapes are diffused. Conversely, focusing the sensing on a smaller area significantly improves the accuracy of the reconstructed shape, but the left upper object is missing. Additionally, the system was tested on phantom made of pig liver and muscle (Fig. 1(C)). The reconstruction results Fig. 1(D) can indicate the non-homogeneous correctly.

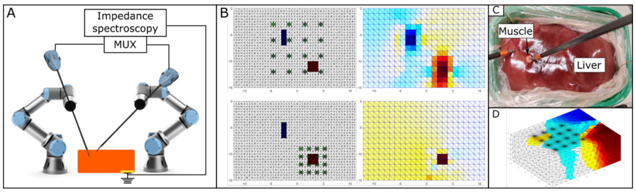

Figure 1: (A) The RAEIS system using two robots to control two electrodes to different positions on the OUT for injecting current excitation and measuring electric voltage during EIT data acquisition; (B) Two simulation examples showcasing the results in different grid settings.

4 Conclusions

This abstract provides a brief overview of the developing RAEIS technology in EIT application. The involvement of robotics enhances the flexibility of data acquisition in EIT, enabling assessments across various locations and scales. The preliminary results based on simulation indicate the system feasibility and its potential in an adaptive EIT sensing strategy. In the conference, more technical details and quantitative results will be provided.

References

[1] Bera T K 2018 *in* 'IOP Conference Series: Materials Science and Engineering' Vol. 331 IOP Publishing p. 012004.

[2] Cheng Z, Dall'Alba D, Fiorini P and Savarimuthu T R 2021 *in* '2021 20th International Conference on Advanced Robotics (ICAR)' IEEE pp. 234–240.

[3] Hou T C and Lynch J P 2009 *Journal of intelligent material systems and structures* **20**(11), 1363–1379.

[4] Murphy E K, Mahara A and Halter R J 2016 *IEEE Transactions on Medical Imaging* **35**(7), 1593–1603.

Impact of arm position on chest electrical impedance tomography

Antoine Dupré[1], Alexandre Broc[1]

[1]Sentec AG, Landquart, Switzerland, antoine.dupre@sentec.com

Abstract: Although the effects of posture have extensively been studied in chest Electrical Impedance Tomography (EIT) little is known about the effects of arm position except in the sitting posture. We present the study protocol and the first results of a clinical investigation studying the effects of arm position in sitting and supine postures. The primary goal is to assess if guidance concerning clothing that would reduce electrical contact between arms and thorax is needed.

1 Introduction

Literature has shown arm position can have significant impact on some EIT parameters, in particular the End-Expiratory Lung Impedance (EELI) [1]. We have set up an experimental study on healthy volunteers (n=3) to replicate the findings in sitting position (typical in Pulmonary Function Testing) and explore the effect in supine position (typical in ICU setting). The study protocol has been adjusted to investigate if the observed impact in [1] is caused mainly by the electrical contact between the chest and the arm or by the motion of the arm itself that would cause physiological changes in ventilation distribution in the thorax.

2 Methods

The volunteers do not wear clothing covering chest: this ensures that electrical currents can flow from the chest to the arm in the absence of an electrically insulating sheet. The volunteers are asked in each position (sitting and supine) to take 5 consecutive stable breaths in the following scenario (shown in Figure 1):

A) Arm along chest, insulating “barrier”
B) Arm along chest, insulating sheet removed
C) Arm at 45° from chest
D) Arm at 90° from chest

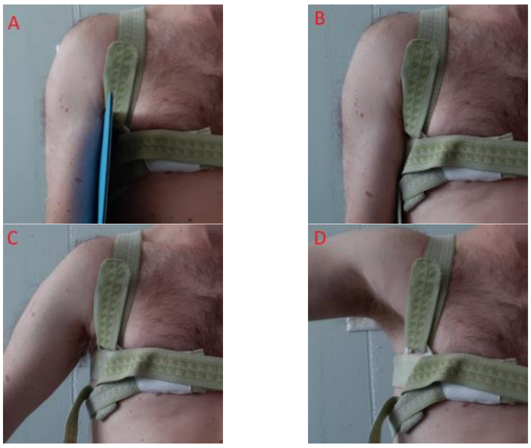

Figure 1: Experimental protocol: A) insulating sheet between arm and chest B) arm electrically contacting chest C) arm lifted at 45° D) arm lifted at 90°.

Figure 1 is shown to volunteers prior to experiment as guidance. At each step, after the five consecutive breaths, the volunteer marks a short breath hold for breath selection in data analysis. An assistant removes the insulating sheet between A) and B) so the volunteer can remain still.

For each breath selected, we compute the EELI and EILI images. Then, using left ROI and right ROI corresponding to Sentec quadrants corresponding to the model used for image reconstruction, we compute the regional EELI/EILI by summing over all pixels in either the left or right ROI of the chest: $EELI_{left}$and $EELI_{right}$.

From the 5 breaths in each sequence, we compute the mean and standard deviation. Finally, we express all lung impedance values relative to the EELI in reference scenario A. The results are shown in Figure 2.

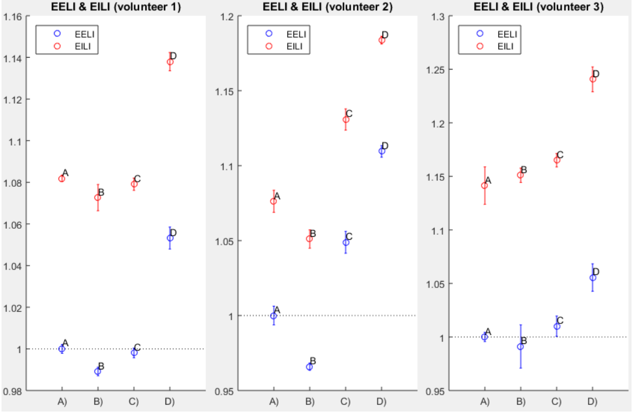

Figure 2: Regional EELI/EILI (ROI corresponding to arm lifted), normalised to EELI value in scenario A.

3 Conclusions

The regional increase of EELI in the region corresponding to elevated arm observed in [1] was confirmed. We found that the electrical contact between arm and chest reduce the EELI, in a small magnitude. The changes in EELI observed even in the case of 90° arm elevation were found smaller than the average breath Tidal Variation (EILI-EELI)

4 Acknowledgements

The authors would like to express their gratitude to the colleagues that agreed to volunteer, and Inez Frerichs for valuable suggestions for study design.

References

[1] B Vogt, L Mendes et al., *PhysiolMeas*, 37 :904, 2016

EIT monitoring of breathing dolphins

Andy Adler[1], Andreas Fahlman[2], Martina Mosing[3]
[1]Systems and Computer Engineering, Carleton University, Ottawa, Canada, adler@sce.carleton.ca
[2]Fundación Oceanogràfic de Valencia, Spain
[3]Anaesthesiology and Perioperative Intensive-Care Medicine, Vetmeduni, Vienna, Austria

Abstract: We show first EIT images of breathing in dolphins. Several technical solutions are described to permit EIT imaging in water. Early results show interesting changes in air distribution with breathing.

1 Introduction

Diving mammals seek to maximize time underwater but must eventually surface to exchange metabolic gasses. We want to understand the respiratory and cardiovascular adaptations to diving in marine mammals, and then compare to human breath-hold divers, and how factors affect diving capacity [2]. Here we report on the feasibility of EIT studies of lung function and mechanics in diving dolphins.

2 Methods and Results

EIT data were collected with the Sentec pioneer set, using a custom neoprene belt with conductive polymers electrodes. Tests of the first prototype belt showed the conductivity of the water to be an issue, since electricity will preferentially flow through the water ($\sigma_{\text{seawater}} \approx 5\,\text{S/m}$), rather than the body ($\sigma = 0.1$–$0.7\,\text{S/m}$) [1]. This issue was solved with the design of a belt/vest system which covers and insulates the electrodes from the water.

Using our EIT belt, EIT data were collected from dolphins in several orientations. Our goal was to evaluate the feasibility of our test configuration and the equipment developed.

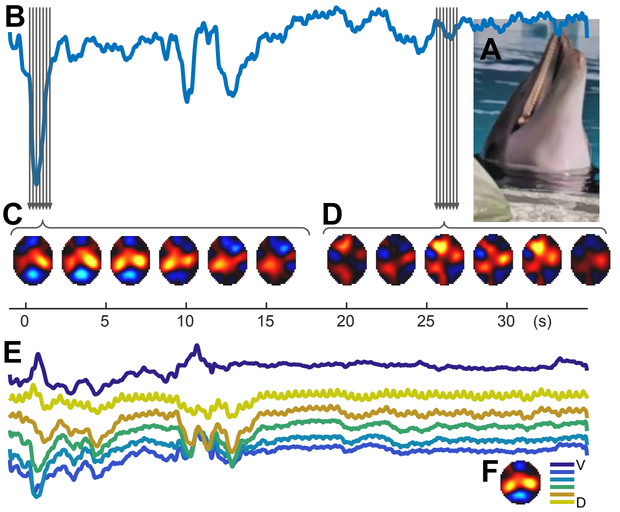

Figure 1: Sample EIT images and waveforms from (A) dolphin oriented vertically in the water. (B) Global EIT signal for a 30 s data window. C & D: EIT images during breath (C) and apnea (D). Conductivity changes (+=red, −=blue). (E) EIT waveforms for ROIs (Ventral to Dorsal) indicated in (F)

Data from a dolphin holding its position vertically in a pool is shown in Fig 1. In the bottom panel, regions of interest are shown. Detailed images are shown for two 1.5 s intervals in the data. The first shows a breath (expiration then inspiration in the dolphin) and the second shows a heart beat and the EIT-associated pulsatility.

After the breath, the dolphin maintains the vertical posture without breathing, and sequential segments of these data are shown as images. In this configuration, the dolphin is making muscular efforts to maintain itself in position in the water, and a 140 cycles/minute signal is shown in the dorsal region of the image, which may be musclular activity to move the tail.

In Fig 2, we show a detail of a breath in a dolphin positioned horizontally: waveforms at regions of interest show the different time courses. In the six central ROIs, there is a progressive expiratory delay. Expiration starts in the ventral lung and moves dorsally. Interestingly, inspiration shows little delay. This effect is similar to expiratory flow limitation in humans, especially at high flows and in lung disease (asthma). The lateral regions of the image show an increase in air content. This could be due to a pendelluft-type effect, or due to abdominal gas pushed into the image plane by the diaphragm.

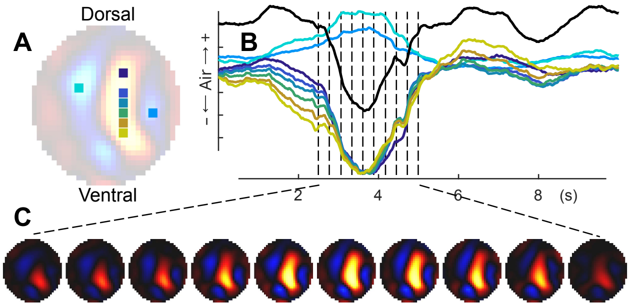

Figure 2: Sample EIT images and waveforms from a dolphin oriented horizontally, (A) color-coded points corresponding to waveforms. (B) EIT signals vs time (s) during a breath and the global signal (black). Waveforms are normalized to the same maximum value. (C) EIT images corresponding to vertical lines in (B). Note the phases during expiration, where dorsal regions respond 0.5–1.0s later than ventral regions. Much less phase difference occurs during inspiration. The red indicates decreased air in the central region, with some blue (air) lateral spaces.

3 Discussion

Results demonstrate the feasibility of EIT-based monitoring in dolphins. In the very short and forceful breathing of dolphins, there is considerable heterogeneity between lung regions. In addition to our results, several challenges have been identified. One is that the movement of dolphins does interfere with the data quality. It will therefore be important to develop protocols in which we can identify and segment data corresponding to quiet activity in the animals. (Acknowedgement: ONR Award #: N000142312002)

References

[1] “Feasibility of Thoracic Impedance Measurements in Seawater”, A Adler *et al* p.68, Conf EIT 2021

[2] A Fahlman *et al*, “Cardiorespiratory coupling in cetaceans; a physiological strategy to improve gas exchange?”, J Exp Biol 223:jeb226365, 2020

Effect of Individualized Positive End-expiratory Pressure Titrated by EIT on Ventilation-perfusion Distribution in Patients with Acute Respiratory Distress Syndrome

Xueyan Yuan[1], Haibo Qiu[1] and Ling Liu[1]

[1] Jiangsu Provincial Key Laboratory of Critical Care Medicine and Department of Critical Care Medicine, Zhongda Hospital, School of Medicine, Southeast University, Nanjing, 210009, Jiangsu, China, 18826401594@163.com

Abstract: This study aimed to describe the effects of individual PEEP titrated by EIT on regional ventilation and perfusion distribution in patients with acute respiratory distress syndrome (ARDS). The results suggested that individual PEEP titrated by EIT improves V/Q matching by reducing shunt without altering dead space in patients with moderate to severe ARDS.

1 Introduction

Electrical impedance tomography (EIT) has recently been introduced as a simple bedside tool to guide individual positive end-expiratory pressure (PEEP) selection by minimizing alveolar overdistension and collapse [1, 2]. However, the effects of PEEP titrated by EIT on ventilation/perfusion (V/Q) distribution remain unclear. Therefore, this study aimed to describe the effects of individual PEEP titrated by EIT on regional ventilation and perfusion distribution in patients with acute respiratory distress syndrome (ARDS).

2 Methods

This is a prospective, cross-over randomized study in a single medical ICU. Sixty-nine patients with moderate to severe ARDS undergoing mechanical ventilation. After a PEEP titration using EIT during a decremental PEEP trial, patients were then randomized to three different PEEP strategies which were set according to (1) crossing points method using EIT (PEEP_{EIT}), (2) low PEEP-FIO_2 table (PEEP_{low}), or (3) high PEEP-FIO_2 table ($\text{PEEP}_{\text{high}}$) [3]. Each PEEP level was maintained for 15 minutes, and subsequently, gas exchange, lung mechanics, and EIT data were collected. Pulmonary ventilation and perfusion were measured using the saline method. Patients were defined as high recruiters (Recruitment-to-Inflation ratio [R/I] > 0.5) or low recruiters (R/I < 0.5).

3 Results

Among the included patients, the cause of ARDS was pulmonary ARDS (44.9%). PEEP_{EIT} was higher compared with PEEPlow, but lower compared with $\text{PEEP}_{\text{high}}$ (11.6 ± 2.6 cm H_2O vs. 8.7 ± 1.9 cm H_2O and 15.8 ± 2.0 cm H_2O, respectively; $P < 0.001$ each). V/Q matching was higher with PEEP_{EIT} compared to PEEP_{low} (76.4 ± 8.7 % vs. 70.9 ± 12.4 %, $P = 0.007$), whereas there was no difference between PEEP_{EIT} and $\text{PEEP}_{\text{high}}$. PEEP_{EIT} and $\text{PEEP}_{\text{high}}$ reduced total shunt compared to PEEP_{low} (10.7 [6.5, 18.3] % and 11.0 [6.6, 16.4] % vs. 15.5 [10.2, 20.2] %, $P = 0.012$ and $P = 0.031$, respectively). Dead space at global and ventral regions did not differ among different PEEP strategies. For high recruiters, V/Q matching was higher using PEEP_{EIT} compared to PEEP_{low} and $\text{PEEP}_{\text{high}}$. For low recruiters, there was no difference in the V/Q matching among three PEEP strategies.

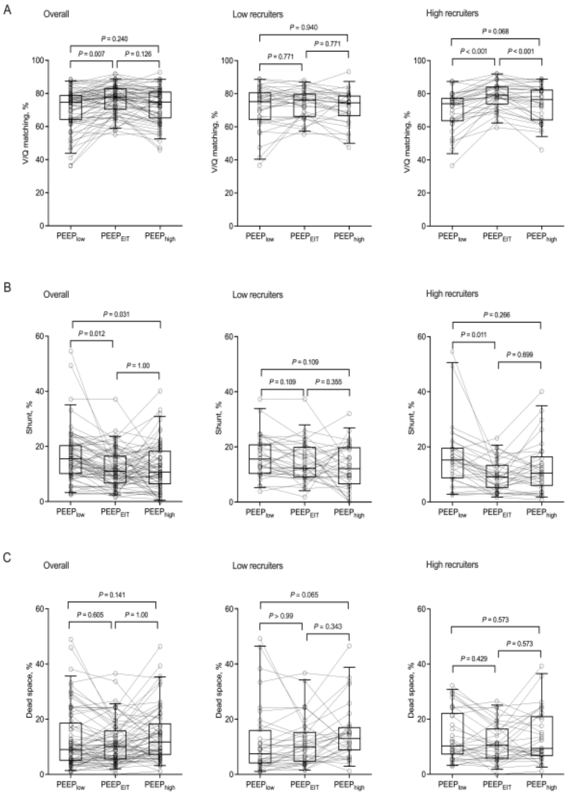

Figure 1: Effect of three different strategies on ventilation and perfusion distribution

4 Conclusion

Individual PEEP titrated by EIT improves V/Q matching by reducing shunt without altering dead space in patients with moderate to severe ARDS.

5 Acknowledgements

The authors would like to express their gratitude to the National Natural Science Foundation of China (81950058, 82270083).

References

[1] Jonkman AH, Alcala GC, Pavlovsky B *Am J Respir Crit Care Med*, 208(1): 25-38, 2023.

[2] Jimenez JV, Munroe E, Weirauch AJ *Crit Care*, 27(1): 21, 2023.

[3] Brower RG, Matthay MA, Morris A *N Engl J Med* 351: 327-336, 2004.

Imaging of Brain Tumor Tissues by Principal Component Analysis-based Electrical Impedance Tomography

Ruimin Zhou[1], Daisuke Kawashima [1], Songshi Li[1], Iori Kojima[2], and Masahiro Takei[1]

[1] Chiba University, Chiba, Japan, dkawa@chiba-u.jp
[2] Chiba University Hospital, Chiba, Japan

Abstract: This study presents a novel method combining electrical impedance tomography (EIT) with principal component analysis (PCA) for brain tumor diagnosis. Optimizing characteristic frequency through PCA significantly improves the differentiation and imaging of normal and abnormal brain tissues, demonstrating superior performance over traditional EIT methods in identifying brain tumors.

1 Introduction

Brain tumors pose a significant challenge in medical diagnostics, necessitating innovative techniques for accurate identification and characterization [1]. Traditional pathological diagnosis methods are complex and heavily reliant on the expertise of physicians, often leading to variability in diagnoses. Electrical impedance tomography (EIT) imaging has been introduced as a solution to the challenges. EIT simplifies the diagnostic process by providing real-time, non-invasive imaging that requires less interpretative expertise, thus reducing dependency on individual physician experience. This study proposes a novel approach by integrating principal component analysis [3] with EIT, termed PCA-EIT, aimed at enhancing the diagnostic accuracy for brain tumors through the optimized selection of characteristic impedance frequencies and improved imaging of tissue electrical properties.

2 Methods

A novel pathological approach is proposed for diagnosing brain tumors by combining electrical impedance tomography (EIT) and principal component analysis (PCA). Firstly, the electrical impedance spectrometer collects impedance data of cell suspensions (U87 and U138) from the brain tumor. Secondly, the impedance spectrums of cells are extracted from the impedance data of cell suspensions based on an equivalent circuit model [4], from which the influence of impedance from extracellular solution and electrodes is minimized. Thirdly, PCA is used to extract the optimum characteristic frequency for the identification of cells. Finally, the EIT imaging is implemented on the ex-vivo brain tumor tissues based on characteristic frequency extracted by PCA.

3 Experiment

Measurements were performed on four cancer cell suspensions to obtain impedance spectroscopy data. **Figure 1** demonstrates the impedance spectrum data acquisition system, which consists of an impedance analyzer and a test head (Model IM7581: Hioki E.E Corporation, Japan), a coaxial sensor (RPSMAJ-SMAP: To Conne Corporation, Japan), a PC. The experimental conditions were set as follows: the concentration of the cells was 1×10^6 cells/ml. The measurements were carried out in a frequency range from 0.1 to 5 MHz. An injection current of 0.01mA was employed. In addition, the measurements were repeated ten times for each cell sample.

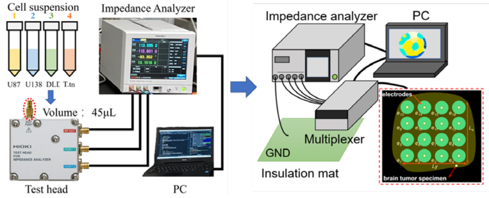

(a) EIS (b) EIT

Figure 1: Experiment setup

4 Results

The experiment results show that among all parameters of magnitude, phase angle, real part, and imaginary part of impedance, the phase angle has the optimum discrimination capability in the characteristic frequency range from 1.2MHz to 2.5MHz. By imaging the distribution of electrical properties of normal and abnormal tissues with the characteristic frequency, the abnormal tissue is able to be diagnosed effectively from the abnormal one.

5 Conclusions

A combination of electrical impedance tomography and principal component analysis (PCA-EIT) has been proposed for the diagnosis of brain tumors. The key findings of this research are:

1). The phase angle component most accurately represents the characteristics of cellular impedance.

2). The PCA-EIT method has a better capability in imaging the distribution of the electrical properties of abnormal tissues, which demonstrates a promising application in the pathological diagnosis of brain tumors.

6 Acknowledgements

This work was supported by JSPS KAKENHI Grant Number JP23H00544.

References

[1] Srinivasan, S., Francis, D., Mathivanan, S. K., Rajadurai, H., Shivahare, B. D., & Shah, M. A. *BMC Medical Imaging*, 24(1): 21, 2024.

[2] M Wang, Y Ma, N Holliday, et al. *IEEE Sensors Journal*, 5(2): 289-299, 2005.

[3] Mishra S P, Sarkar U, Taraphder S, et al. *International Journal of Livestock Research*, 7(5): 60-78, 2017.

[4] X Zhang, W Zhang, G Lei. *Transactions on Electrical and Electronic Materials*, 17(6): 311-316, 2016.

Closed-Loop Tumor Treatment Fields for Lung Tumor Therapy: A Simulation Study

Minmin Wang[1], Maomao Zhang[2]

[1]School of Biomedical Engineering and Instrument Science, Zhejiang University, Hangzhou, China, minminwang@zju.edu.cn
[2]Tsinghua Shenzhen International Graduate School, Tsinghua University, Shenzhen, China

Abstract: Tumor Treatment Fields (TTFields) is a non-invasive anticancer modality that utilizes alternating electric fields to disrupt cancer cell division and growth. Traditional TTFields therapy for lung tumors faces challenges due to the influence of respiratory motion. Therefore, we design a novel closed-loop TTFields strategy for lung tumors to mitigate the impact of respiratory motion. Real-time respiratory phase monitoring and dynamic parameter optimization are incorporated into the treatment regimen. Furthermore, we conduct theoretical analysis to evaluate the performance of the proposed method using the lung motion model. Compared to conventional TTFields settings, employing our proposed closed-loop TTFields strategy with the same dose setting (The total dose was the same as traditional setting, 2400 mA) allowed us to achieve a more extensive distribution of the treatment field (1.30 V/cm), maintaining consistency within the tumor across diverse respiratory phases.

1 Introduction

Tumor Treatment Fields (TTFields), as a non-invasive approach that uses low-intensity (1-3 V/cm) and intermediate -frequency (100-300 kHz) alternating electric fields, harnesses the power of electric fields to disrupt the division of cancer cells, impeding their growth and progression [1]. In the management of TTFields for lung cancer, the respiratory cycle introduces dynamic changes in the shape and electrical properties of lung tissue [1]. These fluctuations impact the therapeutic electric field within the tumor, potentially diminishing treatment efficacy and resulting in sub-optimal outcomes. Therefore, we introduce a novel TTFields strategy ensures dependable and efficient treatment field delivery by incorporating real-time respiratory phase monitoring and dynamic adjustment parameters of TTFields, effectively addressing the challenges posed by respiratory motion.

2 Methods

As illustrated in Figure 1, a fundamental component of our proposed closed-loop TTFields method is the incorporation of real-time respiratory phase monitoring and dynamic parameter optimization into the ongoing treatment regimen. For respiratory phase monitoring, we utilized EIT to real-time measure regional lung ventilation distribution by calculating the conductivity changes in the corresponding regions. As patients undergo TTFields, real-time EIT data continually updates the current respiratory phase. Subsequently, the dynamic optimization algorithm of TTFields utilizes this information to adjust and refine parameters in response to morphological changes in the lung.

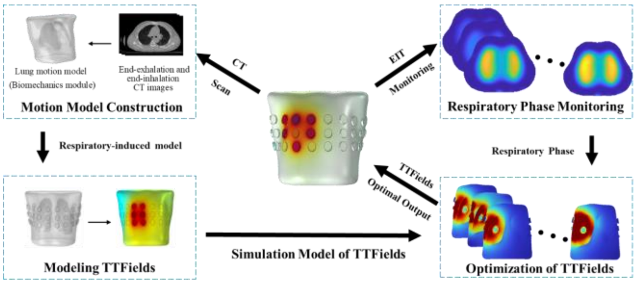

Figure 1: Illustration of adaptive closed-loop TTFields.

3 Results and Conclusions

As shown in Figure 2, we observed that within the traditional setting of TTFields, variations in the electrical conductivity of lung during different respiratory phases led to a decrease in the average electric field intensity within lung tumors, transitioning from end-expiratory (1.08 V/cm) to end-inspiratory (0.87 V/cm) phases. However, employing our proposed dynamic optimization approach with the Same dose setting (The total dose was the same as Traditional setting, 2400 mA) allowed us to achieve a more extensive distribution of the treatment field (1.30 V/cm), maintaining consistency within the tumor across diverse respiratory phases. Furthermore, when we maintained an average treatment field intensity of 1 V/cm at the tumor shell with dynamic TTFields optimization (Different dose setting), we were able to achieve a 23.10% reduction (1338 mA) in the required total output dose compared to the Traditional setting.

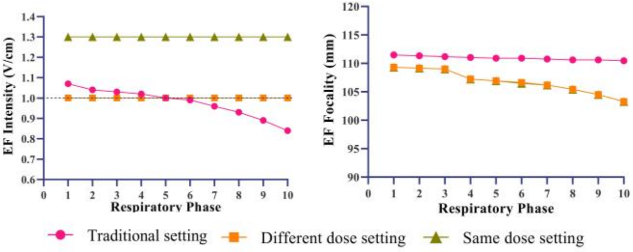

Figure 2: Distribution of mean electric field intensity and focality generated within tumor shell by different TTFields settings.

Our proposed closed-loop TTFields method has the potential to significantly advance lung tumor therapy by mitigating the impact of respiratory motion.

References

[1] Karanam, N. K., Story, M. D. *International Journal of Radiation Biology*, 97: 1044-1054, 2021.
[2] Korshoej, A.R., Sørensen, J.C.H., von Oettingen, G., Poulsen, F.R., Thielscher, A. *Physics in Medicine & Biology*, 64: 04NT03, 2019.
[3] Zhou, T., Liu, S., Lu, H., Bai, J., Zhi, L., Shi, Q. *Computer Methods and Programs in Biomedicine*, 232: 107445, 2023.

Challenges and Benefits of Integrating EIT and MRI: Liver Fat Spectral Modelling in Preclinical Swine Models

Ishfaque Ahmed[1], Greg Simchick[3], Erin Kaiser[2], Sydney Sneed[2], Franklin West[2], and Qun Zhao[1,2,*]

[1]Bioimaging Research Center, [2]Regenerative Bioscience Center, University of Georgia, Athens, GA., USA
[3]Department of Radiology and Medical Physics, University of Wisconsin-Madison, USA

Abstract: Accurate quantification of liver fatty acid composition provides critical information in diagnosis and treatment of many liver diseases. Chemical-shift encoded MRI allows for quantification of fatty acid composition, including proton-density fat fraction (PDFF), number of double bonds per molecule (NDB), and chain length (CL), etc. Meanwhile, electrical impedance tomography (EIT) provides critical information of liver conductivity. However, it remains a challenge to integrate low-resolution EIT images and high-resolution of MRI images. As a translational large animal model, pigs have been increasingly used in recent years to study neurological disorders, liver, and heart diseases due to significant similarities between pigs and humans in brain, liver, and heart anatomy and physiology. In this talk, we will present challenges and benefits of integration of the two modalities of imaging, EIT and MRI, in liver fat spectral modelling using translational pig models. Potential correlation of EIT conductivity with MRI PDFF, NDB, and CL will also be discussed.

1 Methods

Chemical-shift encoded magnetic resonance imaging (CSE-MRI) water-fat separation has recently emerged as a useful method for the quantification of triglyceride composition in fatty tissues. Meanwhile, EIT provides a cost-effective and portable method for early and operator-independent detection of fatty liver disease.

Tremendous interest has recently grown in using swine as a translational large animal model to study early development, neurological disorders, and liver diseases due to the significant similarities between pigs and humans in liver/brain anatomy and physiology.

1.1 In vitro experiment

For phantom experiments, three small 5-ml vials (one filled with each oil or butter sample) were placed into a larger cylindrical tube (28 mm in diameter, 114 mm in length) filled with water. Experiments were also performed to scan brown adipose tissue and inguinal white adipose tissue of two two-month old C57/BL6 mice [1] (Fig. 1).

1.2 In vivo experiment.

MRI images were acquired from swine livers (10-week-old) using IDEAL IQ sequences on a 3T MRI scanner. Quantitative measurements of Proton density fat fraction and R2* (iron concentration) measurements were conducted to quantify their spatial distributions (Fig. 2).

1.3 Integration of EIT/MRI: challenges and benefits

Integration of low-resolution EIT images and high-resolution MRI images would enable clinical applications of EIT in diagnosis and treatment of liver diseases. However, there exist many challenges, such as how to fuse the two modalities and achieve optimal information [2]. Feasible solutions include using deep learning (convolutional neural network) or a cascaded cycle generative adversarial network model. Pearson's correlation analyses comparing EIT conductivity and MRI PDFF, NDB, and CL with other measurements (body mass index, torso circumference, etc.) also offer critical information for diagnosis/treatment of many liver diseases.

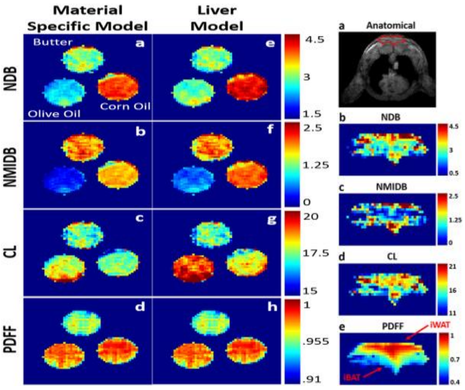

Figure 1: (Left) Representative ndb (first row), nmidb (second row), cl (third row), and PDFF (fourth row) maps obtained using material specific spectroscopy models and the 9-peak liver model; Second column (e–h) for olive oil (bottom left vial), corn oil (bottom right vial), and butter (top vial); (Right) Anatomical image(a) and ndb (b), nmidb (c), cl (d), and PDFF (e) maps displaying intercapsular region.

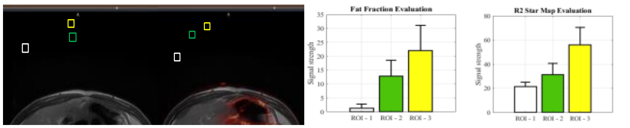

Figure 2. Proton density fat fraction and iron concentration measurements from swine livers (10-wwek old).

2 Conclusions

This paper investigates quantification of liver fatty acid in a large translational swine model and explores benefits and challenges of integrating MRI and EIT for clinical diagnosis and treatment of liver diseases.

2. References

[1] Simchick G, Yin A, Yin H, Zhao Q. Fat spectral modelling on triglyceride composition quantification using chemical shift encoded magnetic resonance imaging. Magn Reson Imaging. 2018 Oct; 52: 84-93.

[2] Luo Y, et.al. TK. Non-Invasive Electrical Impedance Tomography for Multi-Scale Detection of Liver Fat Content. Theranostics. 2018 Feb 8; 8(6): 1636-1647.

Acknowledgement: This work is supported by the National Institutes of Health grants R21NS11.

In vivo temperature-dependent electrical properties of the healthy and cancerous hepatic tissue in a mouse model between 1Hz and 1MHz

Yitong Guo[1,2,3], Weice Wang[1,2], Junyao Li[1,2], Mingxu Zhu[1,2], Ruteng Song[1,2], Xuetao Shi[1,2]

[1]Shaanxi Provincial Key Laboratory of Bioelectromagnetic Detection and Intelligent Perception, Xi'an, China
[2]Department of Biomedical Engineering, Air Force Medical University, Xi'an, China, shixuetao@fmmu.edu.cn
[3]Department of Ultrasound Diagnosis, Tangdu Hospital, Air Force Medical University, Xi'an, China

Abstract: Knowledge of dielectric properties of healthy and cancerous hepatic tissue during heating is essential in hyperthermia. Through *in vivo* heating and measurement on mice, this research concluded the *in vivo* temperature-dependent dielectric characteristics for liver and hepatic tumor tissue, which would contribute to both procedure design and EIT monitoring during hyperthermia.

1 Introduction

Hyperthermia is an effective, non-invasive and relatively safe treatment for liver cancer [1]. The temperature-dependent changes in electrical properties not only significantly affect the efficacy of thermal therapy, but also contribute to monitoring during treatment using electrical impedance tomography (EIT)[2].Researches showed a significant different in resistivity between removed organs and those measured *in vivo* [3, 4]. In order to thoroughly understand the electrical characteristics of tissues during thermal treatment, systematically *in vivo* temperature-dependent dielectric properties of both healthy liver and cancerous hepatic tumor in the same animal type should be conducted.

2 Methods

2.1 Cell lines and animals

Eight-week-old male C57BL/6J mice were obtained from the Animal Center of the Fourth Military Medical University. To establish the tumor bearing mice, mice were subcutaneously injected with 1×10^7 of Hepa1-6 cells in the right flank.

2.2 *In vivo* dielectric property measurement

The *in vivo* heating of liver or tumor tissue, from 30 °Cto 90 °C, was achieved by the irradiation of an 808-nm laser with adjustable power (0-5W). The measurement was performed using the Solartron 1260+1294A impedance analyzer at frequency between 1 Hz to 1 MHz with injection current of 0.2 mA.

2.3 Statistical analysis

Equivalent circuits with parallel resistors and constant phase angle element (CPE) were built based on the multi-order Cole-Cole equivalent model.The impedance data were normalized with that at 30°C, named as k-value, in order to remove individual difference. After confirmation of normality, Pearson analysis was performed to investigate the correlation between two datasets, and P values of <0.05 indicate statistical difference.

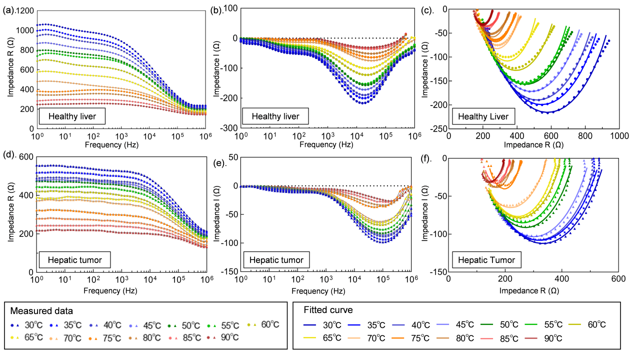

Figure 1: Plots of real and imaginary parts of impedance for healthy livers ((a) and (c)) and hepatic tumors ((b) and (e)). (c) and (f) were plots of temperature-dependent Cole-Cole models for healthy livers and hepatic tumors, respectively.

3 Conclusions

In vivo temperature-dependent dielectric properties for the liver and hepatic tumor were displayed in Figure 1, and the normalized impedance was linearly correlated with temperature (Table 1). The results will contribute not only to the development of ablation systems but also techniques for temperature monitoring during hepatic hyperthermia.

4 Acknowledgements

This work was supported by Basic Strengthening Plan of the Science and Technology Committee (2019-JCJQ-JJ-096).

References

[1] HP Kok, E N K Cressman, W Ceelen. *Int J Hyperthermia*, 37:711–741, 2020
[2] R Poni, E Neufeld M Capstick. *Cancers (Basel)*, 13,2021
[3] D Meroni, D Bovio, M Gualtieri *Conf 40th Annual International Conference of IEEE, EMBC*,July 2018
[4] S Salahuddin, A L Gioia , M A Elahi *Proceedings to the 2017 ICEAA*, Sept. 2017

Table 1: Coefficients in the linear regression of k-values and temperatures for livers and tumors at six different frequencies.

	1kHz		10kHz		50 kHz		100 kHz		500 kHz		1MHz	
tissue	liver	tumor	liver	tumor	liver	tumor	liver	tumor	liver	tumor	liver	tumor
a	-0.013	-0.009	-0.012	-0.009	-0.011	-0.008	-0.009	-0.008	-0.007	-0.007	-0.008	-0.007
b	1.407	1.277	1.384	1.260	1.345	1.247	1.308	1.233	1.214	1.219	1.242	1.211
r-square	0.939	0.848	0.948	0.919	0.954	0.903	0.940	0.925	0.920	0.898	0.937	0.816

Portable Adjustable Electrical Impedance Tomography System

Zekun Chen[1] and Shili Liang[1,*]
[1]School of Physics, Northeast Normal University, Changchun 130022, China
[*]lsl@nenu.edu.cn

Abstract: This paper presents a Portable Adjustable Electrical Impedance Tomography System (PAEIT), which consists of 16/32 electrodes, is a small size, and the excitation frequency, scanning mode and frame rate can be adjusted by keystrokes. The default current source frequency is 40 kHz, the amplitude is 0.65 mA, and good signal-to-noise ratio (36dB). Data acquisition is performed in adjacent drive mode, and the acquisition rate is stable (7/2 frames/SEC, corresponding to 16/32 electrodes).

1 Introduction

Electrical Impedance Tomography (EIT), as a new non-invasive, non-radiation and non-invasive imaging technology, has important clinical applications in respiration monitoring , brain imaging and cancer screening. Compared with magnetic resonance, CT and X-ray imaging technology, it has better real-time performance and security. The principle is to inject a safe current to the surface of the human skin through electrodes, while measuring the response voltage of the remaining electrodes and reconstructing the conductivity distribution of the internal tissues or organs of the human body.

2 Methods

The hardware of the PAEIT system is shown in Fig. 1. The PAEIT is designed as a standalone portable device, which is small and lightweight, with dimensions of 8 cm × 8 cm × 8 cm and a weight of only 268 g. Furthermore, the PAEIT system is modularly designed in a cascade fashion and consists of five independent PCB circuit modules, including the main control circuit board, the current source and voltage detection circuit boards, the signal generating circuit board, the multiplexing circuit board, and the system power supply circuit board. The use of a combination of pin connectors between each board enhances the scalability, flexibility and portability of the circuit system.

The PAEIT system works as follows: firstly, the MCU STM32 acts as the main controller to coordinate all the other modules. Secondly, the signal generator provides a sine wave voltage signal using a direct digital synthesiser (DDS). Then, the sinusoidal voltage signal is converted to a current signal by a voltage-to-current converter (VCCS). In addition, four 16/32-selective multiplexers are used so that two adjacent electrode sets are current inputs and the remaining two adjacent electrodes are used as voltage detection terminals. The voltage detection is performed by a multi-stage amplifier circuit consisting of an instrumentation amplifier, and the sampled signal is obtained by ADC analogue-to-digital conversion, and the current voltage measurement is calculated using Fast Fourier Transform (FFT) or IQ demodulation. One frame when all electrodes are cycled once consists of 928/208 measured values. Finally, the acquired data is transmitted to a notebook computer via Bluetooth or USB for image reconstruction.

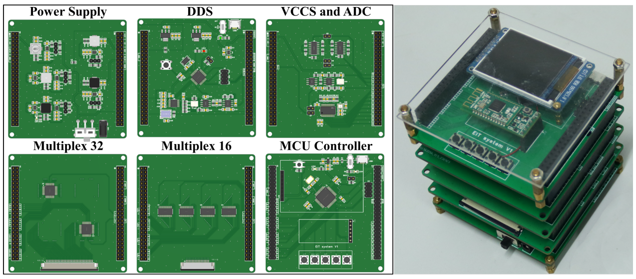

Figure 1: PAEIT System Hardware.

3 Results

To demonstrate the capabilities of the proposed PAEIT, where the number of electrodes in the PAEIT system is adjusted to 16. The simulated thorax region is two circular water tanks with diameters 16cm and 20cm, respectively, with a background constructed by saline and a conductivity adjustment of about 1S/m, while the model of the lung is generated by a 3D printer using PETG material with a conductivity of 0 S/m. Three reproducible algorithms are selected, including NOSER [1] (Newton's One Step Error Reconstructor), Total Variation [2] and Block Sparse Bayesian Learning (BSBL) [3] to image reconstruct, as shown in Fig. 2.

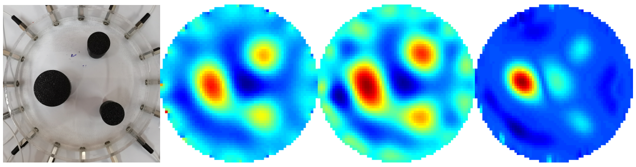
GroundTruth NOSER TV BSBL

Figure 2: Image Reconstruction Results.

4 Conclusions

In this paper, we design a 16/32-channel PAEIT system with portability and real-time performance, and the ability to set the system functions on demand, which is suitable for general data acquisition. Future work will focus on improving the hardware system so that it can be applied to real respiratory data acquisition.

5 Acknowledgements

This work is supported by the Natural Science Foundation of Jilin Province [grant number YDZJ202201ZYTS506].

References

[1] M Cheney, et al. *International Journal of Imaging systems and technology*, 2(2):66–75, 1990
[2] A Borsic, et al. *he University of Manchester*, 1-26, 2007
[3] S Liu, et al. *IEEE transactions on medical imaging*, 37(9):2090–2102, 2018

Multi-Frequency Electrical Impedance Tomography for Dynamic Multiphase Flow Imaging

Junzhe Qiu[1], Shengnan Wang[1]*, Yunjie Yang[2], Ming Kong[1]
[1]China Jiliang University, Hangzhou, China, snwang@cjlu.edu.cn
[2]The University of Edinburgh, Edinburgh, UK

Abstract: This study evaluates the performance of multi-frequency electrical impedance tomography (MF-EIT) in visualizing complex dynamic multiphase flows using a Three-Dimensional Fluid-Electric field Coupling Model (3D-FECM). We adopt five current frequencies: 10 kHz, 100 kHz, 200 kHz, 500 kHz, 1MHz, and 10MHz. Through numerical experiments, time-difference (TD) real and imaginary components of EIT data are collected and the amplitude and phase at each frequency can be calculated. Additionally, we obtain the frequency-difference (FD) data for the amplitude and phase parts, using 10 kHz as the reference frequency. Image reconstruction is performed using the Standard Tikhonov Regularization (STR) algorithm and is evaluated by the Structural Similarity Index (SSIM) and Peak Signal-to-Noise Ratio (PSNR). Results demonstrate that FD imaging achieves its best image quality at 1 MHz.

1 Introduction

Multi-frequency Electrical Impedance Tomography (MF-EIT) is a cutting-edge imaging technique that visualizes the electrical properties of objects or tissues across different frequencies [1]. It holds great promise for dynamic multiphase flow imaging, offering insights into the frequency-dependent behaviours of electrical properties, which can significantly vary among different phases of multiphase flow. However, the complex nonlinear and hierarchical multi-scale characteristics of multiphase flows make it challenging to obtain ground truth profiles in practice. This challenge complicates the modelling and evaluation of MF-EIT's performance, leading to a shortage of reference standards for the agile assessment of MF-EIT image reconstruction algorithms. Such limitations hinder the advancement of MF-EIT in multiphase flow testing applications. To address this issue, we developed a 3D-FECM that simulates dynamic multiphase flows. Integrated with MF-EIT, this model enables the acquisition of corresponding EIT measurements instantaneously. We then employ a suite of metrics, including the SSIM and PSNR, to quantitatively evaluate the quality of images reconstructed by MF-EIT.

2 Methods

We utilized the 3D-FECM to simulate dynamic water-gas flow and designed 16-electrode EIT sensor with excitation currents ranging from 10k to 10MHz for flow measurement (see Figure 1). The fluid-electric field coupling simulation employs a laminar two-phase flow interface to model gas-liquid interactions, expressed as follows:

$$\rho\frac{\partial \mathbf{u}}{\partial t}+\rho(\mathbf{u}\cdot\nabla)\mathbf{u}=\nabla\cdot[-p\mathbf{I}+\mu(\nabla\mathbf{u}+(\nabla\mathbf{u})^{\mathrm{T}})]\mathbf{F}+\mathbf{F}_g \quad (1)$$

$$\nabla\cdot\mathbf{u}=0 \quad (2)$$

where ρ is the mixture density; $\mathbf{u}$ is the mass-averaged velocity vector; p is the pressure; $\mathbf{I}$ is the identity tensor; $\mathbf{F}$ is the volume force vector, $\mathbf{F}_g$ is the gravity force vector; μ is the mixture dynamic viscosity.

For EIT image reconstruction, the STR algorithm is employed, formulated as:

$$\Delta\hat{\boldsymbol{\sigma}}=\arg\min_{\Delta\sigma}\frac{1}{2}(\|\Delta\mathbf{V}-\mathbf{J}_{EIT}\Delta\sigma\|^2+\|\lambda\mathbf{E}\Delta\sigma\|^2 \quad (3)$$

where $\Delta\hat{\boldsymbol{\sigma}}$ represents the estimated conductivity variation, λ is the regularization coefficient, $\mathbf{E}$ is an identity matrix, $\Delta\mathbf{V}$ is the change in voltage, and $\mathbf{J}_{EIT}$ is the Jacobian matrix related to the conductivity changes.

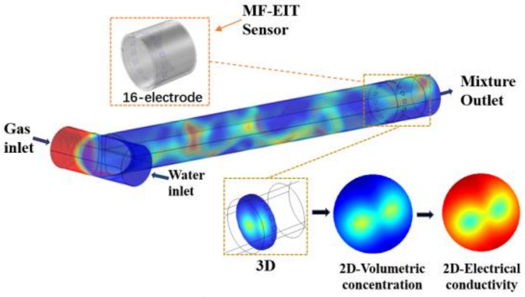

Figure 1: Geometric structure of the 3D-FECM.

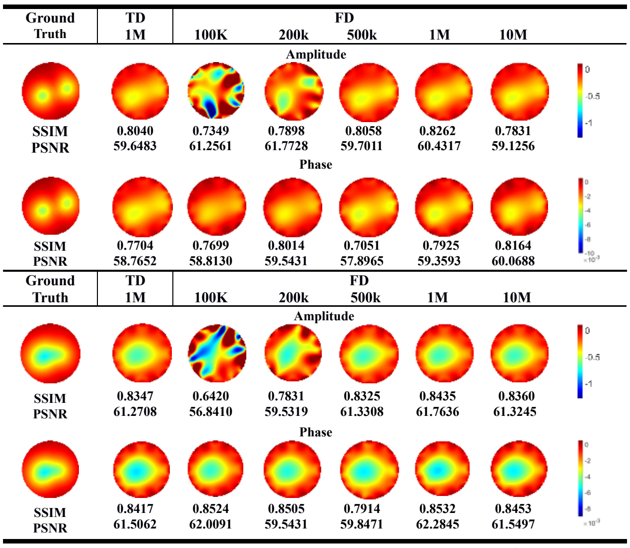

Figure 2: Quantitative evaluation results. FD uses 10k as the reference.

3 Conclusions

We proposed 3D-FECM integrated with MF-EIT to simulate dynamic multiphase flows. We demonstrate this approach a numerical platform to evaluate the imaging performance of MF-EIT. The evaluation results show that the MF-EIT achieves its best FD image reconstruction at a frequency of 1 MHz, as indicated by peak SSIM and PSNR values of 0.8532 and 62.2845, respectively.

References

[1] Yang Y, Jia J. A multi-frequency electrical impedance tomography system for real-time 2D and 3D imaging. Review of Scientific Instruments, 2017, 88(8).

Ventilation and Perfusion Observation in Renal Hemorrhagic Fever Combined with ARDS Based on Electrical Impedance Tomography

Weichen Li[1,2], Chunfu Wang[3], Jianqi Lian[3] and Xuetao Shi[2]

[1]School of Life Sciences, Northwest University, Xi'an, China, Email: lycoliver@163.com
[2]Department of Biomedical Engineering, Air Force Medical University, Xi’an, China
[3]Department of Infectious Disease, Tangdu Hospital, Air Force Medical University, Xi'an, China

Abstract: Renal haemorrhagic fever combined with ARDS may resulting in severe respiratory and circulatory disturbances. EIT was utilised to observe ventilation and perfusion in a Renal haemorrhagic fever patient combined with ARDS. The reconstructed EIT images demonstrated the changes in ventilation and perfusion distribution before and after treatment.

1 Introduction

Renal haemorrhagic fever (RHF) is an epidemic disease caused by hantaviruses, with rodents as the main source of infection [1]. The progression of RHF may be combined with ARDS, which results in pulmonary congestion and oedema, and affects the normal ventilation and air exchange of alveoli, resulting in severe respiratory and circulatory disturbances [2]. For such patients, radio examinations are not always permitted due to the possibility of renal rupture by frequent movement, hence lacking suitable methods to assess the recovery of pulmonary circulation and ventilation during treatment. Here, EIT was utilised to observe ventilation and perfusion in a RHF patient combined with ARDS.

2 Methods

2.1 Data collection

The patient was received treatment in the department of infectious diseases from 28 November 2023 to 19 December 2023, and the observational study was conducted after being informed consent (Ethics Approval: TDLL-202308-05). When the patient was in a supine position, 16 electrodes were placed equally spaced between the third and fourth ribs around the chest. The EIT data (40 frames per second) were acquired by using EC-100 PRO (UTRON Technology Co., Ltd., Hangzhou, China). Meanwhile, A photoplethysmography (PPG) sensors was used to record the cardiac pulse information. After breathing for one minute, the patient was instructed to take a breath-hold about 10 seconds, during which data for all cardiac cycles within the breath-hold period and respiratory impedance data for the entire acquisition process were gathered. Data were collected on 1 December 2023 and 17 December 2023, earlier and later in the admission period, respectively.

2.2 Data Analysis

All EIT and PPG data are aligned according to the time sequence. Based on the global ventilation impedance variation measured by EIT, the first and maximum point of one cycle were identified as the background and foreground frame for reconstruct imaging, respectively. Based on the feature points of PPG signal, the corresponding impedance data during breath-hold will be selected for reconstructing the lung perfusion EIT images. EIT reconstruction images were completed based on GREIT through EIDORS V3.10 software platform.

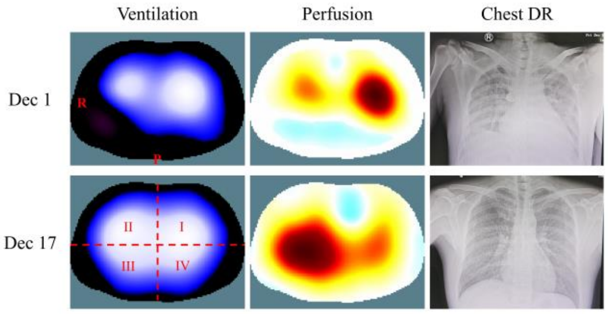

Figure 1: Distribution of lung ventilation and perfusion based on EIT reconstruction images on Dec 1 and Dec 17, 2023.

Reconstructed EIT images were divided equally into four quadrants, and the proportion of ventilation impedance and perfusion impedance within each quadrant was calculated separately.

Table 1: Proportion of ventilation and perfusion in each quadrant of the EIT reconstructed images.

Quadrant	Ventilation proportion (%)		Perfusion proportion (%)	
	Dec 1	Dec 17	Dec 1	Dec 17
I	35.38	25.76	41.14	20.33
II	27.49	25.31	25.39	23.69
III	13.32	24.44	7.93	32.84
IV	23.81	24.49	25.54	23.14

3 Conclusions

The RHF patient's ARDS symptoms disappeared, and his ventilation and perfusion returned to normal with effective treatment, which could be observed by EIT.

4 Acknowledgements

The authors would like to express their gratitude to the Key Project Grant of the MOST (2022YFC2404803), China. The authors would like to express their gratitude to support from all medical staffs in the ICU of the Infectious Diseases Department, Tangdu Hospital.

References

[1] P. A. Vial, M. Ferres, C. Vial *et al.*, "Hantavirus in humans: a review of clinical aspects and management," *Lancet Infect Dis*, vol. 23, no. 9, pp. e371-e382, Sep 2023.

[2] G. A. Mukhetdinova, R. M. Fazlyeva, V. Mustafina *et al.*, "[Clinical and morphological parallels in lung lesions associated with hemorrhagic fever with renal syndrome]," *Klin Med (Mosk)*, vol. 90, no. 5, pp. 17-20, 2012.

Electrical Impedance Tomography Guided Positive End-expiratory Pressure Titration in Critically Ill and Surgical Adult Patients: A Systematic Review and Meta-analysis

Yelin Gao[1], Huaiwu He[1*], Yi Chi[1], Inéz Frerichs[2], Yun Long[*1], Zhanqi Zhao[*1,3,4]

[1]State Key Laboratory of Complex Severe and Rare Diseases, Department of Critical Care Medicine, Peking Union Medical College Hospital, Peking Union Medical College, Chinese Academy of Medical Sciences, Beijing, China
[2]Department of Anesthesiology and Intensive Care Medicine, University Medical Center of Schleswig-Holstein Campus Kiel, Germany
[3]School of Biomedical Engineering, Guangzhou Medical University, Guangzhou, China
[4]Institute of Technical Medicine, Furtwangen University, Villingen-Schwenningen, Germany

Abstract: Electrical impedance tomography (EIT) has been used to titrate positive end-expiratory pressure (PEEP). This study aims to develop a comprehensive view of the efficacy and long-term prognosis of EIT-guided PEEP compared to other conventional approaches in various clinical scenarios, including patients with acute respiratory distress syndrome (ARDS), hypoxemic acute respiratory failure (hARF) and patients undergoing surgery under general anaesthesia.

1 Introduction

Determining the “ideal” PEEP remains difficult in real-life practice. In recent years, many personalized PEEP titration strategies based on various parameters have been proposed, including lung or respiratory system compliance (C_L/C_{rs}), stress index, pressure-volume (PV) curve, or transpulmonary pressure (P_L). These approaches, unfortunately, are all rooted in global parameters that cannot completely represent regional lung status, especially in diseases with heterogeneous representation. EIT is a non-invasive, non-radiological, and bedside lung monitoring tool that provides real-time and continuous information on regional ventilation distribution. It has been evaluated in many studies to guide PEEP titration in multiple clinical conditions such as ARDS, hARF, and surgery under general anesthesia. Despite its promising benefits and wide range of clinical applications, studies to date have not been able to achieve practical results consistently [1-3], especially in long-term prognosis

2 Methods

The literature search was conducted in PubMed, Web of Science, Embase, and Cochrane Library, from inception to July 30, 2023 (ARDS/hARF) and October 5, 2023 (surgery). The Cochrane risk of bias assessment and the methodological index for non-randomized studies were used for quality appraisal. The main outcomes were PEEP level, PaO_2/FiO_2 ratio, C_L/C_{rs}, driving pressure (ΔP), in-hospital mortality, and postoperative pulmonary complications (PPCs) in surgical studies.

3 Results

Four randomized controlled trials (RCTs), one historical control study, and six before-after studies of ARDS/hARF, as well as eight surgical RCTs, were retrieved. Subgroup analysis has been carried out and analysis of before-after studies was performed separately. Diverse PEEP strategies were adopted in the included studies, such as low/high PEEP-FiO_2-table of ARDS-net, pressure-volume loop, and transpulmonary pressure. In ARDS/hARF studies, the EIT strategy did not result in considerably enhanced respiratory system mechanics, including comparable PaO_2/FiO_2 ratios, comparable ΔP, and increased C_L/C_{rs}. As for long-term prognosis, the rough overall meta-analysis showed decreased in-hospital mortality (risk ratio RR=1.54, 95% CI=(1.09, 2.18), P=0.01). In patients undergoing general anesthesia surgery, the EIT group demonstrated improved PaO_2/FiO_2 ratio, C_L/C_{rs}, and ΔP versus the fixed 4 or 5 cmH_2O PEEP. In postoperative prognosis, incidence of PPCs was generally comparable between the two groups.

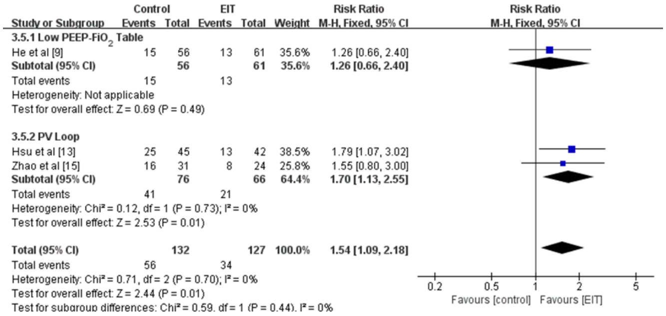

Figure 1: Forest plot of in-hospital mortality in EIT and control groups for ARDS/hARF studies.

4 Conclusion

The EIT-derived PEEP setting strategy might be associated with potential benefits in respiratory outcomes and prognosis in ARDS/hARF and surgical patients. Current data is insufficient to provide solid evidence.

References

[1] He H, Chi Y, Yang Y, et al. Early individualized positive end-expiratory pressure guided by electrical impedance tomography in acute respiratory distress syndrome: a randomized controlled clinical trial. Crit Care. 2021; 25(1): 230.

[2] Jimenez JV, Munroe E, Weirauch AJ, et al. Electric impedance tomography-guided PEEP titration reduces mechanical power in ARDS: a randomized crossover pilot trial. Crit Care. 2023; 27(1): 21.

[3] Hsu HJ, Chang HT, Zhao Z, et al. Positive end-expiratory pressure titration with electrical impedance tomography and pressure-volume curve: a randomized trial in moderate to severe ARDS. Physiol Meas. 2021; 42(1): 014002.

Modification of Calderon's Method for Non-Circular Boundary Objects via Conformal Mapping in EIT

Hangyu Zhong[1] and Benyuan Sun[1]

[1]Sino-European Institute of Aviation Engineering, Civil Aviation University of China, Tianjin, China

Abstract: The electrical impedance tomography for objects with non-circular boundaries often introduces a certain amount of trouble. In this paper, we proposed a modification in the direct method through introducing the conformal mapping to realize the extension of applicability.

1 Introduction

Electrical Impedance Tomography (EIT) is commonly used for objects with circular cross-section, however, it is often troublesome to re-model the forward problem and compute the sensitivity matrix via finite element analysis for objects with non-circular boundary. In this study, we attempt to utilize the principle that a simply connected domain is equivalent to a unit disk, combined with the advantages of point-by-point imaging in direct methods, to achieve fast imaging for objects with non-circular boundary through the use of conformal mapping.

2 Methods

Calderon's method is a direct method for solving the EIT inverse problem. With the special exponentially growing solutions tool known as complex geometrical optics (CGO) solutions, it has achieved inverse problem solving without the aid of sensitivity matrix, and has inspired the creation of D-bar method [1], a family of direct EIT methods. According to the Calderon's method, the estimation of the conductivity changes $\delta\sigma(z)$ at the point $z = x + iy$ is:

$$\delta\sigma(z) = -\frac{1}{2\pi^2}\int_{\mathbb{R}^2}\frac{t(k)}{|k|^2}\exp\left[-i\left(\bar{k}\bar{z}+kz\right)\right]dk$$

where $k = k_1 + ik_2$ can be regarded the complex frequency and $t(k)$ is known as the scattering transform with the form $t(k) := \int_{\partial D} e^{i\bar{k}\bar{z}}\left(\Lambda_\sigma - \Lambda_{ref}\right)e^{ikz}dl(z)$. Note that the Dirichlet-to-Neumann map (DN map) Λ_σ can be obtained by applying the trigonometric patterns, i.e., orthogonal trigonometric basis currents/voltages were applied on all electrodes simultaneously and measured on all electrodes [2].

According to the Riemann mapping theorem, any simply connected region, regardless of the complexity of its boundary shape, can be conformally mapped to the unit disk. Taking a rectangular measurement object as an example, the rectangular domain is denoted as the physical domain D, the unit disk is denoted as the auxiliary domain W. The points in the physical domain D and auxiliary domain W are respectively denoted as z and w. Suppose we have found a conformal mapping $f : D \to W, w = f(z)$ that maps the rectangular domain to the unit circle domain, and we have obtained the conductivity distribution function $\widetilde{\delta\sigma}(w) : W \to \mathbb{R}$ in the auxiliary domain W by the Calderon's method. Now we wish to obtain the conductivity distribution function $\delta\sigma(z) : D \to \mathbb{R}$ in the physical domain D, which can be obtained through $\delta\sigma = \widetilde{\delta\sigma} \circ f$.

Finally, The flow of the modification fo Calderon's method via conformal mapping is : $(\Lambda_\sigma, \Lambda_{ref}) \to t(k) \to \widetilde{\delta\sigma}(w) \to \delta\sigma(z)$.

3 Results

We performed simulations for three different shape objects with 32-electrode configurations. Through applying the trigonometric voltage patterns, DN map Λ_σ and Λ_{ref} (reference measurement without targets) were constructed. After obtaining the reconstructions in the auxiliary circular domain, the imaging in the physical domain was obtained through the one-to-one correspondence of conformal mapping, as shown in Fig. 1.

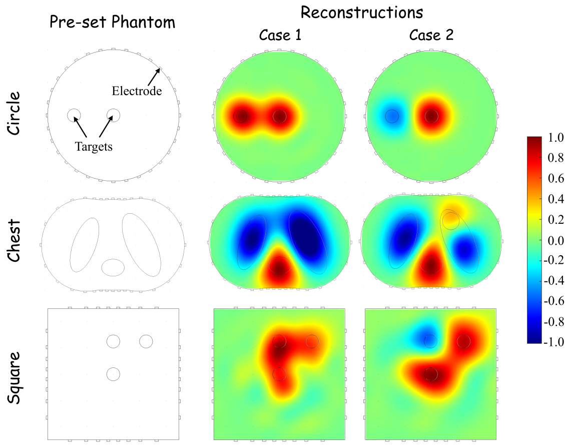

Figure 1: Pre-set phantoms and EIT reconstructions in different cases. First column presents the objects with three different boundary shapes for simulation. The second and third columns show the image reconstruction results for two different conductivity settings.

4 Conclusions

We pose the conductivity reconstruction problem for non-circular boundary objects in the Calderon's method and solve it using the conformal mapping approach. The results show that the modification with conformal mapping effectively extends the applicability of the direct method in boundary shapes. More complex conformal transformations can be realized by Schwarz-Christoffel mapping [3]. The approach is limited to 2D EIT, and is difficult to extend to 3D EIT.

5 Acknowledgments

The authors gratefully acknowledge the support from the Diversified Investment Fund of Tianjin under Grant 23JCQNJC00160 and the Research Innovation Fund for Postgraduate of CAUC under Grant 2023YJSKC12005.

References

[1] J Mueller, S Siltanen. *Inverse Problems*, 36(9):093001, 2020.
[2] S Hamilton, D Isaacson, V Kolehmainen, et al. *Inverse Prob. & Imaging*, 15(5):1135, 2021.
[3] T Driscoll. https://github.com/tobydriscoll/sc-toolbox

An Explainable Artificial Intelligence Framework for Weaning Outcomes Prediction Based on Electrical Impedance Tomography

Pu Wang[1], Meng Dai[1], Yeong-Long Hsu[2,3,4], Feng Fu[1] and Zhanqi Zhao[5,6]

[1]Department of Biomedical Engineering, Fourth Military Medical University, 710032, Xi'an, China; puwangwang@fmmu.edu.cn
[2]Department of Chest Medicine, Far Eastern Memorial Hospital, New Taipei City 220216, Chinese Taipei;
[3]Department of Healthcare Management, College of Medical Technology and Nursing Yuanpei University of Medical Technology, No. 306 Yuanpei Street, Hsinchu, Chinese Taipei;
[4]Department of Electrical Engineering, Yuan Ze University, Taoyuan, Chinese Taipei;
[5]School of Biomedical Engineering, Guangzhou Medical University, Guangzhou, China;
[6]Department of Critical Care Medicine, Peking Union Medical College Hospital, Chinese Academy of Medical Sciences, Beijing, China

Abstract: The present study aimed to propose a complete artificial intelligence (AI) framework for predicting the weaning outcomes of weaning patients, using features captured by various electrical impedance tomography (EIT) indexes. Feature selection, data balance processing, optimal model screening, and the Shapley additive explanations (SHAP) model interpretability were comprehensively considered.

1 Introduction

Prolonged mechanical ventilation (PMV) might cause ventilator-associated pneumonia and diaphragmatic injury and may lead to worsening clinical outcomes and hard-to-wean [1]. In recent years, artificial intelligence technology has been used to predict weaning outcomes. However, the features used in existing artificial intelligence (AI) models lack real-time regional ventilation information of patients during weaning, and ventilator-related parameters cannot be obtained due to the need to remove ventilator-related parameters in some weaning models. Electrical impedance tomography (EIT) is a non-invasive, real-time, bedside imaging technique that can monitor the distribution of ventilation in lung regional areas [2]. We proposed a complete ML framework for predicting the weaning outcomes of PMV patients, using EIT features.

2 Methods

The data were collected at Far Eastern Memorial Hospital, Chinese Taipei. The original study [3] was approved by the local Ethics Committee (FEMH-IRB-103133-E). 30 PMV patients were included (weaning success: weaning failure=21:9). A total of 84 complete samples were collected from 30 patients under different weaning modes (the incidence rate of weaning failed is 42.4%). The training set and the test set are divided in a 7:3 ratio.

As shown in Figure 1, the ML model establishment process was as follows: (1) continuously collecting the EIT data of PMV patients during the weaning process, extracting the EIT data features, and recording the weaning outcomes of patients; (2) the feature selection, including identifying the number of features and specific feature selection; (3) the samples division into training set and test set, and the use of SMOTE method to balance the training set samples. (4) the weaning outcomes prediction model establishment with ten-fold cross-validation to obtain the best model hyperparameters. (5) evaluation of the model performance with test sets; (6) SHAP model explanation with SHAP plot.

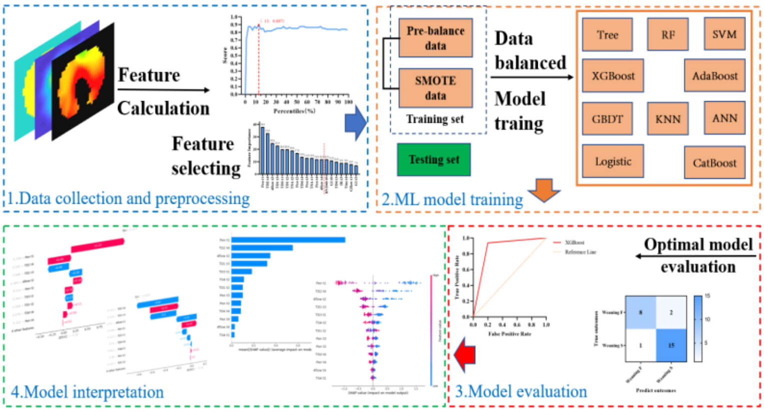

Figure 1: Predictive model construction process.

2.1 Main results

To improve the performance of the ML model, 13 important features were selected from 95 EIT features for subsequent training. These features mainly included the evenness of ventilation time and spatial distribution, the ability of spontaneous breathing, and the degree of alveolar asynchronous occurrence.

As shown in Table 1, the XGBoost model has the highest AUC, accuracy, precision, and f-score.

Table 1 The overall performance of ML models for test set

No.	Model	AUC	Sensitivity	Specificity	Accuracy	Precision	f-score
1	Tree	0.725	0.750	0.700	0.731	0.800	0.774
2	RF	0.788	0.875	0.700	0.808	0.824	0.848
3	SVM	0.806	0.813	0.800	0.808	0.867	0.839
4	**XGBoost**	**0.869**	**0.938**	**0.800**	**0.885**	**0.882**	**0.909**
5	AdaBoost	0.769	0.938	0.600	0.808	0.789	0.857
6	GBDT	0.819	0.938	0.700	0.846	0.833	0.882
7	KNN	0.819	0.938	0.700	0.846	0.833	0.882
8	ANN	0.838	0.875	0.800	0.846	0.875	0.875
9	Logistic	0.756	0.813	0.700	0.769	0.813	0.813
10	CatBoost	0.838	0.875	0.800	0.846	0.875	0.875

3 Conclusions

In this study, the AI framework of weaning can effectively predict weaning outcomes while providing clinicians with global and individual sample-level interpretation of model predictions. This is expected to help clinicians better manage PMV patients weaning.

References

[1] J.M. Boles, J. Bion, A. Connors, M. Herridge, B. Marsh, C. Melot, R. Pearl, H. Silverman, M. Stanchina, A. Vieillard-Baron, and T. Welte, The European respiratory journal 29 (2007) 1033-56.

[2] I. Frerichs, M.B. Amato, A.H. van Kaam, S. Leonhardt, and A. Adler, Thorax 72 (2017) 83-93.

[3] Z. Zhao, S.Y. Peng, M.Y. Chang, Y.L. Hsu, I. Frerichs, H.T. Chang, and K. Moeller, Acta Anaesthesiologica Scandinavica 61 (2017) 1166-1175.

Feasibility study of EIT image technology for non-invasive real-time monitoring and early warning of pulmonary embolism

Junyao Li[1,2], Weichen Li[3], Mingxu Zhu[1,2],Yitong Guo[1,2], Weice Wang[1,2], Xuetao Shi[1,2*]
[1]Department of Biomedical Engineering, Air Force Medical University, Xian, China, ljyczy0424@163.com
[2]Shanxi Provincial Key Laboratory of Bioelectromagnetic Detection and Intelligent Perception
[3]School of Life Sciences, Northwest University, Xian 710127, China

Abstract: The aim of this study was to use electrical impedance tomography (EIT) to find a completely non-invasive means for real-time monitoring and early warning of pulmonary embolism, so as to replace hypertonic saline angiography (invasive) in clinical application.

1 Introduction

Monitoring and early warning of pulmonary embolism is a key factor to guide clinical treatment, especially for critically ill patients. However, bedside monitoring is not possible with existing medical technology and is accompanied by radiation. Pulmonary EIT, as a new monitoring technique, has been developed in the past few years, but it remains to be explored in terms of blood perfusion. A large number of animal experiments have shown that hypertonic saline angiography is closely related to the gold standard for detecting pulmonary embolism (CTPA), but this technique cannot give early warning of pulmonary embolism and increases the risk of infection in patients [1-2]. Therefore, it is urgent to seek a new technical means to achieve the purpose of real-time monitoring pulmonary embolism.

2 Methods

The EC-100 system jointly developed by the course team and Hangzhou Yongchuan Technology Co., Ltd. was used to select 12 landrace pigs with a body weight of (18.75± 2.56)kg as experimental subjects. During supine apnea, blood perfusion before and after embolization was monitored by vascular pulsation technique and hypertonic saline angiography (5ml 10%NaCl), as shown in Figure 1.

Figure 1: Establishment of pulmonary embolism model.

The four-quadrant method was used to divide the areas of interest for pulmonary perfusion , and the V/Q parameters obtained by EIT under different perfusions were calculated by combining lung ventilation images[2]. The formula for obtaining the proportion of local pulmonary blood perfusion is as follows:

$$Y_{1\times \text{pixel}_{\text{ROI}_\text{I}}} = \max\left(X_{n\times \text{pixel}_{\text{ROI}_1}}\right) - \min\left(X_{n\times \text{pixel}_{\text{ROI}_1}}\right)$$
$$Y_{\text{ROI}_\text{I}} = \text{mean}\left(Y_{1\times \text{pixel}_{\text{ROI}_1}}\right) \quad (1)$$
$$\text{Proportion}_{\text{ROI}_x} = \frac{Y_{\text{ROI}_x}}{Y_{\text{ROI}_\text{I}}+Y_{\text{ROI}_\text{II}}+Y_{\text{ROI}_\text{III}}+Y_{\text{ROI}_\text{IV}}} \times 100\%$$

3 Results

The results of the two methods for monitoring perfusion before and after pulmonary embolism showed that there were significant differences between pulsation and hypertonic saline angiography in local blood perfusion before and after embolism, as shown in Table 1. The dead cavity fraction of V/Q on the embolized side (left) increased significantly, and the V/Q after embolization was significantly misaligned, as shown in Figure 2.

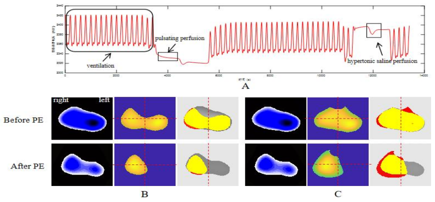

Figure 2: A: one-dimensional impedance signal (red); B: ventilation image, pulsation perfusion image and V/Q matching image; C: ventilation image, saline perfusion image and V/Q matching image.

4 Conclusions

EIT heartbeat technology has shown great clinical application prospect in real-time monitoring of pulmonary embolism, which lays a foundation for clinical research of EIT monitoring of local pulmonary perfusion, and pulsation is expected to monitor and early warning of pulmonary embolism in clinical practice.

References

[1] Nguyen Minh D, Duong Trong L, McEwan A. An efficient and fast multi-band focused bioimpedance solution with *EIT*-based reconstruction for pulmonary embolism assessment: a simulation study from massive to segmental blockage. Physiol Meas. 2022
[2] Gao Y, Zhang K, Li M, Yuan S, Wang Q, Chi Y, Long Y, Zhao Z, He H. Feasibility of 3D-EIT in identifying lung perfusion defect and V/Q mismatch in a patient with VA-ECMO. Crit Care. 2024

Table 1: The blood perfusion before and after pulmonary embolism was monitored by cardiopulsation technique and hypertonic saline angiography, and the area of interest of pulmonary perfusion was divided by four-quadrant method. The P-value is obtained by statistical analysis.

ROI	Pulsate health/H-Saline health	Pulsate embolism/H-Saline embolism	Pulsate p_value/H-Saline p_value
ROI_I%	39.93±4.67/27.07±1.91	55.01±3.72/40.77±2.56	<.001/<.001
ROI_II%	24.81±4.52/24.77±2.91	19.01±1.18/25.65±2.41	<.001/.013
ROI_III%	13.19±3.18/20.95±2.22	9.44±1.34/16.61±1.57	<.001/<.001
ROI_IV%	22.02±2.77/27.20±3.28	16.54±3.34/16.98±2.60	<.001/<.001

Improving Imaging Quality for Electrical Impedance Tomography via Low-Rank Matrix Recovery

Xiao Peng Li[1], Zhang-Lei Shi[2], Lin Yang[3], Meng Dai[3]
[1]Shenzhen University, Shenzhen, China,
[2]China University of Petroleum (East China), Qingdao, China
[3]Fourth Military Medical University, Xi'an, China, daimeng@fmmu.edu.cn

Abstract: We treat the body movement interferences of patient as impulsive noise. Then, a two-stage imaging algorithm, consisting of denosing and imaging, is presented. Experimental results on clinical data demonstrate that the proposed algorithm removes the body movement interferences in EIT data and provides high-quality EIT images.

1 Introduction

Electrical impedance tomography (EIT) [1] has become not only a non-invasive, radiation-free monitoring tool, but also an important direction to improve patient care in critical and respiratory medicine. Currently, most of the existing studies have concentrated on developing algorithms to enhance imaging under ideal conditions, namely, improve quality of EIT images based on measurements without clinical interferences. However, clinical interferences occur frequently in practice because of body movements of patient or poorly connected electrodes [2]. Hence, imaging performance of existing methods may degrade significantly without adopting proper techniques against such interferences.

2 Methods

In the perspective of signal processing, dramatic measurement interferences caused by body movements can be treated as impulsive noise. Inspired by this, we model the EIT measurements as a matrix and propose a robust EIT imaging approach based on the low-rank matrix recovery [3]. To attain high-quality EIT images, we divide the imaging task into two steps, viz. denoising and imaging. In particular, the denoising subtask is of two stages as shown in Fig. 1, where robust statistical analysis and low-rank recovery are utilized to detect outliers and restore the EIT data, respectively. In detail, our denoising algorithm first identifies the entries corrupted by impulsive noise in EIT data and consider them as missing elements. Subsequently, the devised algorithm recovers the missing components by exploiting the low-rank property of EIT data. In doing so, the impulsive noise is removed from EIT data. Finally, the recovered data are used for imaging as in ideal situation. The proposed approach is referred to as robust EIT, short as REIT.

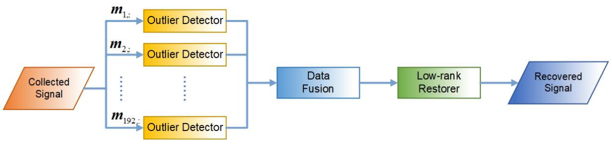

Figure 1: Flowchart of proposed algorithm.

3 Results

In the experiments, the EIT data are continuously collected with the commercial EIT system (VenTom-100, MidasMED Biomedical technology, Suzhou, China). Fig. 2 presents results with various approaches for one patient with bilateral lung ventilation, where w. for with, w/o for without, O for original, and E for estimated. We can observe that the significant artifacts caused by body movement interferences exist in the time-series EIT images and the chest global impedance. The artifacts completely distort the respiratory waveforms and the regional ventilation distribution. Apparently, after the boundary voltages with impulsive noise are processed, only the EIT images recovered by REIT show regional ventilation distribution in the bilateral lungs.

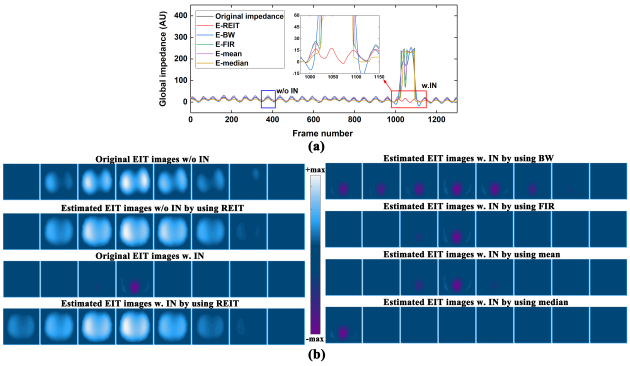

Figure 2: EIT images by different approaches for impulsive noise (IN) composed of multiple measured data points in the patient with bilateral lung ventilation. (a) Original time-series EIT images during a spontaneous breathing cycle, and the estimated time-series EIT images by using REIT, Butterworth filtering, FIR filtering, mean filtering, and median filtering. (b) Original global chest impedance and estimated chest impedance by different methods.

4 Conclusions

To resist the body movement interferences, we formulated the denoising task as the robust low-rank matrix recovery optimization problem. Specifically, the problem was divided into two subtasks, i.e., outlier detection and low-rank recovery. The former was exploited to identify the entries corrupted by outliers and then considered them as missing elements, while the latter exploited the low-rank property to restore the missing entries, such that the body movement interferences were removed. Experimental results on clinic data verifies the effectiveness of our algorithm against body movement interferences.

References

[1] JV Jimenez, RC Hyzy *Am. J. Respir. Crit. Care. Med.*, 208(5): 636–637, 2023.

[2] M Soleimani, C Gomez-Laberge, A Adler *Physiol. Meas.*, 27(5): S103–13, 2006.

[3] X P Li, Z-L Shi, Q Liu, H C So *IEEE Trans. Cybern.*, 53(11): 7199–7212, 2023.

Early Lung Function Screening with EIT

Mingyi Kong[1], Shuoyao Qu[2], Lin Yang[3], Meng Dai[4], Zhanqi Zhao[1]

[1]School of Biomedical Engineering, Guangzhou Medical University, China, zhanqizhao@gzhmu.edu.cn
[2]Department of Pulmonary and Critical Care Medicine, Xijing Hospital, Air Force Medical University, Xi’an, China
[3]Department of Aerospace Medicine, Fourth Military Medical University, Xi'an, China
[4]Department of Biomedical Engineering, Fourth Military Medical University, Xi'an, China

Abstract: This study investigates the possibility of using electrical impedance tomography (EIT) as an early screening method to identify lung function impairment in subjects with normal spirometry.

1 Introduction

Pulmonary function testing (PFT) with a spirometer is a well-established measurement in assessing lung function. However, the sensitivity of spirometry in detecting early lung function deterioration has limitations. Spirometry provides global lung function measures, which fail to capture regional and subtle changes in lung ventilation and gas distribution that may occur early in the disease process. Electrical impedance tomography (EIT) is a promising technology that offers the potential to address the limitations of spirometry and traditional imaging modalities [1, 2]. The aim of the study was to explore the possibility to use EIT as an early screening method to identify lung function impairment.

2 Methods

A belt with 16 equidistantly fixed electrodes was placed around the chest in one transverse plane at the level of the 5th intercostal spaces at the parasternal line. For female subjects, if 5th intercostal space was not accessible, the electrode belt was placed above the breast (~4th intercostal spaces). Data were recorded at 20 Hz. Healthy subjects scheduled for annual body check in Oct. 2023 were screened. Subjects who were unable to complete the forced vital capacity (FVC) maneuver meeting the guidelines; forced expiratory volume in 1 second (FEV1) < 80% predicted; FEV1/FVC<0.8 were excluded.

Time constant map was calculated as described in a previous study [3, 4]. In brief, for every pixel within the lung region, the regional time constant was calculated by fitting the following exponential equation:

$$Z(t) = Z_0 \cdot e^{-t/\tau} + c \qquad (1)$$

Where Z(t) is the relative impedance for a pixel within the lung at time point t, Z_0 is the impedance at the start of expiration, t represents the time from the end-inspiration to the end-expiration, τ denotes the regional time constant, and c the end-expiratory volume. Subjects whose values were above the threshold were recommended to have a follow-up CT examination. For smokers with ⩾10 pack-year tobacco consumption, CT was recommended even if their τ was lower than the threshold. Due to the radiation exposure, the CT examination was conducted based on the voluntary consent of the subjects.

3 Results

A total of 1980 subjects for annual bodycheck were screened, and 216 subjects were included. FVC and EIT measurements were conducted simultaneously. FVC maneuver from 74 subjects did not meet the ATS-ERS criteria. Further 12 subjects had an FEV1 < 80% predicted. At the end, final analysis was conducted in 130 subjects.

For τ_{prod}, 80% of the non-smoker’s threshold was 0.1066 s^2. The positive rate of impaired lung function in EIT-abnormal subjects that was reconfirmed by CT was 0.59 (13/22). Based on the available CT data, the sensitivity and specificity of EIT-based screening were 81.3% and 50.0%, respectively.

Table 1. Summary of the number of CT results classified as abnormal and normal.

Total N=130	τ_{prod} > 0.107 s^2		τ_{prod} ≤0.107 s^2 & smoker ≥10 pack-year		sum
With CT	Total	22	Total	12	34
	Impaired	13	Impaired	3	16
	Inconspicuous	9	Inconspicuous	9	18
w/o CT	Total	4	Total	10	-

τ_{prod}, product of median regional time constant and interquartile range. w/o, without.

The τ_{med}, τ_{iqr} and the corresponding product τ_{prod} were significantly correlated with the tobacco consumption (τ_{med} R=0.52, P<0.0001; τ_{iqr} R=0.42, P<0.001; τ_{prod} R=0.54, P<0.0001), whereas spirometry parameters were not correlated with tobacco consumption.

4 Conclusions

In the present study, we demonstrated the feasibility to use EIT for screening early lung impairment in “healthy” subjects (normal FVC, relatively young and occasional or non-smokers). Using follow-up CT as reference, the sensitivity of EIT-screening was over 80%.

References

[1] Zhao, Z., Müller-Lisse, U., Frerichs, I., Fischer, R., Möller, K., 2013. Regional airway obstruction in cystic fibrosis determined by electrical impedance tomography in comparison with high resolution CT. Physiol. Meas. 34, N107-114.

[2] Vogt, B., Zhao, Z., Zabel, P., Weiler, N., Frerichs, I., 2016. Regional lung response to bronchodilator reversibility testing determined by electrical impedance tomography in chronic obstructive pulmonary disease. Am. J. Physiol. Lung Cell. Mol. Physiol. 311, L8-L19.

[3] Karagiannidis, C., Waldmann, A.D., Róka, P.L., Schreiber, T., Strassmann, S., Windisch, W., Böhm, S.H., 2018. Regional expiratory time constants in severe respiratory failure estimated by electrical impedance tomography: a feasibility study. Crit. Care 22, 221.

[4] Strodthoff, C., Kähkönen, T., Bayford, R.H., Becher, T., Frerichs, I., Kallio, M., 2022. Bronchodilator effect on regional lung function in pediatric viral lower respiratory tract infections. Physiol. Meas. 43.

A Stable Symmetry Difference EIT Algorithm for Stroke Detection Based on Dual-Frequency Difference and Edge Region Suppression

Zhibo Zhao[1], Feng Fu[1] and Lin Yang[2]

[1]School of Military Biomedical Engineering, Air Force Medical University, Xi’an, China, aiyazzb@163.com
[2]School of Aerospace Medicine, Air Force Medical University, Xi’an, China

Abstract: Electrical impedance tomography (EIT) is promising in the rapid detection of stroke. One famous image reconstruction algorithm used the anatomical symmetry of the human head to detect stroke lesions, i.e. symmetry difference EIT (SDEIT). However, due to the distribution complexity of head tissues, SDEIT is unsatisfactory. In this study, we proposed a stable SDEIT algorithm, in which dual-frequency difference was used to eliminate the influence of complex tissues, and an improved GREIT method was used to suppress the conductivity changes of non-brain tissues in the edge region.

1 Introduction

Based on the symmetry of the human head and the asymmetry of unilateral stroke, SDEIT for stroke detection was proposed [1-2]. In SDEIT, the asymmetric stroke lesion is supposed to be detected, by subtracting the conductivity distribution on the left side of the head from the right one. However, the head is not perfectly symmetrical, especially for non-brain tissues, such as the skull with low conductivity and its adjacent cerebrospinal fluid (CSF) with high conductivity. The slight asymmetry can cause significant artifacts in the images from SDEIT, which results in great difficulty in identifying stroke lesions. Therefore, a novel stable SDEIT algorithm is proposed to eliminate the influence of non-brain tissues in this study.

2 Methods

2.1 Symmetry difference EIT

Normally, the conductivity distribution on the left side of the human head is symmetrical to that on the right side, while for stroke patients, stroke lesions can break this symmetry [1]. The conductivity distribution $\boldsymbol{\sigma}_{\mathbf{s}}$, which is symmetric with the current conductivity distribution $\boldsymbol{\sigma}$, is taken as the reference conductivity $\boldsymbol{\sigma}_{\mathbf{r}}$. The difference between $\boldsymbol{\sigma}$ and $\boldsymbol{\sigma}_{\mathbf{r}}$ is estimated to reconstruct the image of the asymmetric conductivity distribution on both sides of the head.

2.2 Dual-frequency difference

The conductivity of head tissues at two frequencies of 10Hz and 50.1Hz is shown in Tab. 1.

The SDEIT images with current stimulation frequencies of 10Hz and 50.1Hz were calculated respectively, and subsequently subtracted one from the other to get the dual-frequency symmetry difference (DFSD):

$$\hat{x}_f = R \cdot \left(V^f - V_s^f\right) \approx \sigma^f - \sigma_s^f \tag{1}$$

$$\begin{aligned} \hat{x}_{f_1} - \hat{x}_{f_2} &\approx \left(\sigma^{f_1} - \sigma_s^{f_1}\right) - \left(\sigma^{f_2} - \sigma_s^{f_2}\right) \\ &\approx \left(\sigma^{f_1} - \sigma^{f_2}\right) - \left(\sigma_s^{f_1} - \sigma_s^{f_2}\right) \\ &\approx \Delta\sigma^f - \Delta\sigma_s^f \end{aligned} \tag{2}$$

From formula (2), the DFSD is equivalent to the SDEIT of frequency difference conductivity distribution, and the frequency difference conductivity distribution eliminates the tissue difference between the skull and CSF (Tab. 1).

2.3 Edge region changes suppression

The Graz consensus reconstruction algorithm for EIT (GREIT) is a data-driven EIT algorithm, and its key is to map the training data to the desired image [3]. We set the desired image of the training data in the edge region to 0 in calculating the reconstruction matrix to realize the edge region changes suppression (ERCS).

Finally, DFSD eliminated the tissue differences between the skull and CSF, and ERCS eliminated the differences between the scalp and adjacent tissues. The result is shown in Fig. 1.

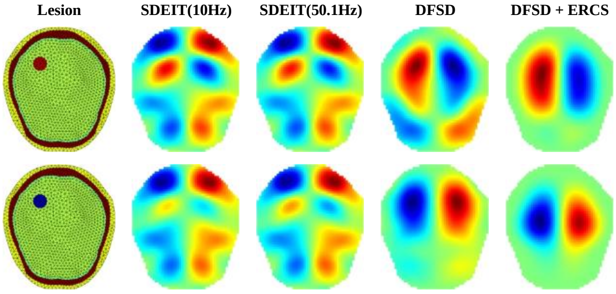

Figure 1: The imaging result of bleed and ischemic lesion.

3 Conclusions

A stable head symmetry difference imaging algorithm with the strategies of dual-frequency difference and edge region changes suppression was proposed to detect stroke.

References

[1] J. Ma, C. Xu, M. Dai Scientific World Journal, 2014: 534012, 2014.
[2] B. McDermott, E. Porter, M. Jones *PhysiolMeas*, 39: 044007, 2018.
[3] A. Adler, J.H. Arnold, R. Bayford *PhysiolMeas*, 30: 35-55, 2009.

Table 1: Conductivity of human head tissues at 10 Hz and 50.1 Hz

Frequency	Conductivity (S/m)					
	scalp	skull	CSF	brain	bleed	clot
10 Hz	0.230	0.012 3	1.75	0.188	0.56	0.06
50.1 Hz	0.245	0.012 3	1.75	0.210	0.56	0.15
$\boldsymbol{\Delta\sigma^f}$	−0.015	0	0	−0.022	0	−0.090

$\boldsymbol{\Delta\sigma^f}$: The difference between the conductivity of each tissue at two frequencies of 10 Hz and 50.1 Hz

Bronchoalveolar Lavage Linearly Correlated with the Electrical Impedance Tomography Parameters of ΔDefect Score and ΔCOV

Aijie Yang[1], Zhanqi Zhao[2], Hui Yuan[1], Dexian Huang[3], Meng Dai[4], Feng Fu[4] and Wei Gao[1*]
[1]Department of Anesthesiology, the First Affiliated Hospital of Xi'an Jiaotong University, Xi'an, China, gaowei2906@xjtufh.edu.cn
[2]School of Biomedical Engineering, Guangzhou Medical University, China
[3]Department of Research and Development, the Northwest Machinery Company limited, Xi'an, China
[4]Department of Biomedical Engineering, the Fourth Military Medical University, Xi'an, China

Abstract: Bronchoalveolar lavage (BAL) often results in hypoxemia. We used electrical impedance tomography (EIT) to monitor patients undergoing general anesthesia soft bronchoscopy, and found that BAL increased ventral ventilation and ventilation defects, ΔDefect score and ΔCOV showed a linear correlation with BAL.

Introduction

BAL induces alveolar surfactant loss [1], intrapulmonary tidal volume decline [2], ventilation perfusion mismatch and other comorbidities [3, 4], especially in critical patients.[3] We aimed to explore the regional ventilation changes and identify the most sensitive BAL parameters to improve the safety of bronchoscopy.

1 Methods

Patients who underwent general anesthesia soft bronchoscopy were screened to non-BAL or BAL groups. The EIT parameters of regional ventilation delay (RVD), changes in end-expiratory lung impedance (ΔEELI), center of ventilation (COV), global inhomogeneity index (GI) and defect score at perioperative period were recorded by Draeger PulmoVista 500 and analyzed offline (T1, before bronchoscopy; T2 for non-BAL: 10 minutes after bronchoscopy; T2 for BAL: at last alveolar lavage; T3, the 2nd respiratory point after the end of the bronchoscopy operation; T4, after the tracheal tube was removed). Generalized linear models and multiple linear regression analysis were used to compare the parameters between and within groups and determine their correlation with lavage.

2 Results

A total of 85 patients were included in the study. Among these patients, 14 were in non-BAL group and 71 were in BAL group. The BAL group had significantly higher Defect score (P=0.022) and COV (P=0.032) than non-BAL group. In BAL group, COV moved to the ventral side [46.60 (40.50–51.50) vs. 42.80 (37.90–48.10), P<0.001] and Defect score increased [2.00 (1.00–3.00) vs. 3.00 (1.50–4.00), P<0.001] compared BAL (T2) with before BAL (T1), and only Defect score was continually affected at after BAL (T3) and after removing the tracheal tube (T4). Defect score and COV increment from T2 to T1 (ΔDefect score, ΔCOV) respectively showed a linear correlation with BAL (β=0.355, 95%CI:0.586–2.240, P=0.001; β=-6.816, 95%CI: -10.305–-3.327, P<0.001).

Table 1: For the comparison of parameters between the two groups, Defect score and COV had significantly higher Defect score and COV than non-BAL group.

	β	95%CI	P
Defect score			
BAL	0.539	0.077- 1.001	**0.022**
Airway stenosis	0.817	0.459- 1.175	**<0.001**
BAL* Airway stenosis	0.293	-0.855- 1.441	0.616
COV			
BAL	-2.870	-5.494- -0.245	**0.032**
Airway stenosis	1.912	-0.124- 3.948	0.066
BAL* Airway stenosis	-1.575	-0.809- 4.949	0.635

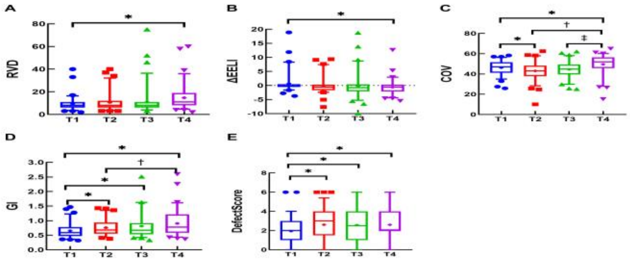

Figure 1: Comparative analysis of parameters at each time point in the BAL group. *P <0.05 compared with T1 in the same group; †p <0.05 compared with T2 in the same group; ‡p <0.05 compared with T3 in the same group.

Table 2: The linear correlation between BAL, Defect score and COV increment from T2 to T1 (ΔDefect score, ΔCOV)

	β	95%CI	P
Δ Defect score			
BAL	0.355	0.586-2.240	**0.001**
Airway stenosis	0.116	-0.295-1.037	0.271
Δ COV			
BAL	-6.816	-10.305- 3.327	**<0.001**
Airway stenosis	-0.682	-3.491-2.126	0.630

3 Conclusions

Defect score and COV has the potential to be a predictive EIT parameter for BAL. ΔDefect score and ΔCOV had linear correlation with BAL and thus EIT parameter has the potential to predict BAL in clinics.

References

[1] Duan J. Zhonghua Lao Dong Wei Sheng Zhi Ye Bing Za Zhi. 2014; 32(3): 223-5.
[2] Cereda M, Emami K, Xin Y, Kadlecek S, Kuzma NN, Mongkolwisetwara P, et al. Crit Care Med. 2013; 41(2): 527-35.
[3] Ergan B, Nava S. Expert Rev Respir Med. 2018; 12(8): 651-63.
[4] Bernhard C, Masseau I, Dodam J, Outi H, Krumme S, Bishop K, et al. J Feline Med Surg. 2017; 19(6): 665-71.

The High Frame EIT System and Its Validation for Lung Ventilation

Jinchi Xian[1], Wukai Zhang[1], Haining Long[1], Tao Wang[1], Guangyou Fang[1,2]
[1]GBA Branch of Aerospace Information Research Institute, Chinese Academy of Sciences, Guangzhou, China,
xianjinchi115@foxmail.com
[2]Aerospace Information Research Institute, Chinese Academy of Sciences, Beijing, China

Abstract: The paper introduces a miniaturized, high frame EIT system for medical application. The system can be used for regional lung monitoring in human subjects. The preliminary results indicate that the developed high frame EIT system has good stability and consistency, and can continuously monitor lung ventilation with greater temporal resolution.

1 Introduction

Electrical impedance tomography (EIT) can reconstruct the changes of the admittance or impedance distribution of human tissue by injecting currents and measuring their boundary voltages [1]. The EIT system is a passive 16-electrode system, with the main application target for pulmonary functions. The EIT acquisition system has a compact size of 180mm in length, 150mm in width, and 30mm in height, with a weight of less than 1kg (Figure 1). The tablet provides the interface to facilitate user interaction with the EIT system.

2 Methods

The EIT system mainly consists of three parts: the field programmable gate array (FPGA) control module, the current driver, and the signal acquisition module. The FPGA is used for controlling data sampling logic, current waveform generation, and TCP communication with the tablet. The LTC1668 DAC in the current driver module acquires the generated signal via the DDS module, and the output current signal of the DAC is converted to a voltage signal by current sensing resistor. The voltage signal is amplified by an operational amplifier (OA) with programmable gain, and then applied to different excitation electrodes via the analogue switch matrix. The collected signals are first buffered by a voltage follower for stabilization, then filtered using an anti-aliasing filter to remove high-frequency noise and reduce signal aliasing. The analogue to digital interface is implemented using 24-bit analogue to digital converter ADS1675 ADC. The collected discrete sinusoidal data is transmitted via TCP to a tablet for post-processing, with data rate of 2 Mbps.

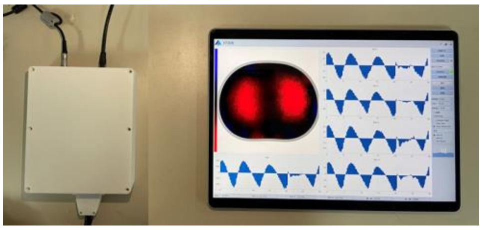

Figure 1: The high frame EIT system.

The current injection frequency range of the system supports 50~250kHz, with the current amplitude ranging from 0.1mA to 5mA rms. The current drive complies with the IEC 60601-1 standard. The system performance was tested on a 50 Ω 0.1% precision resistor network, achieving a signal-to-noise ratio of 80 dB for the current source over continuous measurements lasting 3 hours.

The scan pattern of the EIT system is fully programmable, supporting multiple excitation and measurement modes. The frame rate of the EIT system is primarily determined by the sample window per measurement and the speed of channel switching. With the analogue switch switching speed of 200 ns and the signal stabilizing quickly after switching, during post-processing, only the first period needs to be discarded. Using the 16-electrode protocol for adjacent excitation [2] at 125kHz frequency, with difference imaging based on one-step Gauss-Newton algorithm or GREIT method [3, 4], the system can achieve an actual imaging frame rate of 100 fps.

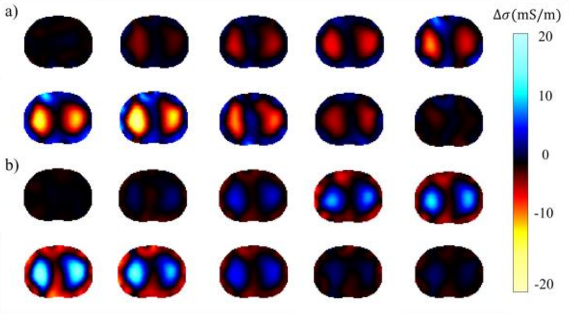

Figure 2: Reconstruction image of the respiratory cycle, (a) Image starting from the end of expiration, (b) Image starting from the end of inspiration.

3 Results

Lung imaging was performed on a 28-year-old healthy male subject. The iterative Gauss-Newton method is used for image reconstruction in Figure 2, selecting data from the end of inspiration or expiration as reference frames for inversion to obtain changes in conductivity.

4 Conclusions

This article introduces the EIT system, which can provide high frame rate dynamic lung imaging monitoring. The system features a compact design, making it portable. It can dynamically display imaging results on a tablet, allowing for interactive human-computer interaction via touchscreen.

5 Acknowledgements

This work is supported by the Science and Technology Planning Project of Guangdong Province under Grant 2019B090909011.

References

[1] Frerichs I, Amato M B P, Van Kaam A H, et al *Thorax*, 72(1): 83-93, 2017.
[2] Adler A, Gaggero P O, et al *Physiological Meas*, 32(7): 731, 2011.
[3] Lionheart W R B. *Physiological Meas*, 25(1): 125, 2004.
[4] Adler A, Arnold J H, et al *Physiological Meas*, 30(6): S35, 2009.

Time-dependent Effects of Prone Position on Ventilation-Perfusion Matching Assessed by Electrical Impedance Tomography in Patients with COVID-19 ARDS: Sub-analysis of a Prospective Physiological Study

Yuxian Wang[1], Ming Zhong[1]

[1]Zhongshan Hospital of Fudan University, Shanghai, 200032, China, wang.yuxian@zs-hospital.sh.cn

Abstract: The aim of this physiological study was to further elucidate the longitudinal effect of PP on regional ventilation-perfusion matching and distribution of ventilation and perfusion in COVID-19-associated ARDS patients, utilizing contrast-enhanced EIT.

1 Introduction

Contrast-enhanced electrical impedance tomography (EIT) has emerged as a valuable instrument for bedside monitoring of pulmonary ventilation and perfusion [1]. It has furnished crucial insight into the physiological mechanisms that underpin the oxygenation responses to prone position (PP) in patients with acute respiratory distress syndrome (ARDS) [2]. Nonetheless, the impact of PP duration on the alterations of ventilation and perfusion remains unclear.

2 Methods

This study analyzed COVID-19 ARDS patients who were mechanically ventilated and undergone PP treatment. EIT evaluations and PaO_2/FiO_2 measurements were performed at five distinct time points during the initial PP session: prior to the initiation of PP while in the supine position (SP), 1h post-PP (PP_1), 3hs post-PP (PP_3), at the end of PP (PP_{16}), and 3h subsequent to reverting to the supine position ($RE\text{-}SP_3$).

3 Results

This study enrolled 18 patients with ARDS induced by COVID-19. When comparing PP to SP, PP led to significant improvements in oxygenation. The PaO_2/FiO_2 showed a consistent increase at each evaluated PP time point (127.22 ± 34.29 vs.166.22 ± 58.66 vs. 196.74 ± 75.72 vs.211.39 ± 82.06 vs. 139.00 ± 45.12 mmHg, P <.001), reaching its peak at PP_{16}.

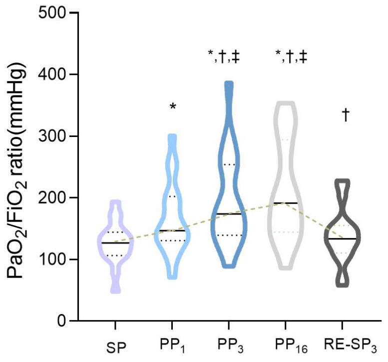

Figure 1. Evolution of PaO_2/FiO_2(%) within the same session.* vs. SP, $p < 0.05$, † vs. PP_1, $p < 0.05$, ‡vs. RE-SP $_3$, $p < 0.05$.

When compared with SP, dorsal ventilation increased significantly at PP_1 ($P< 0.05$), and continued to change throughout the duration of PP, with a higher percentage of dorsal ventilation at PP_{16} than PP_1 ($P<.001$).

Dorsal and ventral perfusion distribution remained unchanged during the initial three hours of PP, but dorsal perfusion increased significantly at PP_{16}. Ventilation and perfusion returned to their baseline levels at $RE\text{-}SP_3$.

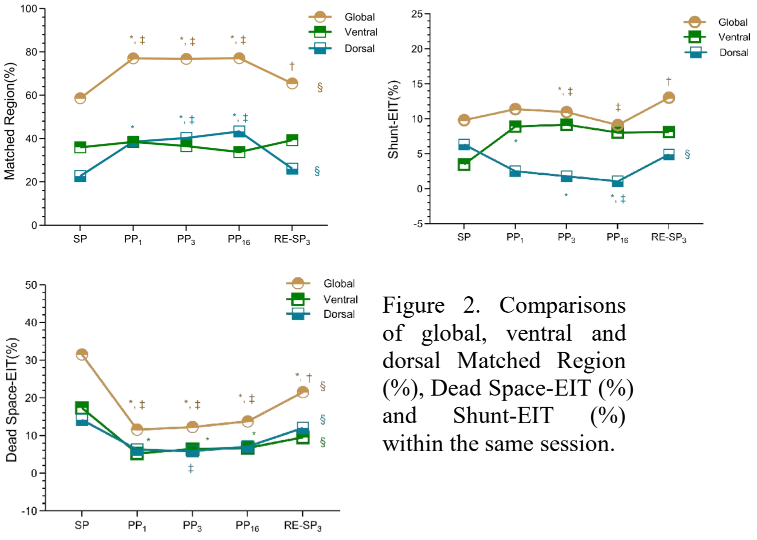

Figure 2. Comparisons of global, ventral and dorsal Matched Region (%), Dead Space-EIT (%) and Shunt-EIT (%) within the same session.

In comparison to SP, there was a significant increase in global V/Q matching and a decrease in Dead space-EIT (%) at PP_3, primarily occurring in dorsal area. Dorsal shunt-EIT (%) decreased over the PP period.

4 Conclusions

In patients with ARDS induced by COVID-19, the early improvement of oxygenation and global V/Q matching observed during PP was primarily attributed to the immediate and early alterations in ventilation distribution, which decreased dead space and persisted into the late stages. However, changes in perfusion only became apparent at a later stage of PP, contributing to further improvements in oxygenation and global V/Q matching.

Acknowledgements

The authors would like to express their gratitude to Zhanqi Zhao.

References

[1] Frerichs I, Amato MB, van Kaam AH, et al: Chest electrical impedance tomography examination, data analysis, terminology, clinical use and recommendations: consensus statement of the TRanslational EIT developmeNt stuDy group. Thorax 2017, 72(1):83-93

[2] Guerin C, Reignier J, Richard JC, et al: Prone positioning in severe acute respiratory distress syndrome. N Engl J Med 2013, 368(23):2159-2168.

Three-Dimensional Shape Reconstruction Algorithm of Electrical Impedance Tomography for Breast Tumour Visualization

Jie He[1], Yuanjing Zhang[1], Mingjie Zheng[2], Kai Liu[1] and Jiafeng Yao[1]
[1]Nanjing University of Aeronautics and Astronautics, Nanjing, China, jiaf.yao@nuaa.edu.cn
[2]Jiangsu Province Hospital, Nanjing, China

Abstract: A 3D Electrical Impedance Tomography (EIT) algorithm based on Dimensional Grey Wolf Optimization (DGWO) algorithm is proposed for reconstructing 3D images of breast tumours, overcomes the inherent defects of 3D EIT with high shape sensitivity and position sensitivity. Simulation result shows that DGWO algorithm outperforms traditional algorithm and improves the image correlation coefficient. The proposed algorithm is expected to be applied to the clinical detection of breast tumour.

1 Introduction

Breast cancer is one of the most common malignant tumours in women worldwide. However, most current studies are limited to two-dimensional cross-sectional imaging without information on tumour depth, which is eager to induce under-diagnosis in practice [1]. Therefore, a high-precision 3D imaging algorithm is required.

2 Methods

Figure 1 shows the flowchart of Dimensional Grey Wolf Optimization (DGWO) algorithm for solving the EIT inverse problem, which consists of four steps [2].

In step 1: a sensitivity matrix is constructed by solving the forward problem. In step 2 and step 3, a relevant encoding and decoding method based on the Dimensional Grey Wolf Optimization algorithm is proposed. In step 4, the DGWO algorithm is used to search for the tumour conductivity distribution in space which consists of 1) constructing a mathematical model of breast tumours, 2) solving the model by encoding the algorithmic inputs, and 3) reducing the obtained results to the desired imaging results by decoding.

3 Result

3.1 Simulation Model Setting

Finite element simulations are performed which are compared with the combination of Tikhonov and NOSER regularization algorithm (TK-NOSER) in this study.

Image correlation coefficient I_C are used as evaluation metric which is calculated as follows:

$$I_C = \left[(\boldsymbol{\sigma}-\bar{\boldsymbol{\sigma}})^T(\boldsymbol{\sigma}_0-\bar{\boldsymbol{\sigma}}_0)\right] \Big/ \sqrt{\|\boldsymbol{\sigma}-\bar{\boldsymbol{\sigma}}\|^2 \|\boldsymbol{\sigma}_0-\bar{\boldsymbol{\sigma}}_0\|^2} \qquad (1)$$

3.2 Simulation result

Figure 2 shows the image reconstruction and numerical evaluation results. By optimizing the angle-based fitting function $f(\Delta\sigma)$ (Step 4-1) and searching the solution space in position and shape direction individually (Step 4-2), DGWO reaches a better performance of edge target.

4 Conclusion

The proposed algorithm can better express the shape characteristics of target in comparison with TK-NOSER algorithm. Particularly, in the case of target being located in edge position, the advantage of the DGWO algorithm is more obvious.

5 Acknowledgements

We thank Qi Deng for his support and inspiration of this research.

References

[1] L. Yang *IEEE Sens J*, 22(13): 130312-13022, 2022.
[2] M. H. Nadimi-Shahraki *Expert Syst Appl*, 166: 113917, 2021.

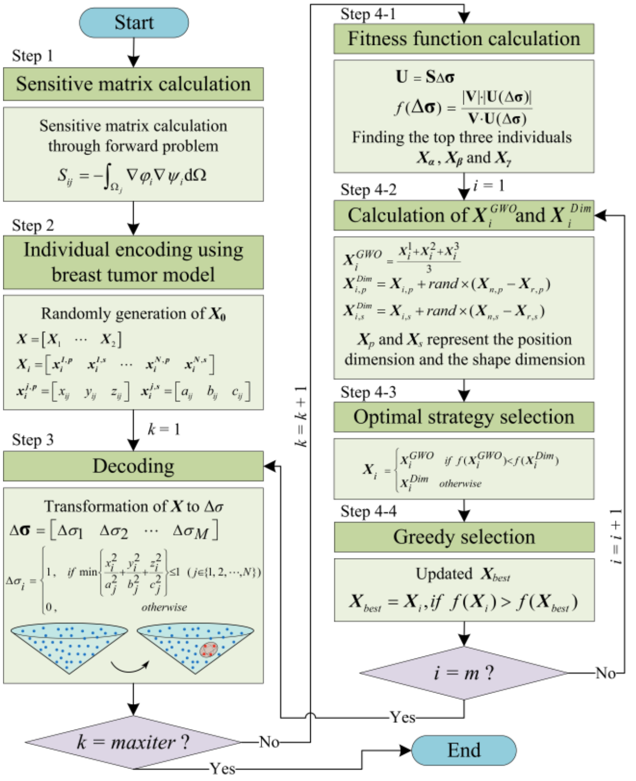

Note: *m* - the number of individuals in the grey wolf population; *maxiter* - the maximum number of iterations.

Figure 1: Flowchart of DGWO solving the inverse problem.

NO.	Ground Truth	TK-NOSER	DGWO
1	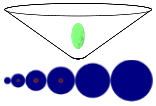	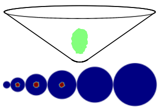 I_C = 0.804	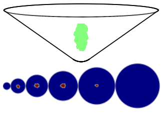 I_C = 0.813
2	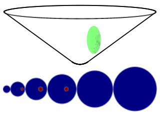	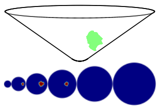 I_C = 0.829	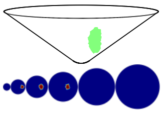 I_C = 0.872

Figure 2: Simulation result

Bayesian Reconstruction of EIT Using Split Gibbs Sampler

Yuzhe Ling, Huihui Wang and Qingping Zhou*

Central South University, Changsha, China, 222112020@csu.edu.cn (huihuiwang@csu.edu.cn, qpzhou@csu.edu.cn)

Abstract: Our study focuses on Bayesian inference and uncertainty quantification for Electrical Impedance Tomography (EIT) image reconstruction. We propose a split Gibbs sampler that utilizes a score-based diffusion model and Laplace approximation to sample from the two sub-posterior distributions. We conduct various numerical and visual experiments to demonstrate that the proposed method leads to considerably superior reconstructions and lower uncertainty compared to state-of-the-art methods.

1 Introduction

Electrical Impedance Tomography (EIT) reconstructs inner conductivity from boundary voltages [1]. Bayesian methods offer uncertainty quantification, enhancing diagnostics [2]. Recent focus shifted to full posterior distribution computation [3]. We propose an enhanced Split Gibbs Sampler (SGS) to address EIT's computational challenges. Our Bayesian framework integrates numerical sub-sampling strategies, aiming for accurate and reliable EIT reconstructions.

2 Methods

In EIT image reconstruction, we use y to represent voltage observations and x to represent the conductivity we are interested in. With the finite element method, we can define a mapping $F: R^{n_x} \rightarrow R^{n_y}$ representing the discrete version of the forward operator

$$y = F(x) + \varepsilon, \quad \varepsilon \sim N(0, \sigma^2 I)$$

Hence, if we assume a prior for x as

$$\pi(x) \propto exp\{-g(x)\}$$

the posterior probability can be expressed as

$$p(x|y) \propto exp\{-\frac{1}{2\sigma^2}||y - F(x)||^2 - g(x)\}$$
$$= exp\{-f(x,y) - g(x)\}$$

SGS introduces an auxiliary variable z which leads to an augment distribution

$$p(x,z|y;\gamma^2) \propto exp\{-f(x,y) - g(z) - \frac{1}{2\gamma^2}||x - z||^2\}$$

and then partitions the augment distribution into likelihood and prior components

$$p(x|z,y;\gamma^2) \propto exp\{-f(x,y) - \frac{1}{2\gamma^2}||x - z||^2\} \qquad (1)$$

$$p(z|x;\gamma^2) \propto exp\{-g(z) - \frac{1}{2\gamma^2}||x - z||^2\} \qquad (2)$$

where γ is a positive parameter that controls the coupling between x and z. We iteratively samples from these approximations to obtain theoretically accurate samples. For distribution (1) Laplace approximation is applied to model it as a Gaussian distribution. For distribution (2) we use diffusion models as a denoiser to obtain the estimation of score of prior, whose logarithm is $-g$. The score can be learned by a neural network and represented by the result of the denoiser simultaneously.

$$s_\theta(x) = \frac{1}{1-\bar{\alpha}(t)}(\sqrt{\bar{\alpha}(t)}Denoiser(x) - x)$$

where $\bar{\alpha}(t)$ is a predefined parameter in diffusion models and $s_\theta(x)$ is the estimated score.

2.1 Figures and tables

In the analysis of EIT image reconstruction results, after sampling posterior samples using SGS, we calculate the average, std (standard deviation), and 90% credibility interval of the posterior samples to quantify the uncertainty of the reconstruction. The results are shown in Figure 1. Furthermore, by computing the MSE (Mean Squared Error) and SSIM (Structural Similarity Index Measure) between the average of posterior samples and the ground truth, we compare the effectiveness of the proposed method with other sampling methods (such as RTO-MH).

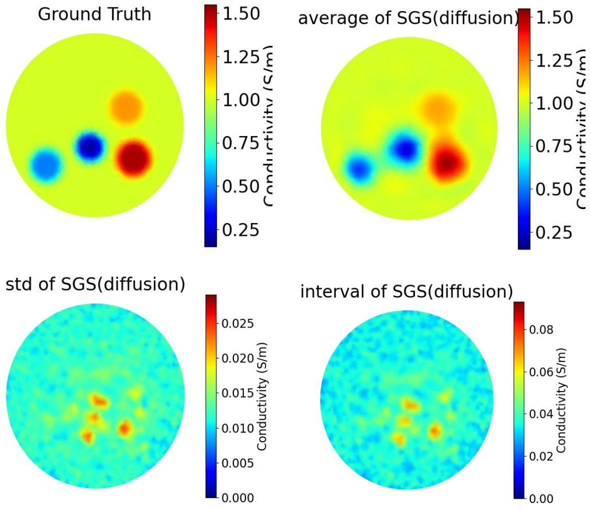

Figure 1: Sampling results of proposed method, which sequentially display the ground truth, followed by the average, standard deviation, and 90% credibility interval of the samples.

3 Conclusions

Through experimentation, we demonstrate superior accuracy and stability compared to conventional techniques like Random Than Optimize-Metropolis Hastings (RTO-MH), especially in complex sample regions. Specifically, the PnP Split Gibbs sampler exhibits superior performance, demonstrating better stability and accuracy, particularly in challenging scenarios. This underscores the effectiveness of our proposed methods in tackling nonlinear ill-posed inverse problems like EIT.

4 Acknowledgements

The work is supported by the National Natural Science Foundation of China under Grant 12101614.

References

[1] Adler, Andy and Holder, David *CRC Press*, 2021
[2] Kaipio, J. P., Kolehmainen, V., Somersalo, E., & Vauhkonen, M. Inverse Problems, 16(5), 1487 - 1522, 2000
[3] Dunlop, M. M., & Stuart, A. M., 2016

Table 1: Comparison of MSE and SSIM.

		1 anomaly	2 anomalies	3 anomalies	4 anomalies
MSE	**Proposed method**	$\mathbf{5.39 \times 10^{-4}}$	$\mathbf{7.86 \times 10^{-4}}$	$\mathbf{1.09 \times 10^{-3}}$	$\mathbf{1.73 \times 10^{-3}}$
	RTO-MH	1.07×10^{-3}	2.75×10^{-3}	2.56×10^{-3}	5.90×10^{-3}
SSIM	**Proposed method**	**0.86**	**0.92**	**0.91**	**0.92**
	RTO-MH	0.72	0.82	0.81	0.80

A Monitoring System for Muscle Training Evaluation Based on Electrical Impedance Tomography

Junwen Peng[1], Anqi Li[1], Bo Sun[2], Kai Liu[1] and Jiafeng Yao[1*]

[1]Nanjing University of Aeronautics and Astronautics, Nanjing, China, jiaf.yao@nuaa.edu.cn
[2]Xi’an University of Technology, Xi’an, China

Abstract: Outer space operations can lead to problems such as muscle loss and abnormal body fluids. Therefore, a monitoring system for electrical changes of calf muscles is proposed. The response of spatial-mean conductivity σ to muscle physiological changes after different days of muscle training was investigated. Results of the study demonstrates that σ exhibits a high sensitivity to muscle physiological changes. What’s more, the bio-impedance curve measured at different lactate concentrations can also effectively reflect the fatigue of subject's muscles.

1 Introduction

When astronauts perform space operation tasks, they will encounter abnormal conditions such as loss of muscle atrophy and disruption of humoral system due to effects of complex radiation and microgravity in space [1]. The prolonged abnormal state will result in the attenuation of astronauts' strength and the chaos of their immune system, even endangering their lives. Therefore, there is an urgent need for a real-time and non-invasive method that can quantitatively assess muscle status of astronauts.

Electrical Impedance Tomography (EIT), as a method for real-time portable functional imaging, has been widely used in biomedical detection recent years. In this work, a real-time monitoring system for physiological condition of human calf muscles based on Recurrent Neural Networks (RNN) is proposed [2].

2 Methods

Figure 1 shows the EIT system, which consists of a sensor module, an excitation/acquisition module, and an image reconstruction module.

In addition, researchers randomly selected two pairs of opposing electrodes and measured the bio-impedance curve of sink model at different lactate concentrations. Impedance curve can also reflect the fatigue of calf muscles.

3 Results

To evaluate the effects of rehabilitation training, researchers designed a 14-day experiment. Subjects' initial impedance data was recorded in advance. Then, 1-hour long-distance running and 1,000 heel lifts were performed every day to fully exercise calf muscles. After daily training, impedance data of subjects' calf muscles was measured in the same way, and spatial-mean conductivity σ was calculated. Finally, changes of σ during the experiments were plotted. To assess muscle fatigue levels, we simulated the process of human muscle fatigue by adding different numbers of lactic acid drops to the sink. Bio-impedance was used to measure the global impedance of sink model.

As shown in Fig. 2, Electrical Characteristic Responses (ECR) of M1 and M2 muscle compartments changed significantly under different days of calf muscle training. Spatial-mean conductivity σ reflects overall performance of human calf muscles, increasing with the number of training days of the subjects. It can be concluded that the internal changes inside muscles are mainly related to lactate concentration, intracellular and muscle fiber growth. Among them, lactate concentration can highly represent the effectiveness of muscle training.

Figure 3 simulates the process of muscle fatigue by dripping different amounts of pure lactic acid solution. As the concentration of lactic acid increases, conductivity of sink model also increases, and the radius of circle in Nyquist plot decreases accordingly.

4 Conclusions

In conclusion, this study confirms the ability of EIT for muscle training monitoring and gives a method to prevent muscle fatigue damage.

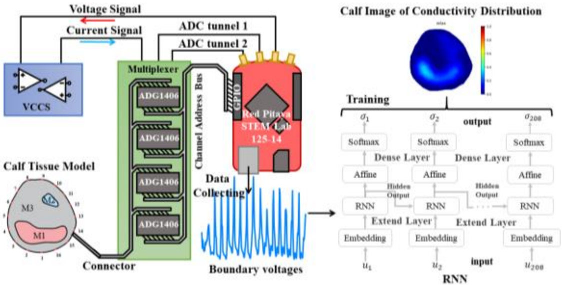

Figure 1: EIT experimental system diagram.

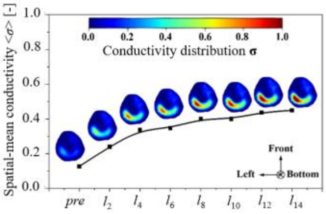

Figure 2: Image reconstructions of calf muscle after different days of muscle training.

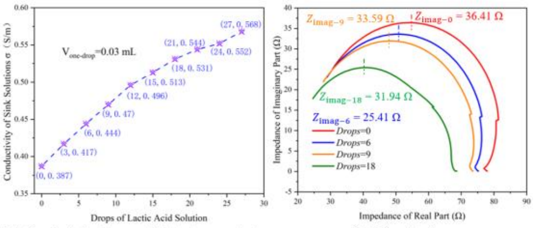

(a) Conductivity change with lactate concentration
(b) Nyquist diagram

Figure 3: Experimental results of distinguishing calf muscle fatigue.

References

[1] Elisia D. Tichy, Ji-Hyung Lee, Grant Li, Katrina N. Estep, F. Brad Johnson, Foteini Mourkioti. *npj Microgravity*,9(1): 2373-8065,2023.
[2] Sun Bo, Panji Nursetia Darma, Zhang Quan-cheng, Yao Jiafeng. *PROG BIOCHEM BIOPHYS*, 50(6): 1443-1453, 2023.

Comparison of Pulmonary Dead Space Fraction Based on Electrical Impedance Tomography, Blood Gas, and Ventilators in Lung Transplant Recipients

Hui Jiang[1], Xia Zheng[1]

[1]The First Affiliated Hospital, Zhejiang University School of Medicine, Hangzhou, China, jianghui1998@zju.edu.cn

Abstract: After lung transplantation, patients usually require postoperative care in ICU. Therefore, monitoring the graft's pulmonary function is one of the most concerning issues. EIT is a non-invasive, and real-time imaging tool. Ventilatory ratio is a bedside indicator of pulmonary ventilation disorders. We included 21 lung transplant recipients who admitted to the ICU after surgery. Bland-Altman analysis and Pearson's correlation analysis were used to comparison. We found that EIT-estimating dead space fraction was in good consistency with ventilator measurements and was positively correlated with ventilatory ratio.

1 Introduction

After lung transplantation, patients usually require postoperative care and mechanical ventilation in an intensive care unit (ICU). Therefore, one of the most concerning issues for physicians is monitoring the graft's pulmonary ventilation and perfusion function [1]. Electrical impedance tomography (EIT) is a radiation-free, non-invasive, and real-time imaging tool [2]. This study aims to compare the pulmonary dead space fraction based on electrical impedance tomography, blood gas, and ventilators in lung transplant recipients.

2 Methods

The study included the lung transplant recipients who admitted to the ICU after surgery in the First Affiliated Hospital, Zhejiang University School of Medicine. This study was approved by the clinical research ethics committee. We performed EIT for the evaluation in ventilation and profusion. An EIT belt was placed at the 4th intercostal space level around the patient's chest wall. During an expiratory hold for at least 8 seconds, a bolus of 10 mL of 10% NaCl was injected through the central venous catheter. In the EIT images, EIT-based ventilated and perfused regions were determined with 20% of the maximum pixel value as the threshold. Dead space was defined as the percentage of the area that was only EIT-based ventilated globally [3].

$$V_k > 20\% \times \max(V_K)\,, K \in lung \tag{1}$$

$$P_g > 20\% \times \max(V_G)\,, G \in lung \tag{2}$$

$$\text{EIT} - \text{Dead Space} = \frac{R_V}{(R_V + R_P + R_{V+P})} \tag{3}$$

Ventilatory ratio (VR) is an easily accessible bedside ndicator of pulmonary ventilation disorders. The formula for calculating VR was shown in Equation (4). Based on the Enghoff-Bohr equation, the dead space fraction for arterial blood gas (C-V_D/V_T) was calculated as follows. The V-V_D/V_T was measured in the ventilator device. Bland-Altman analysis was used to test the consistency of the three methods of calculating the dead space.

$$VR = \frac{MV \times PaCO_2}{PBW \times 100 \times 37.5} \tag{4}$$

$$C - V_D/V_T = \frac{PaCO_2 - ETCO_2}{PaCO_2} \tag{5}$$

3 Results

The study included 21 patients who met the inclusion criteria. We performed EIT ventilation and perfusion monitoring within 24 hours of the first admission to the ICU for these lung transplant recipients, recording parameters such as the most recent arterial blood gas and ventilator settings at the time of the EIT procedure to calculate the variables.

Bland-Altman analysis

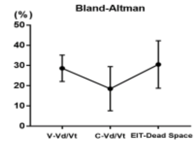

Figure 1. The line graph includes Means and 95% confidence interval (CI) in three dead space calculation.

Comparisons	Means of difference	95%CI of difference	*p*
V-V_D/V_T *vs.* C-V_D/V_T	10.108	-15.90，36.11	0.002
V-V_D/V_T *vs.*EIT-Dead Space	-1.882	-27.68，23.92	0.520
C-V_D/V_T *vs.*EIT-Dead Space	-11.990	-44.47，20.49	0.003

Figure 2. Bland-Altman analysis.

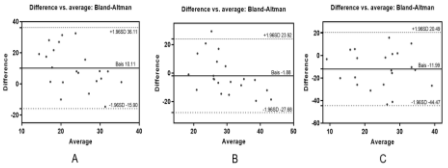

Figure 3. Bland-Altman plots in three dead space calculation.

Pearson's correlation analysis

var1	var2	correlation coefficients	*p*
VR	V-V_D/V_T	0.376	0.093
VR	C-V_D/V_T	0.025	0.914
VR	EIT-Dead Space	0.531	0.013

Figure 4. Pearson's correlation analysis.

4 Conclusions

In this study, EIT-estimating dead space fraction was in good consistency with ventilator measurements and was positively correlated with VR.

References

[1] Fuehner, T, Kuehn, C, Welte, T, et al. *Chest*, 150: 442-450, 2016.
[2] Frerichs, I, Amato, M, Tingay, D, et al. *Thorax* 72: 83-93, 2017.
[3] He H, Chi Y, Long Y, et al. *Crit Care*; 24: 586, 2.

Chest EIT based on Lagrange Multipliers reconstruction

Nima Seifnaraghi[1] and Richard Bayford[1]

[1]Middlesex University, London, UK, n.seifnaraghi@mdx.ac.uk, r.bayford@mdx.ac.uk

Abstract: A Lagrange Multiplier reconstruction method has previously been shown to provide some advantages in terms of producing image even with loss of some boundary data, however, it was limited to circular domains. We present an adaption of this method for adult human chest. The results of the reconstruction are compared with Gauss-Newton reconstruction method.

1 Introduction

The motivation behind this study was to create a fast, reliable algorithm which could be applied in practical situations without the necessity of adjusting hyper parameters to achieve an interpretable reconstructed image.

We are also exploring whether the Lagrange Multiplier approach could be a method that would enable reconstruction even if a segment of the boundary data has been lost during data collection on patients.

In EIT the gradient boundary potentials are distributed along the curved equipotential lines at each current injection. Whilst these borderlines can be mathematically calculated via conformal mapping when the domain is circular, such lines are not easy to formulate for irregular shapes like an adult thorax. We have approached this by estimating these paths numerically using FEM, However, this in turn would be adding the dependency to how fine the applied mesh is able to resolve these paths. Here, a rectangular grid model of 64x64 pixels has been chosen and applied to both reconstruction methods in order to null out the effect of this issue on the results.

2 Methods

Assuming a resistivity image $\rho(x,y)$ the following minimization problem can be defined via considering a variance model for the resistivity image [1]:

$$\mathbb{C} = \iint \frac{1}{2}\rho(x,y)^2 dxdy \qquad (1)$$

subject to the following boundary constraints:

$$g_{ki} = \int_{A(\omega_{ki})}^{B(\omega_{ki})} \int_{\mu_i}^{\mu_{i+1}} \rho(x,y)\sigma_k(x,y)d\mu_{ki}d\omega_{ki} \qquad (2)$$

where g_{ki} is the normalized boundary potential measured at the k^{th} projection and the i^{th} measurement. Whereas σ_k represents the weighted current density on equipotential strip ki^{th}. Lagrange multipliers can help integrate the constraints into the optimization problem:

$$\mathbb{C} = \iint C(x,y)dxdy + \int \sum_{k=1}^{N} \lambda_k \left(g_{ki} - \int_{A(\omega_{ki})}^{B(\omega_{ki})} \rho(x,y)\sigma_k d\mu_{ki}\right) d\omega_{ki} \qquad (3)$$

with λ_k indicating continuous 1D Lagrange multipliers at projection k. Solving (3) via taking derivatives with respect to $\rho(x,y)$, the resistivity image can be found:

$$\rho(x,y) = \sum_{k=1}^{N} \lambda_k \ \sigma_k \qquad (4)$$

Inserting (4) into (2) the linear equation to find the unknown multipliers gives:

$$g_{ki} = \int_{A(\omega_{ki})}^{B(\omega_{ki})} \int_{\mu_i}^{\mu_{i+1}} \sum_{n=1}^{N} \lambda_n \ \sigma_n(x,y)\sigma_k(x,y)d\mu_{ki}d\omega_{ki} \qquad (5)$$

3 Results

A 16 array of electrodes were used for both the simulations and to collect human data. An adjacent current pattern was used given 208 measurements. The simulated voltages were generated by introducing two objects with half of the conductivity of the background at 3.5 cm far from the origin with an extra 10% noise on the data, whereas the human data were collected using stick on ECG electrodes equally spaced around the thorax at the level beneath the nipple line mark. The subject was a healthy male at 40 years of age. The resistivity change within a tidal breath is plotted by selecting the frames corresponding to the beginning and end of an expiration. The overlaid lung contours have been drawn according to the MRI scans of the subject in order to present a measure of the spatial accuracy of the reconstructed images.

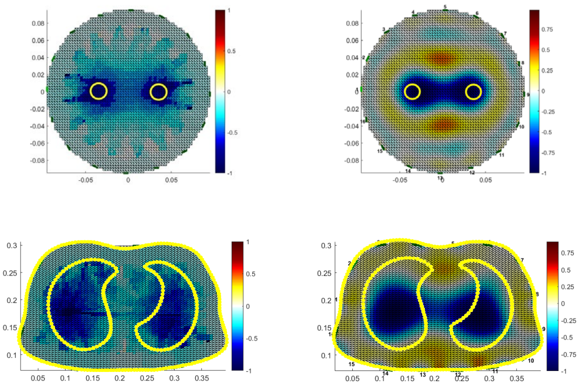

Figure 1: Left panels reconstructed using Lagrange multipliers whereas right column was created via one-step Gauss-Newton with hyperparameters as 1e-3 and 1e-4 respectively.

4 Conclusions

The accuracy at localizing the objects, (circle centers on top row and lungs at the bottom) which becomes significant when computing clinical parameters dependent on a predefined region of interest (ex. silent spaces), in addition to no requirement for hyperparameter adjustment during image reconstruction, make this method a suitable candidate for chest EIT.

5 Acknowledgements

Work was funded by EPSRC under grant no EP/T001240.

References

[1] R. Bayford, Y. Hanquan, K. Boone, and D. S. Holder, *Physiol Meas*, vol. 16, no. 3A, 1995.

Low-rank plus sparse matrix decomposition for 3D dynamic Electrical Impedance Tomography

Tianchen Zhao[1], Tao Zhang[1], Xiuyan Li[1] and Qi Wang[1]

[1]School of Electrical and Information Engineering, Tiangong University, Tianjin,China, zhaotianchen@tiangong.edu.cn

Abstract: The inverse problem of 3D dynamic-EIT shows serious ill-posedness and indeterminateness, while the real-time information is not considered in the continuous reconstruction methods. To address the abovementioned inferiority of the dynamic EIT, a low-rank plus sparse (L+S) imaging algorithm is proposed. In specific, the reconstruction task is split into background recovery and dynamic components enhancement. nuclear norm and l₁-norm are implemented for low-rank information constraint and sparse structure representation, respectively. The reconstructions show that the L+S model has good performance in representing the conductivity distributions concerning the time variation and 3D structure of lung respiration.

1 Introduction

The time-dynamic 3D EIT is a promotional imaging modality in medical applications, which could demonstrate the expensive anatomical and time-various features in lung respiration. According to [1], the non-obvious changed conductivities show low-rank characteristics in the observation domain, while the electrical parameters of the lungs exhibit rapid changes in the respiration process corresponding to sparse features. In this paper, we propose a low-rank plus sparse (L+S) imaging method for reconstructing the temporal-wise conductivities and spatial-wise lung structure features simultaneously. The numerical experiments show that the proposed scheme can significantly improve the 3D dynamic EIT reconstruction.

2 Methods

The image reconstruction of the EIT inverse problem shows an ill-posed nature [2], which could be simply solved utilizing the regularization constraint. This problem could be transferred as an optimization framework, which is described as:

$$\begin{cases} min\frac{1}{2}\|\mathcal{J}\Delta\sigma-\Delta V\|_2^2+R(\Delta\sigma) \\ \Delta\sigma=(\Delta\sigma_1,\Delta\sigma_2,\dots,\Delta\sigma_j) \end{cases} \quad j=1,2,\dots,t \quad (1)$$

Here, $\mathcal{J}$ is sensitivity matrix, $\Delta\sigma$ is the time-differential conductivity matrix., ΔV represents the time-differential voltages. $\Delta\sigma_j=\sigma_j$-σ_0 is the difference in conductivity at different moments in time.

The reconstruction problem Eq. (1) is performed by solving the following minimization problem described as Eq. (2):

$$min\|L\|_*+\lambda\|TS\|_1 \quad s.t.\ \Delta\sigma=L+S \quad (2)$$

where, $\|L\|_*$ is the nuclear norm of the matrix L, $\|TS\|_1$ is l_1-norm of the matrix S after the sparse transformation T. λ is tuning parameter.

Based on Eq. (1) and (2), the optimization problem can be rewritten as a relaxed constrain problem with the hybrid regularization pattern, which is demonstrated as:

$$min\frac{1}{2}\|\mathcal{J}(L+S)-\Delta V\|_2^2+\lambda_L\|L\|_*+\lambda_S\|TS\|_1 \quad (3)$$

Here, λ_L and λ_S are the weights of the regularisation terms, we approximate the optimal solution step by step by the following iterative process:

$$\begin{cases} L_k=SVT_{\lambda_L}(\Delta\sigma_{k-1}-S_{k-1}) \\ S_k=T^{-1}(\Lambda_{\lambda_S}(T(\Delta\sigma_{k-1}-L_{k-1}))) \\ \Delta\sigma_k=L_k+S_k-\mathcal{J}^T*(\mathcal{J}(L_k+S_k)-V) \end{cases} \quad (4)$$

Λ_λ is the soft threshold function, $(\Lambda_\lambda(x)=\frac{x}{|x|}\max(|x|-\lambda,0)$ and SVT is the singular value threshold. For the lung respiration data, we set up 30 iterations to process the continuous respiration moments.

3 Conclusions

We demonstrate four states of expiration using simulation models, and the reconstructions are shown in Fig. 1. The method can effectively reconstruct the conductivity distribution corresponding to the respiratory states (t_1,t_2,t_3,t_4) at different moments relative to the conjugate gradient algorithm.

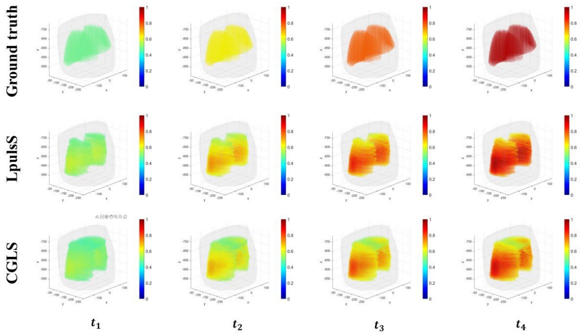

Figure1: Results of 3D lung respiratory reconstruction

The reconstructed image quality metrics (RMSE and SSIM) are shown in Table 1. It can be concluded that the L+S method can be effectively applied to the study of dynamic 3D EIT and provides a new monitoring method for practical clinical applications.

Table 1: The reconstructed image quality metrics

Metrics	t_1	t_2	t_3	t_4
RMSE(CGLS)	0.716	0.689	0.687	0.683
RMSE(LplusS)	0.485	0.483	0.464	0.463
SSIM(CGLS)	0.513	0.547	0.552	0.558
SSIM(LplusS)	0.738	0.740	0.775	0.787

4 References

[1] Otazo R, Candes E, Sodickson D K, Magnetic resonance in medicine, 73(3): 1125-1136, 2014

[2] Frerichs I, Schädler D, Becher T. Current Opinion in Critical Care, 30(1): 43-52, 2024

An Endoscopic Convex Electrical Impedance Tomography Sensor for Soft Robot in Early Gastric Cancer Identification

Songpei Hu[1], Bin Zou[1], Zhongwei Wang[1], Kai Liu[1] and Jiafeng Yao[1*]

[1]Nanjing University of Aeronautics and Astronautics, Nanjing, China
*jiaf.yao@nuaa.edu.cn

Abstract: An endoscopic Convex Electrical Impedance Tomography (cEIT) Sensor for early gastric cancer Identification is proposed. Experimental results shows that cEIT sensors can detect cancer depths up to 46% of wall thickness. The average absolute relative difference of infiltration depth assessment was 0.18, effectively identifying Tis and T1 stage cancers.

1 Introduction

Gastrointestinal cancer has always been a daily concern for people. Endoscopic cancer detection methods such as indocyanine green (ICG) have disadvantages of invasiveness, inconvenient detection. Electrical impedance tomography (EIT) can detect cancer based on the differences in electrical characteristics of tissue lesions. Ye et al. designed a flexible EIT sensor with three layers of electrodes and achieved 3D EIT imaging through an improved U2 Net neural network[1]. However, the combination of soft robots and single con-vex array electrodes for 3D EIT of gastric cancer has not been studied yet.

2 cEIT sensor and detection methods

2.1 cEIT sensor fabrication

The cEIT sensor consists of two parts: a substrate and a convex concentric array electrode, as shown in Figure 2(a). A concentric array electrode with a "1+6+9" ring layout was fabricated on the surface of FPC.

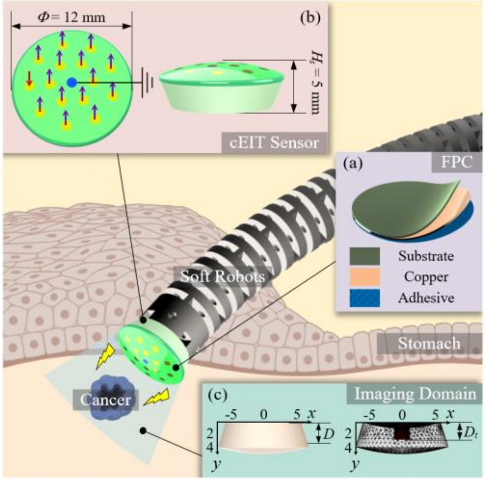

Figure 2: cEIT sensor for detecting early gastric cancer; (a) the fabrication of sensor; (b) cEIT incentives and measurement methods; (c) finite element mesh division of cEIT field.

2.2 The incentive and measurement modes of cEIT

Figure 2 shows the single electrode excitation and acquisition modes of cEIT. Selecting a single electrode in sequence for excitation, while collecting the potentials of the other electrodes, a total of 15 × 14 = 210 potential cycles were obtained. Finally, based on 210 potentials, the conductivity distribution in the field is calculated by equal:

$$\mathbf{\Delta\sigma} = (\mathbf{S}^{\mathrm{T}}\mathbf{S} + k_t \cdot \mathbf{I} + k_n \cdot \mathbf{D})^{-1} \cdot \mathbf{S}^{\mathrm{T}} \cdot \mathbf{\Delta V} \qquad (1)$$

2.3 cEIT experiment of early gastric cancer

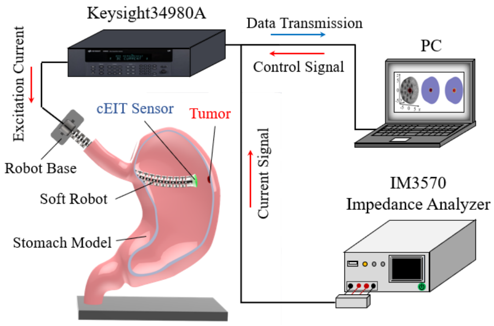

Figure 2: Experimental equipment diagram

Figure 2 is a schematic diagram of the experimental equipment. PC controls the Keysight 34980A gate switch to excite the 0.1 mA AC signal from IM3570 to the area where the cancer is located.

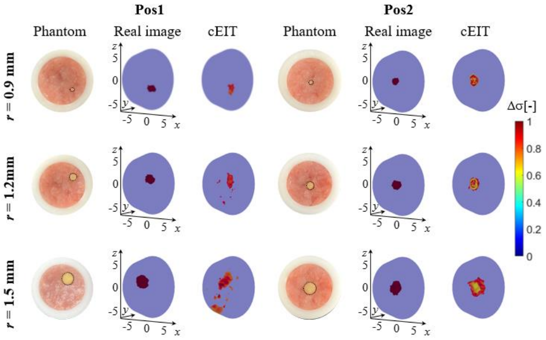

Figure 3: cEIT of gastric cancer size and location.

The cEIT experimental results are shown in Figure 7, which shows the partial grid in the cEIT reconstructed image with a relative conductivity change greater than 0.6. The average *ICC* of cEIT at Pos1 is 0.461, and the average *ICC* of cEIT at Pos2 is 0.624. The maximum depth that cEIT sensors can detect is 1.84 mm, which is 46% of the wall thickness.

3 Conclusions

The cEIT sensor can be applied to early screening of gastric cancer, providing a new detection method for in vivo and real-time detection of gastric cancer.

4 Acknowledgements

Thank you to Mr. Xiaowu Sun and Mr. Chao Wang for providing technical support.

References

[1] Ye, M.; Zhou, T.; Li, X.; Yang, L.; Liu, K.; Yao, J., U2-Net for 3D Electrical Impedance Tomography with Combined Electrodes. IEEE sensors journal 2023, 23 (5), 1-1.

A Magnetic Induction Phase Sensor for Cerebral Hemorrhage Detection

Jie Liu[1], Mingsheng Chen[1]

[1]Army Medical University, Chongqing, China, JieLiures@163.com

Abstract: To enhance the sensitivity of magnetic induced phase detection signals and quantify hematoma detection, a zero-flow sensor was proposed. The uniform primary magnetic field and its counteraction were analysed. Phase change responses to solutions of varying conductivities and rabbits with cerebral haemorrhage were investigated. The proposed sensor provides a more sensitive method for the quantitative detection of intracranial haemorrhage.

1 Introduction

Magnetic induction phase detection technology is a promising non-invasive method for cerebral haemorrhage (CH) detection. A symmetric cancelation-type sensor [1], the Bx-sensor [2] and the gradiometer [3] were proposed to improve detection sensitivity by the primary field counteraction. Nonetheless, most of these efforts do not consider the ununiform and divergent main magnetic field in detection area. A zero-flow sensor was proposed to better quantify the hematoma and improve the detection sensitivity.

2 Methods

2.1 Detection principle

The transmitting coil excited by a sinusoidal signal generates the primary magnetic field (B). The receiving coil detects the superimposed magnetic field (B+ΔB) and transmits this signal to the data processing module which calculates the phase difference ($\Delta\theta$) between the reference and detection signals.

$$\Delta\theta = \theta_{\text{det}} - \theta_{\text{ref}} \qquad (1)$$

Here, θ_{det} denotes the phase of the detection signal from the receiving coil, and θ_{ref} signifies the phase of the reference signal.

2.2 Design of the sensor

The sensor model comprised the excitation and detection coils. The excitation coil was composed of end-rings (ERs), legs and capacitors inserted into the ERs between conductive legs. The design details of the excitation coil are shown in Table 1. The detection coil with an inner diameter of approximately 84 mm was wound using 10 turns of copper wire (diameter 1mm). In this study, radio frequency electronic feedback circuits were constructed to match the impedance. The schematic diagram of the sensor is presented as Figure 1.

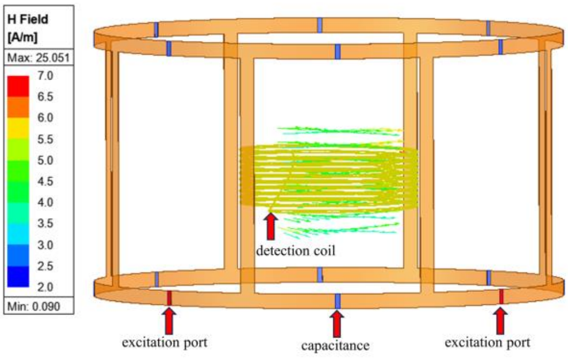

Figure 1: Schematic diagram of the sensor

2.3 Experimental system

The function signal generator generated two orthogonal sinusoidal signals of equal amplitudes at the same frequency. The detection signal was inputted into the NI high speed data acquisition card. The self-programmed data processing module in LabView was used to perform phase difference calculation.

3 Conclusions

The uniform primary magnetic field with higher magnetic field strength and its counteraction were achieved. The experimental results for solutions with different conductivities showed that the sensitivities were 2.01, 1.22 and 6.3 times higher than those for low-pass birdcage coil [4], planer gradiometer [3] and co-axil coil, respectively. The adjusted R^2 of the first-order linear fit with no weighting between phase difference and liquid volume was 0.98. The linearity was improved than sensors mentioned above. The proposed sensor provides a more sensitive method for the quantitative detection.

4 Acknowledgements

This work is supported by the National Natural Science Foundation of China (62171444).

References

[1] Gui Jin, Sun Jian, Qin Mingxin *Biosensors and Bioelectronics*, 52: 374-378, 2014.

[2] Watson S, A Morris, RJ Williams *PhysiolMeas*, 25(1): 271-279, 2004.

[3] Yixuan Chen, Tan Chao, Zhao Shu *IEEE Trans. Instrum. Meas*, 71: 1-11, 2022.

[4] He Z, Chen J, Chen M *MED PHYS*, 50(4): 2565-2576, 2023.

Table 1: Details of the excitation coil

Frequency	Legs number	Legs length	Legs width	ERs radius	ERs widths	Thickness	Capacitor
60 MHz	8	80 mm	5mm	80mm	5mm	0.1mm	100 pF

Analyse Intra-abdominal Hemorrhage Electrical Characteristics by Electrochemical Impedance Spectroscopy

Zihan Zhao[1], Jingshi Huang[2], Hui Feng[3], Tong Zhao[1] and Bo Sun[1]

[1]Xi’an University of Technology, Xi’an, China, bosun0814@gmail.com
[2]Shanghai University of Engineering Science, Shanghai, China
[3]The Affiliated Jiangning Hospital of Nanjing Medical University, Nanjing, China

Abstract: The electrical characteristics of abdominal haemorrhage model is investigated in order to provide a preliminarily assessment of the electrical specificity for detecting intra-abdominal haemorrhage by electrical impedance tomography (EIT). In this study, 100 ml of bovine blood is sequentially injected into the abdominal cavity phantom in 4 ml increments to mimic sustained intra-abdominal haemorrhage. A 16-electrode EIT sensor is used to investigate the electrical characteristics of the abdominal cavity phantom. The results show that the measured target impedance values decreased significantly as the blood volume increasing in the tissues within the model. Significantly, the impedance difference with increasing blood volume is most pronounced at a frequency of 430 kHz.

1 Introduction

- Intra-abdominal haemorrhage is typically insidious with a lack of continuous bedside monitoring for the detection of haemorrhagic events [1].
- Electrochemical impedance spectroscopy (EIS) allows the detection of the response of electrical characteristics of human tissues in different physiological conditions [2].

1.1 Design of EIS experiment

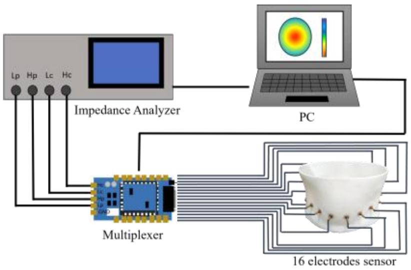

Figure 1: The data acquisition system.

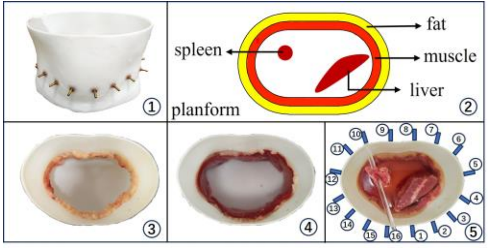

Figure 2: The mimicked abdominal cavity phantom.

Figure 1 shows the data acquisition system, which consists of an abdominal cavity phantom, an impedance analyser, a multiplexer, and a personal computer. In this study, 16 electrodes around the abdominal cavity model are excited sequentially using the adjacent method, as shown in **figure 2**. The sweep frequency is from 100 Hz to 10 MHz. The excitation current is 1 mA. Firstly, 4 ml of bovine blood is gradually injected into the beef block which mimics the spleen until a total volume of the bovine blood reached 48 ml. Data acquisition is performed after each blood injection. Afterwards, the saline water is replaced and the bovine blood is gradually injected into the beef block which mimics the liver by repeating the above-mentioned steps.

1.2 Experimental detection method

EIS is a non-invasive, radiation-free, portable measurement method that enables prolonged bedside real-time monitoring. In this study, the EIS method is used to investigate changes in electrical characteristics caused by abdominal haemorrhage by performing frequency sweep measurements on an abdominal cavity phantom under conditions where different amounts of bovine blood are added. Thus, the theoretical and technical basis is provided for the detection of abdominal haemorrhage by using EIT.

2 Results

Figure 3 shows the relationship between electrical impedance value Z and measurement frequency f under different blood volume injected into the beef blocks mimicing the spleen (figure 3 (a)) and liver (figure 3 (b)). The results show that the Z decreased significantly as the blood volume increasing in the mimiced spleen and liver. Moreover, at a measurement frequency f_c = 430 kHz, the Z reduction rate reached a maximum with increasing blood volume.

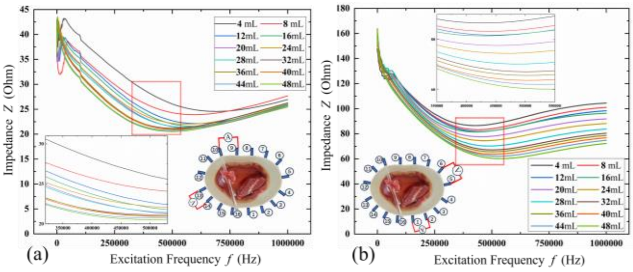

Figure 3: Impedance vs. frequency plot (a) Bovine blood injected into the spleen (b) Bovine blood injected into the liver

3 Conclusions

EIS allows the detection of changes in electrical characteristics within the abdominal cavity phantom through the fat and muscle layers.
The electrical characteristics of the abdominal cavity change in response to intra-abdominal haemorrhage.

References

[1] G. A. Franklin, and S. R. Casós, “Current advances in the surgical approach to abdominal trauma,” *Injury*, vol. 37, no. 12, pp. 1143-1156, Dec. 2006.

[2] Kemp, Neil T. *IEEE Sensors Journal* 21, no. 20 (October 15, 2021): 22232-45.

A universal lung modeling method for 2D/3D EIT imaging based on CT scan

Sirui Qiao[1], Zeyi Jiang[1], Yi She[1], Qin Liu[1], Huawei Wu[2], Shan Xue[2], Zhibin Kong[3] and Yixin Ma[1]
[1]Shanghai Jiao Tong University, Shanghai, China, y.ma@sjtu.edu.cn
[2]The 6th People' s Hospital, Shanghai Jiao Tong University School of Medicine, Shanghai 200235, China
[3]Renji Hospital, Shanghai Jiao Tong University School of Medicine, Shanghai, China

Abstract: The goal of this study is to develop a universal method for the construction of finite element models from lung CT images. The method is introduced. Experimental results show that this method can successfully build FEM model from 95% of NSCLC-Radiomics collection from The Cancer Imaging Archive (TCIA) without necessitating manual intervention.

1 Introduction

The construction of a finite element model is an indispensable part of most EIT imaging algorithms [1]. Researches suggest that precise FEM model contributes to the reduction of artifacts and enables a more accurate localization of conductivity changes in EIT image [2], hence, build FEM model for individual patient became a research trend in EIT technique [3]. Furthermore, image reconstruction methods based on deep learning relay on large amount of FEM models to building up dataset for model training [4]. Therefore, a universal method to construct FEM model from CT images is highly demanded. In this paper, we present a universal lung modelling method based on an adaptive thresholding segmentation approach coupled with enhanced image morphological processing, to efficiently adapts to a wide range of CT images for the precise extraction of thoracic and pulmonary contours. The modelling method and experimental results are presented.

2 Methods

As depicted in Fig.1, the proposed method including segmentation, contour extraction, object modelling and Mesh generation, in total four steps.

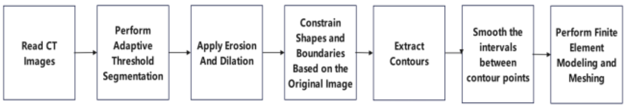

Figure 1: Methodology flow.

The adaptive threshold segmentation is depicted in Equation 1,

$$Hu > 0.4 \times \text{median} \tag{1}$$

where $median$ denotes the median value of Hu below zero in the CT images.

Following the initial segmentation processing of CT images, morphological operations like erosion and dilation are used to repair lung/chest regions and smooth lung/chest boundaries. Concurrently, we use the original image as a mask to ensure that the processed image retained its original shape and boundaries. Chest/lung contour data are then extracted by calculating the connected regions of the image, then spline interpolation is applied to uniform the intervals between neighbouring contour points. The finite element mesh is then constructed using the open-source software Gmsh [5]. We adjusts the edge lengths of each elements at and around the electrodes to attain varying degrees of grid uniformity, simultaneously controlling mesh density to meet user requirements. The 2D and 3D FEM mesh examples are shown in Fig. 2 and Fig. 3 respectively.

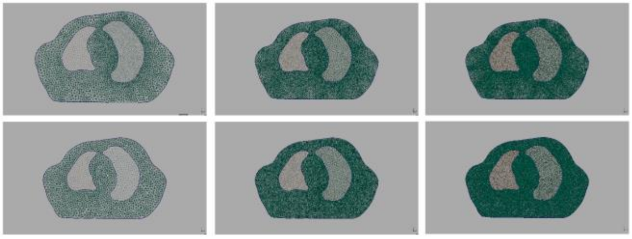

Figure 2: 2D FEM meshes. The first row shows non-uniform meshes, while the second row shows uniform meshes. In each row, from left to right, the mesh density increases.

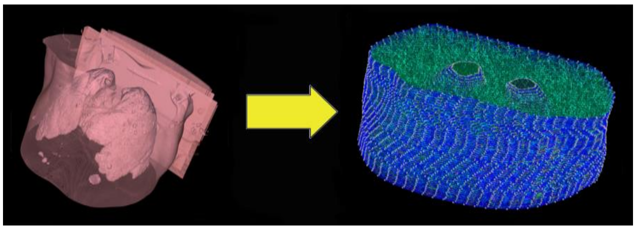

Figure 3: A 3D FEM meshing.

3 Conclusions

This study developed a method with notable versatility to generate EIT FEM model from CT images. The dataset used in the study is the NSCLC-Radiomics collection from The Cancer Imaging Archive (TCIA), which encompasses 422 subjects of CT scans. The proposed method can precisely segment 404 of these CT scans, corresponding to a success rate of over 95%. The method is coded with an intuitive graphical interface, and accessible on GitHub.

4 Acknowledgements

This study is supported by Shanghai Jiao Tong University joint Clinic-Engineering program (YG2021QN37).

References

[1] WRB Lionheart Physiol. Meas.25:125-142,2004
[2] A Zifan, P Liatsis, H Almarzouqi Computers in Biology and Medicine, 107:97-108,2019
[3] MZ Zhang, S Xue, H Qin, ZB Kong, YX Ma Conf IST, p.6, Kaohsiung, Taiwan, Aug. 2021
[4] T Zhang, X Tian, XC Liu, JA Ye, F Fu, XT Shi, RG Liu, CH Xu Front. Bioeng. Biotechnol, 10:1019531,2022
[5] C Geuzaine, JF International Journal for Numerical Methods in Engineering, 79:1309-1331, 2009
[6] Aerts et. al Data From Data From NSCLC-Radiomics (version 4) The Cancer Imaging Archive.

Deep Generative Model-Integrated 3-D EIT Image Reconstruction

Ke Zhang[1], Rui Guo[1], Zhichao Lin[1], Maokun Li[1], Fan Yang[1], Shenheng Xu[1], Aria Abubakar[2]

[1]Department of Electronic Engineering, Beijing National Research Center for Information Science and Technology (BNRist) ,
Institute of Precision Medicine, Tsinghua University, Beijing 100084, China, maokunli@tsinghua.edu.cn

[2] Schlumberger, Houston, TX 77056 USA

Abstract: We transform the 3-D time-difference EIT imaging into a constrained optimization problem. A deep generative model, trained on a 3-D lung dataset, is used to constrain the unknowns through two different functionals. Numerical results demonstrate the algorithm's effectiveness in imaging ventilation and pulsatility activities in the thorax.

1 Introduction

EIT image reconstruction is a challenging task due to its ill-posed nature and it usually requires prior information to improve accuracy [1, 2]. To address this, we recently proposed a deep generative model-based framework for 3-D time-difference lung imaging [3]. This framework transforms the EIT image reconstruction into a constrained optimization problem, where the unknown conductivity is constrained by a deep generative model through user-designed relationships. In this paper, we demonstrate the effectiveness of this framework using two kinds of constraints: one is linear and the other is based on cross-gradients (CG) functional, for 3-D lung ventilation and pulsatility imaging.

2 Methods

We formulate the EIT difference image reconstruction into the following constrained minimization problem

$$\begin{aligned} &\underset{\delta\sigma}{\arg\min}\, ||\mathbf{J}_0\delta\sigma - \Delta\mathbf{d}||^2 \\ &s.t. \quad \Phi(\delta\sigma, \mathcal{D}(\mathbf{z})) = \mathbf{0}, \end{aligned} \tag{1}$$

where $\mathbf{J}_0$ is the Jacobian matrix of EIT forward model; $\delta\sigma$ and $\Delta\mathbf{d}$ are the difference conductivity and difference voltage between two time points, respectively; $\mathcal{D}(\mathbf{z})$ is a deep generative model where $\mathbf{z}$ is the input latent code.

Here we apply two kinds of constraints:

$$\Phi = \begin{cases} \nabla[\delta\sigma - \mathcal{D}(\mathbf{z})] & \text{(linear)} \\ \nabla(\delta\sigma) \times \nabla(\mathcal{D}(\mathbf{z})) & (\mathrm{cross-gradients}), \end{cases} \tag{2}$$

where ∇ and $\times$ are the gradient and cross-product operators, respectively. To solve the above problem, we employed an optimization scheme in [3] which is based on the alternating direction method of multipliers (ADMM).

The deep generative model was implemented by a 3-D variational autoencoder (VAE). The VAE is comprised of an encoder $\mathbf{z} = \mathcal{E}(\mathbf{x})$ and a decoder $\hat{\mathbf{x}} = \mathcal{D}(\mathbf{z})$, where $\mathbf{x}$ is the input image and $\hat{\mathbf{x}}$ is the decoded image. The training dataset was constructed by segmenting the lungs from the CT images of 165 patients. After a data augmentation process, a total number of 50,040 3-D lung images (no heart information) were generated for training. After training, the decoder $\mathcal{D}(\mathbf{z})$ was integrated into (1). More details on the training dataset and VAE architecture can be found in [3].

3 Results

The proposed algorithms was tested using synthetic data from 3-D lung models and a two-loop excitation-measurement pattern [3]. We simulated three cases: (1) ventilation-healthy lungs, (2) pulsatility-healthy lungs, and (3) pulsatility-left inferior pulmonary embolism. The reconstructed images and the ground truths are shown in Fig. 1. It can be seen that the algorithm with cross-gradients constraint was capable of accurately imaging both the lungs and the heart in healthy and pathological conditions. In contrast, the algorithm with linear constraint only succeeded in reconstructing the lungs since the training dataset only contains the lungs.

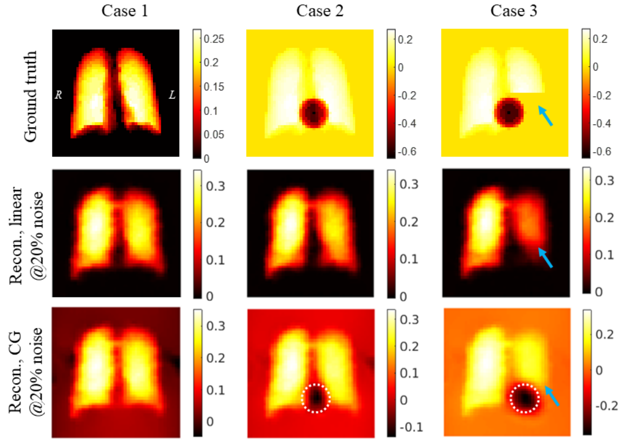

Figure 1: Reconstructed images (coronal view) using synthetic data (20% white Gaussian noise) from three lung models. Blue arrows indicate defects in lung perfusion. White circles indicate regions of the reconstructed heart. CG: cross-gradients.

4 Conclusions

When trained using only the lung dataset (no heart information), the algorithm with cross-gradients constraint was able to reconstruct the lungs while preserving the heart at the same time. It reduces the complexity in dataset construction, and provides a potential choice for both ventilation and pulsatility imaging.

5 Acknowledgements

This work was supported by the National Science Foundation of China (61971263) and the Tsinghua Precision Medicine Foundation.

References

[1] K Zhang, M Li, F Yang *IEEE Transactions on Biomedical Engineering*, 66:2470-2480, 2019

[2] K Zhang, R Guo, M Li *IEEE Transactions on Biomedical Engineering*, 68:1360-1369, 2020

[3] K Zhang, L Wang, R Guo *IEEE Transactions on Instrumentation and Measurement*, 72:4501212, 2023

Comprehensive Dataset for EIT Grounded in Human Physiology

Zeyi Jiang[1], Sirui Qiao[1], Huawei Wu[2], Shan Xue[2], Zhibin Kong[3] and Yixin Ma[1]
[1]Shanghai Jiao Tong University, Shanghai, China, y.ma@sjtu.edu.cn
[2]The 6th People' s Hospital, Shanghai Jiao Tong University School of Medicine, Shanghai 200235, China,
[3]Renji Hospital, Shanghai Jiao Tong University School of Medicine, Shanghai, China

Abstract: Deep-learning has demonstrated superior performance in EIT image reconstruction. The most significant challenge of these methods is the requirements of vast datasets for model training, while the acquisition of large-sets of *in vivo* data is not convenient. In this study, we establish an EIT dataset from CT scans, to support large, static/dynamic, and multi-frequency EIT AI algorithms. The method and the results are presented.

1 Introduction

Deep learning significantly enhances medical tomographic images, especially with SOTA AI models. But it heavily depends on the quality of datasets. Large-scale EIT datasets based on real human subjects are seldom explored in previous research, with existing data falling into three categories: simulation-based datasets from Eidors or COMSOL, laboratory measurements from a limited number of individuals. These datasets struggle to meet the demands of applying large AI models on actual human body data. In this study, targeting lung EIT, we utilize the LIDC-IDRI dataset [1] to create the SJTU-Thorax-EIT dataset, theoretically enabling the generation of over factorial 1000 cases through pre-processing, augmentation, and meshing. We detail our methods and results.

2 Methods

The LIDC-IDRI dataset is not inherently suitable for training EIT-related deep learning models as CT scans imaging density distribution while EIT imaging conductivity property. The high spatial resolution and contrast of CT images also surpass the current capabilities of EIT technique. Moreover, CT scans produce static, snapshot images, unlike EIT's dynamic and sustained monitoring. Therefore, we have devised specialized methods to tailor the CT dataset for use with deep learning-driven EIT models.

2.1 Pre-processing

Raw CT data (Sinogram) is reconstructed into a digital model, Fig.1(a). The lung's complex contours are shaped by bronchi and fissures, which can complicate EIT image reconstruction by increasing computational demand and reducing algorithm flexibility. To address this, we simplify by extracting smooth external contours of the thorax and lungs for FEM models and EIT dataset development. This involves segmenting the thorax and lung mask (Fig.1(b)) and obtaining the lung contour's concave hull, depicted in Fig.1(c).

2.2 Data augmentation

The original CT dataset lacks both quantity and compatibility with EIT application scenarios. To remedy this, we use Data Mashup and Dynamic Image Simulation (Fig.1(e) and (f)) to adapt the CT dataset for lung ventilation monitoring with EIT. Data Mashup cross-combines thoracic and pulmonary contours from various individuals, while Dynamic Image Simulation scales the lung mask to mimic breathing.

2.3 Forward problem and Inverse problem

After step 2.2, we utilize Gmsh to generate meshes, then we calculate the lung's conductivity at various frequencies based on [2]. We obtained measured boundary voltages, leading to voltage-conductivity distribution pairs, Fig.1(d). We confirmed the discretization's accuracy and the direct problem's precision via mesh independence tests, resulting in an EIT dataset suitable for real human bodies.

For inverse problems requiring a different mesh from forward problems, and subjects often lack *in vivo* data, we propose the 'EigenChest' model (Fig.1(h)) as a solution.

3 Conclusions

We created thorax and lung masks for all over 1000 cases in the LIDC-IDRI dataset, and used dynamic generation to train large deep learning algorithms. Each case's mask has unique identifiers, allowing us to randomly generate 1000 pairs of voltage-conductivity distribution data for every training batch to effectively train the deep learning models.

4 Acknowledgements

This study is supported by Shanghai Jiao Tong University joint Clinic-Engineering program (YG2021QN37).

References

[1] Samuel et al. *Medical Physics*, Vol. 38, 915-931, 2011
[2] S. Gabriel et al. *Gabriel, and biology, vol. 41, no. 11, p. 2251, 1996*

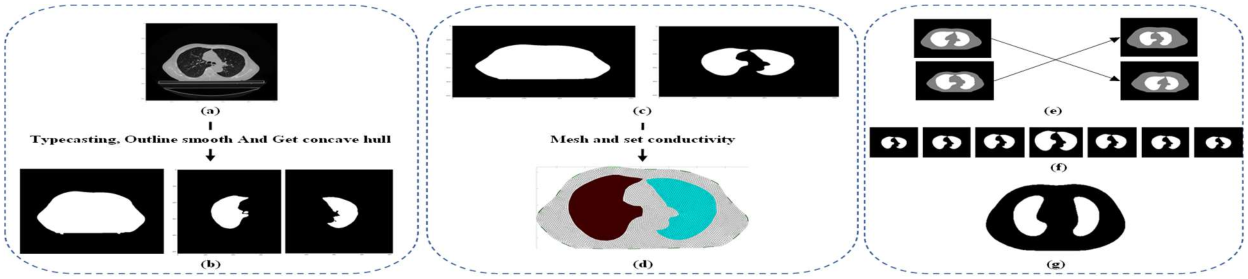

Figure 1: (a) Cross-sectional views of the thorax (CT scans) (b) Unmodified outline of thorax and lungs, (c) Pre-processed mask, (d) Mesh and Set condivity, (e) Data Mashup, (f) Dynamic Image Simulate, (g) EigenChest.

Quantitative Metrics for Evaluating V/Q Matching in EIT Images

Yuxuan Cai[1], Ke Zhang[1], Xin Zhang[2], Hongyu Duan[2], Maokun Li*[1], Fan Yang[1], Shenheng Xu[1]

[1]Department of Electronic Engineering, Beijing National Research Center for Information Science and Technology (BNRist), Institute of Precision Medicine, Tsinghua University, Beijing, 100084, China, maokunli@tsinghua.edu.cn

[2]Infivision Medical Imaging Technology Co., Ltd., Beijing, China

Abstract: This study introduces a set of metrics, termed as matching index, dead space index and shunting index, to quantitatively assess the ventilation-perfusion (V/Q) matching based on EIT lung images. The proposed metrics take into account both the intensity and distribution of the assessed images.

1 Introduction

EIT can provide insights into the V/Q matching[1, 2], but traditional assessments often rely on empirical judgment or simple calculations of the percentage of regions of interest (ROI) and overlap of binary images, which may fail to provide detailed information about the spatial and intensity relationships between ventilation and perfusion.

In this work, we introduce a new evaluative tool within EIT, named the Match Index (MI), which specifically designed to assess the V/Q matching. Furthermore, two derived indices are proposed to calculate dead space and shunt rates. We have conducted a series of experiments to validate the effectiveness of this method.

2 Methods

In this section, we will describe the formulas of the proposed metrics.

2.1 Match Index

The Match Index (MI) is defined as follows:

$$MI = \frac{\sum_{i=1}^{N} \left(P\left(i\right) \times V\left(i\right)\right)^2}{\sum_{i=1}^{N} P^2\left(i\right) \times \sum_{i=1}^{N} V^2\left(i\right)} \times 100\% \tag{1}$$

where $P(i)$ and $V(i)$ represent the pixel values of perfusion and ventilation in the image at the i-th pixel respectively, N is the total number of pixels in the images.

2.2 Dead Space Index and Shunt Index

The Dead Space Index (DI) and Shunt Index (SI) are further derived as follows:

$$DI = \frac{\sum_{i=1}^{N} V^2\left(i\right) - \sum_{i=1}^{N} \left(P\left(i\right) \times V\left(i\right)\right) \times K}{\sum_{i=1}^{N} V^2\left(i\right)} \times 100\% \tag{2}$$

$$SI = \frac{\sum_{i=1}^{N} P^2\left(i\right) - \sum_{i=1}^{N} \left(P\left(i\right) \times V\left(i\right)\right) / K}{\sum_{i=1}^{N} P^2\left(i\right)} \times 100\% \tag{3}$$

where $P(i)$, $V(i)$ and N are defined as in MI. The K serves as a normalization factor defined as follows:

$$K = \sqrt{\frac{V_{max}}{P_{max}} \times \frac{V_{avg}}{P_{avg}}} \tag{4}$$

where $V_{max} = \max\{V\left(i\right)\}$ and $P_{max} = \max\{P\left(i\right)\}$ are the maximum pixel values of ventilation and perfusion in the image, respectively, calculated over all N pixels. V_{avg} and P_{avg} represent the average pixel values of ventilation and perfusion in the lung regions.

The MI, DI and SI satisfy the following relation:

$$MI = (1 - DI) \times (1 - SI) \tag{5}$$

3 Experiments

3.1 Sensitivity Study

As shown in Fig. 1, a strong match between perfusion and ventilation images (Case 1) yields a high MI and low DI and SI values. However, introducing defects in perfusion (Case 2) or ventilation (Case 3) significantly reduces MI and alters DI and SI, reflecting the metrics' sensitivity to changes in lung image distribution. These metrics can be calculated for individual ROIs to provide more detailed analysis.

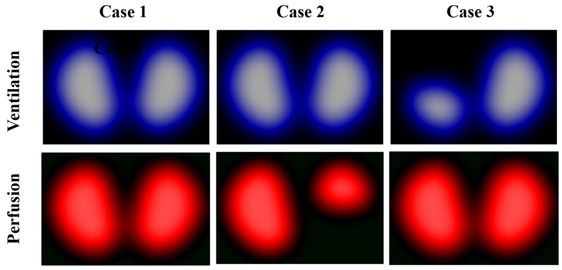

	MI	DI	SI
Case 1	99.97%	0.54%	0.00%
Case 2	77.57%	21.80%	0.80%
Case 3	80.19%	0.57%	19.35%

Figure 1: The sensitivity evaluation of MI, DI and SI.

3.2 Comparison with Region-Overlapping Method

The comparative analysis in Fig. 2 shows that the region-overlapping method, based on binary images with a threshold of 20% of the maximum pixel value, does not capture intensity information, whereas our method successfully incorporates the intensity difference between the left lungs of ventilation and perfusion images.

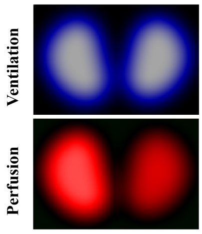

Region-Overlapping method

Match	Dead space	Shunt
92.54%	7.46%	0.92%

Our method

MI	DI	SI
78.77%	21.91%	0.00%

Figure 2: Comparison of region-overlapping and our method.

4 Conclusion

Our study presents new metrics for EIT that incorporate both intensity and spatial information, offering enhanced sensitivity and superior assessment of V/Q matching.

References

[1] S Leonhardt, B Lachmann *Intensive Care Med*, 38(12):191729, 2012

[2] E Spinelli, M Kircher *Crit Care*, 25(1):192, 2021

A new solution to the Inverse Power flow problem in network models in Magnetic Induction Tomography

Martin Wachs[1] and Miriam Primbs[2]

[1]Ruhr West University of Applied Sciences, Mülheim an der Ruhr, Germany, martin.wachs@hs-ruhrwest.de
[2]Ruhr West University of Applied Sciences, Mülheim an der Ruhr, Germany

Abstract: In the analysis of the inverse problem of network models in Magnetic Induction Tomography only external edge voltage sources and resulting edge currents are known, aiming to get all edge resistances. In this work we present a new calculation method for the edge resistances $\boldsymbol{R}$. We show that in most typical networks a sequence of only 2 or 3 measurement pairs $(\boldsymbol{u}_1, \boldsymbol{i}_1), \ldots, (\boldsymbol{u}_3, \boldsymbol{i}_3)$ are sufficient to calculate $\boldsymbol{R}$ uniquely.

1 Introduction

In Magnetic Induction Tomography, external coils induce eddy currents within an object, a process replicable through network modeling. Within this framework, the induction by external coils can be represented by external voltage sources $\boldsymbol{u}$ acting on individual edges. In the forward problem, edge resistance $\boldsymbol{R}$ and edge voltage sources $\boldsymbol{u}$ are given, allowing the calculation of edge currents $\boldsymbol{i}$ through established algorithms. Conversely, the inverse problem entails the derivation of edge resistances $\boldsymbol{R}$ from known edge voltage sources $\boldsymbol{u}$ and associated edge currents $\boldsymbol{i}$ inferred from sensor data. A solution to this inverse problem in Alternating Current (AC) networks is given in [1]. However, the required number of measurements is at least equal to the number of nodes inside the network. An alternative approach for small networks utilizing Direct Currents (DC) has also been documented in [2]. In this work, we show a new method applicable to arbitrary DC networks. Our findings show that only 2 or 3 measurements are required to resolve the inverse problem uniquely.

2 Methods

We use properties of the forward problem and algebraic methods to find a new solution to the inverse power flow problem.

2.1 The Forward Problem

In the analysis of the forward problem, the vector $\boldsymbol{u} \in \mathbb{R}^m$ of edge voltages sources and the diagonal matrix $\boldsymbol{R} = \operatorname{diag}(R_i)_{i=1}^m$ are given to calculate the resulting edge currents $\boldsymbol{i} \in \mathbb{R}^m$. This is done using nodal analysis [3]. We denote by $\boldsymbol{N} \in \mathbb{R}^{n \times m}$ the vertex-edge incidence matrix and by $\boldsymbol{Y} \in \mathbb{R}^{n \times n}$ the corresponding nodal admittance matrix, defined by

$$\boldsymbol{Y} = \boldsymbol{N} \cdot \boldsymbol{R}^{-1} \cdot \boldsymbol{N}^T \tag{1}$$

With $\boldsymbol{u} \in \mathbb{R}^m$ being the voltages-vector of the network, we first get by nodal analysis the nodal potential $\boldsymbol{\phi}$ as a unique solution of

$$\boldsymbol{Y} \cdot \boldsymbol{\phi} = -\boldsymbol{N} \cdot \boldsymbol{R}^{-1} \cdot \boldsymbol{u}. \tag{2}$$

Using $\boldsymbol{\phi}$, we further get the edge currents by evaluating

$$\boldsymbol{i} = \boldsymbol{i}(\boldsymbol{u}, \boldsymbol{R}) = \boldsymbol{R}^{-1} \cdot (\boldsymbol{N}^T \cdot \boldsymbol{\phi} + \boldsymbol{u}). \tag{3}$$

We use properties of the forward problem, especially the kernel of nodal analysis:

Lemma 1 *For any vertex $k \in \{1, \ldots, n-1\}$ let*

$$\boldsymbol{u}_{\text{sink}}(x) := \boldsymbol{N}^T \cdot \boldsymbol{e}_k. \tag{4}$$

Then the set

$$\mathcal{U}_{\text{sink}} = \operatorname{span}\{\boldsymbol{u}_{\text{sink}}(k) | k \in \{1, \ldots, n-1\}\} \tag{5}$$

is the $(n-1)$-dimensional kernel of the nodal analysis, independent of $\boldsymbol{R}$.

2.2 The Inverse Problem

Assuming to have 2 or 3 measurements of edge voltages $\boldsymbol{u}$ and edge currents $\boldsymbol{i}$, the inverse problem is to find a unique diagonal matrix $\boldsymbol{R}$, such that (2) and (3) hold. First, we can show that for each measurement pair the set of all diagonal matrices $\boldsymbol{R}$ satisfying (2) and (3) is an affine subspace

$$\mathcal{R}_{(\boldsymbol{u},\boldsymbol{i})} = \left\{ \operatorname{diag}\left(\frac{\boldsymbol{u}}{\boldsymbol{i}} + \frac{\boldsymbol{u}_{\text{sink}}}{\boldsymbol{i}} \right) | \boldsymbol{u}_{\text{sink}} \in \mathcal{U}_{\text{sink}} \right\}. \tag{6}$$

The quotient of two vectors is always to be considered element-wise.

Second, we can show, that by intersecting these affine subspace of $k = 2, 3$ measurement pairs we get a unique solution

$$\bigcap_{k=1}^{\kappa} \mathcal{R}_k = \{\boldsymbol{R}_{solution}\}. \tag{7}$$

3 Conclusions

In the majority of standard networks, typically 3 measurements are necessary. However, certain network geometries can suffice with only 2 measurements. An example of such geometry is found in cuboid networks, the type utilized in Magnetic Induction Tomography.

References

[1] Y. Yuan, S. H. Low, O. Ardakanian, and C. J. Tomlin, IEEE Transactions on Control of Network Systems, 2022.
[2] C. W. Morgenstern, J. H. Morgenstern, R. Yang, and E. Cook, in 2022 IEEE Power & Energy Society Innovative Smart Grid Technologies Conference (ISGT), IEEE, 2022, pp. 1–5.
[3] P. Dimo, Abacus Press, Kent, England, 1975.
[4] M. Klein and D. Rueter, Progress In Electromagnetics Research B, vol. 2017, no. 78, pp. 155–173, 2017.
[5] M. Klein, D. Erni, and D. Rueter, Sensors, vol. 20, no. 5, p. 1306, 2020.
[6] M. Klein, D. Erni, and D. Rueter, Sensors, vol. 21, no. 22, p. 7725, 2021.
[7] Y. Tian, Missouri Journal of Mathematical Sciences, vol. 14, no. 2, pp. 92–95, 2002.
[8] M. Clemens and T. Weiland, Progress In Electromagnetics Research, vol. 32, pp. 65–87, 2001.

A 24-Electrode Three-Dimensional Electrical Impedance Tomography System

Zhiwei Li[1], Kai Liu[2] and Jiafeng Yao[3]

[123] Nanjing University of Aeronautics and Astronautics, Nanjing, China

Abstract: This paper presents a 3D-EIT system with 24 electrodes distributed in three equidistant planes and the Tikhonov-Noser regularization algorithm is used to reconstruct the images of a 3D lung model. Based on the simulation and experiment, the performance of the system has been tested and the scheme is practicable to apply research in the lab from the results.

1 Introduction

Electrical impedance tomography (EIT) is a technique for reconstructing the conductivity distribution in the field by measuring the boundary voltages. However, the information in 2D images is finite, which cannot reflect impedance changes in the vertical direction of the field. Especially in clinical, 2D-EIT cannot monitor lung ventilation in the whole region, which makes it hard to diagnose certain lung diseases.

2 Methods

2.1 Adjacent-drive adjacent-measurement pattern

The adjacent-drive and adjacent-measurement pattern is implemented, and a total of 504 voltage difference data are measured for imaging one frame.

2.2 Multiplex strategy and data acquisition

The commercial instrument Agilent 34980A was used as the data acquisition module, and the liquid conductivity ratio (LCR) instrument TH2832 was selected for the output voltage excitation signal. The excitation signal is 1mA, 100kHz AC. Fig. 1 shows the 3D-EIT experimental model system. The sensor model is manufactured using 3D printing and the phantom is a double-lung model.

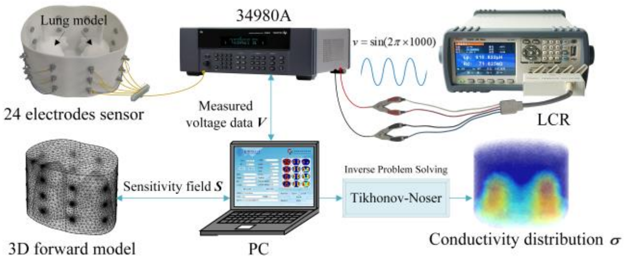

Figure 1: The diagram of a 3D-EIT system with 24 electrodes.

2.3 Algorithm

Combining the advantages of Tikhonov and Noser algorithms, a Tikhonov-Noser hybrid regularization algorithm was proposed [1][2]. It is expressed as follows:

$$\hat{\boldsymbol{\sigma}} = (\boldsymbol{S}^T\boldsymbol{S} + \lambda\boldsymbol{I} + \mu diag(\boldsymbol{S}^T\boldsymbol{S}))^{-1}\boldsymbol{S}^T\boldsymbol{U} \tag{1}$$

where λ is 0.01 and μ is 100. $\hat{\boldsymbol{\sigma}}$ is the approximate solution of the conductivity distribution. $\boldsymbol{S}$ is the sensitivity matrix. $\boldsymbol{U}$ is the boundary voltage matrix of the measurement domain. $\boldsymbol{I}$ is an identity matrix.

3 Results

The image reconstruction results are shown in Fig. 2, and the results of ICC and RMSE are showed in Table I.

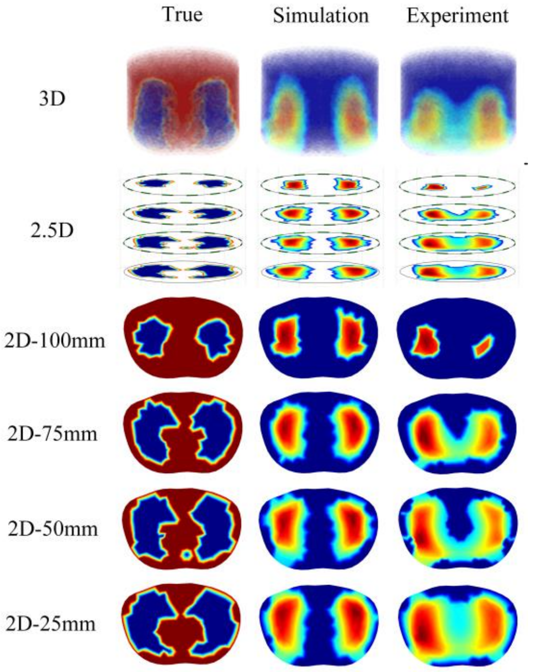

Figure 2: The diagram of the image reconstruction results.

4 Conclusions

In this paper, a 3D-EIT system with 24 electrodes was designed for research in the laboratory, and the feasibility of the system was initially demonstrated by the results of imaging the 3D lung model.

References

[1] WANG Q, The Review of scientific instruments, 83(10):104707,2012.
[2] CHENEY M, International Journal of Imaging Systems &Technology, 2: 66-75, 1990.

TABLE 1: QUANTITATIVE ANALYSIS OF IMAGE RECONSTRUCTION RESULTS

Metric	ICC	RMSE
True	1.000	0.000
Simulation	0.933	0.648
Experiment	0.820±0.019	0.720±0.038

Study on Time Delay between EIT Signal and Ventilator Volume Pulse

Shuzhe Chen[1,2], Hongyu Duan[3], Yibing Wang[3], Mingtao Guan[3], Jinglei Liu[4], Pulin Yao[4], Maokun Li[1,2], Shenheng Xu[1], Fan Yang[1]

[1]Beijing National Research Center for Information Science and Technology (BNRist), Department of Electronic Engineering, Tsinghua University, Beijing 100084, China, maokunli@tsinghua.edu.cn

[2]Institute for Precision Medicine, Tsinghua University
[3]Huarui Boshi Medical Imaging Technology Co., Ltd., Beijing
[4]Shenzhen Mindray Bio-Medical Electronics Co., Ltd.

Abstract: This study explores the time delay between Electrical Impedance Tomography signals and the air pulse of a ventilator. Results from in-vivo measurements show that the signal is delayed by a frame rate-related time, leading to uncertainty in clinical use. Three components of the time delay are identified.

1 Introduction

The use of electrical impedance tomography (EIT) in clinical practice, particularly in mechanically ventilated patients, is increasing [1]. This study examines the time delay between the air pulse of a ventilator and the measured electrical impedance tomography (EIT) signal in mechanically ventilated patients. The asynchronism of multiple monitoring signals can result in messy records [2, 3] and confusing inter-relationships explanation[4]. The causes of the time delay are investigated to better understand the interplay between the ventilator and EIT.

2 Methods

The air pulse travels from the ventilator to the patient through a long tube, and the volume is monitored by a sensor at the end of the machine. Assume that the length and the diameter of the tube are L and D, and the peak inspiratory flow at volume control ventilation (VCV) mode is Q. Then the cross-sectional area of the tube $S = \pi D^2/4$, and the flow rate $V = Q/S$. Therefore, the time delay caused by the ventilator $T_\mathrm{v} = L/V = LS/Q = \pi LD^2/4Q$.

The electrode belts are placed around the chest for real-time data collection at a preset frame rate F. Data will be loaded by the EIT software development kit with a delay. Assume the delay is m frames. The corresponding time delay $T_\mathrm{t} = m/F$.

The measured EIT data is filtered with a low-pass Butterworth filter (cutoff frequency $0.5Hz$), causing a phase delay. The phase delay is estimated using MATLAB fdatool, and the time delay caused by the filter is calculated as $T_\mathrm{f} = \theta_{delay}/2\pi f_r$, where f_r is the respiratory frequency.

In summary, the estimation of total time delay T_e is:

$$T_\mathrm{e} = T_\mathrm{v} + T_\mathrm{t} + T_\mathrm{f} = \frac{\pi LD^2}{4Q} + \frac{2}{F} + \frac{\theta_{delay}}{2\pi f_r} \qquad (1)$$

3 In-vivo Measurements

The study was done on a 26-year-old healthy male (180cm, 80kg) with the SV600 ventilator (Mindray, Shenzhen, China) at VCV mode (1m length, 22mm diameter, 60L/min peak flow, 0.2Hz respiration frequency). EIT data was recorded by the ET1000 (Huarui Boshi, Beijing, China) at 5 different frame rates (10, 20, 30, 40, 50 Hz).

The time delay T at each framerate is evaluated by selecting the end of the inspiratory as the marker point, shown in Fig.1(a) (shaded area). The results are listed in Fig.1(b) showing a time delay of approximately 400 ms at each framerate, except when $F = 10Hz$ with a delay of 1000 ms. The estimated time delay was calculated using Eq.1 with the given parameters and labeled on the T_e column. The estimated values are in close agreement with the measured values, with a minimum error of 10%. Further interpretation is required to understand the multiple factors that contribute to the delay, including sensor performance and noise.

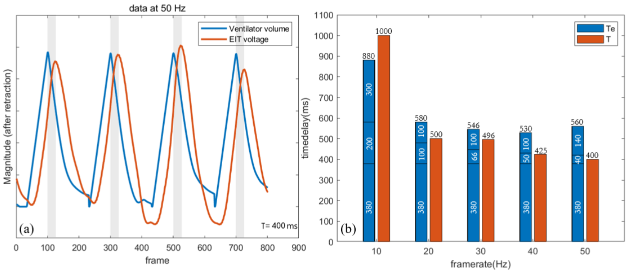

Figure 1: (a) the time delay(shaded) between EIT voltage signals and volume pulse of the ventilator (framerate = $50Hz$) (b) estimated and measured values of time delay at different framerate

4 Conclusions

The present study is the first, to our knowledge, to examine the cause of the time delay between the EIT signals and volume pulse of the ventilator. Understanding the cause of this delay could reduce uncertainty. Further research involving additional measurements on different subjects and frame rates is needed to strengthen the findings and to inspire future work in multi-signal synchronization.

5 Acknowledgements

This work was supported in part by the Institute for Precision Medicine, Tsinghua University, National Natural Science Foundation of China (61971263 and 62171259), Biren Technology, and BGP Inc.

References

[1] C.Nestler,P.Simon,Intensive Care Med, 40:S218—S219,, 2014
[2] W. Kaye, M. E. Mancini, T. L. Truitt *Resuscitation*, 65:285–290, 2005
[3] Z.M.Grinspan,S.Pon,*semin Pediatr Neurol*, 21:291–298, 2014
[4] J.C.Hemphill, P.Andrews,Nat. Rev. Neurosci, 7:451–460, 2011

Assessment of Pulmonary Perfusion with Electrical Impedance Tomography: A Special Case with Pulmonary Embolism

Lingming Wang[1], Lingqing Zhou[1], Chunling Zhao[1], Picong You[1]ID and Zhanqi Zhao[2]

[1]Tianjin Hospital, Tianjin, China, 18678666260@163.com
[2]Guangzhou Medical University, Guangzhou, China

Abstract: Pulmonary thromboembolism (PE) is a disease with high mortality risk. CT pulmonary angiogram (CTPA) is often unsuitable for patients in ICU. Here we presented a special case, in which electrical impedance tomography (EIT) was used for rapid and early diagnosis of PE.

Keywords: EIT, pulmonary embolism

1 Introduction

PE is a potentially life-threatening condition, may cause ≤ 300 000 deaths per year in the US, ranking high among the causes of cardiovascular mortality [1]. PE diagnosis is often missed because presentations are highly variable and may even be asymptomatic. Early and convenient diagnostic methods are of significant important [2]. The common diagnostic methods of PE have certain limitations in clinical practice, especially in ICU. Previous studies suggested that EIT can be used to assess regional ventilation and perfusion at the bedside [3]. This abstract describes a particular case of pulmonary embolism using EIT to evaluate lung perfusion.

2 Case presentation

An 83-year-old woman with a medical history of hypertension and arthritis, regularly taking antihypertensive medications and occasionally using NSAIDs, presented to our hospital's emergency department. She complained of wheezing for three days and sudden unconsciousness lasting for three hours. The patient had been on bed rest for a week prior due to poor appetite and weakness. Upon admission, she exhibited severe hypoxemia, metabolic acidosis, significantly elevated myocardial markers, and acute kidney injury.

Laboratory tests revealed a significantly increased D-dimer level of 4100 ng/L (normal range: 0-300 ng/L). Echocardiography indicated a mostly normal right ventricle (RV) with no pulmonary artery blockage. However, an ultrasound revealed a floating thrombus in the left main femoral vein. Additionally, a new complete right bundle branch block was observed on the ECG. CT scans primarily showed signs of infection (Fig. 1).

The patient was promptly intubated and placed on mechanical ventilation. Despite these interventions, her oxygenation continued to deteriorate, necessitating high ventilator support.

Pulmonary Embolism Severity Index (PESI) risk score [1] was 141 points, indicating a high mortality risk based on age, sex, respiratory rate, mental status, and oxygen saturation levels. Unable to perform CTPA due to the patient's instability, we employed EIT monitoring with saline contrast [4], revealing a significant V/Q mismatch leading to poor lung perfusion and oxygenation (Fig. 2; the lungs had good ventilation but no perfusion in both left and right). This observed phenomenon, exceeding previous dead space thresholds [4], represents a novel finding in EIT-assessed lung perfusion.

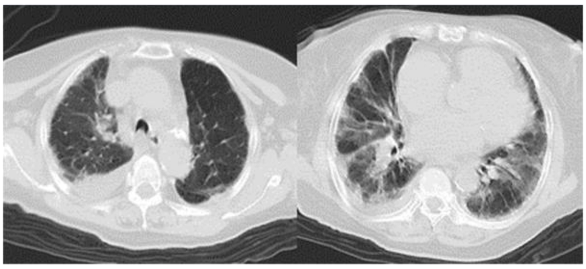

Figure1. CT mainly showed infection(There were more artifacts due to the patient's restlessness)

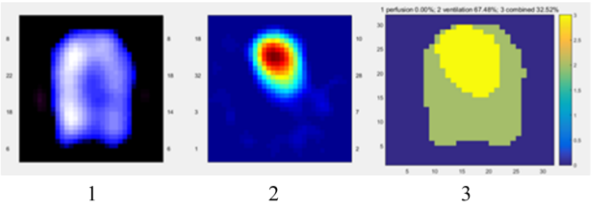

Figure2. EIT imaging. 1.Lung ventilation image. both lungs were well ventilated. 2.Lung perfusion images (without removal of blood flow in the heart). showed no perfusion in both lungs and only blood flow in the cardiac region. 3.Ventilation/perfusion map. the yellow area was both ventilation and perfusion, accounting for 32.52%(The effect of blood flow within the heart); The green area was ventilation without perfusion, accounting for 67.48%(actually 100%, if removing of blood flow in the heart). The area with ventilation and no perfusion was 0.

3 Discussion and conclusions

The patient's history of prolonged bed rest, severe oxygenation disorder, elevated D-dimer, and a floating thrombus in the main femoral vein strongly suggest PE even without CTPA. The presence of persistently worsening hypoxemia, high PESI risk score, unstable thrombus, and abnormal pulmonary perfusion on EIT underscore the PE diagnosis, despite the absence of shock. EIT revealed inadequate perfusion in both lungs, indicating embolism in the pulmonary arteries. Post-PE, lung perfusion decreased significantly, leading to V/Q mismatch and hypoxemia. Although our EIT method had limitations, focusing on lower lung lobes, future studies will explore multiple sites to provide a comprehensive lung perfusion assessment. While CTPA remains the gold standard for PE diagnosis, EIT emerges as a bedside tool without radiation risks. Hypertonic saline injection with EIT offers a safe and efficient way to evaluate V/Q matching.

References

[1] Konstantinides SV et al. Eur Heart. 21; 41(4): 543-603, 2020.
[2] Essien EO et al. Med Clin North Am, 103(3): 549-564, 2019.
[3] Prins SA et al. Crit Care Explor,17; 5(1): e0843, 2023.
He H, et al. Am. J. Respir. Crit. Care Med. 202 (6) 881-882, 2020.

Generative Adversarial Network for Extraction of Cardiac-Related Signals in EIT

Yuxuan Cai, Ke Zhang, Maokun Li*, Fan Yang, Shenheng Xu

Department of Electronic Engineering, Beijing National Research Center for Information Science and Technology (BNRist), Institute of Precision Medicine Tsinghua University, Beijing, 100084, China, maokunli@tsinghua.edu.cn

Abstract: This study introduces a novel end-to-end generative adversarial network (GAN) based method for extracting cardiac-related signals (CRS) from raw electrical impedance tomography (EIT) data. Experiments on a synthetic dataset demonstrate that our method effectively separates CRS from overlapping ventilation components.

1 Introduction

Electrical impedance tomography (EIT) captures dynamic changes in lung conductivity induced by both respiratory and cardiac activities, allowing EIT to simultaneously monitor lung ventilation and perfusion. The EIT signal includes ventilation-related and cardiac-related components. Although cardiac-related signals (CRS) are significantly weaker and frequently obscured by noise or modulated by the more dominant ventilation-related signals (VRS), their accurate isolation holds substantial clinical value.

Various methodologies such as ECG-gated averaging, frequency-domain filtering, and principal component analysis (PCA)[1] have been developed for signal separation in EIT. However, each method has its challenges, such as the struggle of frequency-domain filtering with overlapping spectral or energy distributions of CRS and VRS. Moreover, these techniques are based on certain assumptions and usually focus on single aspects of the signals, which may not fully capture the complex interaction between cardiac and ventilation influences.

In this work, we propose an end-to-end CRS extraction method based on the generative adversarial network (GAN) framework. This method employs adversarial training to update the generator (G) network, enabling it to automatically model the underlying complex signal distribution of the raw EIT signal and perform CRS extraction. Meanwhile, the discriminator (D) network serves as an auxiliary network, helping the G network produce CRS that closely resemble breath-holding signals (BHS).

2 Methods

The overall architecture of the Generative Adversarial Network (GAN) is illustrated in Fig. 1. The GAN consists of a generator (G) and a discriminator (D). The G network, which follows an auto-encoder architecture, takes preprocessed EIT signals as input and outputs the extracted CRS in an end-to-end manner. The D network acts like a loss function in some sense, transmitting information to G and help G's output to look real. To be specific, it receives both the BHS and the CRS to update parameters using a loss function on its output. The BHS is particularly utilized because it does not have the VRS component, providing a clean signal that is assumed to share similar features with the CRS present in the raw EIT signals[2]. Once the model training is complete, the generator model is saved for real-time online inference. In this phase, the raw EIT signals are preprocessed and cut into fixed-length segments, which are then fed into the trained G network for CRS extraction.

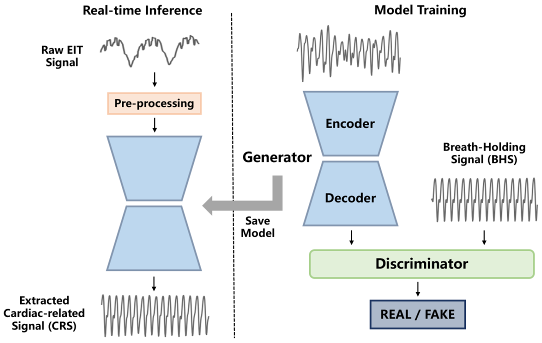

Figure 1: GAN architecture.

3 Experiments

In this section, we evaluated the effectiveness of our proposed GAN-based method on a synthetic dataset crafted using real data collected from clinical situation. As illustrated in Fig. 2, two cases are presented to demonstrate the performance of our method. The original raw EIT data, which contains VRS component alongside the CRS component of very weak amplitude, was input into the trained G network to extract the CRS. Analysis of the results in both the time domain (TD) and frequency domain (FD) reveals that the extracted CRS waveforms closely resemble the ground truth. Notably, these waveforms are free from the high-order harmonics of the VRS, indicating that our method can effectively isolate the cardiac signal even in the presence of frequency overlapping situation.

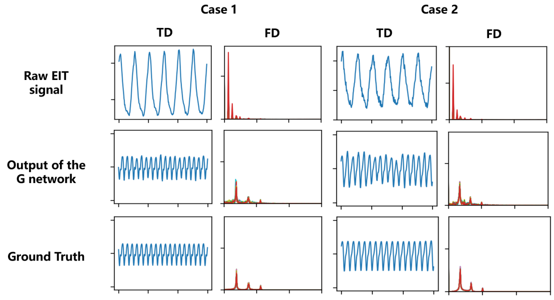

Figure 2: Extraction results of two cases.

4 Conclusions

In this study, we developed an end-to-end method for extracting cardiac-related signals using a GAN framework. The model adopts an encoder-decoder architecture with a fully convolutional structure, enhancing its speed in processing waveform chunks. The findings demonstrate that this method is not only feasible but also offers an effective alternative to existing signal extraction techniques.

References

[1] R Pikkemaat, S Leonhardt *J. Phys.*, 224 012028, 2010
[2] K Zhang, M Li *Physiol Meas*, 43 125005, 2022

Integration of Electrical Impedance Tomography, Microwave Tomography, and Ultrasound Tomography Based on Feature Decoupling for Human Thorax Imaging

Zhichao Lin[1], Rui Guo[1], Ke Zhang[1], Maokun Li[1], Fan Yang[1], Shenheng Xu[1]

[1]Beijing National Research Center for Information Science and Technology (BNRist), Department of Electronic Engineering,
Tsinghua University, Beijing, China, maokunli@tsinghua.edu.cn

Abstract: We propose a feature-based joint inversion method that simultaneously reconstructs the electrical impedance, microwave, and ultrasound images of a target. The structural features of the three modality images are decoupled from the value features and interacted during the inversion process to enforce the structural similarity.

1 Introduction

Electrical impedance tomography (EIT), microwave tomography (MT), and ultrasound tomography (UT) are radiation-free, non-invasive, low-cost medical imaging techniques. They have been studied for human thorax imaging due to their unique advantages[1, 2]. EIT reconstructs the conductivity distribution in the domain of investigation (DoI) and is resistant to measurement noise and variations in the thorax during respiration. MT determines the permittivity and conductivity distributions in the DoI and has high contrast for abnormal tissues. UT rebuilds the compressibility and attenuation distributions in the DoI and provides high-resolution information about organ tissues. Integrating these three modalities has the potential to provide more comprehensive insights into physiological changes in the thorax.

2 Methods

The structural and value features of the three modality images are decoupled by a disentangled variational autoencoder (DVAE). Specifically, the DVAE encoder parameterizes an image of any modality into structure code $\mathbf{z}_s$ and value code $\mathbf{z}_v$. For the same medical target, images of different modalities should have the same structure code but distinct value codes. This goal is achieved through a group training strategy. In detail, two images $\mathbf{x}_1$ and $\mathbf{x}_2$ with different structures and values are input into the DVAE encoder to obtain two groups of structure and value codes. The value codes are exchanged and input to the DVAE decoder together with the structure codes to get two reconstructed images $\mathbf{x}_3$ and $\mathbf{x}_4$. Each group of training dataset contains $\mathbf{x}_1$, $\mathbf{x}_2$, $\mathbf{x}_3$, and $\mathbf{x}_4$, where $\mathbf{x}_1$ has the same structure as $\mathbf{x}_3$ and the same value as $\mathbf{x}_4$, and similar for $\mathbf{x}_2$.

In separate inversions of the three modalities, we aim to seek the structure codes $\mathbf{z}_s$ and value codes $\mathbf{z}_v$ that minimize the following objective function,

$$\phi(\mathbf{z}_s,\mathbf{z}_v)=\frac{\|\mathbf{d}_*-\mathcal{G}(\mathbf{z}_s,\mathbf{z}_v)\|^2}{2\|\mathbf{d}_*\|^2}+\frac{\beta}{2}(\|\mathbf{z}_s\|^2+\|\mathbf{z}_v\|^2) \quad (1)$$

where $\mathbf{d}_*$ is the measurement data, $\mathcal{G}(\cdot)$ is the forward modeling operator, and β is the regularization parameter. The optimization of (1) is conducted iteratively by the Gauss-Newton method. The interaction among the three modalities is performed by averaging their structure codes every K steps,

$$\bar{\mathbf{z}}_{s,n}=(\mathbf{z}_{s,n}^{(\mathrm{EIT})}+\mathbf{z}_{s,n}^{(\mathrm{MT})}+\mathbf{z}_{s,n}^{(\mathrm{UT})})/3 \quad (2)$$

where the subscript n denotes the n-th iteration. The final reconstructed images are obtained by feeding the final $\mathbf{z}_s$ and $\mathbf{z}_v$ to the DVAE decoder.

3 Numerical Examples

We randomly select a thorax model from the test dataset of DVAE to demonstrate the performance of the proposed method. The total variation (TV) method is also implemented for comparison. The results are summarized in Fig. 1. It can be observed that the proposed method significantly improves the performance of the three modalities.

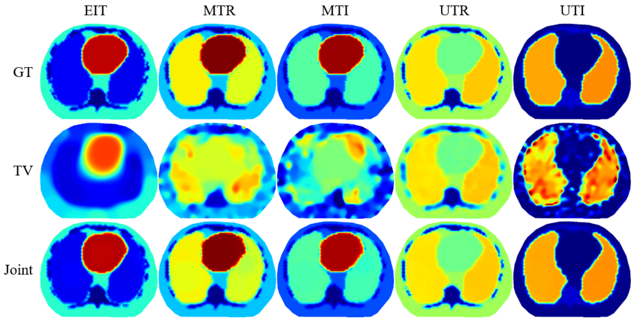

Figure 1: Inversion results of TV and the proposed method. GT denotes the ground truth, MTR and MTI are the real and imaginary parts of the MT model, respectively, and similar for UTR and UTI. All images are normalized to 0 to 1 and use the same color bar.

4 Conclusions

This work integrates the EIT, MT, and UT based on the feature decoupling. The structural and value features of the three modality images are decoupled by the DVAE. The consistency of the structural features of the reconstructed images is enforced in the inversion process. Numerical examples validate the effectiveness of the proposed method.

5 Acknowledgments

This work was supported in part by the Institute for Precision Medicine, Tsinghua University, National Natural Science Foundation of China (61971263 and 62171259), Biren Technology, and BGP Inc.

References

[1] Z Lin, R Guo, K Zhang, M Li, F Yang, S Xu, A Abubakar *IEEE Transactions on Instrumentation and Measurement*, 71:1-12, 2022

[2] X Song, M Li, F Yang, S Xu, A Abubakar *IEEE Journal on Multiscale and Multiphysics Computational Techniques*, 4:2-11, 2019

Pseudo-Domain Adversarial Network with Electrical Impedance Tomography for Electrode Offset Error

Gengchen Xu[1,2], Haofeng Chen[1,2], Xuanxuan Yang[1,2], Gang Ma[*2] and Xiaojie Wang[*1]
[1]Hefei Institutes of Physical Science, Hefei, China
[2]University of Science and Technology of China, Hefei, China
[*]Correspondence: magang93@mail.ustc.edu.cn, xjwang@iamt.ac.cn

Abstract: This paper presents the Pseudo-Domain Adversarial Network (PDAN), a novel transfer learning framework designed to address electrode displacement in Electrical Impedance Tomography (EIT). Leveraging adversarial learning with noisy data simulation, PDAN enhances the robustness of EIT systems, improving classification accuracy and generalization without requiring recalibration, even under conditions of electrode rotation.

1 Introduction

Electrical Impedance Tomography (EIT) is increasingly applied in diverse fields, from medical imaging to human-computer interaction, due to its non-invasive nature. However, electrode displacement caused by movement or improper operation introduces significant data errors, impeding the effective use of previously trained models and complicating continuous operation without recalibration. Traditional methods for addressing electrode displacement involve costly hardware modifications or require entirely new training of recognition algorithms. These approaches either lack scalability due to high costs or lack practicality because of the frequent retraining they necessitate. This paper introduces a novel transfer learning framework, the Pseudo-Domain Adversarial Network (PDAN), which leverages adversarial learning enhanced with noisy data simulation to tackle the electrode displacement issue in EIT. By incorporating images altered to simulate post-electrode rotation scenarios, PDAN improves the robustness of the system against minor displacements without the need for recalibration.

2 Methods

The PDAN method utilizes a three-stage approach to address challenges in leg movement classification due to electrode displacement. The process begins with data collection, where impedance data is gathered and a feature subset is created by calculating variance and applying Pearson Correlation to remove irrelevant features. To enhance classification accuracy and expand the training dataset, Gaussian noise is introduced to these features, preparing the model for real-world conditions including electrode rotation.

The model employs deep adversarial learning to improve robustness and generalization across various real-world datasets. During training, the network adaptively selects parameters and generates convolutional features automatically during both forward and backward propagation. Skip connections and adaptive aggregation mechanisms are incorporated to streamline larger network regions, and domain loss is utilized to further refine parameter selection autonomously.

This strategic application of advanced technology ensures that PDAN can effectively adapt to simulation scenarios and excel in real-time verification of performance. Our approach is based on transfer learning and is inherently robust to different forms of electrode excursions and performs well in real-time validation of performance, these techniques applied to noise enhancement, adversarial learning, and adaptive architecture also enable the model to adapt to other types of system electrode excursions, such as displacement changes caused by patient motion. Figure 1 illustrates these modifications, showing how the network architecture incorporates impedance images and adapts parameters dynamically, which includes gradient reversal, cross-layer connections, and neuron modulation.

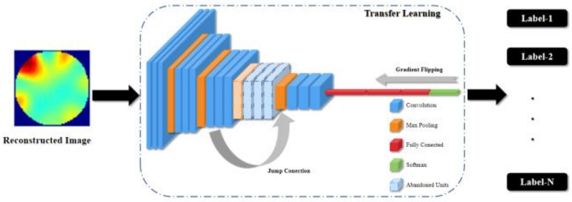

Figure 1: The PDAN network architecture adopts impedance images as inputs. Based on transfer learning methods, the network autonomously adjusts parameters, including but not limited to gradient reversal, cross-layer connections, and addition or pruning of neurons.

3 Results and Conclusion

The PDAN was applied to analyse six leg movements: sitting, lifting, crossing, standing, walking, and lying, under both ideal and displaced electrode conditions. The models were evaluated for their classification accuracy and ability to generalize in real-world scenarios. The network's initial classification accuracy for these movements was nearly 100%. After rotation, PDAN's classification accuracy improved to 99.46%, a significant increase from the 22.60% accuracy achieved without adjustments. This demonstrates that pseudo domain adversarial techniques effectively mitigate electrode displacement effects.

Acknowledgements

Special thanks to the foundation for their support (Grant No.WK5290000004).

EIT-DPM: Diffusion Probabilistic Model for Electrical Impedance Tomography Reconstruction

Qilin Zhang[1,2], Haofeng Chen[1,2], Xuanxuan Yang[1,2], Gang Ma[*2] and Xiaojie Wang[*1]
[1]Hefei Institutes of Physical Science, Hefei, China, zhangqilin@mail.ustc.edu.cn
[2]University of Science and Technology of China, Hefei, China
[*]Corresponding author

Abstract: This paper presents an iterative denoising algorithm, a novel approach to addressing the challenges of precise regularization term selection and the absence of prior knowledge in Electrical Impedance Tomography (EIT) image reconstruction. By employing the diffusion model, our method can implicitly learn regularization parameters, resulting in a significant enhancement in reconstruction performance.

1 Introduction

The inherent nonlinear and inverse problem nature of image reconstruction in EIT presents significant challenges, particularly in the presence of noisy measured data. Traditional iterative methods like NOSER and IDBP algorithms encounter difficulties such as lack of prior knowledge and constraints in selecting regularization.

To address these issues, we propose a novel diffusion model-based reconstruction method that amalgamates the strengths of probabilistic model and data-driven deep learning solutions. Our model offers a flexible framework, plug-and-play feature, and easy training for implicit learning of regularization parameters. EIT-DPM eliminates the need for explicit sampling, thereby sidestepping potential sample bias and overfitting problems inherent in traditional sampling methods, consequently enhancing the quality and diversity of generated samples.

2 Methods

Our model comprises two distinct components. The first segment employs the L1 regression method to analyse the input voltage data, yielding pre-reconstruction outcomes. Subsequently, the second part, the diffusion model, acts as a post-processing operator, exhibiting exemplary denoising capabilities. It enforces constraints during sampling to ensure data consistency. By incorporating the initial results derived from the L1 regression method, we expedite the sampling process, infusing valuable physical properties into EIT reconstruction while mitigating the risk of converging towards local optimal solution. The detailed sampling process is illustrated in Figure 1.

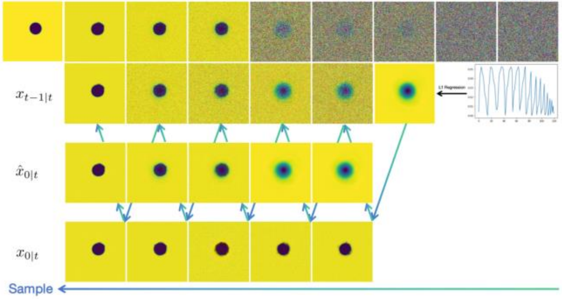

Figure 1: The architecture of the EIT-DPM network.

3 Results

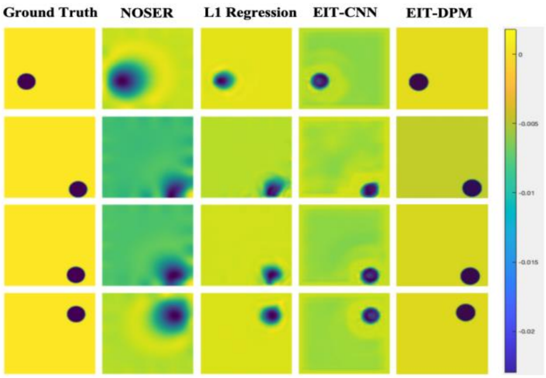

Figure 2: Comparison of reconstruction effects of several methods.

Figure 2 shows the comparison results of several algorithms. Our method significantly reduces artifacts and improves image quality compared to traditional algorithms.

Table 1: Algorithm performance comparison.

	Distortion		Perception	
	PSNR↑	SSIM↑	LPIPS↓	FID↓
NOSER	16.169	0.845	0.262	219.386
TV	24.476	0.982	0.130	202.168
L1	24.354	0.987	0.072	168.835
EIT_CNN	19.815	0.974	0.079	154.543
EIT_DPM	23.522	0.989	0.023	34.771

We measured indicators in image reconstruction, as shown in Table 1. Experiments show that when distortion is equivalent, EIT-DPM can achieve more than 60% perception improvement compared to traditional electrical impedance imaging methods such as NOSER and TV.

4 Conclusion

We introduce a novel EIT image reconstruction network that outperforms traditional methods in terms of performance and robustness. The EIT-DPM proposed in this study represents a promising network architecture that has demonstrated efficacy across diverse image generation tasks. Looking ahead, we aim to tackle more demanding challenges, including the reconstruction of medical EIT images, leveraging the strengths of our proposed approach.

Employing Physics-Informed Neural Networks (PINN) to Address EIT Problems with Discrete Electrodes

Xuanxuan Yang[1,2], Yangming Zhang[1], Yaoyue Wang[3], Haofeng Chen[1,2] and Gang Ma[*2]

[1]Hefei Institutes of Physical Science, Hefei, China
[2]University of Science and Technology of China, Hefei, China
[3]University of Southern California, Los Angeles, USA
[*]Corresponding author: magang93@mail.ustc.edu.cn

Abstract: In the realm of Electrical Impedance Tomography (EIT), the application of Physics-Informed Neural Networks (PINNs) has predominantly been confined to ideal scenarios that presuppose the existence of continuous current excitation and Neumann-Dirichlet mappings along boundaries. This study extends this methodology to address more realistic situations involving EIT problems with discrete electrode stimulation.

1 Introduction

Physics-Informed Neural Networks (PINNs) represent an unsupervised, model-driven approach that is increasingly utilized in the study of inverse problems. PINNs are distinguished by their mesh-free nature, which eliminates the need for extensive finite element mesh partitioning and reduces the dependency on large volumes of training data when applied to the domain of Electrical Impedance Tomography (EIT). Traditional iterative EIT algorithms focus on using boundary-measured voltages to deduce the internal conductivity distribution. While effective to a degree, this approach heavily relies on appropriate regularization techniques. PINN methods leverage Maxwell's equations as physical constraints to infer the internal electric potential distribution and subsequently solve for the conductivity distribution, thereby addressing the inverse problems of EIT. However, current PINN applications are largely restricted to ideal scenarios that assume continuous current excitation at the boundaries, leading to Neumann-Dirichlet mappings [1, 2]. While effective for training, this does not align with real-world EIT problem-solving, where the boundary is limited to a finite number of electrodes providing stimulation. Thus, we propose a novel PINN approach tailored for practical EIT challenges, accommodating the discrete electrode configurations encountered in real settings.

2 Methods

As depicted in Figure 1, our experimental setup consists of a domain with a background conductivity of 1, into which three circular regions are introduced. We utilize 16 electrodes for current stimulation, evenly split between 8 anodes and 8 cathodes. This configuration allows the circular sensors to generate an electric potential field. By computing the partial derivatives in the x and y directions, we can observe internal variations, indicative of the abrupt changes in the field as the current passes through the objects. A multilayer perceptron (MLP) model is constructed to harness this setup. Maxwell's equations are employed as physical constraints within our training process, guiding the neural network to effectively solve for the conductivity distribution across the domain. This approach not only adheres to the physics involved but also leverages the computational power of neural networks to tackle the inverse problem of EIT under realistic conditions.

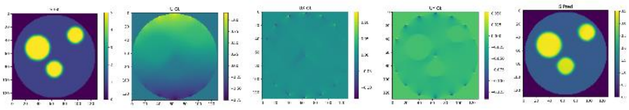

Figure 1: Real conductivity, internal electric potential distribution under discrete electrode stimulation, partial derivatives of the internal electric potential distribution with respect to x and y, and predicted conductivity.

PINNs are categorized under unsupervised learning models, necessitating retraining for each distinct Electrical Impedance Tomography (EIT) issue. Each training session currently takes more than 15 minutes, highlighting the need for further exploration in real-time imaging applications. Additionally, the accuracy of electrode placement is crucial as it directly impacts our ability to precisely calculate the internal electric potential field within the human body. These challenges underscore the ongoing efforts required to refine and enhance the applicability of PINNs in practical scenarios.

3 Conclusion

The predictive results demonstrate that our PINN method effectively resolves the complete inverse problem in practical EIT scenarios, offering a robust tool for accurate conductivity mapping in diverse applications.

4 Acknowledgements

Special thanks to the foundation for their support (Grant No.WK5290000004).

Reference

[1] L. Bar and N. Sochen, "Strong Solutions for PDE-Based Tomography by Unsupervised Learning," SIAM Journal on Imaging Sciences, vol. 14, no. 1, pp. 128-155, 2021.
[2] A. Pokkunuru, P. Rooshenas, T. Strauss, A. Abhishek, and T. Khan, "Improved Training of Physics-Informed Neural Networks Using Energy-Based Priors: A Study on Electrical Impedance Tomography," in The Eleventh International Conference on Learning Representations, 2022.

Ventilation Distribution in Infants Post-Liver Transplantation

Xiaolan Chen[1,2], Chen Chen[1], Yuan Gao[1], Yuxiao Deng[1], Zhe Li[1*] and Zhanqi Zhao[3,4]
[1]Shanghai Jiao Tong University School of Medicine Affiliated Renji Hospital, Shanghai, China. slamy1987@126.com
[2] Shanghai Pulmonary Hospital, Shanghai, China.
[3] School of Biomedical Engineering, Guangzhou Medical University, Guangzhou, China.
[4]Institute of Technical Medicine, Furtwangen University, Villingen-Schwenningen, Germany

Abstract: This study investigates ventilation variations during controlled mechanical ventilation (MV), spontaneous breathing trial (SBT), and the weaning process in infants following liver transplantation.

1 Introduction

Pediatric liver transplantation (PLT) is critical for managing end-stage liver disease in children [1]. Due to the liver-lung proximity, postoperative respiratory recovery is influenced by surgery, directly affecting prognosis[2]. Utilizing electrical impedance tomography (EIT), our pilot study observed mainly right-sided gas distribution postoperatively, with varying recovery [3]. The present study further investigated typical postoperative ventilatory patterns in PLT recipients who were successfully extubated.

2 Methods

The prospective study, approved by the Local Ethics Committee, included PLT patients admitted to the ICU postoperatively under anesthesia. All patients underwent four phases of respiratory recovery monitored by EIT (VenTom-100, MidasMED, Suzhou, China): 1) mechanical ventilation (PCV); 2) pressure support (PSV at 15/5 cmH_2O); 3) spontaneous breathing trial (PSV at 12/3 cmH_2O for 2 hours 4) spontaneous breath after weaning. Analysis was conducted on 30 subjects who successfully met the SBT criteria (S_PO_2≧95%; Exhaled tidal volume≧5ml/kg ideal weight; Respiratory rate: 20-60bpm for <6 months or 15-45bpm for 6 to 24 months) and were extubated. Demographic data and EIT records were collected. Tidal impedance variation (TIV) distribution in the left/right regions and the ventral/dorsal regions, along with the Global Inhomogeneity (GI) index and center of ventilation (CoV), were evaluated.

3 Results

Thirty patients (median age: 8 months, median weight: 7.5 kg, median height: 66 cm; 53.3% male) were included in the study. Ventilation distribution predominantly favored the right and ventral sides during the 4 phases (Fig. 1). As the transition from PCV to spontaneous breathing occurred, the CoV gradually shifted ventrally. The increase in the GI index from PCV to spontaneous breathing reflects an increase in inhomogeneity (Fig. 2), for detailed results, please refer to Table 1.

4 Discussion and Conclusions

We investigated the ventilation distribution patterns during lung recovery after PLT. Our findings revealed that gas distribution was predominantly on the right and ventral side in all patients. We hypothesize that due to the placement of the transplanted organ on the left side, it restricts diaphragmatic movement, thereby reducing left chest wall compliance and resulting in physiological compensation on the right side. Another interesting observation was the shift in the center of ventilation towards the ventral side during the recovery of spontaneous breathing, contrary to the dorsal ventilation increase observed in previous studies [4,5]. While we acknowledge the potential specificity of our study population, these findings underscore the importance of bedside monitoring for post operative respiratory recovery in pediatric patients.

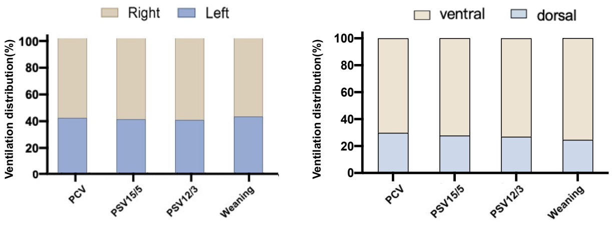

Fig.1: Variations in ventilation characters

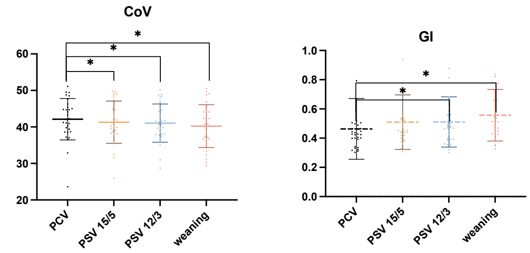

Fig.2: Variation in ventilation center and inhomgeneity

Table 1: Ventilation Distribution variation during mechanical ventilation and spontaneous breathing after pediatric liver transplantation

Variables/Phases	PCV	PSV15/5	PSV12/3	weaning
TIV_{right} (%)	57.97±16.68	58.91±17.38	59.86±18.51	56.96±17.3
TIV_{left} (%)	42.11±16.59	41.15±17.62	40.63±18.21	43.14±17.04
$TIV_{ventral}$ (%)	70.22±14.17	72.28±14.4*	73.16±13.26*	75.64±15.46*
TIV_{dorsal} (%)	29.8±14.21	27.83±14.42*	26.92±13.17*	24.63±15.3*
CoV	41.11±5.67	41.3±5.77*	41.05±5.24*	40.21±5.86*
GI	0.46±0.21	0.51±0.19	0.51±0.17*	0.56±0.18*

CoV,Center of Ventilation; GI,Global Inhomogeneity Index; TIV, Tidal impedance variation *,$P<0.05$(compared with PCV)

References

[1] M Spada et al. *World J Gastroenterol* 15:648–74, 2009.
[2] C Araz et al. *Transplant Proc*. 36:214-7, 2004
[3] Xiaolan Chen et al.*Proceedings EIT2023.*
[4] Clasen D et al. BMC Anesthesiol. 2023;23(1):118.
[5] Nascimento MS, et al. PLoS One. 2023;18(3):e0283039.

Anatomically accurate torso mesh for EIT

Bartłomiej Grychtol[1] and Andy Adler[1]

[1]Systems and Computer Engineering, Carleton University, Ottawa, Canada, adler@sce.carleton.ca

Abstract: We describe an anatomically accurate torso mesh and set of tools to allow arbitrary electrode placement. The work is made available through EIDORS and on Zenodo.

1 Introduction

Anatomically-accurate finite element meshes (FEM) are needed for EIT forward and inverse simulations. While many such meshes are publicly available, EIT also requires the ability to specify and refine body surface electrodes. To investigate novel EIT configurations (e.g. for 3D EIT) tools are needed to support arbitrarily electrode positions.

2 Methods and Results

The base geometry was taken from BodyParts3D[6]. Separate surface triangulations were merged and modified to avoid overlaps and increase quality. Closed organ surfaces were created, meshed with Gmsh [3] and merged in EIDORS [1]. A torso shape without arms was derived from the whole-body skin surface in BodyParts3D, on which electrodes can be placed in EIDORS [4]

The mesh contains the heart, lungs, and major vessels. The heart is segmented into the heart wall and left and right blood pools, without valves. Simplified vessels (aorta, left and right pulmonary artery, inferior/superior vena cava, pulmonary veins) are modelled with $\sim$ 2 mm thick walls, truncated, and capped, enclosing the blood pool in their lumen. The lumen of the trachea and major bronchi is modelled as void space. Equipped with electrodes, the model torso consist of $\sim$ 7 million elements.

Example image of the FEM mesh are shown in Fig.1. All software to generate the component subimages is part of the latest EIDORS release [2] (function `mk_thorax_model_bp3d`).

3 Discussion

We hope this contribution helps the EIT and bioimpedance community to more easily model detailed anatomical features of the thoracic anatomy. To facilitate access to this model, it has been made available as part of EIDORS[2], and also uploaded to Zenodo[5].

References

[1] Adler A, Lionheart WRB, *Physiol Meas* 27:S25–S42, 2006.
[2] Adler A, Grychtol B, “EIDORS Version 3.12”, Conf EIT 2024
[3] Gauzaine C, Remacle J-F, *Int J Numer Methods Eng* 79(11) , 2009.
[4] Grychtol B, Adler A, *IEEE EMBS 2013* 6429–32, 2013.
[5] Grychtol B, 10.5281/zenodo.11047831, 2024.
[6] Mtsuhashi N et al. *Nucleic Acids Res.* 37:D782–5, 2009.

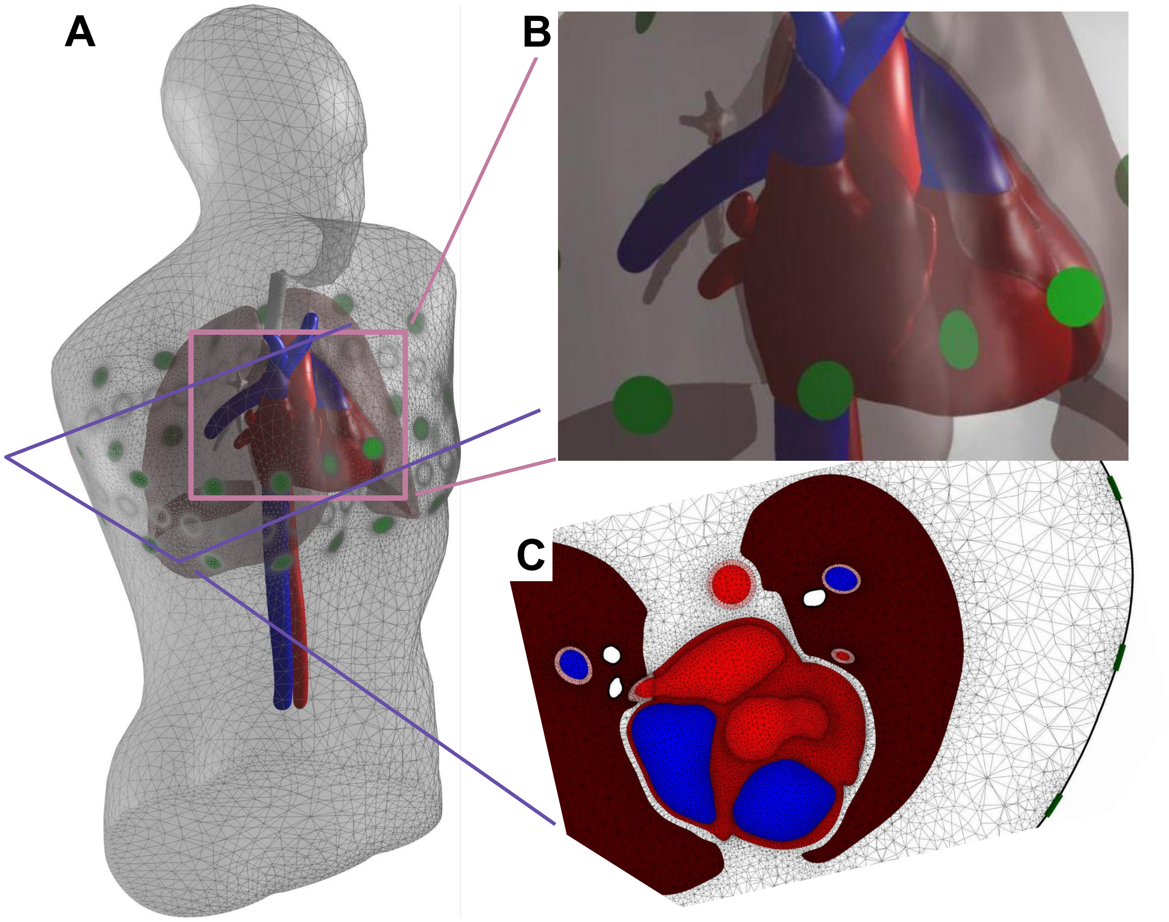

Figure 1: Illustrations of the generated FEM with multiple electrode planes. A) Full model with coloured organ regions, B) zoomed image into the full model in the heard region, C) FEM mesh in a slice through the ventricles.

Pilot Clinical Trial of Monitoring Hemorrhagic Transformation after Thrombectomy in Acute Ischemic Stroke Using EIT

Hailong Yu[1], Bin Yang[2], Guoqing Su[3], Feng Fu[2] and Luhang Tao[1]

[1]Northern Jiangsu People's Hospital, Yangzhou, China
[2]Department of Biomedical Engineering, Fourth Military Medical University, 710032 Xi'an, China
[3]Nanjing EI Medical Equipment Co., Ltd., Nanjing, China, gq_su@njeime.com

Abstract: Hemorrhagic transformation is a common and serious complication that often occurs after thrombectomy in cases of acute ischemic stroke (AIS), potentially worsening the patient's clinical condition. This study introduces a pilot clinical trial utilizing brain EIT to monitor hemorrhagic transformation following thrombectomy in AIS. Initial findings suggest that EIT is capable of identifying alterations in intracranial impedance resulting from reperfusion injury, indicating the potential for real-time detection and estimation of hemorrhagic transformation risk post-thrombectomy.

1 Introduction

Acute ischemic stroke (AIS) has become a prominent global health concern, contributing significantly to mortality rates and serving as a primary contributor to long-term disabilities. The abrupt and unpredictable nature of this condition presents significant challenges to healthcare systems and imposes a substantial burden on patients and their families. Thrombectomy is frequently utilized in the management of AIS to promptly reestablish normal cerebral blood flow, thereby reducing the extent of brain tissue damage.

Mechanical thrombectomy is utilized with the goal of expeditiously reestablishing blood flow to cerebral tissue, thereby preserving the ischemic penumbra and mitigating damage to brain tissue. This procedure has garnered widespread adoption on a global scale, with a notable surge in its utilization in China, where the volume of procedures has increased by over tenfold in recent years. Nonetheless, as the procedure becomes more prevalent, the potential complications associated with it, particularly hemorrhagic transformation (HT), are gaining heightened scrutiny.

HT is characterized by the sudden onset of bleeding in ischemic brain tissue following the restoration of blood flow, which can lead to significant adverse outcomes that may negate the benefits of surgery and worsen the patient's condition, potentially endangering their life. Timely detection of HT is essential for prompt medical intervention. Emerging Imaging Technology (EIT) serves as a novel monitoring approach that offers continuous, convenient, and noninvasive support to conventional imaging modalities [1, 2].

2 Methods

This trial study was performed in the intensive care of Neurosurgery of Northern Jiangsu People’s Hospital. The inclusion criteria for this study encompass patients diagnosed with acute ischemic stroke who are deemed suitable candidates for thrombectomy surgery, are aged 18 years or older, have no comorbid serious illnesses, provide informed consent, and consent to postoperative EIT monitoring. Patients who exhibit signs of postoperative bleeding, have allergies to electrode materials, or have recently participated in other studies should be excluded from the study. EIT using EIT-B300 device (EI Medical, Nanjing, China) was recorded to monitor and assess the likelihood of intracranial hemorrhage.

3 Results

In the present study, a cohort of 30 patients was examined, revealing that 4 patients exhibited HT following thrombectomy surgery as detected by EIT, with subsequent confirmation of this finding through CT scans. As depicted in Figure 1, a 51-year-old male patient with AIS exhibited a reduction in impedance in the left basal ganglia region as detected by EIT within 12 hours following thrombectomy. Subsequent CT scans further confirmed the occurrence of HT in this particular anatomical area.

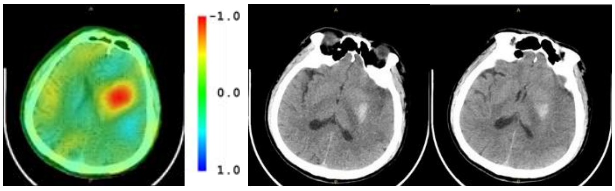

Figure 1: EIT and CT of postoperative HT in AIS.

4 Conclusions

Clinical research on these cases has shown that EIT has potential for monitoring HT after AIS surgery. While still in early clinical research, the use of EIT in monitoring neurological diseases shows great potential. In the future, this technology can create an early warning system for HT after AIS thrombectomy and monitor brain conditions in real-time to evaluate treatment effectiveness and personalize treatment plans. The integration of organic imaging with other medical technologies will enhance diagnostic accuracy and support treatment decisions.

References

[1] Yang Bin, Li Bin, Xu Canhua, Hu Shijie, Dai Meng, Xia Junying, Luo Peng, Shi Xuetao, Zhao Zhaoqi, Dong Xuezhen, Fei Zhou, Fu Feng. Comparison of electrical impedance tomography and intracranial pressure during dehydration treatment of cerebral edema. Neuroimage Clinical 2019. 23, 101909.

[2] Dai Meng, Liu Xuechao, Li Haoting, Xu Canhua, Yang Bin, Wang Hang, Shi Xuetao, Dong Xuezhen, Fu Feng. EIT Imaging of Intracranial Hemorrhage in Rabbit Models Is Influenced by the Intactness of Cranium. Biomed Res Int 2018, 1321862.

A data compensation method for reducing impact of cerebrospinal fluid change in electrical impedance tomography

Xuechao Liu[1,2,3], Xiang Tian[1,2,3], Canhua Xu[1,2,3], Meng Dai[1,2,3], Bin Yang[1,2,3] and Feng Fu[1,2,3]

[1]The Fourth Military Medical University, Xi’an, China, xuechaoliu@fmmu.edu.cn
[2]Shaanxi Key Laboratory for Bioelectromagnetic Detection and Intelligent Perception, Xi’an, China
[3]Research Institution, Xijing Hospital, Xi’an, China

Abstract: This work proposes a data compensation method based on a priori information which aims to reduce the influence of cerebrospinal fluid (CSF) change on electrical impedance tomography (EIT) of hemorrhage. The difference between boundary voltages under hemorrhage and CSF change was quantitatively analyzed based on a three-dimensational cranial model, which is the basic of the prior matrix. Based on this, we conducted data compensation, and reconstruction of a hemorrhagic target with the new method and traditional damped least-squares (DLS) algorithm. Results show that the DLS algorithm cannot reconstruct the impedance change accurately in the case of CSF change, while the compensation method is able to achieve an effective characterization of hemorrhagic target.

1 Introduction

Electrical impedance tomography has significant advantages in hemorrhage monitoring. Theoretically, intracranial impedance decreases after hemorrhage, but it has been found that impedance changes in EIT show a trend toward higher or lower impedance[1,2], which may be due to CSF change under closed-cranial conditions that have an effect on hemorrhagic targets’ imaging[3]. The Impedance of CSF is lower than that of blood. When the occupancy effect of hematoma foci creates a compression of the surrounding brain regions, it leads to the drainage of CSF with better electrical conductivity, which increases intracranial impedance and affects the hemorrhage characterization. To address this problem, this study proposed an EIT reconstruction method based a prior information data compensation, carries out simulation experiments, and compares the imaging results of this method with those of the DLS algorithm.

2 Methods

A 3D cranial simulation model with the CSF layer was built and was divided into four brain regions. The CSF change was abstracted as an EIT imaging problem for its volume changes in different brain regions in the physical field for simulation experiments. First, the effect of different volumes of CSF change on EIT measurement data was quantitatively analyzed. Next, the measured voltage changes in the case of bleeding 5 ml and CSF reduction 5 mL were comparatively analyzed. Furthermore, a priority matrix was built based on the above data and data-compensated imaging was performed.

2.1 Figures and tables

The 3D brain model with CSF layer divided into four regions was showed in Figure 1.

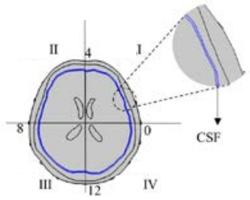

Figure 1: Cerebrospinal fluid (CSF) layer in brain model.

The reconstruction images were shown in Figure 2.

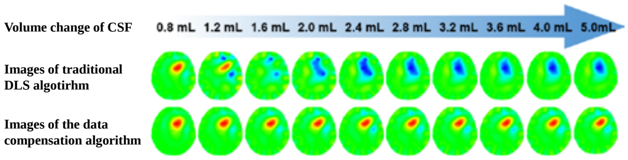

Figure 2: The reconstruction images based on traditional DLS algorithm and the data compensation method.

2.2 Equations

The compensation voltage change which was used to reconstruction could be expressed as equation 1.

$$\Delta V_{af} = \Delta V_{bf} - \Delta V_{csf} \tag{1}$$

where ΔV_{af} was the compensation voltage change, ΔV_{bf} was the measured voltage change, and ΔV_{csf} was the calculated voltage change by a direct linear relationship matrix between the voltage and the volume change of CSF.

3 Conclusions

In this paper, a data compensation method for reducing the impact of cerebrospinal fluid change on hemorrhage reconstruction of EIT is proposed. Simulated Experiments have been conducted, which shows this method can accurately reconstruct hemorrhagic target in the development of brain injuries with CSF change.

4 Acknowledgements

This work was supported by the National Nature Science Foundation of China under Grants 51837011, and the Natural Science Basic Research Program of Shaanxi under Grant 2022JQ-872.

References

[1] Xu C, Wang L, Shi X, Journal of International Medical Research, 38(5):1596-1604, 2010
[2] Tang T, Weiss M D, Borum P, Physiological Measurement, 37(6):751-764, 2016
[3] Dai M, Liu X, Li H, BioMed Research International, 1321862:1-10,2018

Pendelluft May Increase in Obstructive Lung Diseases after 6-min Walk Test

Lu Cao[1], Yaping Li[2], Zhanqi Zhao[3], Fei Xie[1]

[1]Chinese PLA General Hospital, Beijing, China xiefei0522@163.com
[2]MidasMED biomedical technology, Suzhou, China
[3]Guangzhou Medical University, Guangzhou, China

Abstract: The 6-minute walk test (6MWT) is a valuable tool for assessing obstructive lung diseases. Regional ventilation patterns have not been evaluated during 6MWT. The present study showed some preliminary results.

1 Introduction

When assessing lung functions for patients with obstructive lung diseases, we face several challenges, e.g. in completing forced vital capacity (FVC) maneuvers, high level patient cooperation is required. Since obstructive lung diseases like chronic obstructive pulmonary disease (COPD) and asthma can cause airflow limitation and breathing difficulties, some patients may struggle to perform FVC maneuvers effectively, impacting the accuracy of the results obtained through spirometry.

The 6-minute walk test (6MWT) [1] serves as a valuable alternative or complementary tool for assessing these patients. It offers a more comprehensive evaluation of functional capacity and endurance in real-world situations. The present study showed some preliminary results evaluating subjects' regional ventilation changes before and after 6-min walk.

2 Methods and results

Six subjects were scheduled for 6MWT. Their regional lung function was examined with EIT (VenTOM-100, MidasMED, Suzhou, China) before (T1) and at the end of 6MWT (T2) for 1 minute during relax tidal breathing period. To be exact, T2 is the last minute during the 6MWT (it was feasible with the wireless data collection module). The electrode belt was positioned at the 4-5 intercostal spaces to prevent any interference from abdominal volume changes in the EIT data. Pendelluft amplitude measured with EIT was calculated according to a previous study [2].
The indications of these subjects for 6MWT were: 2 were patients with COPD, 1 with asthma, 1 with hypertension, 1 reported chest tightness and abdominal distension, 1 had colon cancer. The asthma patient had bronchodilator before the 6MWT. The results were presented in Table 1.

Table 1. EIT-based pendelluft results (amplitude over tidal variation).

	T1	T2
1 (COPD)	7.0%	47.8%
2 (COPD)	0.5%	14.3%
3 (asthma post BD)	3.3%	2.9%
4	1.5%	2.3%
5	0.4%	2.1%
6	2.6%	3.5%

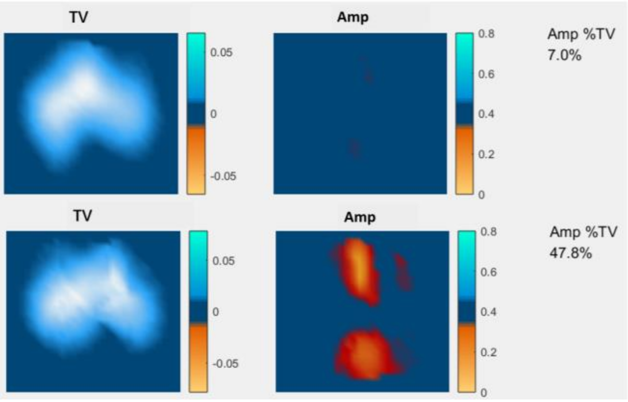

Figure1. The tidal variation (TV) and pendelluft amplitude (Amp) at T1 (1st row) and T2 (2nd row).

3 Discussion and conclusions

Attempts were made to assess lung functions during tidal breathing in patients with obstructive diseases without performing FVC [3]. Unfortunately, without the workload, patients with COPD might not exist any flow limitation. Therefore, we designed this study to add workload to the subjects' respiratory system to provoke their potential flow limitation. The preliminary results from 6 patients with and without obstructive lung disease indicated that our study design has the potential to identify the obstruction without performing FVC maneuver. Patients with COPD had a much higher increase in pendelluft after 5 minutes walking, which did not occur in other subjects, not even for the one with asthma, after he had the bronchodilator. Perhaps due to increased physical activity, the uneven distribution of alveolar air in COPD patients is exacerbated, cause an increase in pendelluft.
Unlike spirometry, which may be challenging for patients with obstructive lung diseases due to the forced breathing maneuvers involved, the 6MWT is generally well-tolerated as it involves walking on a flat surface at a self-selected pace for six minutes. This can be more feasible for patients who struggle with performing complex breathing tests. Unlike the controlled environment of spirometry, the 6MWT mimics daily activities by measuring the distance a person can walk in six minutes. This test reflects the individual's exercise tolerance and response to physical exertion in a practical setting.
Future study may include more subjects and evaluate the changes during 6MWT, instead of assessing only the changes before and at the end period.

References

[1] Holland AE, et al. Eur Respir J 2014; 44: 1428-1446.
[2] Sang L et al. Ann Transl Med. 2020; 8(19): 1216.
[3] Frerichs I et al. Front Physiol 2021; 12: 762791.

Comparing EIT Ventilation/Perfusion Assessment Approaches in Experimental Hypoxemic Acute Lung Injury

Zhe Li[1,2]*, Kilian Meissner[1], Guenter Hahn[1], Zhanqi Zhao[3,4,5], Mattia Busana[1], Simone Gattarello[1], Michael Quintel[1], Konrad Meissner[1], Leif Saager[1], Federica Romitti[1], Luciano Gattinoni[1], Onnen Moerer[1]
[1]Department of Anesthesiology, University Medical Center Göttingen, Göttingen, Germany. * Correspondence: slamy1987@126.com
[2]Department of Critical Care Medicine, Renji Hospital, School of Medicine, Shanghai Jiao Tong University, Shanghai, China
[3]School of Biomedical Engineering, Guangzhou Medical University, Guangzhou, China.
[4]Institute of Technical Medicine, Furtwangen University, Villingen-Schwenningen, Germany
[5]Department of Critical Care Medicine, Peking Union Medical College Hospital, Beijing, China

Abstract: This study compares two electrical impedance tomography (EIT) ventilation/perfusion (V/Q) assessment approaches in experimental hypoxemic Acute Lung Injury (ALI) pigs under extracorporeal membrane oxygenation (ECMO) support.

1 Introduction

EIT facilities bedside V/Q assessment and is increasingly used in supporting clinical management of hypoxia, especially during ALI. Various methods for calculating lung V/Q match have been reported to investigate the impact of clinical treatments on V/Q (prone positioning, positive end-expiratory pressure, etc) [1]. However, the consistency of different methods is uncertain. We compared two commonly used EIT V/Q assessment approaches in empirical ALI animal model to identify potential pitfalls when adapting current EIT V/Q analysis approaches to-clinical scenarios.

2 Methods

Four ALI pigs inducted by Oleic acid in a previous study were studied [2]. For regional lung perfusion monitoring, a 20 ml bolus of 10% NaCl was injected through the central venous catheter during an end-expiratory respiratory pause (>20s). EIT (Pulmovista 500®, Dräger Medical, Lübeck, Germany) continuously recorded ventilation and perfusion impedance values at 50Hz. Cardiac output (CO) was recorded through a pulmonary artery catheter (Arrow, International, USA). EIT ventilation and perfusion data at baseline and 8 hours after ALI were calculated using customed software (The MathWorks Inc., Natick, MA). Functional perfusion maps were derived from the slope of regional impedance-time curves post saline bolus injection [3]. For V/Q match assessment, the Area-limit-Approach (ALA) and Absolute-value-Approach (AVA) were employed, detailed approach describe refer to legend of Figure 1.

3 Results

The two V/Q approaches showed decreasing trends in V/Q match following ALI induction. At both baseline and 8 hours post-injury, the ALA exhibited a 3-18 times higher percentage of match compared to the AVA (Table 1). Additionally, the match region in the ALA corresponded to low V/Q regions in the AVA (Figure 1).

4 Conclusions

EIT V/Q assessment indicates a decline in match trends post-injury, aligning with disease physiology. However, V/Q match solely relying on the overlap of separately calculated ventilation and perfusion areas (ALA), may overestimate match areas by neglecting quantitative mismatches. Conversely, incorporating absolute resistance values (AVA) shows potential in quantifying V/Q value mismatches, albeit requiring further validation against gold standards. It's worth noting that this approach has been adapted to account for systemic abnormalities in the MV/CO ratio, potentially stemming from pathological and clinical conditions affecting CO and MV. In conclusion, a thorough evaluation of methods and application scenarios is essential before interpreting EIT V/Q match results.

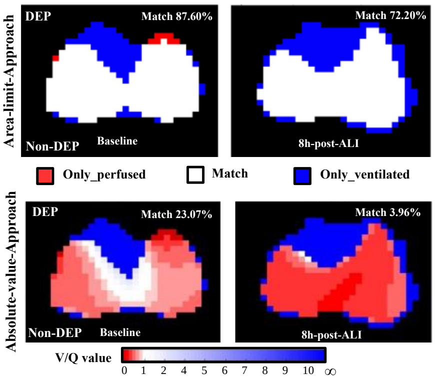

Figure 1: Representative lung V/Q match images from two EIT approaches in ALI pig model. In the Area-limit-Approach, areas were defined as ventilated by an impedance change exceeding 15% of the maximum global ventilation impedance change and perfused by 20% for perfusion, respectively. Ventilated areas with no perfusion are shown in blue, perfused regions with no ventilation in red, and Match areas with both ventilation and perfusion in white. In the Absolute-value-Approach, the absolute V/Q value was calculated by dividing pixel impedance values in ventilation normalized to alveolar minute ventilation (MV) by pixel values in perfusion normalized to cardiac output (CO). The color bar indicates V/Q values, with values between 0.8 and 1.25 considered normal (Match) [4].

Table 1. Ventilation/Perfusion Assessment in ECMO Supported ALI Pig Model by two EIT approaches.

EIT V/Q Assessment	Baseline	8h-post-Injury
Aera-limit-Approach(%)		
Only-ventilated	7.20 (6.20, 9.50)	27.00 (15.10, 35.00)
Only-perfused	9.50 (3.30, 5.60)	3.60 (0.80, 9.20)
Match	87.60 (85.90, 89.60)	72.20 (59.70, 81.30)
Absolute-value-Approach# (%)		
MVA (l/min)	4.53 (3.53, 4.76)	2.8 (2.60, 3.00)
CO (l/min)	5.90 (5.10, 6.20)	5.7 (4.90, 6.50)
non-ventilated	3.28 (2.93, 3.94)	3.65 (1.18, 7.46)
low V/Q	57.15 (47.89, 59.31)	70.70 (60.74, 75.40)
Normal (Match)	23.07 (17.85, 31.70)	3.96 (1.78, 7.11)
high V/Q	7.09 (5.72, 10.16)	0.14 (0.00, 0.28)
non-perfused	8.90 (6.35, 13.61)	27.01 (18.68, 32.87)

Abbreviations: ALI = acute lung injury; ECMO = extracorporeal membrane oxygenation; V/Q = ventilation/perfusion; MVA = alveolar minute ventilation; CO = Cardiac output. #non-ventilated: V/Q ratio ≤ 0.1; low V/Q: V/Q ratio 0.1–0.8; normal (Match): V/Q ratio 0.8–1.25; high V/Q: V/Q ratio1.25– 10; non-perfused: V/Q ratio ≥ 10. Data are described as median (Q1, Q3).

References

[1] Xu M, et al. Front Physiol. 2021; 12: 748724.
[2] Brusatori S, et al. Am J Respir Crit Care Med. 2023; 207(9): 1183-93.
[3] He H, et al. Am J Respir Crit Care Med. 2020; 202(6): 881-2.
[4] Pavlovsky et al. Critical Care (2022) 26: 211.

Smart Adhesive Bandage System for Detection of Intravenous Infusion Leakage Using Bioelectrical Impedance Measurement

Zhijun Li[1], Changhong Wang[1]

[1]Sun Yat-Sen University, Shenzhen, China

Abstract: This article introduces a smart adhesive bandage system designed for detecting intravenous infusion leakage using bioelectrical impedance measurement technologies. The system incorporates flexible electrode patches to enhance comfort and skin compatibility, identifying leakage events based on changes in electrical impedance measurements. Our experiments, simulating leakage on biological tissues, demonstrate that the system can detect extremely small leaks (~0.1 mL) with a high sensitivity of 90%.

1 Introduction

In intravenous infusion scenarios, leakage problems are common and may lead to serious complications, such as tissue necrosis. Traditional leakage detection mainly relies on naked eye observation by doctors. This method has obvious limitations in detecting small leakage, resulting in a low early detection rate. The development of leakage detection devices is of great clinical significance.

However, existing detection methods like Impedance threshold judgment [1], RF measurements [2] and Infrared light reflection measurement [3], are facing problems such as low detection accuracy, limited measurement depth, and low sensitivity to trace leakage. Therefore, this article is devoted to the development of an effective and low-cost device for detecting trace liquid leakage.

2 Methods

2.1 System design

The system consists of two main components: the impedance measurement module, responsible for measuring and transmitting bioelectrical impedance values of biological tissues, and the host computer calculation module, which utilizes various machine learning algorithms including Support Vector Machine (SVM), K-Nearest Neighbor (K-NN), decision trees, neural networks, etc., to analyse impedance data and produce leakage detection outcomes. Through experimentation, the most effective machine learning method is selected based on performance metrics. The cost of building the system is lower than $15, while the patch is as low as $1.

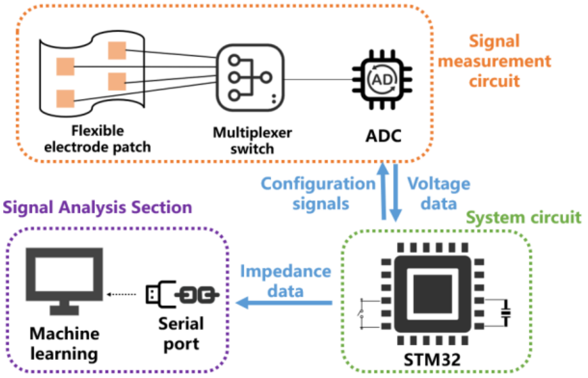

Figure 1: Impedance measurement process.

2.2 Experiment

Data collection was performed on a piece of pig leg to evaluate the accuracy, sensitivity, and minimum measurement volume of the system. In details, we injected a certain amount of saline into a piece of pig leg tissue multiple times to simulate constant leakage. Additionally, we introduced motion artifact data in some experiments to simulate four types of motion interferences: bending, stretching, torsion, and translation. Such introduction was aimed at evaluating the real performance of the system for coping with the motion interferences.

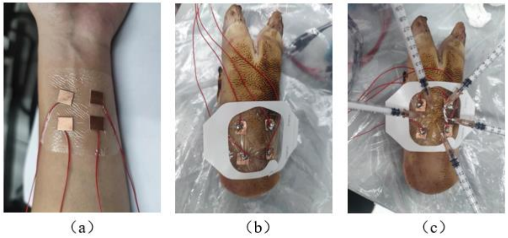
(a) (b) (c)

Figure 2: Pictures of experiment. (a) Soft electrode patch. (b) Measure the impedance value on pig leg. (c) Injecting liquid to simulate leakage.

3 Result

Among various machine learning methods, SVM demonstrates the highest performance. The system achieves an accuracy of 85%, sensitivity of 90%, and specificity of 80%.

Table 1: System performance comparison.

	Sensitivity (%)	Minimum detectable volume(mL)	Detection depth
Nelson R C [1]	90	2.8	Deep
Carr K L [2]	99.8	20	Shallow
Winchester L W [3]	93	0.1	Shallow
Ours	90	0.1	Deep

4 Conclusions

In this study, we introduce a smart adhesive bandage system designed to detect intravenous infusion leakage. This system accurately identifies extremely small leaks, even amidst motion artifact events, by measuring changes in bioelectrical impedance. Our findings suggest that this technology could be a promising tool for enhancing the safety of intravenous infusion procedures.

References

[1] Nelson R C, Anderson F A, Birnbaum B A, et al. Contrast media extravasation during dynamic CT: detection with an extravasation detection accessory[J]. Radiology, 1998, 209(3): 837-843.

[2] Carr K L. Use of gallium arsenide in medical applications[C]//GaAs IC Symposium IEEE Gallium Arsenide Integrated Circuit Symposium 17thAnnual Technical Digest 1995. 1995: 1013.

[3] Winchester L W, Chou N Y. Optical detection of intravenous infiltration[C]//COHN G E, GRUNDFEST W S, BENARON D A, et al. Biomedical Optics 2006. San Jose, CA, 2006: 608016.

Clinical trial feasibility evaluation of the effectiveness of an EIM system for breast cancer examination

Gerald Sze[1], Zhao Song[1,3] and Wei Wang[1,3,4]

[1]Micro Image Biotech Ltd, Ningbo, China
[2]Shanghai International Peace Maternity and Child Health Hospital of China Welfare Institute, China
[3]Micro Image Biotech International Ltd., Cambridge, UK
[4]Ningbo Weiying Biotechnology Co., Ltd., Ningbo, China

Abstract: This paper presents the evaluation of the clinical trial for seventy volunteers that carried out between August 2021 to January 2022 using an Electrical Impedance Mammography (EIM) system that was designed to detect human breast cancer.

1 Introduction

An electrical impedance mammography (EIM) system [1] has been developed and went through a series of clinical trials in the China Welfare Institute International Peace Maternal and Child Health Hospital. Results were evaluated with postoperative EIS experiment for the identification of cancer objects in EIM images reconstructed by a customized 3D image reconstruction algorithm [2]. There was a total of 100 cases in the first phase of clinical trial, 30 cases were eliminated in the early "system calibration/researcher training. Within the 70 cases, there were 75 sides of data (left or right side of breast) have been enrolled into the statistical analysis: 34 sides are benign (among 29 cases), 41 malignant sides (among 41 cases), plus 49 tumour-free sides, total 124 sides.

2 Methods

The preliminary results of these 70 cases in the first phase are mainly divided into two parts: A. Preliminary summary of "4+2 main evaluation indicators" using bioimpedance breast detector (EIM); B. Control group mammography, Preliminary summary of "4+2 main evaluation indicators" for combined breast ultrasound and mammography-ultrasound.

2.1 4+2 main evaluation indicators of EIM

Preliminary results of the “4+2 main evaluation indicators” conducted by EIM are listed in Tab. 1.

2.2 4+2 main evaluation indicators of EIM, US and combined EIM-US

Preliminary results of the "4+2 main evaluation indicators" of EIM, breast ultrasound and combined EIM-ultrasound are listed in Tab. 2.

3 Conclusions

Clinical studies have found that the missed detection rates of mammography and ultrasound equipment are still high, 30.77% and 14.63% respectively. If the "double gold standard" of "mammography-ultrasound combined examination", which is recognized as the best test for breast disease screening at home and abroad, is used, the missed detection rate can be significantly reduced to 7.69%; at the same time, the detected EIM "missed detection" rate” is currently controlled at around 12.2%.

This proves that with the full support of the international clinical trial team and the two teams (breast department and pathology department) of Shanghai International Maternity and Children's Hospital, a higher level of diagnosis of malignant tumours has been achieved. "Mammography + Breast Ultrasound" The "accuracy" and "specificity" of the joint test have reached a high level of between 92-93%.

The preliminary trial also showed that although there are still many aspects of EIM technology that need to be improved and updated, in terms of hard-core technology, it has initially surpassed the internationally accepted gold standard for breast screening "molybdenum and palladium" and the EIM technology that is being tested in China. The gold standard "breast ultrasound" is close to the effect of the combined test of "mammography + ultrasound". The "accuracy rate" and "specificity" of EIM have initially approached 88% and 94% respectively.

The current preliminary results show that EIM can detect most of the benign/malignant breast lesions that can be detected by mammography/breast ultrasound/breast magnetic resonance.

4 Acknowledgements

We acknowledge Shanghai International Peace Maternity and Child Health Hospital of China Welfare Institute who provided all data and the opportunities to run the clinical trial.

References

[1] W Wang, et al, Preliminary results from an EIT breast imaging simulation system. Physiol. Meas. 22, 39–48, 2001.

[2] X Zhang, et al, An image reconstruction algorithm for 3-D Electrical Impedance Mammography, IEEE trans on Medical Imaging vol. 33 no. 12, 2014

Table 1: Preliminary results of the “4+2 main evaluation indicators” conducted by EIM

	Sensitivity =a/(a+c)	Specificity =d/(b+d)	positive predictive value	negative predictive value	Missed detection rate	false positive rate
			=a/(a+b)	=d/(c+d)	=1- Sensitivity	=1- Specificity
Malignant (ma)	90.24%	95.18%	90.24%	95.18%	9.76%	4.82%
Benign (be)	85.29%	93.88%	90.63%	90.20%	14.71%	6.12%
ma+be average	87.77%	94.53%	90.43%	92.69%	12.23%	5.47%

Impact of Electrode Configurations on the Reconstruction of 3D Lung Electrical Impedance Tomography: A Numerical Study

Yifan Liu[1,2], Wenna Feng[1] and Feng Fu[3]

[1]Fourth Military Medical University, Xi'an, China, liuyifan@fmmu.edu.cn
[2]Research Institution, Xijing Hospital, Fourth Military Medical University, Xi'an, China

Abstract: Electrical impedance tomography (EIT) shows promising application value in thorax imaging, where a single layer of electrodes has typically been used to construct a transverse slice of the body. However, such 2D images omitted the inhomogeneities in vertical direction of physiological process above and below the electrode plane. Using two (or more) layers of parallelly arranged electrodes could provide more information on the vertical process in the thorax and be used to reconstruct 3D images. The electrical signals are closely related to the configurations of electrodes. In view of this, the impact of electrode configurations including size, spatial arrangement, and excitation/measurement patterns on the EIT reconstruction are numerically studied. By reconstruction of a series of targets, several FoM are evaluated and the relation between them and electrode configurations are analysed.

1 Introduction

By injecting a safe current into human body and measuring electric potential from the surface, EIT reconstruct the change of conductivity distribution that induced by physiological process in the body, showing promise for monitoring ventilation and blood perfusion in the thorax. In most common applications of EIT, a single transverse plane of electrodes has been used to reconstruct 2D images within the layer. However, the current flow in the body diffuses in 3D [1] and the physiological process is also inhomogeneous in vertical direction, which would be omitted in EIT with single layer of electrodes. With two (or more) layers of electrodes, more information in the vertical direction can be captured and 3D images are more readily to reconstruct. During this procedure, the distributions of current flow and measurement voltage are closely related to the configurations of electrodes, such as the position, size and the excitation/measurement patterns. Therefore, the impact of above electrode configurations on the reconstruction of 3D EIT images are numerically studied in this paper, providing insight into the robustness of 3D EIT and the improving single-slice EIT images from multiple electrode planes.

2 Methods

In this simulation study, two layers of electrodes are arranged in a 3D chest finite element model based on human body geometry. And a serious of small contrast at various positions in the model are simulated, as shown in Fig.1. Firstly, the voltage measurements are calculated with varied sizes of electrode, heights of lower electrode layers, and the different excitation/measurement patterns respectively. Then, 3D EIT images are reconstructed, in addition with 30 dB Gaussian white noise, through the Graz consensus reconstruction algorithm for EIT (GREIT) algorithm [2]. GREIT is a linear reconstruction for difference EIT. The images are obtained by multiplying difference voltage data by a reconstruction matrix **R** as given by

$$\mathbf{R} = \arg\min_{\mathbf{R}} \sum_k \left\| \tilde{\mathbf{x}}^{(k)} - \mathbf{R}\mathbf{y}^{(k)} \right\|^2_{\mathbf{w}^{(k)}} \qquad (1)$$

where $\tilde{\mathbf{x}}^{(k)}$ is the individual desired image, $\mathbf{y}^{(k)}$ is the corresponding measurement voltage, and $\mathbf{w}^{(k)}$ is a vector weighting individual desired image elements.

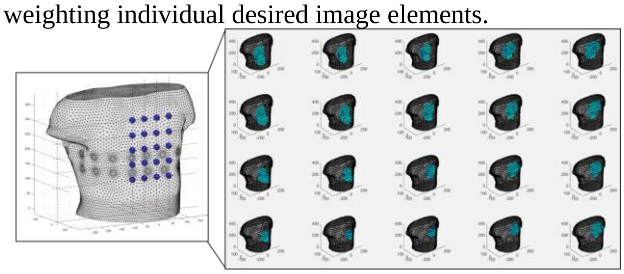

Figure 1: Simulation model with two electrode planes and the reconstructed small contrasts.

To evaluate the impact of different electrode configurations, GREIT FoM and the Z-resolution measure, i.e., amplitude response, position error, resolution, shape deformation, ringing and Z-resolution, are used [3] and the reconstruction images are compared.

3 Conclusions

Different electrode configurations have selective impact on the quality of 3D reconstruction. In general, the square pattern with alternate horizontal and vertical excitation and measurements shows better spatial resolution capability, while adjacent pattern shows more stable amplitude response for different small contrasts. Increasing the distance between the two electrode planes can suppress the ringing effect, but the spatial resolution capability is reduced as well. Smaller electrode improves the spatial resolution and amplitude response stability, but the influence of contact impedance needs to be considered comprehensively.

References

[1] B Grychtol, B Müller, A Adler *Physiol. Meas.*, 37: 785–800, 2016.
[2] A Adler, JH Arnold, R Bayford *Physiol. Meas.*, 30: S35, 2009.
[3] J Wagenaar, A Adler *Physiol. Meas.*, 37: 922–937, 2016.

Pulmonary Ventilation Heterogeneity Determined by Electrical Impedance Tomography during Pulmonary Function Testing in Patients with Normal One-second Rates

Jiayi Li[1], Runze He[1], Huiqing Ge[2], Zhanqi Zhao[3]

[1]Zhejiang university, School of medicine, Hangzhou, Zhejiang Province, China, 22218299@zju.edu.cn
[2]Sir Run Run Shaw Hospital, Zhejiang university, Hangzhou, China
[3]Guangzhou Medical University, Guangzhou, China

Abstract: The study aimed to assess if EIT could detect spatial and temporal heterogeneity during pulmonary function testing in patients with normal one-second rates. Based on pulmonary function testing and EIT, the PRISm (preserved ratio impaired spirometry) group exhibited a higher prevalence of hypertension, CAT score, SGRQ score and greater temporal and spatial heterogeneity. Receiver-operating characteristic curves indicated that the GI discriminated between PRISm and Normal groups. In the Normal group, subgroup analysis revealed differences in regional lung function. We can sensitively identify spatial and temporal heterogeneity in regional lung function among patients with normal one-second rates by EIT.

1 Introduction

Several large cross-sectional and longitudinal studies on PRISm have revealed its high prevalence. Notably, approximately 10% to 40% of patients with PRISm tend to develop COPD [1-2]. Moreover, patients with normal lung function are also at risk of converting to PRISm. In COPD patients, EIT combined with pulmonary function testing can evaluate the spatial and temporal distribution of lung capacity in different regions and identify pathologically induced ventilation heterogeneity [3].

2 Methods

The study is a prospective observational trial that enrolled 131 patients at the Sir Run Run Shaw Hospital. Based on pulmonary function testing and EIT examinations, we categorized 88 individuals into the Normal group and 26 into the PRISm group. The study compared differences in baseline characteristics, comorbidities, questionnaire scores, and EIT-related parameters. Quantitative indicators are compared by t-test or Mann-Whitney U test according to the data distribution. Categorical indicators are by chi-square test or exact probability method. ROC curves were generated to compare the predictive power of EIT parameters in distinguishing the PRISm patients and the Normal patients. P values < 0.05 were considered significant.Subgroup analysis was conducted based on symptom scores. Statistical analysis was performed with GraphPad Prism version 10.

2.1 Figures and tables

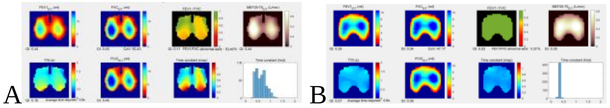

Figure 1: EIT analysis images during lung function testing. A: PRISm group; B: Normal group.

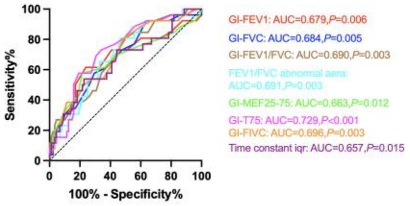

Figure 2: Receiver-operating characteristics (ROC) curves.

3 Results

In comparison to the Normal group, the PRISm group exhibited a higher prevalence of hypertension (*P*<0.001), CAT score (*P*=0.006), and SGRQ score (*P*=0.012). The PRISm group exhibited greater temporal and spatial heterogeneity in lung ventilation. ROC curves indicated that the GI of FVC, FEV1, FEV1/FVC, MEF25-75, T75, and FIVC discriminated between PRISm and Normal patients. In the Normal group, EIT can exhibit partially similar pulmonary function characteristics as observed in the PRISm group. Furthermore, subgroup analysis was conducted using a cutoff score of 25 on the SGRQ, revealing differences in regional lung function.

4 Conclusion

Through EIT-based pulmonary function assessment, we can sensitively identify spatial and temporal heterogeneity in regional lung function among patients with normal one-second rates.

References

[1] Higbee DH, Granell R.Lancet Respir Med 2022, 10: 149-157.
[2] Wijnant SRA, De Roos E, Kavousi M.Eur Respir J 2020, 55.
[3] Vogt B, Pulletz S, Zhao Z. J Appl Physiol (1985) 2012, 113.

Table 1: p-value of EIT parameters

	GI-FEV1	GI-FVC	GI- FEV1/FVC	abnormal area	GI-MEF25-75	GI-T75	Averaged time required	GI-FIVC	Time constant median	Time constant iqr
Normal vs PRISm	.005	.004	.003	.003	.011	.000	.269	.002	.125	.015
SGOQ<25 vs ≥25	.472	.791	.001	.004	.643	.006	.034	.666	.039	.009

A Feasibility Study on the Clinical Application of 3D Thoracic Impedance Imaging

Sheng Zhang[1], Zhe Liu[2,*], Yunjie Yang[2]
[1]Peking University Shenzhen Hospital, Shenzhen, China.
[2]SMART Group, Institute for Imaging, Data and Communications, School of Engineering, The University of Edinburgh, UK
(zz.liu@ed.ac.uk)

Abstract: In this study, we report on the clinical application of 3D EIT for imaging a patient with severe pneumonia. Compared to CT images, the results demonstrate the effectiveness of 3D EIT in visualizing the status of lung ventilation.

1 Introduction

Due to its low cost, absence of radiation risk and high temporal resolution, EIT serves as a powerful tool for monitoring lung function and evaluating patients with respiratory diseases, such as chronic obstructive pulmonary disease (COPD) [1] and acute respiratory distress syndrome (ARDS) [2]. However, in clinical practice, EIT is predominantly confined to 2D imaging. To obtain more comprehensive ventilation information about the patient, 3D EIT presents itself as a promising approach. Therefore, we recruited a patient with severe pneumonia to explore the feasibility of 3D EIT in capturing patients' ventilation features.

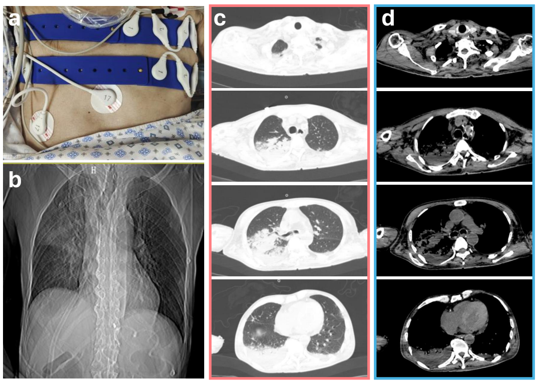

Figure 1: **a** 3D EIT belt setup on the patient. **b** Chest X-ray image. **c** Selected CT slices of the pulmonary window. **d** Selected CT slices of the mediastinum window.

2 Method

We first provide brief information about the patient and then describe the EIT imaging setup. The patient is male and 69 years old. He has had a recurrent cough with sputum for the past two months. Six days before admission, he experienced worsening dyspnea with increased sputum production and decreased oxygen saturation. Examination at the outpatient department diagnosed as severe pneumonia. With the oxygen saturation dropped to 90%, and the blood pressure dropped, he was hospitalized at Peking University Shenzhen Hospital. An emergency lung CT scan showed he suffered from multiple infiltrates, consolidation, and pleural effusion in both lungs, especially in the middle and upper lobes of the right lung. For the 3D EIT imaging setup, we employed two EIT belts: the first one is worn under the armpit, and the second one is worn under the nipple. The 3D EIT setup and the results of the CT examination are illustrated in Fig. 1.

3 Results

Fig. 2 shows the 3D EIT image reconstruction results. We illustrate the 3D images from both the front and back views (Fig. 2 **a** and **b**). The selected 2D images (Fig. 2 **d**) represent the caudal-cranial perspective, following a protocol consistent with the CT images. In Fig. 2 **c**, we map the middle coronal slice of the 3D image to the X-ray image. Suppose the tidal variation (TV) of the region of the right lung that is not ventilating is 1, the TV of the ventilation region is 2.67. The results indicate ventilation in the left lung of the patient while ventilation in the right lung is obstructed. The findings from the EIT images are consistent with those from the CT examinations.

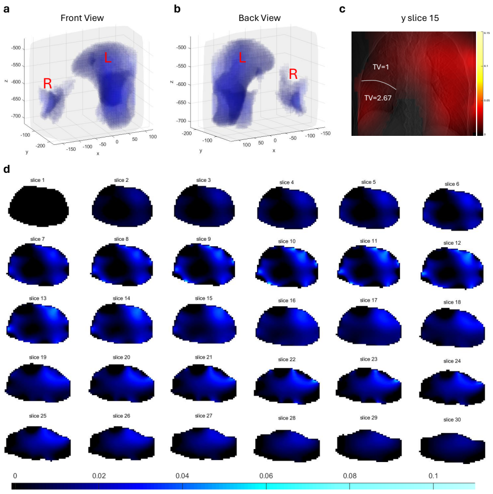

Figure 2: **a** and **b** are reconstructed 3D EIT images of the front view and back view. The 'L' indicates the left lung and 'R' indicates the right lung. In **c**, the white curve defines the boundary between the ventilated region and the non-ventilated region. TV means the tidal variation. Images in **d** are selected 2D caudal-cranial slices. **a**, **b**, and **d** share the same colormap.

4 Conclusions

We utilized 3D EIT for imaging the patient with severely impaired alveolar ventilation. The findings align with those of CT scans. Future work will involve systematically investigating the clinical applications of 3D EIT and optimizing the 3D image reconstruction algorithm.

References

[1] S. Milne et al., "Time-based pulmonary features from electrical impedance tomography demonstrate ventilation heterogeneity in chronic obstructive pulmonary disease," Journal of Applied Physiology, 2019.

[2] Z. Zhao et al., "The incidence and interpretation of large differences in EIT-based measures for PEEP titration in ARDS patients," Journal of clinical monitoring and computing, 2020.

Feasibility of Detecting Ineffective Inspiratory Effort during Mechanical Ventilation Using Electrical Impedance Tomography

Shuyang Jiang[1], Runze He[2], Lifeng Gu[1], Zhanqi Zhao[3], Huiqing Ge[2], and Qing Pan[1*]

[1]College of Information Engineering, Zhejiang University of Technology, Hangzhou, China, pqpq@zjut.edu.cn
[2]Department of Respiratory Care, Sir Run Run Shaw Hospital, School of Medicine, Zhejiang University, Hangzhou, China
[3]Department of Biomedical Engineering, Guangzhou Medical University, Guangzhou, China

Abstract: Accurate detection of patient-ventilator asynchrony (PVA) during mechanical ventilation relies on invasive monitoring of esophageal pressure or electrical activity of the diaphragm. Electrical impedance tomography (EIT) offers a promising opportunity to recognize PVA in a non-invasive manner. We proposed an index regional intensity fraction from EIT recordings to detect ineffective inspiratory effort during expiration (IEE), a typical type of PVA. The index obtains an area under characteristic curve of 0.94 on a cohort of 26 patients, showing promising potential for non-invasive PVA monitoring.

1 Introduction

Patient-ventilator asynchrony (PVA) is common in mechanically ventilated patients, causing increased respiratory workload, discomfort, and self-inflicted lung injury [1]. Esophageal pressure (Pes) is the invasive gold standard for detecting PVA. While a non-invasive method is needed, electrical impedance tomography (EIT) offers a non-invasive solution. This study developed an EIT-based algorithm to detect ineffective inspiratory effort during expiration (IEE), a common PVA type.

2 Methods

Twenty-six patients accepting invasive or non-invasive mechanical ventilation are involved. Patients are ventilated using SV800 or SV70 ventilator (Mindray, Shenzhen, C.N.) and monitored by PulmoVista 500 EIT device (Draeger, Luebeck, D.E.). Data are stored in the devices for off-line post analysis. The study is approved by the ethics committee of Sir Run Run Shaw Hospital, School of Medicine, Zhejiang University (2022 Research No.0375).

Ventilation waveforms (including the Paw, Flow, Volume and Pes) were loaded into a self-developed software for annotation. A junior respiratory therapist carried out the annotation, and a senior RT examined and corrected the result. IEE is marked when a negative deflection occurs in the Pes waveform during expiration or implicit IEE when no feature-specific variation in the ventilator waveform, but the Pes waveform has.

We developed an automated synchronization algorithm for aligning ventilation data with EIT across distinct devices. It first used piecewise linear representation to extract global features from the EIT impedance curve I(t) and ventilation volume waveform V(t). Then, a sliding window found the sequence with the minimum Euclidean distance between I(t) and V(t). Post initial synchronization, we refined the alignment by averaging time diffs within a moving window. We detected peak values from the refined volume waveform V(t) and computed phase differences. Finally, we performed outlier detection on the phase differences and computed the mean to obtain the final result.

Regional intensity fraction (RIF) was designed to capture the imbalanced ventilation distribution between the ventral and dorsal lung regions when IEE events [2]. The formulas for calculating RIF and ΔRIF are given below:

$$RIF(t) = \frac{Norm \cdot I_V'(t)}{Norm \cdot I_D'(t)} \tag{1}$$

$$\Delta RIF = RIF_{max} - RIF_{min} \tag{2}$$

Firstly, the first-order difference result $I_V'(t)$ and $I_D'(t)$ of $I_V(t)$ and $I_D(t)$ is normalized to 0.1to 1 using min-max normalization to get $Norm \cdot I_V'(t)$ and $Norm \cdot I_D'(t)$. Then, the RIF index changing with time can be obtained by using equation 1, where $I_V(t)$ represents ventral impedance and $I_D(t)$ represents dorsal. From equation 2, ΔRIF is defined as maximum change in RIF index during expiration.

3 Results and Conclusions

421 explicit and 8 implicit IEE were annotated from 11401 breaths. The optimal single-factor threshold for ΔRIF to discern IEE was determined as 0.5, yielding an area under the curve (AUC) of 0.94, demonstrating effective discriminatory accuracy. Eight implicit IEE breaths were all detected successfully. Typical IEE and non-IEE breaths are shown in Figure 1.

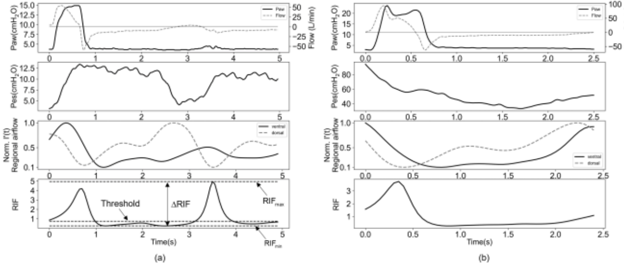

Figure 1: Illustration of IEE recognition based on ΔRIF, **(a)** IEE, **(b)** non-IEE

This study introduces a novel approach leveraging electrical impedance tomography (EIT) signals to identify IEE, highlighting the promising potential of EIT as a non-invasive tool for PVA monitoring.

4 Acknowledgements

This study is supported by National Natural Science Foundation of China (Grant No. 32371372, 82070087).

References

[1] Zhou Y, Holets SR, Li M, et al. *Sci Rep*, 11(1): 12390, 2021.
[2] Pan Q, Jia M, Ge H, et al. *Crit Care*, 25(1): 303, 2021.

Technical Specifications for Regional Lung Function Assessment Based on Electrical Impedance Tomography

Zhanqi Zhao[1,2], Lin Yang[3], Meng Dai[3], Huiqing Ge[4], Jiayi Li[4], Lixin Xie[5], Jingping Zheng[1]

[1]Guangzhou Medical University, Guangzhou, China, zhanqizhao@gzhmu.edu.cn; [2]Peking Union Medical College Hospital, Beijing, China; [3]Air Force Medical University, Xi'an, China; [4]Sir Run Run Shaw Hospital Affiliated to Zhejiang University, Hangzhou, China
[5]The Eighth Medical Center of Chinese PLA General Hospital, Beijing, China

Abstract: Regional lung function using EIT offers real-time functional insights not possible with traditional methods. Emerging from global research, this specification consolidates our centres' expertise, existing research, and expert consultations. Aimed at enhancing EIT's efficacy in detecting lung function, standardizing its application, and refining result interpretations.

1 Introduction

EIT has been widely utilized in the diagnosis and treatment of critically ill patients, such as PEEP titration, assessment of pendelluft, guiding weaning, and identifying pneumothorax [1]. In addition, there is growing interest in regional lung function assessment based on EIT. The impedance changes measured by EIT are highly correlated with changes in lung volume, forming the foundation for assessing regional lung function (flow obstruction and volume restriction), which provides clinicians with regional ventilation information that other detection methods cannot reflect [2]. This technical specification is primarily based on the previous clinical practice of our research groups and relevant literature. It has been discussed and agreed upon by clinical experts and biomedical engineering specialists in this field, with the aim of promoting standardized and improved use of EIT in detecting regional lung function and facilitating unified result interpretations.

2 Indications and Contraindications

Major indications include: (1) Early screening for lung function abnormalities in the general healthy population or high-risk groups to assist in the early diagnosis of regional lung function impairment; (2) Bedside diagnosis and treatment evaluation for patients with obstructive, restrictive, or mixed ventilation dysfunction; (3) Guiding rehabilitation training for patients with lung function impairments.

Relative contraindications: (1) Presence of pacemakers or implantable cardioverter defibrillators (depending on the operating frequency of the EIT device and the model of the implanted device); (2) Local skin infections or open wounds in the chest electrode binding area for EIT monitoring (electrodes cannot adhere to the skin); (3) Pregnancy (the current is within a safe range theoretically posing no risk to the fetus, but lacking clinical research evidence); (4) Subjects with neuromuscular diseases such as myasthenia gravis or muscular dystrophy (electrode binding may restrict their breathing).

3 EIT measurement and data analysis

EIT measurement procedure is documented in detail in the previous consensus [3]. EIT is conducted simultaneously with forced vital capacity manoeuvre, which is specified in a technical statement [4].

Following data reconstruction, a typical single EIT image consists of 32×32 pixels. The main components of data analysis are as follows:

A: Lung ventilation time - global impedance curve quality assessment.

Poor electrode contact tends to occur during forceful expiration. Any significant discontinuities, bends, or fluctuations in the curve during this phase indicate interference and should be identified and eliminated.

B: Construction of regional lung function images (based on traditional lung function metrics).

From pixel-wise impedance-time curves, parameters such as FEV_1, FVC and the corresponding ratio can be derived.

C: Construction of regional lung function images (temporal images)

Time series images characterize regional temporal distribution and variability based on different exhaled volumes during forceful vital capacity. These images accurately reflect time required for specific exhalation volumes, representing respiratory muscle explosiveness, endurance, and lung function integrity. Two types of indicators are often calculated: time constants and gas distribution time for varying exhaled volumes. They offer insights into regional flow limitations and lung damage presence.

4 Perspectives

EIT can quickly provide visual information on lung ventilation and airflow distribution bedside. It features characteristics assisting in early screening of lung function in the general population or high-risk groups to detect regional lung function damage early. Bedside assessment of patients with impaired lung function, as well as guiding the rehabilitation training of patients with impaired lung function, are important applications of significant value.

The clinical application of regional lung function using EIT is still in its early stages. Relevant thresholds and diagnostic criteria in different specific diseases need further validation through large-scale clinical studies. In clinical practice, the application of EIT should be combined with other indicators and methods for mutual confirmation.

References

[1] He H et al. Crit Care. 2021; 25(1): 230.
[2] Zhao Z et al. Physiol Meas. 2013; 34(11): N107-114.
[3] Frerichs I et al. Thorax, 2017; 72(1): 83-93.
[4] Graham BL, et al. Am J Respir Crit Care Med. 2019; 200: e70-e88.